

Bangor University

DOCTOR OF PHILOSOPHY

Compositionally Complex Alloys in Accident Tolerant Fuel Coating Systems

Wilson, Jack

Award date:
2023

Awarding institution:
Bangor University

[Link to publication](#)

General rights

Copyright and moral rights for the publications made accessible in the public portal are retained by the authors and/or other copyright owners and it is a condition of accessing publications that users recognise and abide by the legal requirements associated with these rights.

- Users may download and print one copy of any publication from the public portal for the purpose of private study or research.
- You may not further distribute the material or use it for any profit-making activity or commercial gain
- You may freely distribute the URL identifying the publication in the public portal ?

Take down policy

If you believe that this document breaches copyright please contact us providing details, and we will remove access to the work immediately and investigate your claim.

Download date: 26. Apr. 2024

Compositionally Complex Alloys in Accident Tolerant Fuel Coating Systems

Jack Anthony Wilson



PRIFYSGOL
BANGOR
UNIVERSITY

School of Computer Science and Electronic Engineering

College of Environmental Sciences and Engineering

Submitted in partial satisfaction of the requirements for the
Degree of Doctor of Philosophy in Nuclear Engineering and Science.

December 2022

Declaration

I hereby declare that this thesis is the results of my own investigations, except where otherwise stated. All other sources are acknowledged by bibliographic references. This work has not previously been accepted in substance for any degree and is not being concurrently submitted in candidature for any degree unless, as agreed by the University, for approved dual awards.

Yr wyf drwy hyn yn datgan mai canlyniad fy ymchwil fy hun yw'r thesis hwn, ac eithrio lle nodir yn wahanol. Caiff ffynonellau eraill eu cydnabod gan droednodiadau yn rhoi cyfeiriadau eglur. Nid ywsylwedd y gwaith hwn wedi cael ei dderbyn o'r blaen ar gyfer unrhyw radd, ac nid yw'n cael ei gyflwyno ar yr un pryd mewn ymgeisiaeth am unrhyw radd oni bai ei fod, fel y cytunwyd gan y Brifysgol, am gymwysterau deuol cymeradwy

Abstract

The Hf-Mo-Nb-Ta-Ti-W-Zr system of compositionally complex alloys have been studied in this work by means of density functional theory modelling techniques in order to understand the usage of these novel alloy systems within the nuclear sector. Especially, this endeavour has sought to meet the materials design criteria for an interlayer material between zirconium-based fuel claddings, used in current light water nuclear reactors, and current chromium coatings, using compositionally complex alloys that are characterised as compositing four or more metallic elements in close to equal ratios.

An analysis of the particular environment at the nuclear fuel cladding surface – characterised by its high temperature, corrosiveness and irradiation – has prompted meticulous materials design criteria for combining chromium coatings to zirconium-based claddings. This design criterion is put in place to ensure these two materials can stay separated for a greater period of time should a loss-of-cooling nuclear accident occur. This analysis suggested two equiatomic refractory alloys as a suggested starting point for an interlayered coating system: MoNbTaW and MoNbTaTiW.

With regard to the fundamental thermophysical properties of compositionally complex alloys, atomistic simulation has revealed for the first time a straightforward mechanism for thermal expansion in these alloys, which can be directly related to their constituent elements. By means of alloys in the Mo-Nb-Ta-Ti-W system, it is possible to precisely tailor the thermal expansion response of an interlayer alloy so as to optimise expansion between zirconium-based fuel claddings and coating materials. The role of vacancy defects in these alloys, and their consequences for expansion behaviour are also explored. An in-depth analysis of vacancy defects in the Hf-Mo-Nb-Ta-Ti-W-Zr system has revealed the role configurational entropy plays in the formation of intrinsic defects, and an alternative mechanism to explain the higher concentration of vacancies observed in complex solid solution alloys is suggested. This argument rests upon the chemically disordered environment which occurs around each vacancy site, and may be generalisable to all alloy systems, even more dilute ones. The findings indicate that compositionally complex alloys possess a substantially higher number of vacancies than conventional alloy systems and pure metals, which could have impacts on the radiation damage of compositionally complex alloys.

Regarding the testing of compositionally complex alloys in real zirconium-based alloy coating systems, a pathway is laid out to explore properties such as eutectic reaction

temperatures, oxidation, spalling phenomena, interdiffusion, and chemical reactions, in laboratory-scale testing. It is shown that an adequate assessment of these coating systems is possible on a small scale and can aid future efforts to develop and optimise interlayered materials in zirconium fuel cladding coating systems.

Acknowledgements

I would like to extend my sincere appreciation to the National Nuclear Laboratory and the Nuclear Energy Futures Centre for Doctoral Training for their financial contribution to my PhD project. Their support has been invaluable. I would also like to thank colleagues at the Nuclear Futures Institute for their ongoing guidance and assistance throughout the duration of my studies.

Contents

Introduction.....	10
Chapter 1. Literature review	13
1.1 Accident Tolerant Fuels (ATFs)	13
1.1.1 Leading accident tolerant fuel concepts	14
1.1.2 Chromium coatings	17
1.1.2.1 Current understanding	17
1.1.2.2 Performance during loss-of-coolant accidents	18
1.1.2.3 Spalling and cracking	21
1.1.3 Cr coating interlayers	22
1.1.3.1 Molybdenum.....	23
1.1.3.2 Tantalum.....	26
1.1.3.3 Stainless steel.....	27
1.1.3.4 Tungsten	27
1.2 Compositionally complex alloys.....	29
1.2.1 Definition	30
1.2.2 General properties	32
1.2.3 Radiation resistance.....	34
1.2.4 Welding with compositionally complex alloy fillers	35
1.2.5 Predicting stability.....	36
1.2.5.1 The parametric approach	39
1.2.5.2 Calculation of phase diagrams (CALPHAD).....	49
1.2.5.3 Studying phase stability experimentally.....	50
1.2.6 Fabrication.....	51
1.2.6.1 Solid-state processing	51
1.2.6.2 Liquid-state processing.....	52
1.2.6.3 Thin-film deposition	53
1.2.7 Compositionally complex alloy coatings for nuclear fuel claddings	54
1.2.8 Oxidation of refractory compositionally complex alloys.....	56
1.2.8.1 Oxidation resistance strategies	57
1.2.9 Compositionally complex alloys as Zr-Cr interlayers.....	58
Chapter 2. Methodology	62
2.1 Density functional theory	62

2.1.1. Convergence testing	68
2.2 Special quasi-random structures.....	70
2.3 Quasi-harmonic approximation.....	71
2.4 Density functional perturbation theory	72
2.5 Equation of states	73
2.6 Calculation of phase diagrams	73
2.7 Arc melting.....	75
2.8 High-energy planetary ball milling	77
2.9 Magnetron sputtering	78
2.10 Surface preparation	79
2.11 X-ray diffraction.....	79
2.12 Scanning electron microscopy	81
2.13 Energy dispersive spectroscopy	81
2.14 Simultaneous thermal analysis.....	82
2.15 X-ray fluorescence spectroscopy	83
2.16 Atomic force microscopy	84
Chapter 3. Materials design – selecting an interlayer	85
3.1 Element screening	85
3.1.1 Thermal neutron absorption cross-section.....	85
3.1.2 Physical properties.....	86
3.1.3 Oxidation	89
3.1.4 Thermal expansion	93
3.2 Interlayer selection	94
3.2.1 Phase stability in MoNbTaTiW and MoNbTaW.....	94
3.2.2 Driving forces for oxidation in the Mo-Nb-Ta-Ti-W system.....	97
Chapter 4. Thermal expansion of compositionally complex alloys.....	101
4.1 Introduction	101
4.2 Methodology	104
4.2.1 Convergence testing	105
4.2.2 The Mo-V system	106
4.2.3 Choice of pseudopotentials.....	107
4.3 Results	112
4.3.1 Lattice constant.....	112

4.3.3 Thermal expansion in the Mo-Nb-Ta-Ti-W system	113
4.4 Summary	122
4.5 Further considerations	122
4.5.1 Composite science	122
4.5.2 Effect of vacancy concentration on thermal expansion.....	125
4.5.3 Implications for an interlayer	125
4.5.4 Future work.....	126
Chapter 5. Vacancy defects in compositionally complex alloys	128
5.1 Definitions	128
5.1.1 Vacancy defects	128
5.1.2 Equilibrium vacancy concentration	129
5.1.3 Role of configurational entropy	132
5.2. Assessing vacancies in refractory compositionally complex alloys	136
5.2.1 Convergence testing	137
5.2.2 Calculating local bias.....	138
5.2.3 Calculating vacancy volumes	140
5.2.4 Vacancy formation enthalpy calculations.....	141
5.3 Results	142
5.3.1 Phase stability and structure	142
5.3.2 Lattice constants	145
5.3.3 Vacancy formation enthalpies	148
5.3.4 Migration of monovacancies	154
5.3.5 Population of vacancies in Hf-Mo-Nb-Ta-Ti-W-Zr quinary alloys	156
5.4 Other considerations.....	162
5.4.1 Defect volume and effect on thermal expansion	162
5.4.2 Compositionally complex alloys in the nuclear environment	163
Chapter 6. Evaluating MoNbTaW as an interlayer.....	165
6.1 Tube furnace sintering.....	165
6.1.1 High energy ball-milling followed by sintering	170
6.2 Arc melting.....	170
6.2.1 Etching.....	173
6.3 Magnetron sputtering	173
6.3.1 Magnetron sputtering of MoNbTaW and Cr	175

6.3.2 Crystal structure determination of MoNbTaW thin films	178
6.3.4. Adherence of MoNbTaW-Cr coatings	181
6.4 Eutectic reaction temperatures	182
6.4.1 Gold calibration	186
6.4.2 Zirconium	188
6.4.3 Chromium	188
6.4.5 Zirconium-chromium eutectic	190
6.5 Oxidation and interdiffusion tests of MoNbTaW-Cr coatings.....	193
6.5.1 Oxidative mass gain.....	193
6.5.2 Rapid-onset oxidation temperature.....	196
6.5.2.1 Preliminary Zircaloy-2 oxidations.....	197
6.5.2.2 Zircaloy-2 oxidation baselines.....	202
Chapter 7. Conclusion.....	205
Chapter 8. Further work suggestions	207
7.1 MoNbTaW and MoNbTaTiW as a Zr-Cr interlayered coating system.	207
7.1.1 Thermal cycling of MoNbTaW coating	208
7.2. Searching the multi-dimensional phase space for potential alloys.	208
7.3. Fundamentals of refractory compositionally complex alloys.	209
Bibliography	210

Introduction

The development of accident tolerant fuels (ATFs) for nuclear reactors is an important step towards improving the safety and reliability of nuclear power plants. In 2014, ATFs were first introduced by the US Department of Energy as a set of goals for materials designed to withstand the extreme conditions that occur in a loss-of-coolant accident (LOCA), as well as to improve performance during normal operation. Developing these fuels requires materials capable of withstanding high temperature, corrosive, and radiation environments. As the most common type of reactor, light water nuclear reactors are currently equipped with zirconium cladding fuel pins which can be susceptible to rapid oxidation in high-temperature steam environments, which can lead to catastrophic failure of the fuel pin. Current coating solutions such as a Cr coating have been known to exhibit interdiffusion with the Zr alloy cladding material and lead to brittle intermetallic formation, which can lead to the eventual failure of the fuel pin. This presents an engineering opportunity to design interlayer materials to mitigate diffusion between Cr coatings and Zr-based alloy fuel cladding.

Compositionally complex alloys have been of considerable interest since their introduction in 2004, as they have the potential to revolutionise industries in the aerospace and energy sectors, among others. Their properties, such as thermal stability, high-temperature strength, sluggish diffusion, and radiation resistance, make them attractive for further study and open the design space to exploit novel and tailored alloy compositions. They have been said to possess superior mechanical properties, such as slow diffusion kinetics, high entropy effects, and radiation resistance. However, the mechanisms behind these properties remain underdeveloped and a critical analysis of these alloys is needed to verify these claims and understand their potential application in industry. In particular, the sluggish diffusion effect has yet to be confirmed as a general property of compositionally complex alloys, and the stabilising effect of large configurational entropy has only been observed in a few cases. Additionally, the mechanisms that give these alloys their radiation resistance are only just beginning to be understood. Moreover, the sheer number of alloys available, creates a challenge for scientists, as they traverse multidimensional phase space.

The aim of this thesis is to examine the potential of compositionally complex alloys for use in the nuclear industry, with a focus on their application in fuel pin coating systems, and the challenges which could be encountered in their use. The goal of this thesis is to develop an understanding of some of the fundamental behaviour of compositionally complex alloys in

order that their general properties can be critically evaluated for use as nuclear materials. To achieve this, this thesis investigates the use of compositionally complex alloy interlayers between Zr substrates and Cr coatings to reduce interdiffusion and improve coping times in the event of a LOCA. Specifically, the following research points are addressed:

- The use of atomistic modelling to explore compositionally complex alloys and their potential use in fuel pin coating systems.
- The claim that compositionally complex alloys may provide a more robust alternative to current materials.
- The general thermal expansion behaviour of concentrated solid solutions, with attention paid to the effects of alloy composition.
- Analysis of vacancy defect formation enthalpies and subsequent equilibrium concentrations of vacancies in concentrated solid solutions.
- Finally, the practical considerations regarding the fabrication of compositionally complex alloys are also discussed.

The remainder of the thesis is structured as follows:

In **Chapter 1: Literature Review**, an examination of the pertinent literature is performed to discuss the present understanding of accident tolerant or advanced technology fuels (making use of both terms interchangeably). An elucidation of how the concept came to be and a description of the technologies currently being examined are illustrated. Furthermore, existing fuel pin coating solutions and their advantages and disadvantages are introduced. The concept of interlayered coating solutions is also presented and the few investigations which have been carried out on these materials are evaluated.

Explanations of the atomistic modelling and experimental techniques used in the rest of the thesis are provided in **Chapter 2: Methodology**.

Chapter 3: Materials Design – Selecting an Interlayer explores the periodic table to discuss compositionally complex alloy compositions for evaluation as interlayers between Cr coatings and Zr-based fuel pins. Two alloys are suggested, MoNbTaW, and MoNbTaTiW, as prototypes to evaluate experimentally as Cr-Zr interlayers.

In **Chapter 4: Thermal Expansion of compositionally complex alloys**, the thermal expansion behaviour of alloys in the Mo-Nb-Ta-Ti-W system with increasing complexity is modelled for the first time. First-principles modelling is used to show that the expansion

behaviour of these refractory concentrated solid solutions is an averaging scheme of the constituent elements. Implications for the use of such alloys as interlayers between Cr coatings and Zr-based fuel pins are drawn, including the possibility for tailoring expansion behaviour for specific applications.

Chapter 5: Vacancy defects in compositionally complex alloys explores vacancy defect energetics in 21 quinary equiatomic alloys in the Hf-Mo-Nb-Ta-Ti-W-Zr system. The role of configurational entropy in the equilibrium vacancy concentration is critically evaluated, and a novel mechanism for the high equilibrium concentration of vacancies observed in these concentrated solid solutions is suggested.

Chapter 6: Evaluating MoNbTaW as an interlayer examines efforts to manufacture compositionally complex refractory alloys and describes lab-building efforts to properly evaluate these alloys as fuel coating interlayers.

Chapter 7: Conclusions concludes with summarising the main findings of the thesis and highlights original contributions to the understanding of compositionally complex alloys to accident tolerant fuel coatings.

In Chapter 8: Further work suggestions, potential avenues for the evaluation of the basic materials properties and mechanisms of compositionally complex alloys in a nuclear environment, as well as future efforts to assess the applicability of two model compositionally complex alloys as interlayer materials for Cr coatings in nuclear fuel pins, are explored.

Chapter 1. Literature review

1.1 Accident Tolerant Fuels (ATFs)

The Fukushima Daiichi disaster was the most severe nuclear accident to occur since Chernobyl, and the only other accident to receive the level 7 event classification on the International Nuclear Event Scale [1]. Upon detection of the Tōhoku earthquake and tsunami on Friday, 11th March 2011, active reactors at the Fukushima Daiichi plant shut down their normal fission reactions. Combined with other electrical grid supply problems, external power supply to these reactors was lost, and their emergency diesel generators automatically started. These were required to provide electrical power to pump coolant through the reactor cores and are essential to remove decay heat which continues to be produced for a time after fission has stopped [2]. However, the subsequent tsunami flooded the lower parts of reactors 1 – 4 which is where the generators were located, causing their failure [3]. The resulting loss of coolant flowing through the reactor cores led to three nuclear meltdowns, and three hydrogen explosions, leading to release of fission products into the atmosphere. It is estimated that reactors 1 – 3 each produced 800 – 1000 kg of hydrogen gas. This gas was vented out of the reactor pressure vessel where it mixed with ambient air, until it met explosive concentration limits in units 1 and 3. Unit 4 also filled with hydrogen, either from piping connections between units 3 and 4, or from the same zirconium fuel clad-steam reaction occurring in the spent fuel pool. This too resulted in a hydrogen explosion.

The hydrogen gas which caused both the explosions and subsequent release of fission products originated primarily from reactions occurring at the fuel clad surface. Nuclear fuel, in its current form in generation III light water reactors, is made up of UO_2 pellets encased in zirconium-based alloy cladding which separates the UO_2 pellets from coolant water in the primary circuit loop. The advantages of zirconium as cladding material are its unique combination of good corrosion resistance in the water chemistry at 300°C and low capture cross-section for thermal neutrons, and were known in the 1950s. Zirconium was used in pressurised water reactors in submarines well before the proliferation of the civil nuclear industry [4]. Zirconium was then used later in large civil nuclear reactors when the price of pure zirconium decreased to economical levels [4]. Zirconium cladding has undergone various optimisations via minute additions of other alloying elements, but its categorical presence in fuel cladding has never seriously been challenged, although this may change due to the recent development of iron-based alloys, silicon-carbide composites [5]–[7], and multilayer

molybdenum cladding [8]–[10]. At normal operating temperatures, a film of zirconium oxide, ZrO_2 , protects the zirconium clad and renders it inert [11]. However, above 1200°C zirconium metal (Zr) reacts exothermically with water to form hydrogen gas according to **Equation 1**:



The reaction between Zr and high temperature H_2O is highly exothermic [12]. For a light water reactor under loss-of-coolant accident conditions, this reaction has two main consequences. Firstly, it accelerates the rate of reaction by locally raising the temperature at the clad surface, thereby exacerbating the issues associated with an already overheating reactor [13]. Secondly, the reaction produces hydrogen gas, a highly flammable material which can collect in pockets within the reactor core, prone to igniting unless it is constantly vented. Engineering a solution to remove hydrogen gas from the overheating core is also problematic: loss-of-coolant accidents are often associated with a loss of power, and pumps to remove H_2 gas may be offline. We are also limited by the sheer amount of H_2 gas produced. Modelling work by Saji *et al.* [14] suggested that H_2 gas accumulation shortly after the reactor trips of units 1 – 3 at the Fukushima Daiichi plant exceeded 3000 m^3 . An attempt to remove this H_2 gas from the reactor core is a difficult engineering challenge. A more reasoned approach is to avoid the use of Zr in the reactor core altogether, but the wide-spread use of zirconium as a fuel cladding material was solidified long ago [4], and the material has since developed over 70 years of operational experience. Consequently, there would need to be clear benefits for developers to move away from Zr. Nevertheless, recent events in nuclear history have brought this shortcoming in reactor design to the spotlight and has subsequently led to the development of a range of safety-enhancing concepts known collectively as Accident Tolerant Fuels (ATFs).

1.1.1 Leading accident tolerant fuel concepts

It was after the Fukushima Daiichi nuclear accident that the concept of Accident Tolerant Fuels (ATF) was proposed [15]. ATFs aim to tolerate loss of active core cooling for a considerably longer time, and to a higher temperature than current fuel systems, whilst maintaining or improving fuel performance under normal operation [9]. To this end, two distinct strategies have developed.

The first ideates alternative clad materials, thus avoiding zirconium altogether. These designs include iron-based alloys, silicon-carbide composites [5]–[7], MAX phase materials,

and multilayer molybdenum cladding [8]–[10], which aim to improve on the vulnerabilities of current zirconium cladding. These alternative materials represent a large departure from the current Zr/UO₂ system and as such, may require major redesign of the reactor core; a challenge which naturally suggests long lead-times and delayed deployment.

A second strategy, aiming to avoid long-lead times, utilises protective coatings on already-existing Zr/UO₂ clad designs. It is thought that by modifying the current clad surface, we can mitigate corrosion behaviour without completely overhauling the standard Zr/UO₂ fuel system (**Figure 1**).

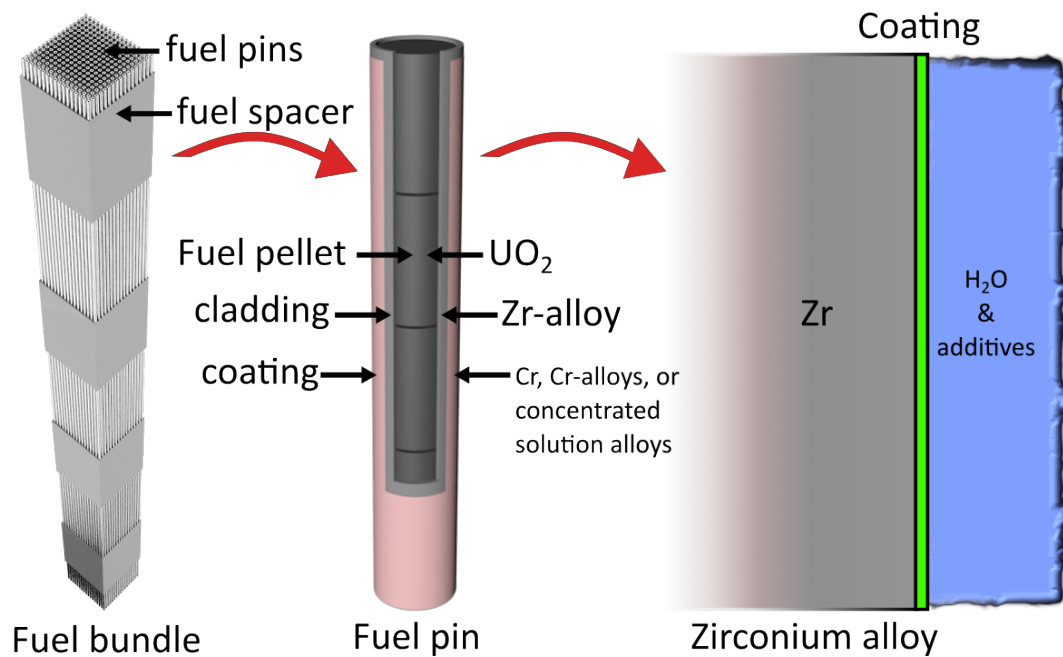


Figure 1. Coatings are seen as a cost-effective method to mitigate oxidation of zirconium at high temperatures.

The requirements for an ATF have been echoed by several institutions [9], [16], [25]–[28], [17]–[24]. Common to most requirements is the need to lower kinetics of the steam-reaction and therefore reduce (or avoid entirely) the production of H₂ gas and accompanying reaction heat in the event of an accident [16], [17], [19]–[22], [26]–[28]. Such changes allow for fuel to tolerate loss of active cooling for longer, giving additional coping time in the event that water cannot be actively supplied to the core, like in a power outage or reactor leg break [9], [17], [18], [23], [24]. An ATF should also maintain strength at high temperature such that the cladding does not lose its coolable geometry nor its structural integrity [16], [21]. The onset of balloon-and-burst phenomena, in which structurally weakened claddings swell outwards in response to high internal rod pressure and eventually rupture, should be delayed to as high a

temperature as possible. During the quench process as active cooling returns, an ATF should delay embrittlement failure of the cladding [17]. Finally, an ATF should not reduce fuel performance compared to current UO_2/Zr systems under normal operations [16], [18], and should be economically competitive to apply to commercial nuclear power plants [23]. The profusion of literature on current general ATF concepts have been reviewed and the reader is referred to these studies [16], [26].

Many coatings have been investigated for Zr-based cladding [29]. These coatings can be broadly categorised as metallic [25], [30]–[38], ceramic [39]–[47], and multilayer coatings [34], [48]–[51]. Metallic coats include Sn [30], Cr [17], [22], [56]–[65], [25], [66], [67], [32]–[34], [52]–[55], doped Zr or intermetallics [36]–[37], and FeCrAl alloy coating [38]–[39]. Ceramic coatings largely consist of oxides [39], carbides [40]–[41] (including MAX phases [41]–[44]), and nitrides [45]–[47] based on Al, Si/Ti/Cr, and Ti/Cr/Al, respectively. Multilayer coatings utilise either interlayers such as Mo [34] or alternating sublayers of aforesaid metallic or ceramic coats [48]–[51].

Much of the design strategy of developing zirconium cladding coatings has been based on exploiting the known oxidation resistance of elements like Cr, Si, Al, and Ti; surface oxidation of these elements is known to form a dense oxide film that renders the metal inert [29]. Tests on Al_2O_3 and SiO_2 scales – which withstand higher temperatures in steam than Cr_2O_3 – are found to be unstable due to water corrosion and solubility in the coolant. Meanwhile, scales of Si and Al-based coatings fail to form the dense oxide scales during high temperature oxidation. Ti, Ni, and Fe-based coatings show good performance under normal conditions, but their improvement over conventional cladding in high-steam environments is limited.

The leading strategy and the solution most near to deployment is a dense, adherent metallic coat of chromium. Although limited to withstand temperatures up to $\sim 1200^\circ\text{C}$, chromium performs well under both normal conditions and in high-temperature oxidising environments. Early studies on metallic chromium coatings were encouraging [57]. The performance of chromium was subsequently corroborated by several studies [20], [22], [54]–[56], [68], [69] and is now an interest to several institutions, confirming a growing international interest in Cr-coated Zr-based alloys [19], [23], [25], [33], [34], [50], [59], [70].

1.1.2 Chromium coatings

1.1.2.1 Current understanding

Pure chromium has been investigated as a coating material because of its mix of good mechanical properties: corrosion resistance, high melting point, good strength, high hardness, and good wear resistance [59]. The metal absorbs fewer neutrons needed for nuclear fission to occur due to its low neutron absorption cross-section. Chromium is abundant in the earth's crust, above nickel, copper, and tin; as a result, chromium is widely available at a reasonable cost. Operational experience for chromium already exists as it was used as a control rod plating to increase wear resistance in some light water reactors [71]. The metal also exists as a common alloying element in core structural steels. Chromium has similar thermal expansion to the underlying zirconium substrate [59]. The mechanical properties of Cr and Zircaloy-4 at room temperature have been compared by Ševeček *et al.* [59] and Wagih *et al.* [62] and are summarised in **Table 1**.

Table 1. Properties of Cr and Zr at room temperature [59], [62].

Material property	Chromium	Zircaloy-4
Ultimate tensile strength [MPa]	413	517
Yield strength [MPa]	362	348
Young's modulus [GPa]	140 (PVD coating)	99.3
Elongation [%]	0%	23%
Poisson's ratio	0.21	0.37
Coefficient of thermal expansion [$\mu\text{m}/\text{m}^\circ\text{C}$]	6.20	6.00
Thermal conductivity [W/m-K]	69.1	21.5
Melting point/Eutectic [$^\circ\text{C}$]	1860/1310	1850/1310
Specific heat capacity [J/g- $^\circ\text{C}$]	0.461	0.285
Density [g/cm^3]	7.19	6.56
Crystal structure	bcc	HCP < $\sim 800^\circ\text{C}$ < HCP + BCC < $\sim 1000^\circ\text{C}$ < BCC
Thermal neutron absorption cross-section, σ_a [barn]	3.1	0.2

Metallic chromium for light water reactor fuel rod coatings have been studied extensively in the academic literature [72]. Various studies have shown that Cr-coat reduces the $\text{Zr-H}_2\text{O}_{(\text{g})}$ reaction rate, delays the onset of balloon-and-burst phenomena, and provides the fuel rod with a harder surface (Cr is harder than Zr) thereby improving structural integrity and

wear resistance. During operation, the chromium can become depleted in two ways. Firstly, Cr can be oxidised near the surface of the fuel rod to form Cr_2O_3 [66], or it can migrate into the β -Zr matrix of the cladding itself. The first mode of consumption is initially protective (Cr_2O_3 is largely impervious to oxygen) but subsequently becomes deleterious at high burn-up as Cr is consumed. Conversely, the second mode of consumption is immediately deleterious; migration of Cr into the Zr matrix, although only currently observed at temperatures above 800°C , promotes formation of ZrCr_2 Laves phase – a brittle intermetallic – which can cause the coating system to spall from the clad surface. Spalling of the coat can expose bare Zr underneath, not to mention how this would affect primary circuit chemistry. For the binary Cr-Zr system, 1332°C has been identified as the low eutectic temperature, above which, Cr-Zr will form a liquid phase [73]. Melting of Cr-Zr eutectic in cladding has been reported in literature [56], [74].

In service performance of Cr-coated Zr cladding and mechanical considerations are reported by Chen *et al.* [17]. For instance, the "breakaway" oxidation phenomenon generally occurs around 1000°C leads to a substantial increase in the actual oxidation rate and hydrogen pick-up [75], [76]. Reducing the susceptibility of the cladding to high temperature steam oxidation can limit and even eliminate these risks [64]. Pressurised water reactor accident scenario models have shown that when water is not re-introduced into the core for around 400 seconds, the zirconium cladding will rapidly react with steam, starting particularly at $\sim 1200^\circ\text{C}$ [77]. Zirconium-based substrates coated with chromium have been studied using various deposition methods. These include vacuum arc deposition [50], Physical vapour deposition [53] [68], and 3D laser coating technology [33]. The cold spray technique [59], however, has emerged as a more cost-efficient method due to its lower energy consumption. Cold spray also has a high deposition rate making it suitable for industrial-scale plating.

1.1.2.2 Performance during loss-of-coolant accidents

Figure 2 shows the typical temperature of the fuel cladding during a loss-of-coolant scenario. The work of Brachet *et al.* [57] showed chromium to exhibit the most promising behaviour compared to uncoated Zr. Ceramic and metallic multi-layered coatings were studied, and it was concluded that chromium-based coatings had a good compromise between oxidation resistance and adhesion to the metallic substrate, good fretting resistance, and improved resistance to oxidation in steam at high temperatures. Another benefit observed from the use

of a fully metallic-based coating was its intrinsic ductility at high temperatures compared to ceramic coatings. The use of chromium is further encouraged by Brachet *et al.* [68], who show that the chromium-based coating is able to reduce steam oxidation kinetics and to prevent the cladding from hydriding at high temperature, and the associated clad embrittlement. Brachet *et al.* [54] were then able to show that chromium-based coating reduced hydrogen pick-up during steam oxidation at 1000°C, compared to uncoated zirconium. Furthermore, chromium is shown to be fully adherent to zirconium even after the fuel pin has experienced ballooning and burst [22]. This holds true even near the burst opening where the Zircaloy-4 clad substrate is highly deformed. Ballooning is a serious issue in light water reactors which can block coolant channels supplying coolant to the core.

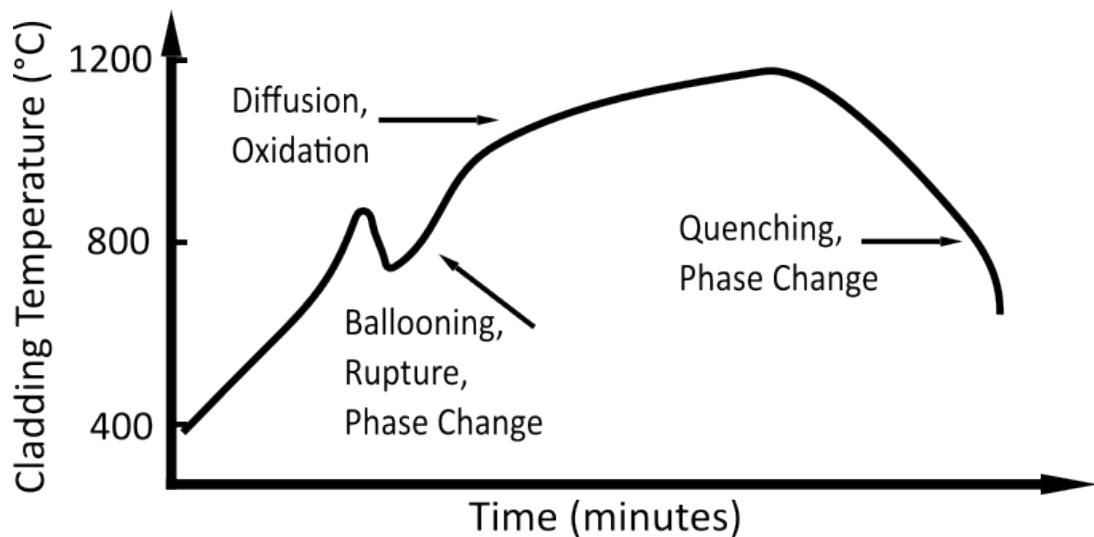
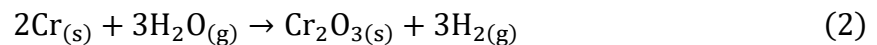


Figure 2. Cladding temperature versus time during a loss-of-coolant accident. Reproduced from Billone *et al.* [75] and Goldner *et al.* [23].

Low oxidation kinetics is important for an accident tolerant fuel cladding. This is essential at high temperatures such as in loss-of-coolant accidents. Fortunately, Cr can form a dense oxide film when it reacts with water according to **Equation 2**:



Several recent investigations have revealed the superior oxidation resistance of Cr-coated Zr cladding. Areva [69], for instance, simulating PWR chemistry in autoclave tests at 360 and 415°C showed that the weight gain of Cr-coated zirconium alloy was on the order of 1 mgdm⁻².

Similarly, it was shown that 20 days exposure at 500°C also had a negligible weight gain of 2.43 mgdm⁻² [59]. High temperature steam oxidation tests have been completed as well. At 1200°C, one-sided steam oxidation tests for Cr-coated M5 showed a ~15 – 20-fold decrease in weight gain than the uncoated cladding [59].

Ma *et al.*, who perhaps gives the best account of high-temperature steam oxidation of Cr-coatings, showed that weight gain of the outer surface of Cr-coated Zr tubes oxidised at 1200°C is low in comparison to the uncoated tube [66]. The thickness of ZrO₂ on the inside tube surface was up to ~144 µm whereas the thickness of Cr₂O₃ on the outside tube surface was < 10 µm. After oxidation it was observed that the Cr coating was still intact, and well adhered to the Zr surface with no observed spalling. The oxidation processes occurring at the Cr-coated clad surface have been described by Ma *et al.* [66] and summarised in **Figure 3** as follows: Cr reacts with H₂O_(g) to produce Cr₂O_{3(s)} which acts as a dense diffusion barrier to oxygen, and greatly reduces the oxidation rate of underlying metal. At the same time, Cr and Zr interdiffuse, which produces a strongly bonding Cr-Zr layer, which improves the adherence of the coating system. However, ZrCr₂, which forms within the Zr-Cr layer, is a Laves phase of the AB₂ type [58], which may be brittle and therefore harmful to the ductility of the clad-coating system. During evolution of the coating system, the thickness of the Cr₂O₃ and Cr-Zr layers increase, and the thickness of the Cr layer decreases. Meanwhile, a secondary redox reaction is underway: Zr in the diffusion layer reduces Cr₂O₃ in the coating to Cr and Zr itself forms ZrO₂ [66], [78]. This secondary reaction is aided by electron transfer from Zr to Cr₂O₃, releasing O²⁻ ions which diffuse to and bond with Zr cations to produce a ZrO₂ layer. The processes of electron transfer, ion diffusion, and redox reactions continue, and as a result, the thickness of the Cr and ZrO₂ layers increase at the expense of Cr₂O₃, which now thins. Finally, when the rate of redox reactions between Cr and H₂O and the Zr and Cr₂O₃ equalise, the thickness of Cr₂O₃ and Cr layers remain unchanged, while the thickness of the ZrO₂ layer now increases. The original Cr coating remains for roughly 2 hours at 1200°C. After the 4-hour mark the observed Cr coating is actually a reduction product from Cr₂O₃ [66]. No obvious differences are observed to the above process at 1300°C. For further reading, the reader is referred to a recent review on the behaviour of chromium coatings by Yang *et al.* [72]. The evolution of Cr coating is summarised in **Figure 3**.

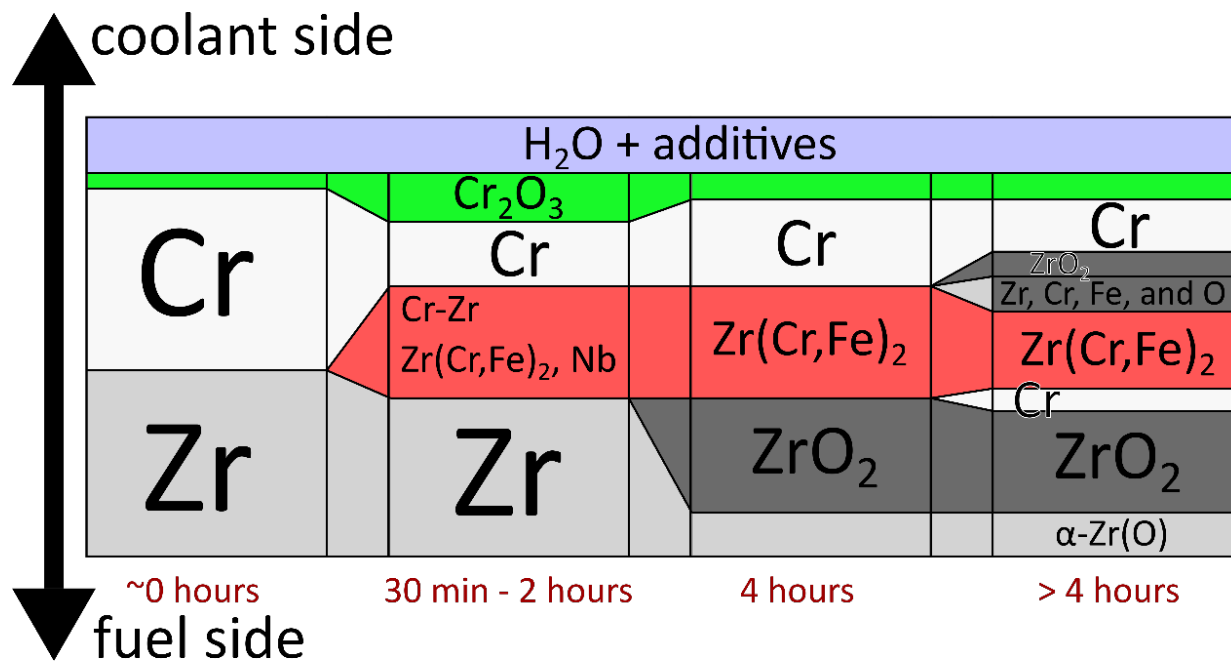


Figure 3. Cr coating evolution during steam testing at 1200°C [63] (not to scale).

1.1.2.3 Spalling and cracking

Spalling and cracking are to be mitigated or prevented entirely in a coating system [79], [80]. The adhesion of a coating system is therefore a key property in achieving its application. The coated layer can easily be damaged by the reactor environment during normal operation or under loss-of-coolant accident scenarios [80]. Cr can react with Zr, forming a C14 Laves compound, which can lead to embrittlement, crack formation and eventual spalling of the coating system [66]. One must also consider the role of radiation damage and material embrittlement on the coating system, over the course of several years of reactor operation. It is noted that in-laboratory testing usually occurs over a shorter timescale of ~ 24 hours. In these shorter tests, the main issues tend to be eutectic reaction temperature and reduction of ductility over time [72], [81]. The adherence of Cr coatings over a longer timescale, such as on the scale of reactor testing, is therefore not yet available in the open literature. Therefore, an in-depth assessment as to the main factors affecting adherence of Cr coatings has not been completed. Some possible factors as to the longevity of the coating include:

- Thermal expansion differential between coating and substrate.
- Coating ductility.
- Elemental migration and intermetallic formation and precipitation.
- Diffusion coefficients of elements in the system.

1.1.3 Cr coating interlayers

An external Cr coating undeniably improves robustness of zirconium-based cladding, especially under accident conditions like LOCAs [81], [29], [58]. However, this coating's performance is limited to below 1332°C [73] at which point Cr-Zr interdiffusion produces a eutectic melt [56], [74]. Preliminary work has been done in way of developing interlayers for Cr-coatings in the form of adherent diffusion barriers such as molybdenum [81] in order to raise the eutectic formation temperature of the clad coating, and to inhibit formation of intermetallic phases such as the Cr₂Zr Laves phase. Other interlayers have been preliminarily investigated such as Ta [63], and austenitic stainless steel [82]. Fortunately, a review of this rapidly expanding area of interest has been completed by Kashkarov *et al.* whose review article is recommended to the reader [83].

The functional criteria of an interlayer are as follows:

- To prevent the formation of Cr-Zr layer altogether (and hence mitigate the decrease in both ductility and mechanical properties).
- To delay the eutectic formation reaction to higher temperatures.
- To limit the consumption of Cr in the Cr-Zr layer.
- To reduce crack formation and propagation.

An interlayer suitable for forming a diffusion barrier must have interdiffusion coefficients with both Cr and Zr that are lower than those of Cr and Zr with themselves and solubility in Zr that is lower than that of Cr. The interlayer should not have a eutectic reaction with either side of the layer or have a eutectic reaction at a temperature higher than 1332°C. Furthermore, it must be capable of withstanding high temperatures (1300°C), oxidation, corrosion, and irradiation. Additionally, it must have a compatible thermal expansion ($6.0 - 6.2 \times 10^{-6} \text{K}^{-1}$) behaviour and be ductile, have low impact on neutron-cross section, thermal conductivity, toxicity, cost, and criticality, and be compatible with the back end of the fuel cycle. Its fabrication process must make it possible to deposit a thin layer without contaminating or degrading the existing Cr-coated zirconium-clad solution [81]. **Figure 4** illustrates the interlayered fuel coating concept.

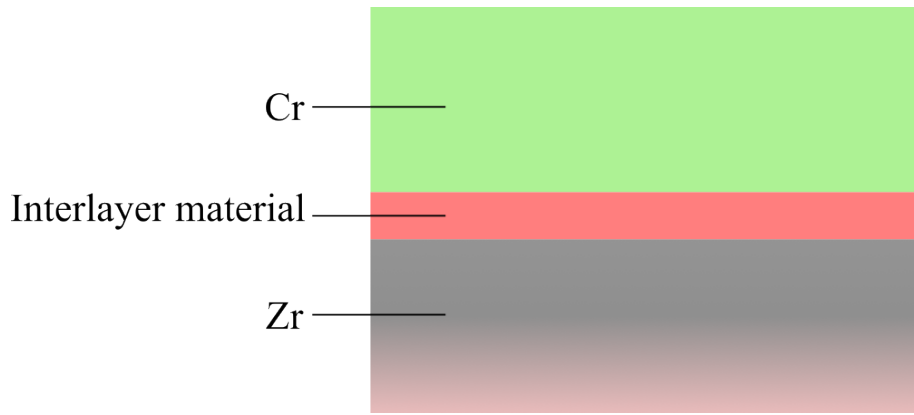


Figure 4. The interlayered coating solution (red: interlayer; green: coating).

1.1.3.1 Molybdenum

To a first approximation, molybdenum metal theoretically fulfils most of these criteria and was investigated as a Cr-Zr interlayer [81]. Michau *et al.* deposited Mo (2 – 4 μm) onto Zr via magnetron sputtering, topped with a layer of Cr ($\sim 12 \mu\text{m}$) (**Figure 5**) [81]. From binary phase diagrams, it appears that the eutectic formation temperature is immediately improved from 1332°C (Cr-Zr) to $\sim 1500^\circ\text{C}$ (Mo-Zr). The thermal conductivity of the Mo interlayer is greater than Cr coat ($139 \text{ Wm}^{-1}\text{K}^{-1}$ versus $94 \text{ Wm}^{-1}\text{K}^{-1}$).

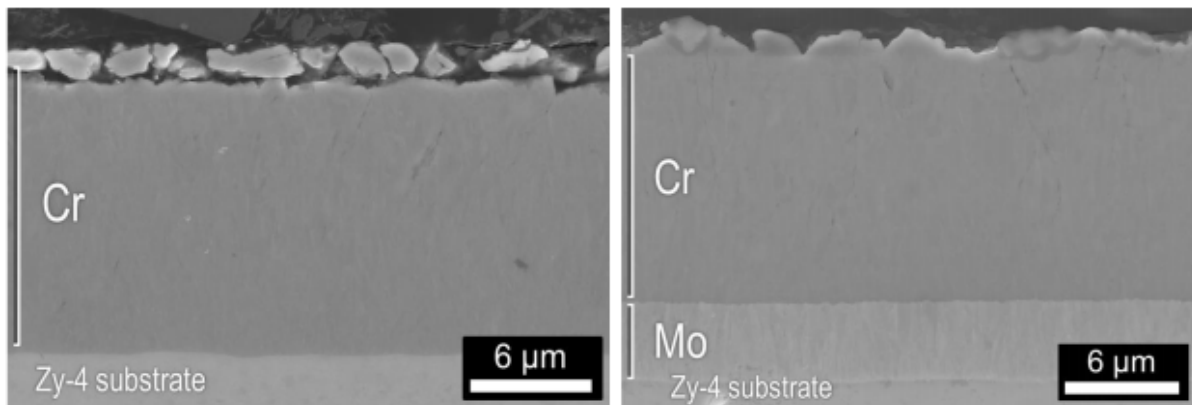


Figure 5. Mo interlayer system in Cr-coated zirconium Michau *et al.* [81].

Michau *et al.* reported that a Mo interlayer raised the eutectic reaction upwards by approximately 40°C from the Cr-Zr eutectic temperature of 1332°C (**Figure 6**). Binary phase diagrams indicate that the Mo-Cr eutectic temperature is approximately 1900°C . The Mo/Cr coating also slowed the depletion of Cr (**Figure 7**). The glow-discharge optical emission spectroscopy profiles (**Figure 8**) for Cr and Mo/Cr after oxidation in air at 1100°C show that diffusion quickly overcame the Mo interlayer within 30 minutes. The liquid observed was the

Cr-Zr eutectic. Consequently, the 40°C increase in temperature was dependent on the ramping rate.

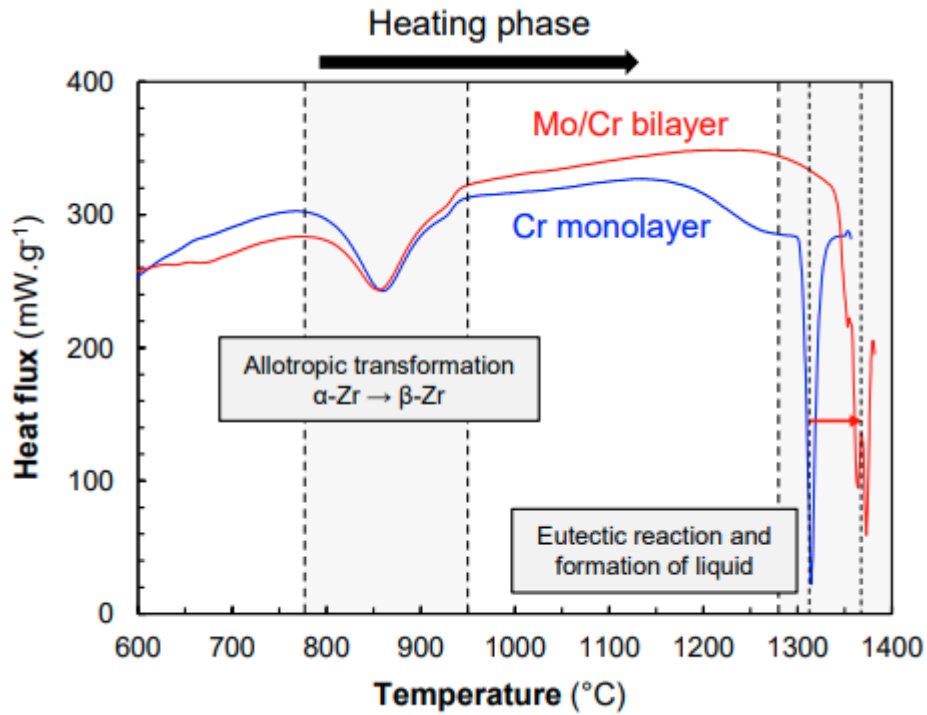


Figure 6. Calorimetry of Cr coating and Mo/Cr coating in argon at 10°C/min [81].

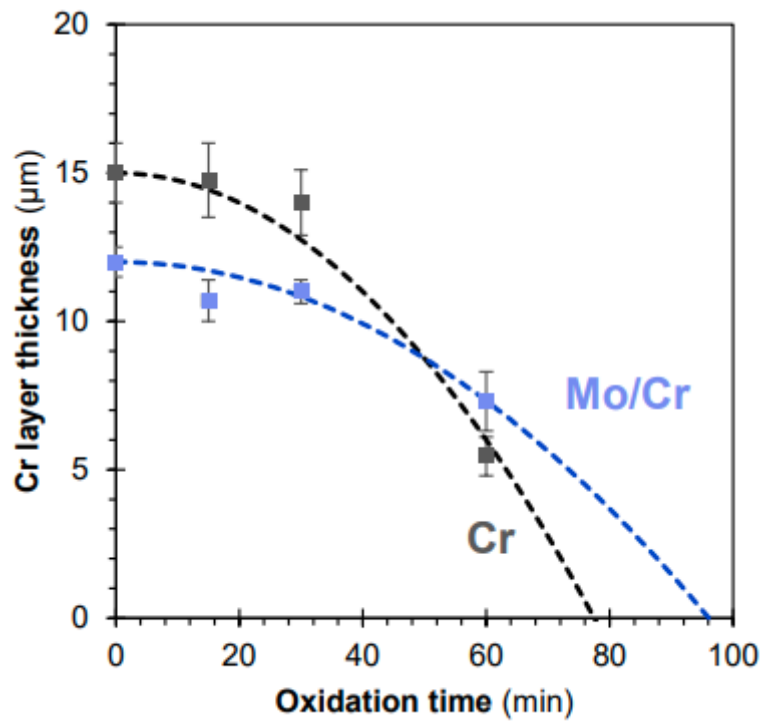


Figure 7. Michau *et al.*, Cr layer thickness versus oxidation of Cr coating and Mo/Cr coating in air at 1100°C [81].

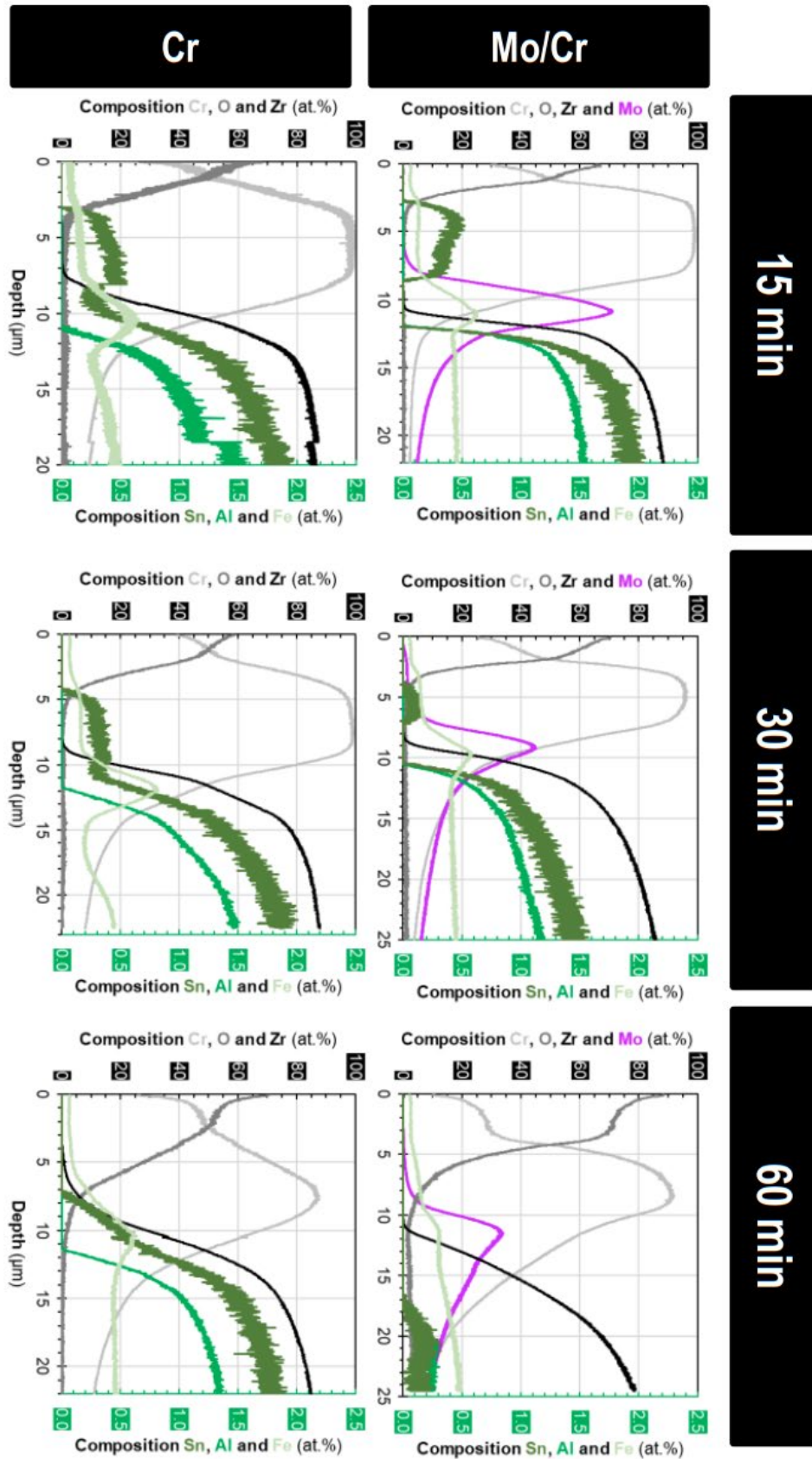


Figure 8. Michau *et al.* Glow-discharge optical emission spectroscopy images of the Cr/Mo coating system at 1100°C in air [81].

4 μm of Mo can raise the eutectic formation temperature by 40°C since Cr and Zr can interdiffuse through the Mo interlayer at elevated temperatures. Mo can therefore only be thought to postpone the eutectic reaction of Zr and Cr and not prevent it entirely. Additional factors which promote overcoming of the interlayer are the solubilities of Mo in both β -Zr and Cr, and diffusion coefficients of Mo in β -Zr and in Cr. Park *et al.* also used a Mo interlayer in FeCrAl coatings and was able to prevent interdiffusion at high temperatures while improving oxidation resistance compared to uncoated Zr alloy at 1200°C [34]. Mo was necessary as an interlayer as rapid eutectic reactions between Zr and FeCrAl occur at 928°C in the Zr-Fe system. Syrtanov *et al.* magnetron sputtered interlayered Cr (8 μm) / Mo (3 μm) coatings onto Zr-1Nb alloys followed by air oxidation at 1100°C for 15 – 60 minutes [84]. Here, Mo was able to postpone Cr-Zr interdiffusion at high temperatures.

1.1.3.2 Tantalum

Evans *et al.* studied the effectiveness of metallic tantalum as a Zr-Cr interlayer [63]. In this study, Ta/Cr coatings were successfully deposited onto Zr alloy substrates using magnetron sputtering. Steam oxidation testing showed a reduced weight gain compared to uncoated substrates. However, the Ta showed some reaction with the Zr at 900°C, shown in the binary phase diagram in **Figure 9**, and was deemed unsuccessful at providing a better coating than Cr alone.

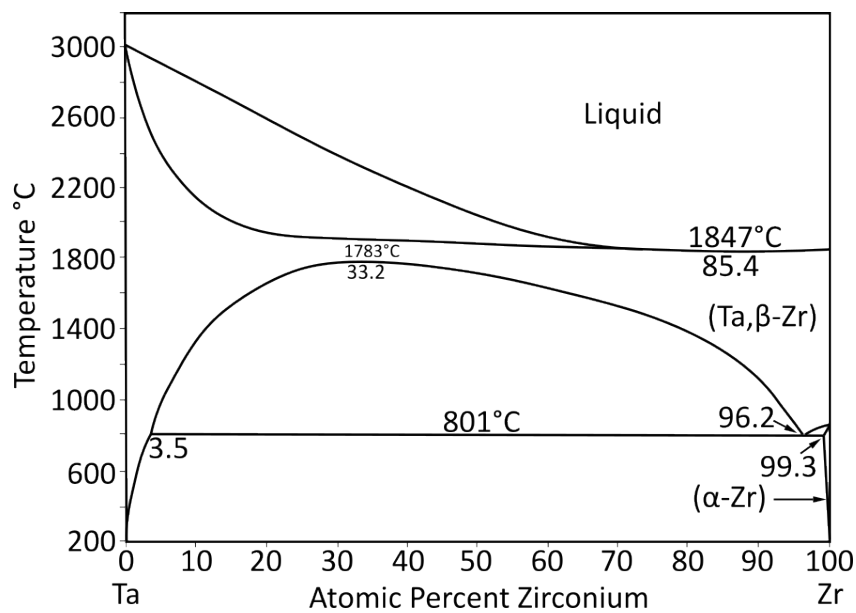


Figure 9. Phase diagram of the Ta-Zr system [85].

1.1.3.3 Stainless steel

Stainless steel was investigated as an interlayer material between Zr and Cr by Yang *et al.* [82]. The eutectic reaction temperature of the Fe-Zr system is 928°C, which does not improve on the Cr-Zr system [73], [86]. Such an interlayer would therefore not improve on the eutectic reaction temperature of current coating solutions and can be deleterious to the coating system in high temperature conditions.

1.1.3.4 Tungsten

Investigation of tungsten as an interlayer material could be beneficial due to its eutectic reaction temperatures with Cr and Zr of 1860 and 1735°C, respectively, which are much improved on the Cr-Zr reaction temperature of 1332°C. Additionally, its solubility in β -Zr is low, and its thermal conductivity is high compared to the other present elements. Furthermore, it does not suffer from any phase transformations up to the required loss-of-coolant temperature. Despite these advantages, tungsten could be limited by its low thermal expansion coefficient compared to both Zr and Cr, and it suffers from brittle behaviour at both room temperature and operating temperature [87]. It is possible to improve the room temperature ductility of the material via alloying additions. Furthermore, alloying with elements such as Mo or Nb, which are isomorphous, could bring the thermal expansion coefficient in line with Zr and Cr.

The properties of W that are relevant are described in **Table 2**. In comparison to both Cr and Zr, W has a higher melting point, and its lowest eutectic reaction temperature of 1735°C is better than that of the Cr-Zr combination (1332°C). At 1300°C, the solubility of W in β -Zr is 3 at%, which is better than that of Ta (~ 15 at%) and is therefore expected to interdiffuse more slowly. Its thermal conductivity is an order of magnitude greater than that of Cr and Zr. However, a W interlayered coating presents challenges, such as its linear thermal expansion coefficient being much lower than that of both Cr and Zr (4.4 compared to $6.0 - 6.2 \times 10^{-6} \text{K}^{-1}$), and its brittleness at room temperature.

Table 2. Properties of W relevant to an interlayer barrier between Cr and Zr.

Possible Eutectics	Melting point (°C)	Solubility in β -Zr at 1300 °C	Linear coefficient of thermal expansion at 298 K (10^{-6} K^{-1})	Thermal conductivity, λ ($\text{Wm}^{-1}\text{K}^{-1}$)	Phase transition	Mechanical Behaviour
1860°C (W-Cr) 1735°C (W-Zr)	3422	< 3 at%	4.4	139	None	Brittle

The relevant properties of a range of potential interlayer metals, including Mo, Ta, Nb, and Re, are described in **Table 3**. It is observed that the eutectic reaction is improved from Cr-Zr (1332°C). In β -Zr, Nb atoms are mobile, thus possibly limiting its application as an interlayer material. The solubilities of Mo, Ta, Nb, and Re in β -Zr are estimated to be around 30, 15, 100, and 10 at%, respectively, not exceeding that of a Cr coating (~8 at%). Moreover, Mo, Nb, Ta, and Re are known to be ductile at room temperature, which could be advantageous for processing these coating systems.

Table 3. Comparison of properties of potential barriers between Cr-based coatings and zirconium alloys. Zirconium and chromium are presented for comparison. Partly reproduced from Kashkarov *et al.* [83].

Interlayer	Possible Eutectics	T _m , °C	Diffusion Coefficient in β-Zr	Solubility in β-Zr at 1300°C	Linear CTE at RT, 10 ⁻⁶ K ⁻¹	λ, W/m/K	Phase transition	Mechanical Behaviour
Zr	-	1855	-	-	7.2 (hexagonal close-packed), 9.6 (body-centred cubic)	22	α _{hcp} – β _{bcc} at 862°C	Ductile
Cr	1330°C (Cr-Zr)	1907	High	< 8 at%	6.5	93.7	No	Ductile/Brittle
Mo	1550°C (Mo-Zr)	2623	Low	< 30 at%	5.5	138	No	Ductile
Ta	1820°C (Ta-Zr) 1760°C (Ta-Cr)	3017	Low	~15 at%	6.5	57.5	Only for metastable β → α at 750 – 775°C	Ductile
Nb	1668°C (Nb-Cr)	2477	High	100 at%	7.1	53.7	no	Ductile
Re	1600°C (Re-Zr)	3186	Unknown	~10 at%	6.1 – 6.6	39.6	no	Ductile

Much interest has been shown in the development of interlayer materials to counter the detrimental effects of Cr coatings in high temperature environments, such as a loss-of-coolant accident, as demonstrated in the literature. Over the past few years, compositionally complex alloys have become a popular and inventive research topic. In the subsequent section, the basic concept of these alloys will be explored, their general properties outlined, and their feasibility as potential interlayer materials between Zr and Cr discussed.

1.2 Compositionally complex alloys

Metallurgy has been a driving force of technological progress for millennia. Ancient peoples knew how to extract high quality metals from their ores, alloy metals together and fashion them into ever superior tools to meet their growing material needs. Indeed, our anthropological epochs, such as the bronze age, and iron age, are categorised according to the metallurgical developments which spurred them. Metallurgy and materials science enable advances in scientific and engineering fields. Nickel-based superalloys for aircraft jet engine

turbine blades, developmental carbon-carbon composites for wings of wide-bodied aircraft, high temperature superconductors, are just a few examples of these improvements. Alongside developments mentioned, excellent elucidation of the structure-property relationship in metals and alloys has been made possible through the development of high-resolution techniques such as scanning and transmission electron microscopy, scanning tunnelling microscopy, atom probe tomography, electron probe microanalysis, glow-discharge optical emission spectroscopy and many other techniques.

Compositionally complex alloys represent an exciting new chapter in the story of metallurgy. Unlike conventional alloys which are based on one principal element, compositionally complex alloys sample the rarely explored centre of compositional space in a multicomponent phase diagram. Discovered twice independently, by Yeh [88] and Cantor [89], they are usually defined as constituting at least five principal elements, all between 5 – 35 at%, and their unusual stability and subsequent material properties are typically attributed to 4 core effects: high configurational entropy, sluggish diffusion, high lattice distortion, and cocktail effects [88]. The term exactly describing the class of alloys is controversial, with some authors preferring the more well-known term *high entropy alloys*.

1.2.1 Definition

The original and most lasting of these terms, *high entropy alloys*, originates from the early work of Yeh *et al.* where it was suggested that the unique phase stability afforded to concentrated solid solution alloys, and their ability to form disordered solid solutions with simple crystal structures, was attributed to the associated large entropy of mixing [88], [90]–[92]. Configurational entropy began to compete with enthalpy of mixing at the point where the number of equiatomic elements was 5. Therefore, a high entropy alloy in its first conception was defined as having 5 or more elements, each in concentrations between 5% and 35% (to give flexibility in composition). Those compositions with 3 – 4 elements were termed 'medium entropy alloys'. The fundamental role that mixing entropy plays in phase stability of concentrated solid solution alloys has since been placed into question, or at least deemphasised by the alloy community [93]–[95]. For example, Otto *et al.* replaced a single element each time in the quinary concentrated solid solution alloy CrMnFeCoNi, keeping same the crystal structure, comparable size, and electronegativity as the atoms they replaced [95]. In every substitution it was found that the resulting alloy was not stable as a single-phase solid solution.

Troparevsky *et al.* predicted that as the number of elements increase, intermetallic formation would become more likely, not less [96]. Indeed, this conclusion was supported by the original work by Cantor *et al.* in which alloys with 16 and 20 elements in equiatomic concentration were not found to form single phase solid solutions [89]. Further compelling results were found by Senkov *et al.* [97], [98]. For example, Senkov *et al.* used a combinatorial approach to rapidly screen compositionally complex alloys using the calculation of phase diagrams method (CALPHAD) [97]. In a screen of over 130,000 alloy systems, they found that the number of solid solution alloys becomes less likely as the number of elements increases. This is in direct contradiction of the premise that gave *high entropy alloys* their original name.

There also exists an ambiguity in the original definition of these alloys, as *high entropy alloys*. For example, equiatomic quaternary and even ternary alloys are often referred to as high entropy alloys [99], [100]. Additionally, there are alloys which coincidentally fit the definition of a high entropy alloy but are not termed as such because they developed separately or prior to the field, such as AlNiCo magnet alloys. Considering the ambiguity surrounding the exact classification of high entropy alloys, Several neologisms have since been coined to refer to these alloys in a more general sense. Terms such as multi-principal element alloys (MPEAs), multi-component alloys (MCAs), concentrated solid solution alloys (CSSs, or CSAs) [101], complex concentrated alloys (CCAs) [102], and highly concentrated alloys (HCAs) [103], [104] have all been coined, seemingly, to de-emphasise the role of configurational entropy, or to make clear the distinctions between compositions which contain intermetallic compounds and those considered traditional alloys.

Li *et al.* performed statistical analysis on naming conventions and found that the term "High entropy alloy" was still used in the title of 93.62% of 2587 papers from the years 2004 – 2019 [105] (**Figure 10**). "Multicomponent alloy" was used in 2.09% of cases and "multiprincipal alloy" was used in just 1.70% of papers. Even though the fundamental premises behind the term "high entropy" have been questioned, the name "high entropy alloy" has remained.

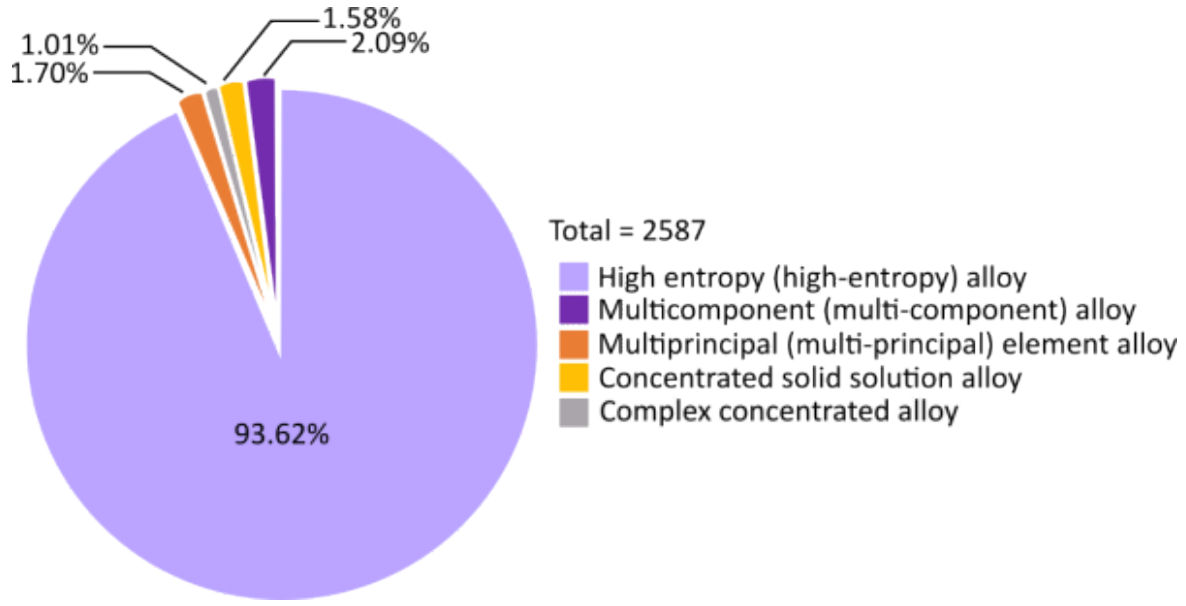


Figure 10. Percentages of naming conventions for compositionally complex alloys. Reproduced from Li *et al.* [105].

It has been noted that interest among the compositionally complex alloys community has been expanded to include work on alloys with secondary phases, intermetallics, and precipitates, duplex, and multi-phase alloys, and has become less focussed on the study of single-phase solution alloys [108]. In this body of work, the broad term *compositionally complex alloys* is referred to when discussing the general class of alloy systems and potential alloys therein. Additionally, when stable solid solutions at the temperature discussed are known, or if the alloy is being modelled specifically as a disordered solid solution, *concentrated solid solution alloys* is the preferred term.

1.2.2 General properties

The base of a compositionally complex alloy is analogous to the base of a conventional alloy, which is formed by a specific combination of principal elements. This combination of unique new alloy bases that can be achieved by taking r principal elements from a palette of n candidates can be calculated via the binomial coefficient from **Equation 3**.

$$C(n, r) = \frac{n!}{r!(n-r)!} \quad (3)$$

Given that there are 67 stable metallic elements, these elements can be combined to form ternary alloy bases, with a possible 47,905 combinations; quaternary bases, with 766,480 combinations, and even more complex alloy bases with 3, 4, 5, and 6 principal elements can

be created, with over 110 million new alloy bases [106]. Given that there are such a great number of bases from which to design alloys, the vastly expanded compositional space of alloys can be quite daunting to navigate. Over 37 elements have been utilised to make hundreds of concentrated solid solution alloys [105], [107]. These alloys offer an opportunity to exploit new compositions which were previously thought to be inaccessible due to the formation of complex intermetallic compounds.

At the outset, it must be said that the relationship between composition, microstructure, and properties in compositionally complex alloys is unclear. The elemental composition of these alloys is of course paramount, but material properties also depend on the microstructure, operating temperatures, and processing or fabrication methods. Additionally, dislocations and dislocation motion, defect formation, and migration energies influence material properties. These factors tend to be intimately interconnected and are therefore difficult to deconvolute into simple cause-and-effect relationships. Research has been conducted into the influence of composition on a mechanical property via the incorporation of Al into concentrated solid solution alloys, in order to enhance strength and hardness by promoting the formation of body-centred cubic structures [108]–[111]. In general, strength is seen to increase with Al addition whereas ductility declines.

Tensile strength and ductility are fundamental in the design of materials for practical structural applications. Both are affected by factors such as substitutional elements, interstitial elements, processing, microstructure, and operational temperature. In most materials there is usually a trade-off between ductility and strength, and so far, concentrated solid solutions do not provide exception to this rule. Research has been conducted in determining the role of constituent elements towards strength and ductility in compositionally complex alloys. For example, Nb can provide a strengthening effect in the CoCrFeNiNb_x alloy due to its large atomic radius [112]–[114]. Likewise, Ti can provide solid solution strengthening in the AlCoCrFeNiTi_x compositionally complex alloy, although in high concentrations of Al, intermetallic compounds form which embrittle the material. Interstitial alloying additions, most commonly small elements including hydrogen, oxygen, nitrogen, carbon, and boron, have also been investigated for their effects on mechanical properties of compositionally complex alloys. For example, mechanical properties of face-centred cubic CoCrFeMnNi charged with hydrogen do not degrade like convention suggests but improves slightly in both strength and ductility [115]. Oxygen interstitials in body-centred cubic HfNbTiZr formed ordered interstitial compounds and this was accompanied with an increase in both strength and ductility [116].

Adding nitrogen and carbon to face-centred cubic $\text{Al}_{7.5}\text{Cr}_6\text{Fe}_{40.4}\text{Mn}_{34.8}\text{Ni}_{11.3}$ [117] and CoCrFeMnNi [118] alloys benefit strength without sacrificing ductility. Boron additions strengthen CoCrFeMnNi , although too much worsens the effect. Therefore, the role of interstitial additions to compositionally complex alloys to improve mechanical properties should not be overlooked when seeking to exploit properties of these new materials.

1.2.3 Radiation resistance

Under irradiation, conventional alloys exhibit non-equilibrium segregation, microstructure changes (dislocation loops, networks, voids, bubbles, precipitates), and hardening [119]. However, there is evidence to suggest a superior radiation resistance of compositionally complex alloys [120]–[126], which is typically attributed to the severe lattice distortion effect, and high levels of atomic stress [126]. For example, Kumar *et al.* showed that FeNiMnCr had superior radiation resistance than conventional austenitic stainless steels in terms of radiation-induced segregation [123]. Yang *et al.* showed that CrMnFeCoNi possessed the best helium-ion irradiation tolerance when compared to 304 stainless steel and pure Ni [125]. Granberg *et al.* observed a substantial reduction in damage accumulation for NiCoCr and NiFe alloys compared to pure Ni, which was attributed to sluggish dislocation mobility in complex alloys caused by the distorted lattice [122]. Zhang *et al.* demonstrated how chemical complexity may alter the thermodynamic and kinetic characteristics of defects, which in turn can influence the evolution of microstructures under irradiation [127]. Liu *et al.* demonstrated excellent void suppression in single-phase compositionally complex alloys of the NiCoFeCrMn system subjected to 1.5 and 3 MeV Ni^+ ion irradiation, which was attributed to the enhanced defect recombination in these alloys [128].

Much of the research into radiation resistance of compositionally complex alloys have focussed on face-centred cubic structures, such as Cantor's original alloy, FeCrMnNiCo , and derivatives thereof [129], [130]. However, the application of these elements to a nuclear environment may be prohibited for several reasons. For example, in a neutron environment, Fe and Co produce significant quantities of ^{60}Co , a gamma-emitting radionuclide, which is responsible for a large portion of the radiation exposure of workers at nuclear facilities. Additionally, Ni has a high hydrogen solubility and therefore contributes to H_2 ingress into structural materials within a nuclear reactor. Ni also contributes to helium bubble formation

via transmutations into Fe. Furthermore, Mn has a high thermal neutron cross-section and reduces neutron utilisation in a nuclear environment.

The body-centred cubic and refractory elements are less studied than their face-centred cubic congeners [124], [131]. However, their properties with respect to radiation resistance is promising [124], [131], [132]. For example, Lu *et al.* showed that single-phase body-centred cubic $\text{Ti}_2\text{ZrHfV}_{0.5}\text{Mo}_{0.2}$ experienced almost zero radiation hardening when irradiated with helium ions [132]. El-Atwani *et al.* showed that magnetron sputtered films of CrTaVW, when irradiated with 1 MeV Kr^{2+} showed no signs of irradiation-induced defects up to 8 displacements per atom [131]. To improve on the ductility of CrTaVW, El-Atwani *et al.* added Hf and showed that the alloy exhibited excellent irradiation resistance to dislocation loop and cavity formation [133].

1.2.4 Welding with compositionally complex alloy fillers

Compositionally complex alloys have the potential to make good weld filler materials [134]–[137]. For example, the high mixing entropy which comes with multiple components could stabilise disordered solid solutions at the expense of brittle intermetallic phases, whose formation could then be suppressed. Such an approach could allow for finer control of melting temperatures, weld flow behaviour and wetting [134]. Moreover, the use of compositionally complex alloys as weld fillers may facilitate the joining of dissimilar metals [135]. CrFeCoNiCu, for example, has been made into a composite brazing filler by the addition of Ti to braze together ZrB_2 -SiC-C and a GH99 superalloy [138]. The same CrFeCoNiCu alloy has been used to join Inconel 718 superalloy [136], and with low level additions of Ga, Ge, and Sn, for the joining of Ni-based superalloys [139]. CrFeCoNiCu has also been used to braze SiC to itself [140] and to Nb [141]. By far the most research on welding of concentrated solution alloys has been done on the original Cantor alloy, CoCrFeNiMn, probably by virtue of it being the most studied composition within the field as well as being the first reported in literature. For more on welding and joining of these alloys, the reader is referred to the more comprehensive recent reviews by Lopes *et al.* [137] and Luo *et al.* [134].

The similarities between using compositionally complex alloys as welds between dissimilar metals and the interlayered coating to mitigate formation of ZrCr_2 Laves phases at the surface of nuclear fuels should not be overlooked. In both concepts the aim is to:

- Join dissimilar metals together; and

- Avoid intermetallic formation.

Although, the interlayered concept does have marked differences:

- The interlayer must have a high melting temperature – not an easily melting eutectic.
- The interlayer must avoid badly performing elements such as Ni (increases H₂ ingress and produces gamma emitting ⁶⁰Co in a neutron environment) and Co (activation).

1.2.5 Predicting stability

Historically, to determine if elements would form a solid solution, the rules of Hume-Rothery would be applied [142]. Named after William Hume-Rothery, this basic set of rules are used to describe the conditions in which an element could dissolve in a metal to form a solid solution. For substitutional solid solutions, the rules are as follows:

1. The atomic radius of the solute and solvent atoms must differ by no more than 15%.
2. The crystal structures of solute and solvent must be similar.
3. Complete solubility occurs when the solvent and solute have the same valence.
4. Solute and solvent atoms should have similar electronegativity.

When applied directly to compositionally complex alloys, the Hume-Rothery rules fail. In a system where elements are in equal or near-equal concentrations, it is impossible to distinguish between the atoms which constitute the solvent and those which constitute the solute [95]. Moreover, some of the requirements laid out in the Hume-Rothery criteria appear to be relaxed for compositionally complex alloys. An example of this is the FeCrMnNiCo alloy, which is composed of elements with four distinct crystal structures in their pure form. However, when combined in the equiatomic alloy, a simple face centred structure is observed [89]. Furthermore, Hume-Rothery rules cannot state why additions of face centred cubic Al to CoCrCuFeNi, can eventually change its crystal structure from face centred cubic to body centred cubic. Clearly, the original rules of Hume-Rothery do not capture the true forces governing phase stabilisation in compositionally complex alloys.

In 2004, Yeh et al. proposed that as the number of components in an alloy increases, so too does the associated configurational entropy [88]. This configurational entropy can be maximised when each component is present in equimolar concentrations, meaning atoms of each element are present in equal amounts. Yeh *et al.* proposed that the increase in configurational entropy could compete with mixing enthalpies when the number of equimolar

elements in solution is ≥ 5 , thereby stabilising simple disordered solid solutions at the expense of intermetallic compounds [88]. These alloys were dubbed *high entropy alloys* by Yeh *et al.* because of the supposed stabilising effect of their high configurational entropy, which was thought to dominate the mixing enthalpy for these alloys. The ideal configurational entropy is calculated from **Equation 4**.

$$\Delta S_{\text{conf}} = -R \sum_{i=1}^n (c_i \ln c_i) \quad (4)$$

where c_i is the atomic fraction of element i . In an equiatomic alloy, **Equation 4** simplifies to

$$\Delta S_{\text{conf}} = R \ln(n) \quad (5)$$

where R is the universal gas constant, $8.31 \text{ JK}^{-1}\text{mol}^{-1}$ and n is the number of equiatomic elements present in the composition. The contribution of configurational entropy has also been devalued since the original work of Yeh *et al.* [95], [96]. For example, Otto *et al.* substituted elements into the CrMnFeCoNi alloy which had comparable atomic sizes, electronegativity and crystal structure to the elements that were being replaced, in order to maximise the chance of solubility [95]. This study found that with any substitution the result was not a single-phase solid solution. Moreover, Troparevsky *et al.* predicted contrary to the compositionally complex alloy design philosophy that as the number of elements in a mixture increases, the more likely intermetallic formation is, not less [96]. This is supported also by the original work of Cantor *et al.* where equiatomic alloys with 16 and 20 elements also did not form single phase solid solutions [89].

It was thought that by exploiting the large configurational entropy associated with the formation of compositionally complex alloys, one can thermodynamically suppress the formation of intermetallic compounds such as ZrCr_2 . Recent work, however, by Bokas *et al.* [143] has proposed a limit to the stabilising effect of configurational entropy. Regarding **Equation 4**, it is important to remember that ΔS_{conf} represents the maximum theoretically possible entropy of the system, and that real systems will never reach this value. As an example, let us consider an equiatomic alloy containing 3 constituent elements, ABC. This solid solution is in direct competition with three binary solid solutions AB, AC, and BC. When the number of elements in our alloy increases to 4, ABCD, the number of lower-order competing phases increases from 3 to 7: ABC, ABD, ACD, BCD, along with the original binary alloys, AB, AC,

and BC. The additional ideal entropy that an equiatomic alloy of n elements has in direct competition with each lower-order solid solution containing $n - 1$ elements can be defined as

$$\Delta S_{n-(n-1)} = R[\ln(n) - \ln(n - 1)] = R \ln\left(\frac{n}{n - 1}\right) \quad (6)$$

Plotting the curve $\Delta S_{n-(n-1)}$ as a function of the number of elements, n , describes the additional ideal configurational entropy that a solid solution has to compete with solid solutions containing $n - 1$ elements (**Figure 11**).

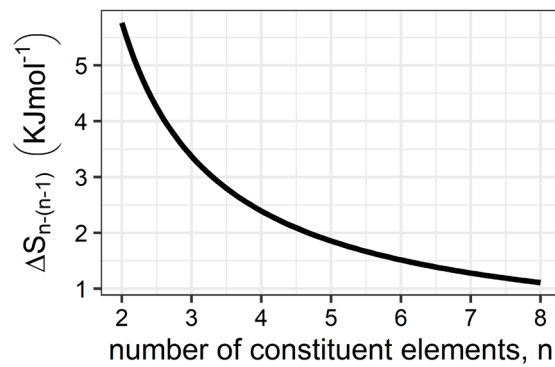


Figure 11. Additional ideal configurational entropy that an n -constituent equiatomic alloy has to compete with an $n - 1$ -component alloy.

However, the equiatomic alloy with n elements is not just in competition with $n - 1$ solid solutions but is also in direct competition with $n - 2$, and $n - 3$ solutions, and so on, until n competes with every binary solid solution possible in the system. In fact, it can be shown that for an equiatomic alloy of n elements, the number of competing lower-order solid solution phases is given by $\frac{1}{2}n^2 + \frac{1}{2}n - 3$ (**Figure 12**).

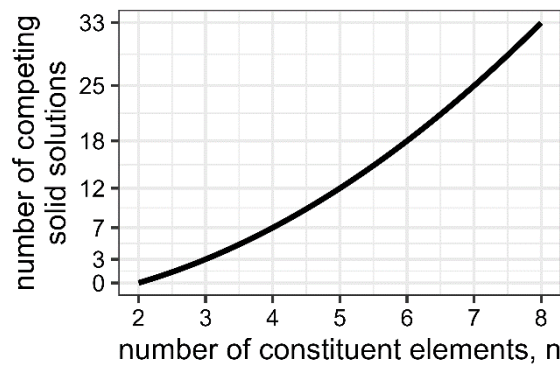


Figure 12. Competing lower-order phases of a single-phase compositionally complex alloy.

It has been questioned why alloys with n exceeding 6, 7, or more are not reported in the academic literature, despite configurational entropy being thought to be the main factor in determining phase stability of concentrated solid solutions. In the original work of Cantor, the view that configurational entropy was the primary driver for phase stability was not supported, even when 16 and 20 elements were being melted in equiatomic proportions, as a concentrated solid solution alloy of 16 – 20 elements did not form [89].

The main points can be summarised as follows:

- Number of competing phases of an equiatomic n -element concentrated solid solution rises with increasing n .
- With increasing n , the additional ideal configurational entropy that an equiatomic n -element concentrated solid solution required to compete with lower-order solid solutions reduces significantly.
- The configurational entropy typically reported in literature is the *ideal* configurational entropy only, which is always reduced in real systems.
- With increasing n more elements with their own electronegativities and valences are included, which increases the likelihood of elements whose mixing enthalpies differ by large values.

This line of thinking suggests that as the number of elements in a compositionally complex alloy increase, configurational entropy contributes to the thermodynamic stability of a single-phase solution, but this effect quickly diminishes as the number of competing lower-order solutions (and intermetallic compounds) increases.

1.2.5.1 The parametric approach

Predicting phase stability of compositionally complex alloys has proven to be a tricky endeavour [101]. Empirical methods such as the Hume-Rothery rules have been extended to incorporate compositionally complex alloys into their predictive domain, leading to thermophysical parameters available for which single-phase concentrated solid solution alloys can be screened. Phase formation, as well as crystal structure, can be predicted from parameters including mixing enthalpy, ΔH_{mix} [144], [145], mixing entropy, ΔS_{mix} [88], Valence electron concentration [146], a thermodynamic parameter, Ω , given by Yang *et al.* [144], atomic size difference parameter, δ , by Yang *et al.* [147], atomic packing parameter, γ , by Guo *et al.* [146],

and finally, φ , a ratio between the Gibbs free energy of a completely disordered solid solution to that of the most likely intermetallic or segregated binary system, given by King *et al.* [148].

$$\Delta H_{\text{mix}} = \sum_{i=1; i \neq j}^n 4\Delta H_{ij}^{\text{mix}} C_i C_j \quad (7)$$

$$\Delta S_{\text{mix}} = -R \sum_{i=1}^n C_i \ln C_i \quad (8)$$

$$\text{VEC} = \sum_{i=1}^n C_i (\text{VEC})_i \quad (9)$$

$$\delta = \sqrt{\sum_{i=1}^n C_i \left(1 - \frac{r_i}{\bar{r}}\right)^2} ; \bar{r} = \sum_{i=1}^n C_i r_i \quad (10)$$

$$\gamma = \frac{1 - \sqrt{\frac{(r_s + \bar{r})^2 - \bar{r}^2}{(r_s + \bar{r})^2}}}{1 - \sqrt{\frac{(r_L + \bar{r})^2 - \bar{r}^2}{(r_L + \bar{r})^2}}} \quad (11)$$

$$\Omega = \frac{T_m \Delta S_{\text{mix}}}{|\Delta H_{\text{mix}}|} \quad (12)$$

$$\varphi = \frac{\Delta G_{\text{ss}}}{\Delta G_{\text{maximum}}} \quad (13)$$

where R is the universal gas constant; n is the number of constituent elements; C_i and C_j are the atomic concentrations as a fraction of the i th and j th element respectively; H_{ij}^{mix} is the mixing enthalpy of constituent binary liquid ij alloys; r_s and r_L are the smallest and largest atomic radii of alloying elements respectively; r_i is the atomic radius of the i th element. ΔG_{ss} is the Gibbs free energy of a completely disordered solid solution and ΔG_{max} the Gibbs free energy of the binary intermetallic most likely to form. $(\text{VEC})_i$ is the valence electron concentration of the i th element. T_m is the theoretical melting point of the concentrated solid solution alloy estimated from the rule of mixtures.

Empirically derived design criteria for the parameters above have been determined by many authors to be as follows: $-15 \text{ kJmol}^{-1} < \Delta H_{\text{mix}} < 5 \text{ kJmol}^{-1}$ [147]; $12 \text{ JK}^{-1}\text{mol}^{-1} < \Delta S_{\text{mix}} < 17.5 \text{ JK}^{-1}\text{mol}^{-1}$ [144], [147]; $\text{VEC} \leq 6.87$ for body-centred cubic structures; $\delta \leq 6.6\%$; $\gamma \leq 1.175$ [149]; $\Omega \geq 1.1$; $\varphi \geq 1$ [148]. The strength of this method is that many compositions can

be screened quickly. A disadvantage is that this parametric approach is entirely empirical [150], and simply infers from already confirmed stable alloys, and assumes continuation between alloy compositions and their phase stability. In some cases, the phase stability of a composition has been confirmed, but only using techniques such as X-ray diffraction which cannot precisely determine whether a single phase has been obtained. Furthermore, thermal ageing is not always conducted, which prevents the confirmation of thermodynamically stable phases and their associated thermophysical parameters and stability cannot be recorded in a parametric approach database. Pickering *et al.* highlighted that a great deal of attention has been given to as-cast microstructures which are not appropriate to assess phase stability of compositionally complex alloys [151]. For example, FeCrCoNi – which has been found not to be a single-phase solid solution below its solidus – should be appropriately heat treated to induce precipitation. The fact that many studies do not heat treat their alloys may undermine the degree to which the parametric approach can be relied upon to determine phase stability. Although the parametric approach has its many problems, it is useful as a first approximation, and to highlight potential alloys for further study.

The story of the parametric approach to alloy phase stability started arguably with Zhang *et al.* [147] where they began the systemisation of empirically-derived thermophysical parameters for predicting single phases solid-solutions. By summarising the compositionally complex alloys to-date along with their atomic size differences, δ , and enthalpy of mixing, ΔH_{mix} , they found that single phase solid solutions occurred only when the following criteria were satisfied: that $\delta < 6.5\%$; $-15 \text{ kJmol}^{-1} < \Delta H_{\text{mix}} < 5 \text{ kJmol}^{-1}$, and $\Delta S_{\text{mix}} > 12 \text{ JK}^{-1}\text{mol}^{-1}$. That is, when the sizes of constituent atoms differ no more than 6.5%, that the enthalpy of mixing was slightly positive or not very negative, and when the mixing entropy is large to suppress intermetallic compounds. Consider an alloy made up of atoms of element A and element B. If the mixing enthalpy is too negative, then A–B bonds are favoured over both A–A bonds and B–B bonds, leading to an ordered intermetallic phase. Conversely, if the energy of the mixing enthalpy is too positive, then A–A bonds and B–B bonds are favoured over A–B bonds, resulting in segregation. Zhang *et al.* used the enthalpy of mixing and atomic size difference parameter, δ , to screen potential concentrated solid solutions (**Figure 13**) [147].

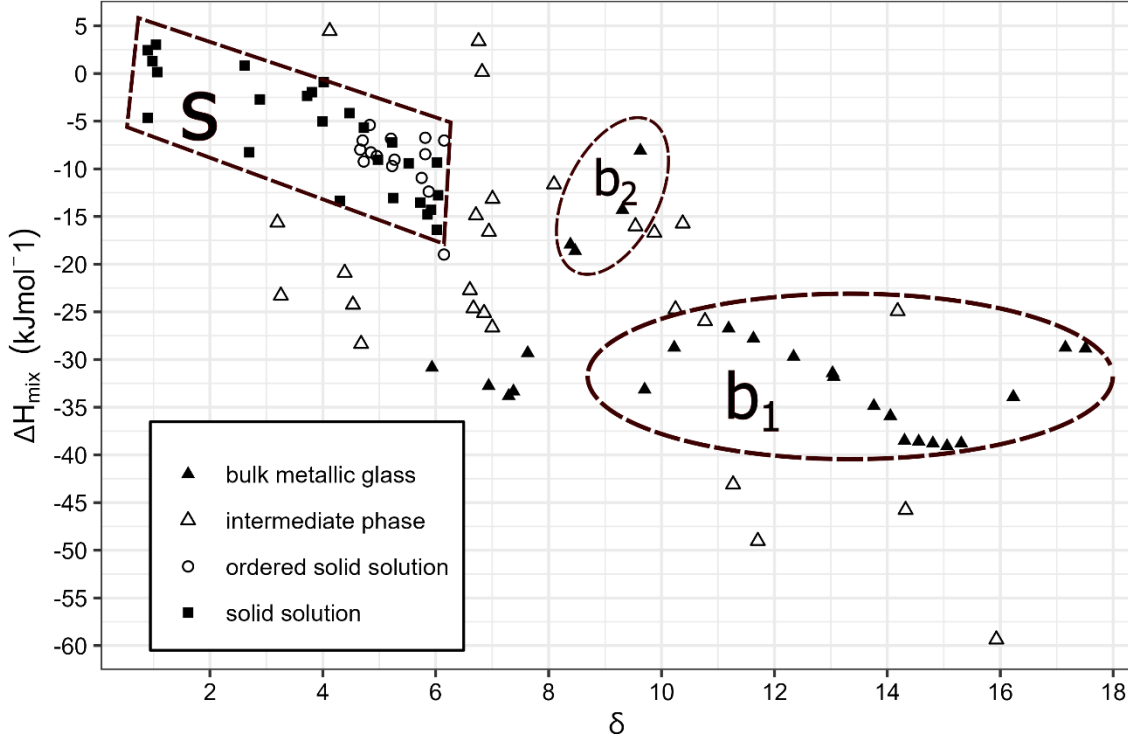


Figure 13. Showing the effect of atomic size difference parameter, δ , and the enthalpy of mixing, ΔH_{mix} , on phase stability of compositionally complex alloys. Reproduced from Zhang *et al.* [147]. Dashed shapes indicate regions of solid solution phases, S, and bulk metallic glasses, b_1 and b_2 .

Guo *et al.* added two more parameters to the work of Zhang *et al.* [146]. The first is the electronegativity difference [152], $\Delta\chi$, out of consideration from the classic Hume-Rothery rule to form solid solution phases, and is here defined by Fang *et al.* [152] as:

$$\Delta\chi = \sqrt{\sum_{i=1}^n c_i (\chi_i - \bar{\chi})^2} \quad (14)$$

where $\bar{\chi} = \sum_{i=1}^n c_i \chi_i$, is the Pauling electronegativity for the i th element. The second parameter proposed by Guo *et al.* was the valence electron concentration (VEC):

$$\text{VEC} = \sum_{i=1}^n c_i (\text{VEC})_i \quad (9)$$

where VEC is the valence electron concentration, c_i is the atomic composition of element i , and $(\text{VEC})_i$ is the valence electron concentration of element i . It is found that a high valence electron concentration (≥ 8) is conducive to forming face-centred cubic phases, and a low valence electron concentration (< 6.87) is conducive to forming body-centred cubic structures.

It was shown that valence electron concentration can be further tuned to optimise properties such as ductility.

Yang *et al.* found that ΔH and ΔS play different roles during the solid-solution formation process, and so the ratio of each, that is, ΔH_{mix} and $T\Delta S_{\text{mix}}$ is used to estimate the solid-solution formation [144]. From this, Yang *et al.* derives the parameter Ω , defined as

$$\Omega = \frac{T_m \Delta S_{\text{mix}}}{|\Delta H_{\text{mix}}|} \quad (12)$$

where T_m is the theoretical melting point of the alloy, defined as:

$$T_m = \sum_{i=1}^n c_i (T_m)_i \quad (15)$$

where c_i is the atomic fraction of element i . In this model, the theoretical melting point (derived from the rule of mixtures) is multiplied by ΔS_{mix} , the entropy contribution towards the free energy. This is divided by the absolute value of the mixing enthalpy, ΔH_{mix} . The parameter Ω therefore takes on a positive value. At the point where $\Omega = 1$, a critical value is proposed where the contribution from $T\Delta S_{\text{mix}}$ competes with ΔH_{mix} for phase formation. If Ω is greater than unity, the contribution of $T\Delta S_{\text{mix}}$ towards the free energy will exceed ΔH_{mix} . If the Ω value is less than unity, then enthalpy of mixing, ΔH_{mix} , is the primary contributor to free energy, and intermetallic compounds or segregation is more likely. Yang *et al.* incorporated the atomic size difference parameter, δ , from Zhang *et al.* to form a general rule for solid solution formation (**Figure 14**). In this model, compositionally complex alloys must satisfy the following criteria: $\Omega > 1.1$ and $\delta < 6.6\%$.

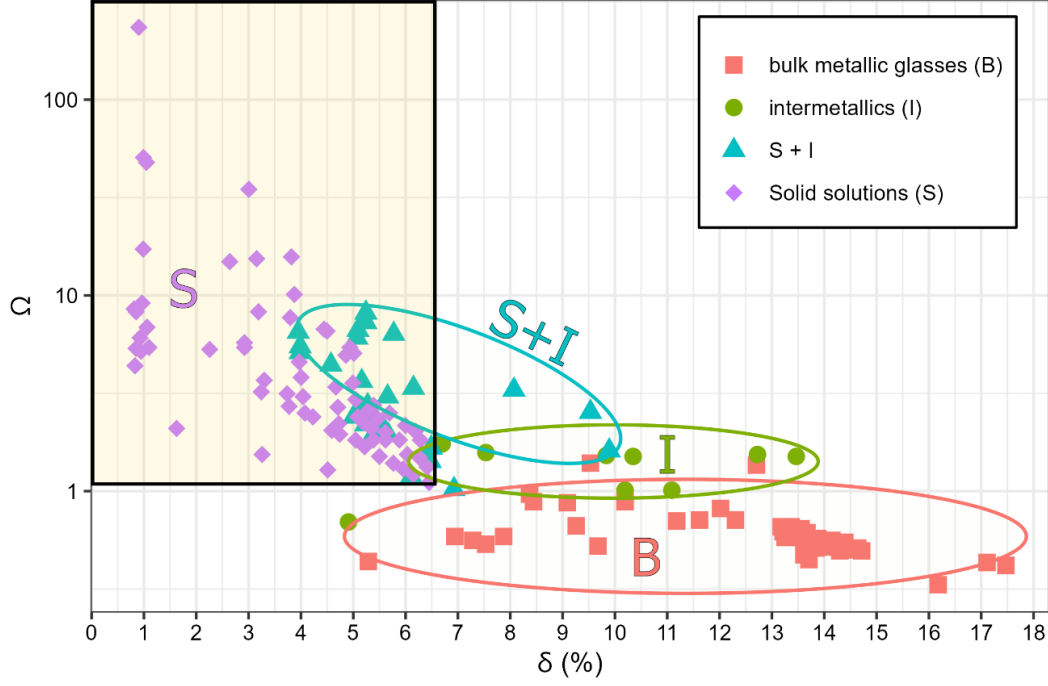


Figure 14. Screening single phase solid solutions using the Ω and δ parameters. Reproduced from Yang *et al.* [144].

According to Wang *et al.*, the atomic size difference parameter, δ , does not adequately characterise the solubility of compositionally complex alloys [149]. For example, many intermetallics with $\delta \approx 0.06$ have been detected. This is because the atomic size difference parameter, δ , considers the average effect of the atomic size difference between alloy elements. However, in compositionally complex alloy systems, the stability of a concentrated solid solution is frequently determined by the packing of the smallest and largest atoms. To address this limitation, Wang *et al.* proposed incorporating the packing behaviour of atoms into atomic size effect calculations. In this model, the packing around the smallest and largest atoms is emphasised to demonstrate how far the atomic packings deviate from the ideal state. The solid angles for the elements of atomic packing for atoms with the smallest and largest atomic radii are selected and geometrically described by using their atomic radii:

$$\omega_s = 1 - \sqrt{\frac{(r_L + \bar{r})^2 - \bar{r}^2}{(r_L + \bar{r})^2}}; \quad \omega_L = 1 - \sqrt{\frac{(r_s + \bar{r})^2 - \bar{r}^2}{(r_s + \bar{r})^2}} \quad (11a)$$

where r_s and r_L are the atoms' smallest and largest radii, respectively. The ratio of these two quantities, that is, the ratio between the solid angles of the smallest and largest atoms, is considered an indicator for atomic packing and topological instability:

$$\gamma = \frac{\omega_s}{\omega_L} \quad (11b)$$

In this model, the original Hume-Rothery rule of 15% atomic size difference in binary alloys corresponds to a critical value of $\gamma = 1.167$. The atomic packing factor, γ , was shown to predict the solid solution formability of compositionally complex alloys better than the previous atomic size difference parameter, δ [149]. **Figure 15** shows a comparison between the two parameters in a selection of experimentally produced alloys from Zhang *et al.* [153].

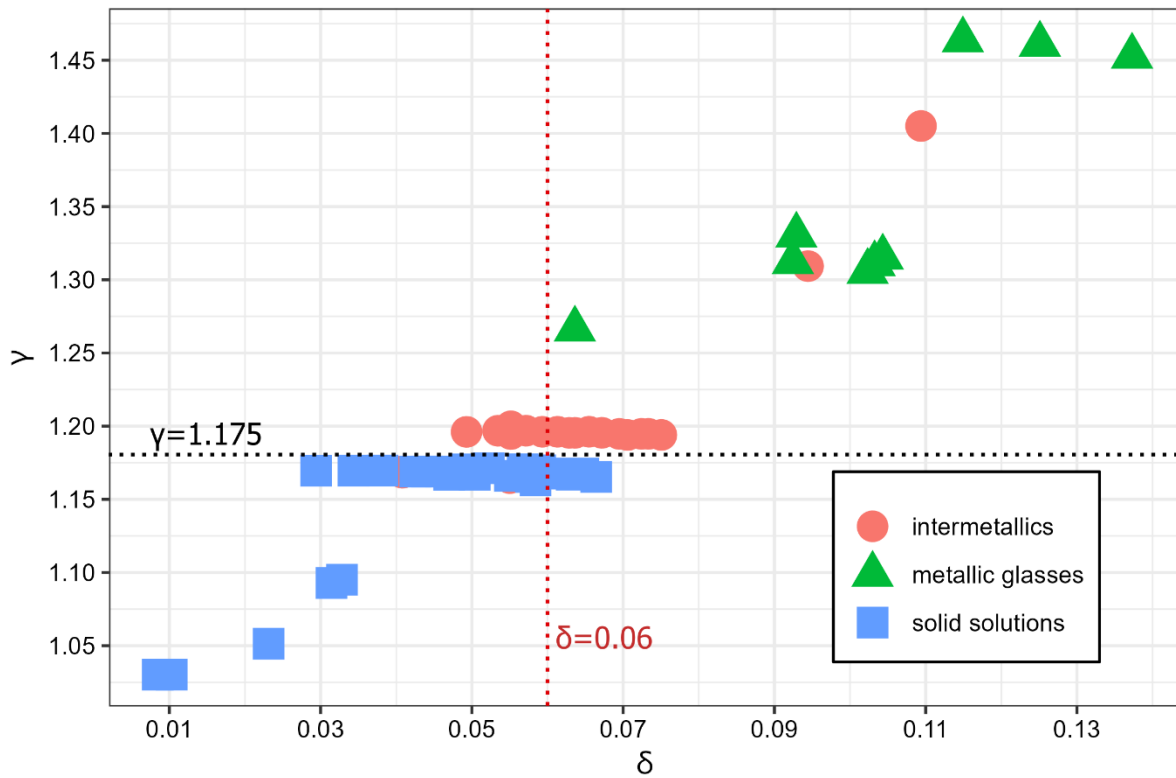


Figure 15. Atomic size difference parameter, δ (%), and atomic packing parameter, γ , for experimental results on the phase selection of compositionally complex alloys. Reproduced from Zhang *et al.* [153].

King *et al.* proposed the thermal stability parameter, ϕ , which compares an estimate of the Gibbs energy of formation for a concentrated solid solution at its melting temperature to the Gibbs energy of formation for the binary intermetallic that is most likely to form in such a system (**Figure 16**) [148].

To estimate Gibbs energy of formation:

$$\Delta G = \Delta H - T\Delta S \quad (16)$$

one must supply the enthalpy of formation, which is approximated as the enthalpy of mixing, ΔH_{mix} , the temperature, T , and the entropy, ΔS . For a concentrated solid solution, King *et al.* estimates the enthalpy of formation as the mixing enthalpy, defined quasi-chemically as:

$$\Delta H_{\text{mix}} = \sum_{i \neq j}^n 4\Delta H_{ij} c_i c_j \quad (7)$$

where c is the concentration, in atomic fraction, of element i and j , and ΔH_{ij} is the enthalpy of mixing per mole between element i and j calculated for a binary alloy. The temperature, T , is the theoretical melting temperature of the concentrated solid solution as estimated by the rule of mixtures, and the concentrated solid solution's entropy, ΔS , is approximated as the ideal configurational entropy, ΔS_{conf} .

The Gibbs energy of formation for the binary intermetallic is estimated by the mixing enthalpy only, scaled to maintain stoichiometry. The entropy of the intermetallic is approximated as $0 \text{ JK}^{-1}\text{mol}^{-1}$. The stability parameter, φ , is then calculated from the ratio of these two quantities as:

$$\varphi = \frac{\Delta G_{ss}}{-|\Delta G_{max}|} \quad (13)$$

where a value $\varphi > 1$ suggests stable solid solution formation at the alloy's melting temperature (**Figure 16**).

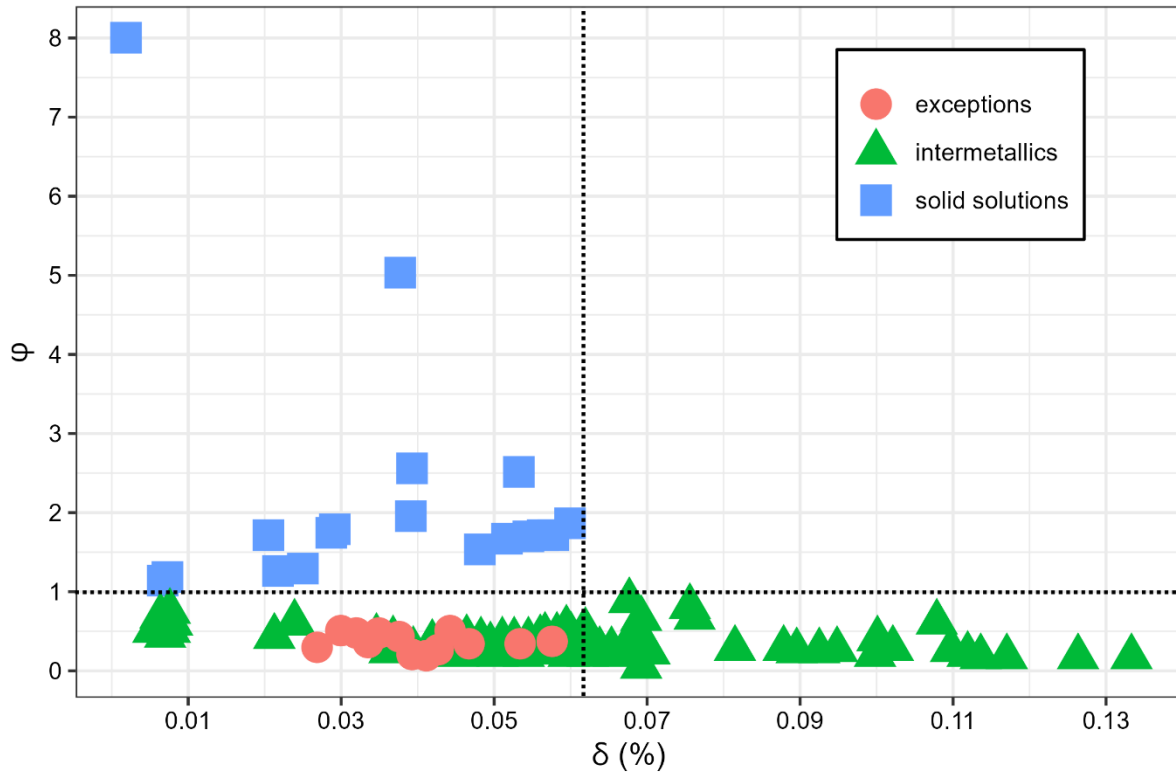


Figure 16. Comparison of experimentally determined compositionally complex alloys with their atomic size difference parameter, δ , and their thermal stability parameter, φ . Reproduced from King *et al.* [148].

The thermophysical parameters discussed in this section are useful for the rapid screening of thousands of compositions and can identify potentially interesting compositions for further study. For an example by Rickman *et al.* used the parametric approach to screen for the solid solution formability of a range of compositionally complex alloys (**Figure 17**) [154].

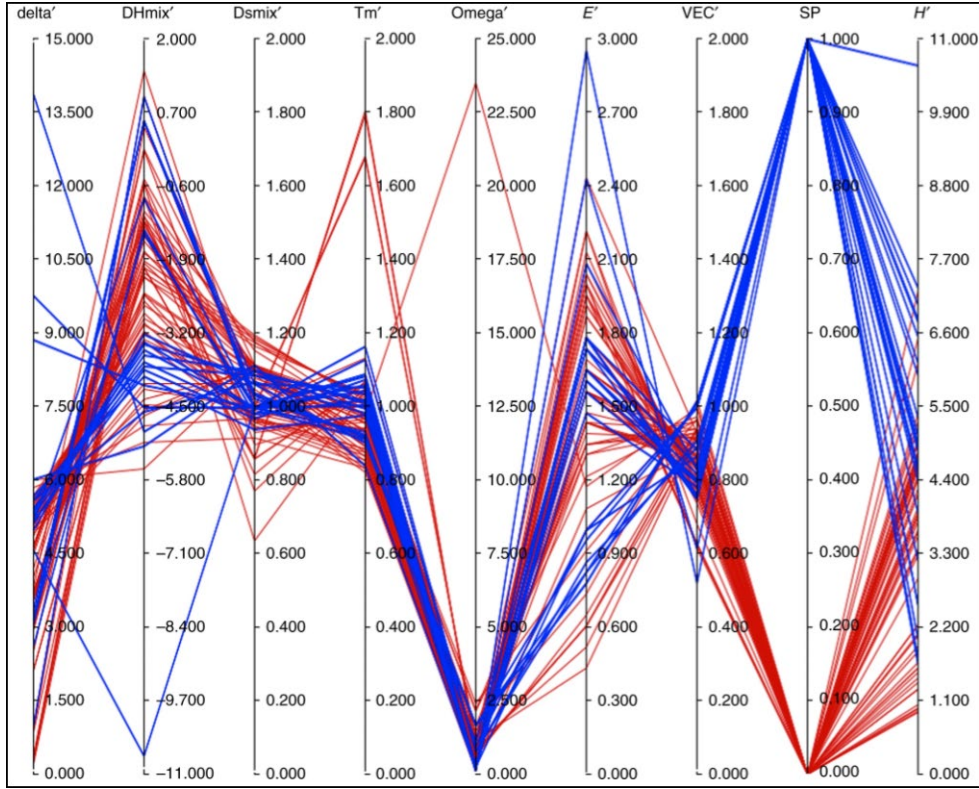


Figure 17. Solid solution formability of a range of compositionally complex alloys. Reproduced from Rickman *et al.* [154]. (SP indicates solid solution formability; blue indicates single-phase solutions; red indicates multi-phase alloys).

Gibbs phase rule

The condition for equilibrium for a binary system containing two phases is that the chemical potentials for each component in each phase must be equal. A consequence of this general rule is called the Gibbs phase rule. The upper bound of the numbers of phases that can form in an equilibrated system is given by Gibbs phase rule [155], [156], which states that if a system containing C components and P phases in equilibrium, then the number of degrees of freedom F is given by:

$$F = C - P + 2 \quad (17)$$

Cantor in his original paper [89] created a 20 component alloy containing Mn, Cr, Fe, Co, Ni, Cu, Ag, W, Mo, Nb, Al, Cd, Sn, Pb, Bi, Zn, Ge, Si, Sb, and Mg. At constant pressure, Gibbs phase rule states that up to 21 phases could form at equilibrium. In experiment, far fewer phases formed, with face centred cubic FeCrMnNiCo forming the predominant phase. This phenomenon of obtaining far fewer phases than the Gibbs rule permits has been attributed to the contribution of configurational entropy to the free energy, which suppresses intermetallics

and results in the observed phase stability. However, attention should be drawn to the fact that the Gibbs phase rule only states how many phases are possible at maximum, given a set of components and degrees of freedom. The rule does not explicitly state how many phases will form under a set of conditions. Therefore, it is not surprising that Cantor's alloy formed fewer phases than the maximum number of phases permitted by the Gibbs phase rule, and this does not lend support to an argument based on large configurational entropy. An example is given by Pickering *et al.* [151] where the following case is described: a binary combination of elements at constant pressure allows for 3 maximum phases, but these phases can only occur at eutectic and peritectic points, which are invariant positions in the phase diagram.

1.2.5.2 Calculation of phase diagrams (CALPHAD)

The CALculation of PHase Diagrams (CALPHAD) methodology was introduced in 1970 by Larry Kaufman [157]. Equilibrium phase diagrams, with axes for temperature and composition of a chemical system, are a very powerful tool for predicting the state of a system under different conditions and are usually a graphical representation of experimental information on states of equilibrium. When dealing with complex systems, CALPHAD is employed as a computational approach to model thermodynamic properties for each phase and simulate multicomponent phase behaviour [158].

A thermodynamic database, constructed from experimental data obtained from constituent binary and ternary phase diagrams, is utilised by the CALPHAD approach to calculate phase stability of multi-component systems [97]. The development of CALPHAD databases for compositionally complex alloys is being undertaken [159]. The ThermoCalc High Entropy Alloy (TCHEA) database, which is currently in its 6th iteration, is the one with the most comprehensive assessment of binary and ternary systems. The accuracy of the assessment of binary and ternary systems will facilitate better predictions of higher order systems. These predictions aim to shorten the time to develop new compositionally complex alloys

CALPHAD has been used to predict phase equilibria for complex systems, such as refractory compositionally complex alloys [160], 3d transition metal alloys [161]–[163], and multicomponent Ni-based superalloys [164]. Other uses include screening the multidimensional phase space for alloy systems of interest [165], in efforts to expedite materials development.

It has been suggested in recent works that CALPHAD has the capability of reasonably predicting the major phases present in compositionally complex alloys, as noted by Senkov *et al.* [166] and Chen *et al.* [167]; however, Miracle *et al.* has recorded that the number of phases, the volume fractions, and their compositions are not often provided correctly by CALPHAD [168]. CALPHAD, therefore, can be a powerful technique to model phase equilibria, but often must be supplemented with experimental data or other theoretical approaches. The CALPHAD methodology is expanded on in **Chapter 2**.

1.2.5.3 Studying phase stability experimentally

Experimentally, the study of thermodynamic phase stability of compositionally complex alloys is time-consuming, costly, and represents a challenge to be optimised by the research community. This is made more challenging when considering refractory materials based on elements like Mo and W. The process involves manufacturing the high-temperature structures, and equilibrating them at a suitable temperature, followed by quenching. The alloys must then be characterised fully, which usually requires more sophisticated techniques than energy dispersive spectroscopy and X-ray diffraction. Fortunately, developments in atom-probe tomography, for example, allow for the exact local structure of compositionally complex alloys to be solved.

There is, however, growing research on the high-throughput synthesis and characterisation of compositionally complex alloys. The most straightforward method is to generate a series of alloys and perform mechanical testing to screen for favourable properties. Moorhead *et al.* produced alloys in the MoNbTaW system using additive powder manufacturing followed by laser remelting to ensure homogenisation [169]. The authors note challenges with this method, including changes to the final composition of the alloy. This challenge was highlighted by other authors [170]. The technique has potential to quickly assess the process-structure-properties relationship in compositionally complex alloys when partnered with high-throughput mechanical testing techniques.

1.2.6 Fabrication

The manufacturing technologies for compositionally complex alloys can be broadly categorised into four groups [171]:

- solid-state processing,
- liquid-state processing,
- thin-film deposition,
- and additive manufacturing technology [172].

1.2.6.1 Solid-state processing

In solid-state processing, alloying elements are mixed at room temperature and then consolidated at elevated temperatures. The predominant solid-state manufacturing techniques for compositionally complex alloys are atomisation with gas or liquid, high-energy ball milling, cold compaction and sintering, hot pressing, and spark plasma sintering.

The method of high energy ball milling involves mixing alloying elements in a milling jar with ceramic or hardened stainless steel grinding balls. Powders are then mechanically blended using a high-energy ball mill. Compositionally complex alloys produced via this method include CoCrNiMnAl_x ($x = 0, 0.1, 0.3, 0.5, 0.7, 1$) (milling time = 45 hours) [173], WMoNbZrV (milling time = 50 hours) [174], AlCuNiFeCr [175], AlCrFeNiCoC [176]. Contamination from the milling jar and milling balls is the primary disadvantage of this method, as it has a direct effect on the final material properties of the powders produced [177].

A cold pressing technique followed by sintering is a straightforward method for producing alloys with complex compositions. In this process, alloying powders are inserted between two punches into a die. Uniaxial pressure is applied to produce a green compact. Cold-pressed compositionally complex alloys include AlCoCrFeNi (625 MPa) [178] and AlCoFeMoNiTi (1.5 GPa) [179]. The pellets can then be densified through a sintering procedure. Typically, the alloy is heated below its melting point in an inert atmosphere for diffusion bonding to take place. Xu *et al.* produced $\text{FeMn}_{28}\text{Si}_x$ ($x = 0, 1, 2, 3, 4$ wt%) via high energy ball milling, cold compaction (400 MPa), and sintered at 1073 K for 1 hour, then 1473 K for 3 hours [180]. These results suggest that compositionally complex alloys can be manufactured using standard sintering techniques.

The simultaneous processes of compaction and sintering are incorporated into hot pressing. Alloys produced in this method include $\text{Al}_{0.6}\text{NiFeCrCo}$ and $\text{Al}_{0.6}\text{NiFeCr}$ (30 MPa;

1273 K; 1 hour) [181], and $\text{Fe}_{18}\text{Ni}_{23}\text{Co}_{25}\text{Cr}_{21}\text{Mo}_8\text{WNb}_3\text{C}_2$ (30 MPa; 673, 873, and 1323 K; 2 hours) [182]. Tang. *et al.* [183] produced AlCoCrFeNi (207 MPa, 1273 K, 1 hour) using a modified isostatic load-applying technique. The benefit of hot pressing is that it reduces porosity and increases the density of the final product.

Spark plasma sintering, also known as field-assisted sintering, is a novel technique that compacts a powder sample by passing an electric current through it via a graphite die. Therefore, the heating is internal to the sample, as opposed to being applied externally as in hot pressing. This method has the benefits of lower sintering temperatures and quicker densification rates. Alloys produced in this method include $\text{Al}_{0.6}\text{NiFeCrCo}$ and $\text{Al}_{0.6}\text{NiFeCr}$ (30 MPa; 1273 K; 1 hour) [181], $\text{Fe}_{18}\text{Ni}_{23}\text{Co}_{25}\text{Cr}_{21}\text{Mo}_8\text{WNb}_3\text{C}_2$ (30 MPa; 673, 873, and 1323 K; 2 hours) [182]. Pan *et al.* produced the compositionally complex refractory alloys $\text{Nb}_{25}\text{Mo}_{25}\text{Ta}_{25}\text{W}_{25}$ and $\text{Ti}_8\text{Nb}_{23}\text{Mo}_{23}\text{W}_{23}$ using mechanical alloying and spark plasma sintering to produce a single stable solid body-centred cubic solution [184]. Spark plasma sintering is an effective method for producing compositionally complex alloys, but challenges include maintaining a sample's symmetrical shape.

1.2.6.2 Liquid-state processing

The predominant liquid-state processing of compositionally complex alloys is via vacuum arc melting, and induction heating, with many compositionally complex alloys produced via these methods. Vacuum arc melting involves placing metals into a Cu crucible inside of a vacuum chamber and struck with a tungsten electric arc under Ar atmosphere [171]. The benefits of vacuum arc melting are that it is quick and uses low amounts of energy. Samples must be remelted several times, however, to ensure homogeneity, and the high temperatures can evaporate low melting point metals during the heating process. The arc melting process is discussed further in **Chapter 2**. This process has been used to manufacture Cantor alloy derivatives such as CoCrFeMnNi [185], AlFeCoNiB_x ($x = 0, 0.05, 0.10, 0.15, 0.20$) [186], FeCrCoNi [187], MnFeCoNiCu [188], AlCoCrFeNi [189], and CoCrFeNiNb_x ($x = 0.5, 0.65$ and 0.8) [190]. Arc melting is also a popular method of producing refractory alloys due to the high temperatures achievable with this method. Some of these refractory alloys include $\text{Ta}_{0.5}\text{HfZrTi}$ [191], MoNbCrVTi and MoNbCrZrTi [192], $\text{Mo}_{0.5}\text{NbTiVCr}_{0.25}$ and $\text{Mo}_{0.5}\text{NbTiV}_{0.5}\text{Zr}_{0.25}$ [124], HfNbTaTiZr and sub-alloys thereof [193], NbTiVZr , $\text{Nb}_{0.5}\text{TiVZr}$, and NbTiV [194], and TiVZrNbHf and sub-alloys thereof [195].

Vacuum induction heating is another liquid-state processing method, which uses electromagnetic induction to heat alloys from the inside. The sample is remelted several times to ensure homogeneity, and then cast into a mould for cooling. Compositionally complex alloys produced via this method include Fe_xCoNiCu ($x = 1.5, 2, 2.5, 3$) [196] and $\text{Co}_{10}\text{Cu}_{20}\text{Mn}_{30}\text{Ni}_{40}$ [197].

In the atomisation method, molten alloying elements are loaded into a vacuum chamber and ejected from a nozzle using a high-pressure gas or water jet. This method directly produces fine- alloyed powders. Compositionally complex alloys manufactured in this manner include AlCoCrCuFeNiSi [198], $\text{Al}_{0.6}\text{CoCrFeNi}$ [199], CoCrFeMnNi [200], [201], and $\text{CrFeCoNiMo}_{0.2}$ [202].

1.2.6.3 Thin-film deposition

Thin film deposition techniques include magnetron sputtering, pulsed laser deposition, and plasma spraying deposition [171].

Magnetron sputtering produces coatings and thin films under a high vacuum. For example, Kim *et al.* produced thin films of MoNbTaW from a single sputtering target via direct current magnetron sputtering [203]. They found that the technique formed a thin film single solid solution phase. Magnetron sputtering has been used to develop Cantor alloy derivative coatings such as MnFeCoNiCu [188], CrCuFeMoNi [204], CoCrFeNiCu and $\text{CoCrFeNiCuAl}_{2.5}$ [205], and has also been used to form coatings comprising refractory elements. These alloys include alloys in the HfTiVZrNb system [206], MoNbTaW [207], [208], TiVZrCrAl [209], AlTiCrNiTa [210], WTaVCr [131], TiVCrZrW [211], AlMoNbSiTaTiVZr [212], AlCrTiVZr [213], AlCrMoNbZr [214], and $\text{AlCrMoNbZr}/(\text{AlCrMoNbZr})\text{N}$ [215].

Pulsed laser deposition uses an intense pulsed laser beam to vaporise target elements. These metal vapours then deposit onto a substrate as a thin film, either in a background gas atmosphere, or high vacuum [171]. Pulsed laser deposition has successfully produced 3d transition metal compositionally complex alloys such as AlCrFeCoNiCu [216] and $\text{CoCrFeNiAl}_{0.3}$ [217], as well as refractory alloys such as MoNbTaW [170], NbTiZr , and NbTaTiZr [218].

Plasma spray deposition has also been used to manufacture compositionally complex alloys. This process involves spraying molten alloy powders onto substrates. The powders are ejected into a plasma flame at a high temperature, where they are heated and accelerated toward a substrate, where they cool to form a coating [171]. Many of the studies on plasma sprayed coatings include alloys from the AlCoCrFeNi system [219], [220]. Readers are referred to the recent reviews by Meghwal *et al.* [220] and Sharma *et al.* [221] for further reading on the development of compositionally complex alloy coatings, including plasma spray deposition.

1.2.7 Compositionally complex alloy coatings for nuclear fuel claddings

The use of compositionally complex alloy coatings for fuel cladding is a relatively new field in the nuclear industry with few authors investigating this [103], [104], [204], [209], [210], [214], [218], [222]. Readers are encouraged to consult the recent review by Kashkarov *et al.* for an extensive overview of current fuel coatings, particularly their short section on the development of novel compositionally complex alloy coatings [83]. Materials properties of compositionally complex coatings can be predicted as a first approximation simply by considering the constituent elements – elements like Al, Cr, Ti, and Si for example are chosen to provide oxidation resistance; Cr, for corrosion resistance; Al, Ni, Co, Fe, for enhanced tribological properties; and Co, and Ni for increased plasticity (**Figure 18**). Zr is chosen for its favourable neutronic penalty. Properties can then be optimised by fine-tuning compositions using high-throughput experiments and computational studies [97].

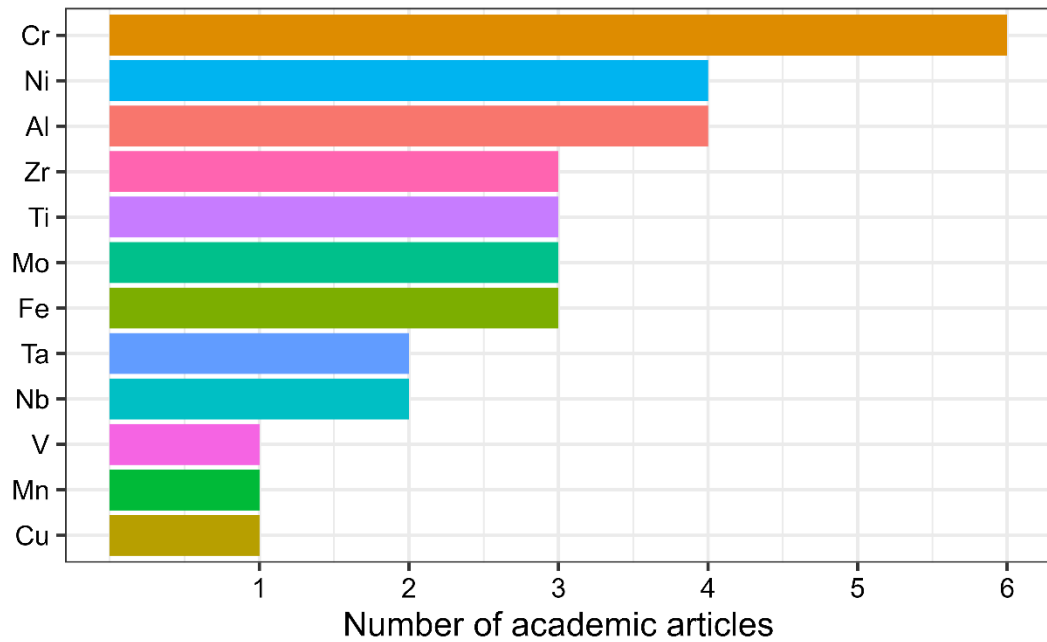


Figure 18. Choices of elements for compositionally complex alloy fuel coatings within the academic literature.

Alloys such as AlTiCrNiTa [97], CrCuFeMoNi [204], AlCrMoNbZr [214], FeCrMnNi [103], [104], TiVZrCrAl [209], AlCrFeMoNi [222], NbTiZr, and NbTaTiZr [218], have been synthesised for their potential to coat zirconium-based cladding material. Fabrication techniques include magnetron sputtering [204], [209], [210], [214], ion beam sputter deposition [103], [104], and pulsed laser cladding [218]. AlCrFeMoNi, however, has only been synthesised in its bulk form via vacuum arc melting [222]. The design criteria for a compositionally complex alloy coating is markedly different from that of an interlayer barrier; most notable, is the increased requirement for hardness is to minimise grid-to-rod fretting [210]. Sputtered AlTiCrNiTi coating onto Zircaloy-4 and achieved a hardness of 18.34 GPa, which is 4.5 times harder than Zircaloy-4, and harder than pure Cr or FeCrAl coatings [210]. However, Al is known to form a Boehmite phase of composition AlOOH , which has extensive solubility in water [46], [214]. $\text{Cr}_{0.26}\text{Cu}_{0.3}\text{Fe}_{0.1}\text{Mo}_{0.15}\text{Ni}_{0.19}$ was found to have superior hardness of 12.5 GPa and was able to form dense continuous oxide films of Cr_2O_3 and FeCr_2O_4 for superior corrosion resistance [204]. AlCrMoNbZr coatings exhibited hardness of 11.8 GPa, and again, proved superior in its corrosion resistance to typical zirconium-based alloys. Here, it was found that $\text{Nb}_2\text{Zr}_6\text{O}_{17}$, ZrO_2 , and Cr_2O_3 all formed, and were able to provide dense protective films [214]. He *et al.* achieved coatings of TiVZrCrAl with nanohardness of 18.28 GPa which they attributed to the severe lattice distortion effect. They also found that the

formation of AlVO_4 (or simply the incorporation of V in the coating system) was successfully able to suppress Boehmite phase formation and its subsequent dissolution in water [209].

1.2.8 Oxidation of refractory compositionally complex alloys

Academic literature on the oxidation of compositionally complex alloys is in its infancy [223]. However, over the last 10 years enough research has been conducted for a recent review article on the topic by Gorr *et al.*, to which the reader is referred [224]. The oxidation behaviour of compositionally complex alloys is undoubtedly influenced by the individual elements which constitute them, although the underlying processes and mechanisms are not typically straightforward; elements can behave synergistically to improve oxidation resistance, or in some cases non-complimentary to cancel the effects of one another. Oxidation resistance of an alloy usually depends on the ability to form dense oxide surface films which are:

- Non-reactive,
- Non-volatile,
- Non-water soluble,
- Impermeable to oxygen.

Non-reactivity requires that the oxide layer be thermodynamically stable and not liable to react with other species present in the coating system. An enlightening example of this is the incorporation of Al into alloys where W is also present. In this example, the oxides Al_2O_3 and WO_3 can react to form $\text{Al}_2(\text{WO}_4)_3$ at the surface which reduces homogeneity of Al_2O_3 and causes a concomitant reduction in oxidation resistance [225]. Volatility of oxides is important as some oxides evaporate away during the oxidation process. For example, V forms V_2O_5 with a low melting point of 675 – 690°C (although mitigation strategies to prevent melting of V_2O_5 will be examined soon). W has famously poor oxidation resistance, with WO_3 evaporating quickly at 1000 – 1150°C [225]–[227]. Mo, which forms MoO_3 performs even worse as it evaporates above 795°C [225]. Al, while useful in air environments is generally avoided in water environments because of its proclivity to form water-soluble AlOOH which quickly dissolves away, resulting in faster oxidation kinetics of the underlying substrate [46], [214]. Nb_2O_5 , on the other hand, is a stable, non-volatile oxide of Nb, but is instead limited by its high solubility and large diffusion coefficients with oxygen [228]–[230]. For this reason, Nb_2O_5 forming alloys tend to have porous oxide film as well as experience severe spalling [231]. Indeed, a viable oxide scale must also resist spalling at high temperatures, which depends on:

- Good adhesion to the substrate,
- Similar thermal expansion to the substrate,
- An acceptable ratio of volume to the volume of underlying metal.

1.2.8.1 Oxidation resistance strategies

Traditional alloy design relies on the incorporation of elements like Al and Cr, and Si to improve oxidation resistance. All elements can form dense and stable impermeable oxide films at the surface. The ability to form surface layers of Al_2O_3 [232], Cr_2O_3 [233], and SiO_2 [234] are all beneficial because they form dense, thermodynamically stable oxides with low permeability to oxygen. Growth rates of Al_2O_3 and Cr_2O_3 are very slow – rate constants are $2 \times 10^{-11} \text{ mg}^2\text{cm}^{-4} \text{ s}^{-1}$ and $7 \times 10^{-12} \text{ mg}^2\text{cm}^{-4}\text{s}^{-1}$ at 1000°C , respectively [235]. It is for this reason that the best alloys, in terms of oxidation resistance, incorporate one or more of the elements Al and Cr. While this design strategy is useful, compositionally complex alloys comprise elements in high concentrations, and the design strategy with respect to oxidation resistance is not as straightforward as in conventional alloys [162]. For example, Nb can counteract the oxidative benefit of Cr because it thermodynamically competes for oxide formation [236]. This is because Nb and Cr oxides have almost identical Gibbs energy of formation. Likewise, Ti reduces oxidation resistance in Al_2O_3 -forming alloys for the same reason [237]. As discussed previously, oxides of W directly react with Al_2O_3 which reduces oxidation resistance. Further analyses are required to draw a clear connection between constituent elements and oxidation resistance.

Fortunately, some synergistic effects are observed between constituent elements to improve oxidation resistance. For example, Ti improves oxidation resistance in alloys where it can support the formation of CrTaO_4 [231], a rarely encountered complex oxide [224] but one that is found to be protective in Ta-containing alloys [236]–[238]. Ability to form CrTaO_4 has also been observed to improve oxidation resistance in some Ni-based superalloys because it hinders both outward diffusion of elements from the substrate and inward diffusion of oxygen [239], [240]. Despite its tendency to form water soluble AlOOH , He *et al.* [209] demonstrated that incorporating V into the oxide scale of Al can prevent AlOOH formation, potentially making it a viable option for coating materials in water environments.

Many other complex oxides have been observed in the literature [211], [241]–[245] including TiNb_2O_7 and $\text{Nb}_2\text{Zr}_6\text{O}_{17}$ in NbTiZrV [241], $\text{Nb}_3\text{Cr}_2\text{O}_{10}$ and $\text{Nb}_2\text{Zr}_8\text{O}_{21}$ in

NbCrMo_{0.5}Ta_{0.5}TiZr [242], CrNbO₄, AlTiO₅ in Al₁₀CrNbTiZr₁₀ [243], CrNbO₄ and YNbO₄, in NbMoCrTiAlY [244], CrTaO₄ and MoTiTa₈O₂₅ in TaMoCrTi [245], MoTiTa₈O₂₅ in TaMoTi and TaMoTiAl [245], and ZrTiO₄ in TiVCrZrW [211]. These oxides could have widely disparate densities, oxygen permeability, lubricating properties, reactivity, volumes, and thermal expansion properties to simple oxide systems. Despite significant progress in the field, the oxidation behaviour of these oxides remains largely unexplored; the impact of the constituent elements of compositionally complex alloys on their subsequent oxidation behaviour is still largely a mystery.

1.2.9 Compositionally complex alloys as Zr-Cr interlayers

The following is a summary of the specifications for an ideal interlayer material between Zr and Cr.

- Possess a high eutectic reaction temperature with both Cr and Zr ($> 1330^{\circ}\text{C}$).
- Avoid intermetallic compounds with Cr and Zr or with itself.
- Exhibit moderate thermal expansion characteristics.
- Exhibit adequate ductility.
- Exhibit a low rate of oxidation.
- Possess the ability to getter H₂ to prevent ingress into the Zr cladding.
- Have low Zr and Cr interdiffusion coefficients.
- Exhibit an elevated thermal conductivity.
- Consist of elements with low neutron cross-sections.
- Contain no activating elements like Co.
- Capable of producing an adherent coating.
- Be readily manufactured using an industrially scalable process.
- Comprise non-toxic elements.
- Contain no long-lasting radionuclides.
- Cheap to acquire and produce.
- Not be susceptible to supply constraints [81], [246].

Currently, the application of Cr coatings is impeded by its eutectic reaction temperature with Zr ($1,330^{\circ}\text{C}$). Temperatures within a reactor can easily exceed this eutectic temperature during a loss-of-coolant accident, resulting in liquid formation on the surface of the Zr

substrate. In the worst-case scenario, the coating system can detach from the Zr fuel pin, leaving it unprotected. Therefore an increase in the eutectic reaction temperature of the system should correlate with increased coping times in the event of a loss-of-coolant accident [81].

Intermetallics, such as the C14 Laves phase ZrCr_2 and $\text{Zr}(\text{Cr,Fe})_2$, must be suppressed to prevent the formation of compounds and phases that could weaken the coating system and cause spalling or cracking.

Important considerations for an interlayer include ductility and thermal expansion. Frequent outages for fuel changes in light water nuclear reactors are accompanied by temperature changes of hundreds of degrees. For a coating system to last the lifetime of the fuel, it is essential to design a thermally cyclable interlayer that is also durable. Medium thermal expansion and high ductility are the most important properties for achieving this robust interlayer. By carefully controlling thermal expansion, it is possible to ensure that there are no significant thermal expansion differentials within the coating system and that stresses caused by thermal changes in the environment are minimal. Ductility is also essential to absorb any stresses that may be induced, thereby preventing crack propagation throughout the coating system.

Moreover, oxidation is an issue. An ideal interlayer should not exhibit a faster oxidation rate than either the Zr substrate or the Cr coating. Even though the interlayer is in theory protected by the Cr coating, if diffusing oxygen causes the interlayer to readily oxidise, this would result in a chemical reaction resulting in multiple metal oxides with different volumes, thermal expansion, adhesion, and mechanical properties to the Zr substrate and Cr coating, which could cause the coating system to fail.

Current Zr claddings experience H_2 ingress and embrittlement [247]–[249]. A perfect interlayer would be capable of gettering this H_2 and preventing its ingress into the Zr cladding material.

The fundamental purpose of the interlayer is to keep the Zr substrate and Cr coating as far apart as possible in the event of a loss-of-coolant accident. Low diffusion kinetics between the interlayer material and surrounding substrate and coating facilitate this function. Therefore, the diffusion coefficients between Zr and the interlayer and between the interlayer and the Cr coating must be as small as possible.

Heat transfer from the interior of the fuel pins to the coolant water is essential for the performance of a nuclear fuel pin. Therefore, no coating system applied to the fuel should hinder this heat transfer. Therefore, the interlayer's thermal conductivity should be at least as high as zirconium-based alloys and Cr.

Neutron flux within a reactor's core has a direct effect on reactivity; every neutron absorbed by the cladding atom is a neutron that cannot contribute to the heat-generating process. Typically, the increase of non-fissionable materials in a reactor is accompanied by an increase in fuel enrichment, which increases the cost of the fuel cycle [250]. Hall *et al.* provides a range of 0.1% to 0.15 % for the increase in enrichment required to counteract the negative reactivity of Cr coatings in pressurised water reactor fuel [250]. Ideally, an interlayer material should contain elements which are neutron transparent. While elements with a low neutron absorption cross-section such as Zr are limited, the negative reactivity caused by an interlayer must be weighed against its benefits.

An ideal interlayer should also be devoid of activating elements such as Co. Similarly, elements that are toxic or pose health risks should be avoided whenever possible. Elements for an interlayer must not be susceptible to supply risk or supply restriction [246].

No research has yet been conducted on the incorporation of a compositionally complex alloy as a Zr-Cr interlayer. This alloy has the potential to offer a combination of high temperature stability and strength, the ability to suppress intermetallic compounds, thermomechanical properties, radiation resistance, and vast tunability – all of which make them viable interlayer materials, as well as potential materials in other nuclear and extreme environments [251]. The aim of this thesis is to examine the fundamental properties of these materials and to spotlight their application to nuclear systems, using the interlayered fuel coating concept as a case study.

Much remains unknown about the properties of these materials. For instance, the rules that dictate solid-solution formation are not fully understood. Research into their diffusion behaviour and evolution at high temperatures and under irradiation is still in its early stages. There is a need to understand the contributions to mixing entropy, interactions between dissimilar atomic pairs, electrical and thermal conductivity, thermal expansion, lattice distortion, phase transformations, elastic modulus, vacancy concentrations, diffusion coefficients, dislocation energies and mobility, stacking fault energy, slip, twinning,

strengthening, toughening, fracture, fatigue, creep, wear, corrosion, oxidation, and radiation resistance [252].

Chapter 2. Methodology

Density functional theory is used in **Chapter 4** and **Chapter 5**. Special quasi-random structures are used wherever density functional theory is used. Density functional perturbation theory, the quasi-harmonic approximation, and Birch–Murnaghan isothermal equation of state are used to access temperature-dependent properties of concentrated solid solution alloys in **Chapter 4**. The calculation of phase diagrams (CALPHAD) methodology is implemented in **Chapter 3** and **Chapter 6**. From then, remaining experimental techniques are implemented in **Chapter 6**.

2.1 Density functional theory

Density functional theory uses fundamental quantum mechanical calculations to calculate the energy of a system of atoms, said to be at its lowest energy, or its ground state energy. Development of the underlying theory spanned much of the 20th century but, by now, density functional theory serves as a common tool for computational chemists and materials scientists alike to predict properties for systems without experimental inputs [126], [206], [260], [261], [249], [253]–[259]. This powerful computational technique can drastically reduce time spent in the laboratory, as well as provide valuable insight into the physical origin of effects observed in chemicals and materials.

Some examples of the properties obtained from density functional theory include lattice constant, electronic behaviours, defect formation and migration energies, surface energies, and mechanical properties, and with additional treatment, non-ground state energies can be obtained which gives access to finite temperature properties (such as thermal expansion or high temperature mechanical properties). Density functional theory is not the only electronic structure method available, but it is the most popular. Common commercial and academic packages which implement density functional theory include CASTEP, Dmol3, Gaussian, and VASP, although free software is available such as Quantum ESPRESSO. Basic treatment is given to the underlying theory of density functional theory below.

Quantum mechanics revolves around finding solutions to the Schrödinger equation. Most commonly, this takes the form of the non-relativistic, time-independent Schrödinger equation shown in **Equation 18**.

$$\hat{H}\Psi = E\Psi \quad (18)$$

where \hat{H} is the Hamiltonian operator, Ψ is a set of solutions (or eigenstates) to the Hamiltonian. The time-independent Schrödinger equation can determine many properties of a system, such as kinetic and potential energies, the most stable geometries, and the vibrational electronic energy levels. The Hamiltonian's solutions each possess a corresponding eigenvalue that fulfils the eigenvalue equation. Certain elementary problems in physics, such as the particle-in-a-box or harmonic oscillator, can be precisely solved; however, the issues typically dealt with by materials scientists and chemists, including molecules, surfaces, and materials, cannot be so easily resolved and must, instead, be solved numerically.

The Hamiltonian contains the information regarding the kinetic and potential energies for all particles of a system. It takes the form:

$$\hat{H} = \underbrace{-\frac{1}{2} \sum_{i=1}^N \nabla_i^2}_{\text{KE Elec.}} \underbrace{-\frac{1}{2} \sum_{A=1}^M \frac{1}{M_A} \nabla_A^2}_{\text{KE Nucl.}} \underbrace{- \sum_{i=1}^N \sum_{A=1}^M \frac{Z_A}{r_{ij}}}_{\substack{\text{Nucl.-Elec.} \\ \text{Attract}}} + \underbrace{\sum_{i=1}^N \sum_{j>1}^N \frac{1}{r_{ij}}}_{\substack{\text{Elec.-Elec.} \\ \text{Repuls.}}} + \underbrace{\sum_{A=1}^M \sum_{B>A}^M \frac{Z_A Z_B}{R_{AB}}}_{\substack{\text{Nucl.-Nucl.} \\ \text{Repuls.}}} \quad (19)$$

Where ∇^2 , is termed the Laplacian, and is the sum of differential operators. M_A is the mass of nucleus A , and Z is its charge. r_{ij} is the distance between electron, i , and another particle, j , whether it be another electron or a nucleus. R_{AB} explicitly represents distance between two nuclei. Such an equation is intractable to solve, as one would need to consider the contribution and interaction of every single electron and nucleus, simultaneously. Fortunately, a major simplification to the Hamiltonian can be made with the following observations:

1. The mass of an electron and the mass of a nucleus differ by more than 3 orders of magnitude.
2. Therefore, when given the same amount of kinetic energy, an electron will travel at least 3 orders of magnitude faster than a nucleus.
3. From the perspective of electrons, therefore, nuclei positions will appear static in space. From the perspective of a nuclei, electron positions will update *instantaneously*.

Such observations form the basis of the Born-Oppenheimer approximation, and effectively disconnects the electronic part of the Hamiltonian from its nuclear counterpart, rendering the Hamiltonian easier to solve. This allows us to treat the nuclei as having fixed

positions with respect to the electrons. In this *clamped nuclear approximation*, one solves for the electronic part repeatedly, as the nuclei positions are updated in small steps. In doing so, the electronic density can be mapped out as a function of nuclei coordinates to produce a potential energy surface. The nuclear part of the Hamiltonian can then be solved using the potential energy surface calculated from the electronic part. Since the Born-Oppenheimer approximation allows the electronic and nuclear parts of the Hamiltonian to be decoupled. Within the clamped nuclear approximation, the rendering of the Hamiltonian becomes:

$$\hat{H}_{\text{BO}} = \underbrace{-\frac{1}{2} \sum_{i=1}^N \nabla_i^2}_{\text{KE Elec.}} - \underbrace{0}_{\text{KE Nucl.}} - \underbrace{\sum_{i=1}^N \sum_{A=1}^M \frac{Z_A}{r_{ij}}}_{\text{Nucl.-Elec. Attract}} + \underbrace{\sum_{i=1}^N \sum_{j>1}^N \frac{1}{r_{ij}}}_{\text{Elec.-Elec. Repuls.}} + \underbrace{\text{const.}}_{\text{Nucl.-Nucl. Repuls.}} \quad (20)$$

Where the positions of the nuclei are fixed, while the electron positions can vary. As the nuclei are not allowed to move, they have zero kinetic energy, and so the term describing this energy becomes *zero*. Additionally for a given set of nuclei-nuclei positions, the repulsion between these nuclei does not change, and so the energy describing this repulsion is a constant. If one focusses only on the electronic part of the problem, one can describe the entire electronic structure using the following simplified Hamiltonian, termed, the *electronic Hamiltonian*:

$$\hat{H}_{\text{elec}} = \underbrace{-\frac{1}{2} \sum_{i=1}^N \nabla_i^2}_{\text{KE Elec.}} - \underbrace{\sum_{i=1}^N \sum_{A=1}^M \frac{Z_A}{r_{ij}}}_{\text{Nucl.-Elec. Attract}} + \underbrace{\sum_{i=1}^N \sum_{j>1}^N \frac{1}{r_{ij}}}_{\text{Elec.-Elec. Repuls.}} \quad (21)$$

Which again, can be expressed simply as:

$$\hat{H}_{\text{Elec.}} = -\hat{T} - \hat{V}_{\text{Ne}} + \hat{V}_{\text{ee}} \quad (22)$$

Where \hat{T} is the kinetic energy of the electrons, \hat{V}_{Ne} is the electrostatic attraction between the electrons and nuclei, and \hat{V}_{ee} is the electrostatic repulsion between the electrons. The solution to the Schrödinger equation, therefore, with an electronic Hamiltonian, is the

electronic wavefunction, Ψ_{elec} , with eigenvalues, E_{elec} . The electronic wavefunction depends only on the electron spatial coordinates, and only on the nuclear coordinates parametrically, and so the nuclei coordinates appear explicitly in Ψ_{elec} . The wavefunction solution of the system which gives the lowest energy, E_{elec} , is termed the ground state. The eigenvalue of the ground state wavefunction is called the ground state energy.

However, beyond trivial systems, it is not possible to exactly determine the electronic wavefunction. This is because the electron-electron repulsion term of the electronic Hamiltonian still explicitly requires that one solve for each electron as it experiences repulsion from every other electron in the system. This is known in physics as a *many-body problem*, and it is intractable without further treatment. One must therefore require an approximation as to the true wavefunction that still gives physically sound results. In developing this approximation, it is important to note that the wavefunction itself cannot be directly measured or observed. However, what can in principle be measured is the probability that there are N electrons at some set of coordinates, $\vec{r}_1, \dots, \vec{r}_N$. This probability is given by the square of the electron wavefunction:

$$|\Psi(\vec{r}_1, \dots, \vec{r}_N)|^2 = \Psi^*(\vec{r}_1, \dots, \vec{r}_N)\Psi(\vec{r}_1, \dots, \vec{r}_N) \quad (23)$$

Where the asterisk, (*), denotes a complex conjugate. Although the electron wavefunction, $\Psi(\vec{r}_1, \dots, \vec{r}_N)$, is a function of the coordinates of all N electrons, it is possible and useful to approximate it as a product of all individual wavefunctions:

$$\Psi(\vec{r}_1, \dots, \vec{r}_N) \cong \psi_1(\vec{r})\psi_2(\vec{r}) \dots \psi_N(\vec{r}) \quad (24)$$

This approximation is known as the *Hartree product*. Another point to make is that electrons are indistinguishable; one cannot label them *electron 1*, *electron 2*, *electron 3*, and so forth. This means that what one can measure, is the probability that any order of a set of N electrons are the coordinates $(\vec{r}_1, \dots, \vec{r}_N)$. Something that is closely related is the density of electrons at a particular position in space:

$$n(\vec{r}) = 2 \sum_i \psi_i^*(\vec{r})\psi_i(\vec{r}) \quad (25)$$

The electron density can be calculated by counting the number of electrons that will, on average, be found at position, (\vec{r}) . This is done by summing over all the probabilities that an electron in the individual electron wavefunction, $\psi_i(\vec{r})$, is located at position (\vec{r}) . The number 2 which appears before the summation is a result of the electrons having a property

called *spin*; the Pauli exclusion principle states that each individual electron wavefunction can be occupied by two separate electrons, each with opposite spins. The electron density equation contains much information that is observable from the full wavefunction, but is only a function of 3 spatial coordinates, unlike the full wavefunction which is a function of $3N$ coordinates.

The question is now, how can one use the equation for the electron density to solve the Schrödinger equation? Fortunately, this question forms the basis of density functional theory, which rests on two main theorems proved by Kohn and Hohenberg:

1. The ground-state energy, E , from Schrödinger's equation is a unique functional of the electron density, $n(\vec{r})$.
2. The electron density that minimises the energy of the overall functional is the true electron density, corresponding to the full solution of the Schrödinger equation.

The ground-state energy of a system can therefore be expressed as a functional of the electron density:

$$E[n(\vec{r})] = E \quad (26)$$

Therefore, instead of finding a function of $3N$ variables i.e., the wavefunction, one can find the function of just 3 variables i.e., the electron density. The complete energy functional, $E[\{\psi_i\}]$, is composed of two parts: a known part, and an exchange correlation, or unknown part:

$$E[\{\psi_i\}] = E_{known}[\{\psi_i\}] + E_{XC}[\{\psi_i\}] \quad (27)$$

The known part, $E_{known}[\{\psi_i\}]$, is a collection of the terms that can be written in a simple analytic form. Everything else is a part of $E_{XC}[\{\psi_i\}]$. The known part, $E_{known}[\{\psi_i\}]$, can be represented as a sum of interaction terms:

$$E_{known}[\{\psi_i\}] = \underbrace{\sum_i \int \psi_i^* \nabla^2 \psi_i d^3r}_{\text{KE Elec.}} + \underbrace{\int V(\vec{r}) n(\vec{r}) d^3r}_{\text{Nucl.-Elec. Coulombic interactions}} + \underbrace{\frac{1}{2} \int \int \frac{n(\vec{r}) n(\vec{r}')}{|\vec{r} - \vec{r}'|} d^3r d^3r'}_{\text{Elec.-Elec. Coulombic interactions}} + \underbrace{E_{ion}}_{\text{Nucl.-Nucl. Coulombic interactions}} \quad (28)$$

The $E_{XC}[\{\psi_i\}]$ term, on the other hand, includes all the difficult to deal with quantum mechanical effects not already included in $E_{known}[\{\psi_i\}]$. The correct electron density can be

calculated by solving a set of single equations, termed the Kohn-Sham equations, each involving only a single electron:

$$\left[\frac{1}{2} \nabla^2 + V(\vec{r}) + V_H(\vec{r}) + V_{XC}(\vec{r}) \right] \psi_i(\vec{r}) = \epsilon_i \psi_i(\vec{r}) \quad (29)$$

Where $\frac{1}{2} \nabla^2$ is the kinetic energy of an electron, $V(\vec{r})$ is the potential due to the interaction between an electron and a collection of atomic nuclei, $V_H(\vec{r})$ is the Hartree potential, and $V_{XC}(\vec{r})$ is the exchange and correlation contributions to the single-electron equations. These set of equations are superficially similar to the previous form of the electronic Hamiltonian but neglect the summations that appear inside the full Schrödinger equation. This is because the solutions to the Kohn-sham equations are single electron wavefunctions that depend only on 3 spatial variables.

The Hartree potential describes the coulombic repulsion between the electron being considered and the total electron density defined by all the electrons in the problem. As a result, the Hartree potential includes a self-interaction contribution because the electron described in the Kohn-Sham equation is also part of the total electron density. Part of the Hartree potential, therefore, includes a coulombic interaction between an electron and itself. This is an unphysical result, and the correction for this is one of the several effects which is lumped into the exchange correlation potential.

The Kohn-Sham equations present a conundrum; for their solution, the Hartree potential must be defined, yet defining the Hartree potential necessitates knowledge of the electron density, which in turn depends on the single-electron wavefunctions, the calculation of which necessitates the solving of the Kohn-Sham equations. To circumvent this circularity, the problem can be solved iteratively.

1. Define an initial, trial electron density, $n(\vec{r})$
2. Solve the Kohn-Sham equations defined using the trial electron density to find the single-particle wave functions, $\psi_i(\vec{r})$
3. Calculate the electron density defined by the Kohn-Sham single-particle wavefunctions from step two, $n_{KS}(\vec{r}) = 2 \sum_i \psi_i^*(\vec{r}) \psi_i(\vec{r})$
4. Compare the calculated electron density, $n_{KS}(\vec{r})$, with the trial electron density used to solve the Kohn-Sham equations, $n(\vec{r})$. If these densities are the same, then this is taken as the ground-state electron density. Otherwise, the trial electron density is updated, and the process iterates from step two.

The process above is what density functional theory packages such as VASP perform. However, to solve the Kohn-Sham equations requires specifying the exchange-correlation functional, whose true form is, in general, not known and must be approximated. Fortunately, there is one case in which this functional can be directly derived. This is in a uniform electron gas, where the electron density is constant at all points in space, and gives a practical way of using the Kohn-Sham equations:

$$V_{XC}(\vec{r}) = V_{XC}^{electron\ gas}[n(\vec{r})] \quad (30)$$

This approximation is the local density approximation and is the one of the most common approximations to use the Kohn-Sham equations. Several other approximations have since been developed. The most widely used is the generalised gradient approximation, which uses information about the local electron density, as well as the local gradient in the electron density. As there are many ways the information from the gradient of the electron density can be included in a generalised gradient approximation functional, there are numerous distinct functionals. The most common functionals for the generalised gradient approximation are the Perdew-Wang functionals, or the Perdew-Burke-Ernzerhof functionals. Because different functionals produce different results for any configuration of atoms, it is always necessary to specify which functional is used for each calculation.

2.1.1. Convergence testing

Calculating the entire potential energy surface is a non-trivial task. However, it can be assumed that the energy of the potential energy surface does not vary greatly with slight changes in position. This allows us to sample the Brillouin zone, a defined primitive cell in reciprocal space corresponding to Wigner-Seitz cells in real space, at a finite number of locations throughout the supercell. The more K-points (locations for sampling the supercell) that are used, the more accurate the calculation, though this also decreases the computational efficiency. To ensure an adequate level of accuracy, it is essential to increase the number of K-points until the total supercell energy is converged to a suitable level.

As an example of K-points convergence testing, a relaxed 54-atom supercell of body-centred cubic Mo is shown in **Figure 21**. The completion time for calculations scales exponentially with increasing number of K-points, whereas the total energy quickly converges after a set of $4 \times 4 \times 4$ grid of K-points around the centre of the Brillouin zone, termed the Γ -

point. This short exercise proves that one can sample only a finite number of locations in K-space and still trust the calculations to provide the correct total energy.

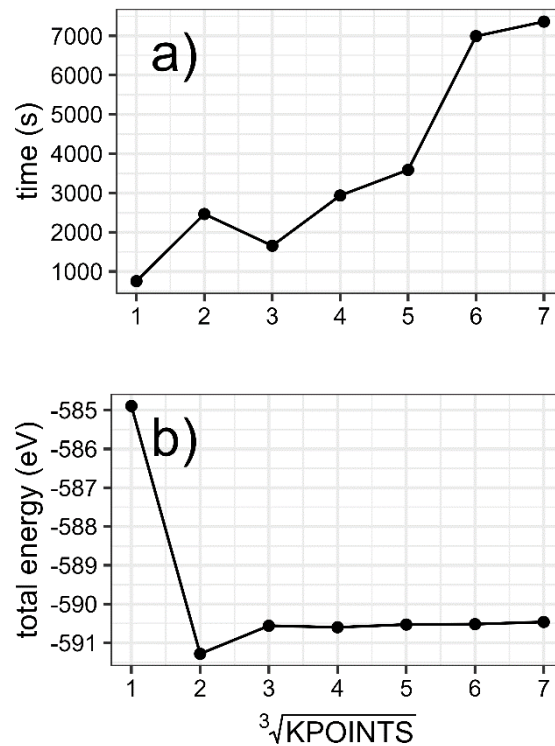


Figure 21. K-points convergence testing for a simple 54-atom body-centred cubic supercell of Mo with symmetry enabled. (a) Calculation time for a sample calculation, and (b) total energy after relaxation.

When modelling disordered concentrated solid solutions such as in this dissertation, one cannot make use of exploiting symmetry to hasten calculation time. For this reason, the calculation for disordered structures tends to take more time than simple symmetrical calculations like the one above. In these studies, either a $4 \times 4 \times 4$ or $6 \times 6 \times 6$ K-point mesh was used to sample the Brillouin zone.

Disordered alloys cannot take advantage of supercell symmetry. This means that density functional theory calculations for alloys such as compositionally complex alloys are very computationally demanding. It is crucial, therefore, to do convergence testing wherever possible to optimise calculation time. One such parameter is the number of computing cores which operates on an individual orbital, shown in **Figure 22**.

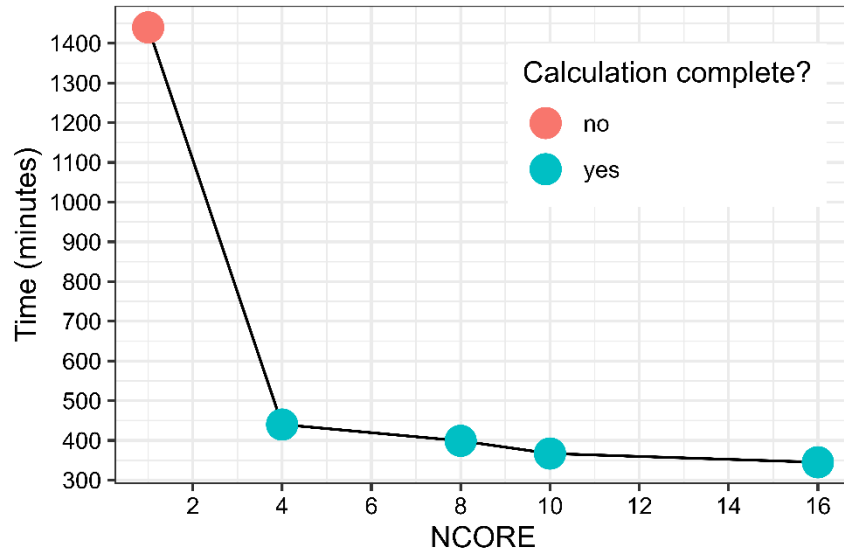


Figure 22. Convergence testing for number of compute cores which work on an individual electron orbital. The supercell is a body-centred cubic 54-atom $\text{Ti}_{11}\text{Hf}_{11}\text{Ta}_{11}\text{Mo}_{10}\text{W}_{11}$ supercell.

2.2 Special quasi-random structures

When attempting to conduct a density functional theory calculation on a solid material, the direct simulation of an entire bulk crystal is not a feasible option due to the extreme computational expense it would incur. As an alternative, a simple repeating cell, known as a supercell, is defined which is replicated in three-dimensional space (**Figure 19**). This supercell can provide accurate bulk properties of the crystal in question, whilst still adhering to the computational constraints imposed by density functional theory.

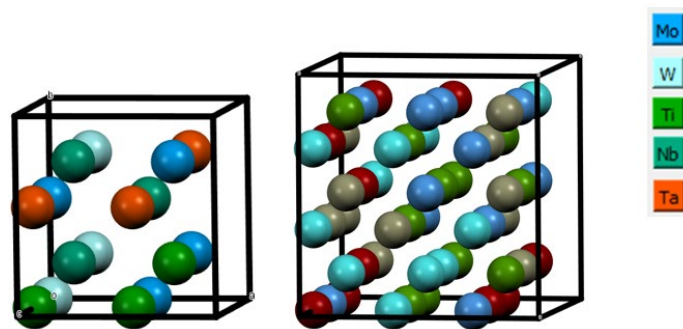


Figure 19. An example a supercell in density functional theory. **Left:** 16-atom body-centred cubic supercell; **right:** 54-atom body-centred cubic supercell.

Periodic boundary conditions have the advantage of reducing the computational effort necessary for performing density functional theory calculations. However, it presents a problem when attempting to simulate disordered systems. By using a repeating block of the supercell, periodicity is introduced to the system, which is not random in nature. To remedy this, the special quasi-random structure approach can be employed. This approach modifies the geometry of the input supercell in such a way as to imitate, within a certain radius from each lattice site, an infinitely random system, as found in concentrated solid solutions and other disordered real systems. By sampling a smaller number of representative 1st and 2nd nearest neighbours around each atom, the time to calculate properties for disordered systems reduces. The original concepts of SQS come from Zunger *et al.* [262] and Wei *et al.* [263]. In these studies, the Automated Alloy Theoretic Toolkit [264] was employed which implements the special quasi-random structure approach via a Monte-Carlo approach. The input cell geometry is input into the code, with appropriate sublattices, and with the probability of finding each element in a sublattice. The code then fills each sublattice as appropriate and fills pseudo-randomly where disorder is required. Once the entire crystal has been defined in this way, correlation functions between each pair (or triplet) of atoms is calculated within an appropriate cut off distance. These correlation functions are fed into an overall objective function to be minimised, which describes how well the disordered part of the crystal represents an infinitely random disordered structure. The simulation is repeated until the objective function is suitably low. It is left to the user to decide when the objective function is low enough, and it usually depends on which property is to be subsequently calculated for the crystal. The special quasi-random structure method was used in **Chapter 4** and **Chapter 5** of this thesis, to construct body-centred cubic supercells of disordered alloys in the Hf-Mo-Nb-Ta-Ti-W-Zr system.

2.3 Quasi-harmonic approximation

Finite temperature properties of materials are typically off-limits to density functional theory. One method for including temperature effects in density functional theory calculations is via the quasi-harmonic approximation, an extension of the harmonic approximation which treats all interatomic forces as purely harmonic. Purely harmonic forces between atoms are unable to capture properties such as thermal expansion which depend entirely on the anharmonicity of the potential well. In the quasi-harmonic approximation, phonon frequencies become volume-dependent such that for each volume, the harmonic approximation holds. The Phonopy code, with its interfaces to software such as VASP [265], CASTEP [266], and

LAMMPS [267], makes quasi-harmonic calculations available. This approach also enables the calculation of the zero-point energy of a system, as well as the bulk modulus and heat capacity as functions of temperature.

2.4 Density functional perturbation theory

The response of a quantum system under small perturbation can be studied through Density Functional Perturbation Theory (DFPT). The calculation of vibrational properties such as phonons, which can be further used to calculate infrared and Raman absorbance, elastic neutron scattering, specific heat, heat conduction, and thermal expansion, is an important application of DFPT.

In a pseudopotential scheme each nucleus interacts with the valence electrons through a smooth pseudopotential, with nuclei and core electrons acting as a frozen ion. The equilibrium geometry is when the structure is relaxed such that forces acting on all nuclei vanish. The forces can be calculated by applying the Hellman-Feynman theorem to the Born-Oppenheimer Hamiltonian (**Equation 31**).

$$F = -\frac{\delta E(\{R\})}{\delta R} \quad (31)$$

where F is the force, $E(\{R\})$ is the nuclear electrostatic energy of nuclear configuration R . For a system near to its equilibrium geometry, the harmonic approximation applies, which reduces the Hamiltonian to a system of independent harmonic oscillators. The frequencies of these vibrations, ω , and the displacement patterns, U_I^a for the a^{th} cartesian component of the I^{th} atom, are determined by the secular equation:

$$\sum_{J,\beta} (C_{IJ}^{\alpha\beta} - M_I \omega^2 \delta_{IJ} \delta_{\alpha\beta}) U_J^\beta = 0 \quad (32)$$

where $C_{IJ}^{\alpha\beta}$ is the matrix of interatomic force constants:

$$C_{ij}^{\alpha\beta} = -\frac{\delta F_I^a}{\delta R_j^\beta} \quad (33)$$

In **Chapter 4**, interatomic force constants are readily calculated in the Vienna *Ab initio* Software Package; phonons are calculated for a range of alloys in the Mo-Nb-Ta-Ti-W system

and used (with the quasi-harmonic approximation) to calculate thermal expansion coefficients in these systems.

2.5 Equation of states

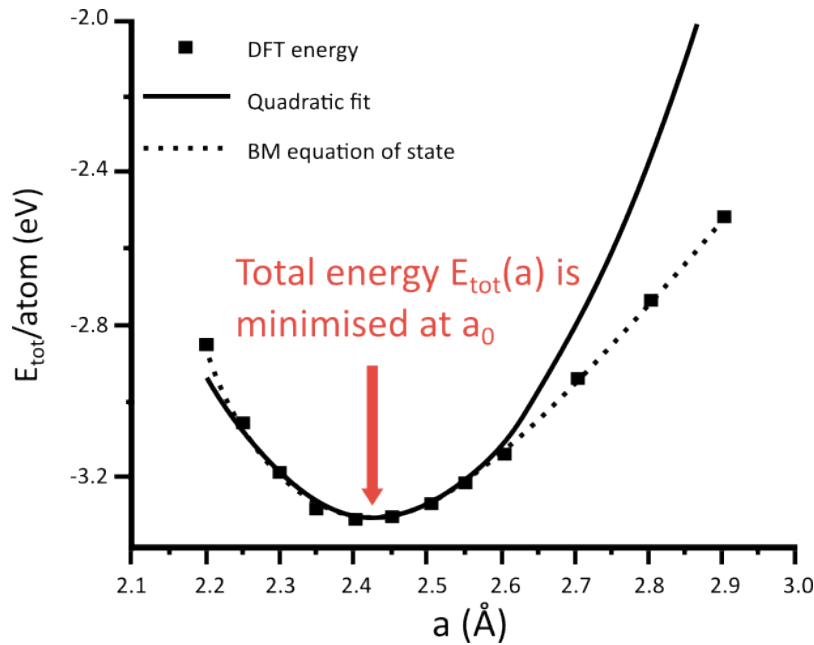


Figure 20. A graph of density functional theory energies versus the Birch-Murnaghan equation of state and a quadratic fit of the central density functional theory data. Reproduced from Scholl *et al.* [268].

The Birch-Murnaghan equation of state is suitable for use with isotropic solids. In cases of concentrated solid solutions, however, it is assumed that the material is isotropic, which can restrict the applicability of the technique. Nevertheless, when the isotropic assumption is valid, the equation of state (**Figure 20**) can be employed to calculate the internal energy with respect to temperature and pressure and is usually combined with the quasi-harmonic approximation to estimate finite-temperature properties of solids.

2.6 Calculation of phase diagrams

At constant pressure, a system's thermodynamic equilibrium is established when the Gibbs energy, G , has achieved its minimum. For multi-phase equilibria, this criterion is fulfilled when the sum of the molar Gibbs energies of the stable phases is minimised (**Equation 34**).

$$G = \sum_{\phi} n^{\phi} G_m^{\phi} = \text{minimum} \quad (34)$$

where n^{ϕ} is the number of moles, and G_m^{ϕ} is the molar Gibbs energy of phase ϕ . The Gibbs energy of a phase can be written as the composition of different contributions:

$$G_m^{\phi} = {}^{ref}G_m^{\phi} + {}^{cfg}G_m^{\phi} + {}^{phy}G_m^{\phi} + {}^{exs}G_m^{\phi} \quad (35)$$

where ${}^{ref}G_m^{\phi}$ represents the weighted molar Gibbs energy of the phase constituents, ${}^{cfg}G_m^{\phi}$ is the configurational term, ${}^{phy}G_m^{\phi}$ describes contributions from other physical phenomena like magnetism, and ${}^{exs}G_m^{\phi}$ describes deviations of the Gibbs energy relative to the other three terms. ${}^{ref}G_m^{\phi}$, ${}^{phy}G_m^{\phi}$, and ${}^{exs}G_m^{\phi}$ are functions of temperature, T, and pressure, P. The configurational term, ${}^{cfg}G_m^{\phi}$, is given by **Equation 36**.

$${}^{cfg}G_m^{\phi} = RT \sum_i y_{is}^{\phi} \ln(y_{is}^{\phi}) \quad (36)$$

Where R is the ideal gas constant expressed in $\text{JK}^{-1}\text{mol}^{-1}$. Temperature dependence of ${}^{ref}G_m^{\phi}$ and ${}^{exs}G_m^{\phi}$ is expressed as a summation of temperature terms (**Equation 37**).

$${}^{ref,exs}G_m^{\phi}(T) = a + bT + cT \ln(T) + \sum_n d_n T^n \quad (37)$$

where a, b, c, and d_n are coefficients and n are intergers. For ${}^{ref}G_m^{\phi}$, the values of n are typically 2, 3, and -1 . Several expressions are usually required for a given phase to cover the entire temperature range of interest. From this expression for the Gibbs energy, other thermodynamic properties can be calculated, such as entropy, enthalpy, and heat capacity.

This formalism for describing Gibbs energy as a function of temperature is used in practically all available thermodynamic databases for compositionally complex alloys. In **Chapter 3** and **Chapter 6**, we use the Gibbs energy minimisation software ThermoCalc [269] with the TCHEA4 database to reveal phase equilibria in the MoNbTaW, MoNbTaTiW, and MoNbTaW-Cr systems.

2.7 Arc melting

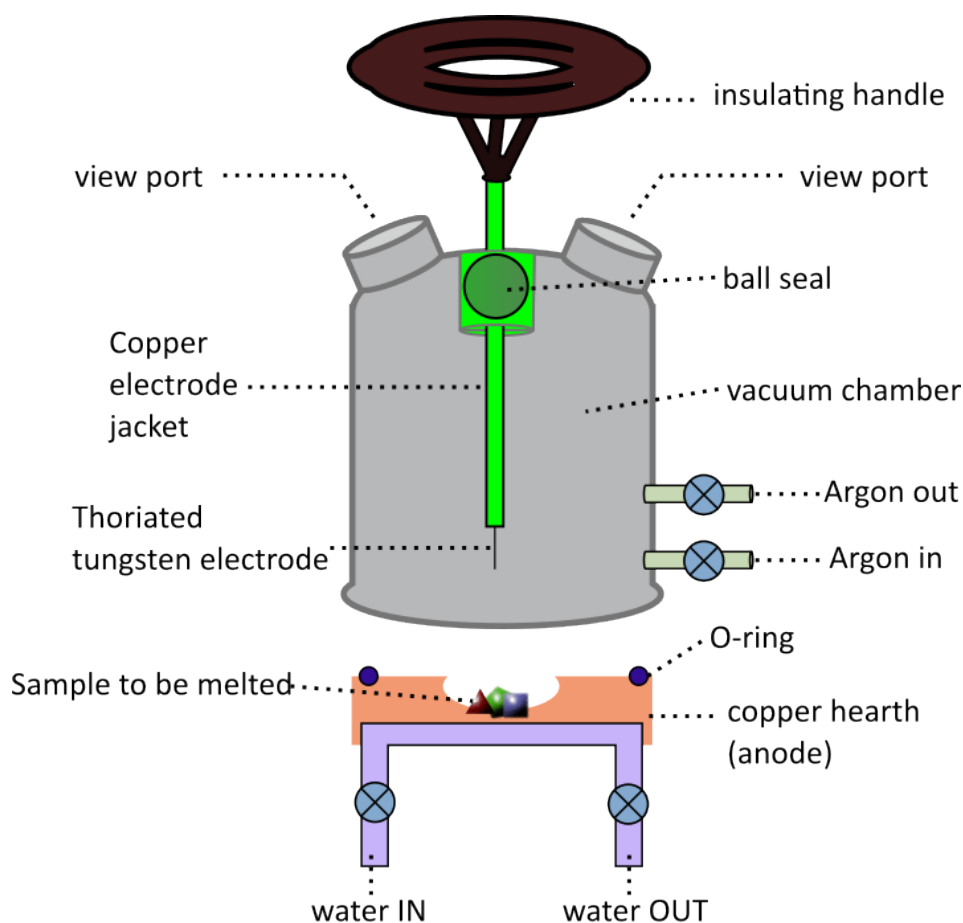


Figure 23. Arc furnace schematic (not to scale).

Arc melting is a common way of producing refractory compositionally complex alloys [124], [191]–[195]. A schematic of the arc furnace set up is in **Figure 23**. An arc furnace uses a tungsten electrode to direct an electric arc to the sample, allowing it to reach temperatures greater than 3000 K (**Figure 24**). The copper hearth underneath can retain its shape through an active cooling system situated below. It allows the outer layer of the melt to immediately solidify, thereby preventing reaction with the crucible.

Determining the melting parameters of an arc melting procedure is a difficult task. It is impossible to know the highest temperature achieved during an experiment or the rate at which the sample cooled. However, the amperage, flow of water, height of the electrode from the sample, and the length at which the electrode protrudes out of the copper-cooled electrode jacket can all be controlled. Furthermore, the choice between supplying a direct-current or an alternating-current is also available. Due to all the ambiguities surrounding the arc melting process, it is hard to attain an objective or scientific control. To have samples suitable for study

of thermodynamically stable phases, a standardised post-melt heat treatment is usually required.

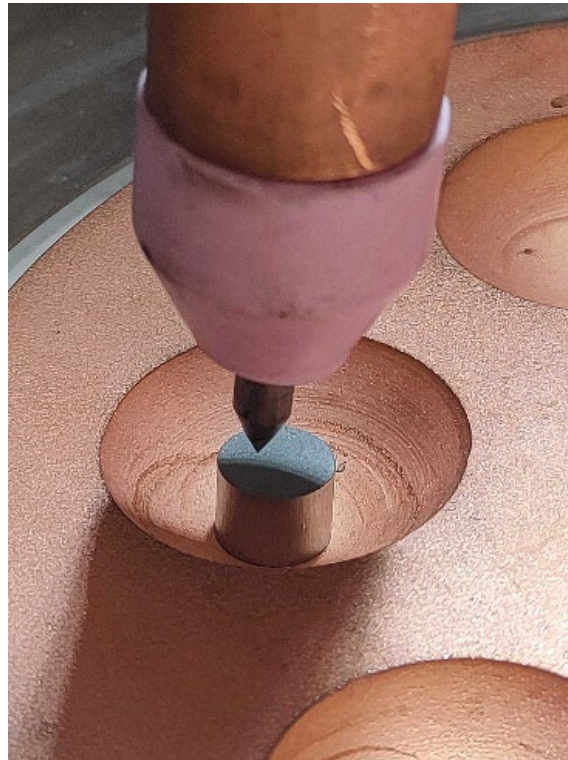


Figure 24. The arc furnace electrode (pictured centre).

When arc melting, achieving homogeneity can be a challenge. Due to the tendency of lighter elements to float to the surface and heavier elements to sink to the crucible base, samples were flipped between each melt and melted between five and ten times to create a homogeneous alloy. Vacuum chamber atmosphere was 5% H₂ in Ar. Melting was done under 0.1 MPa positive pressure, and with currents between 5 – 50 amps.

2.8 High-energy planetary ball milling

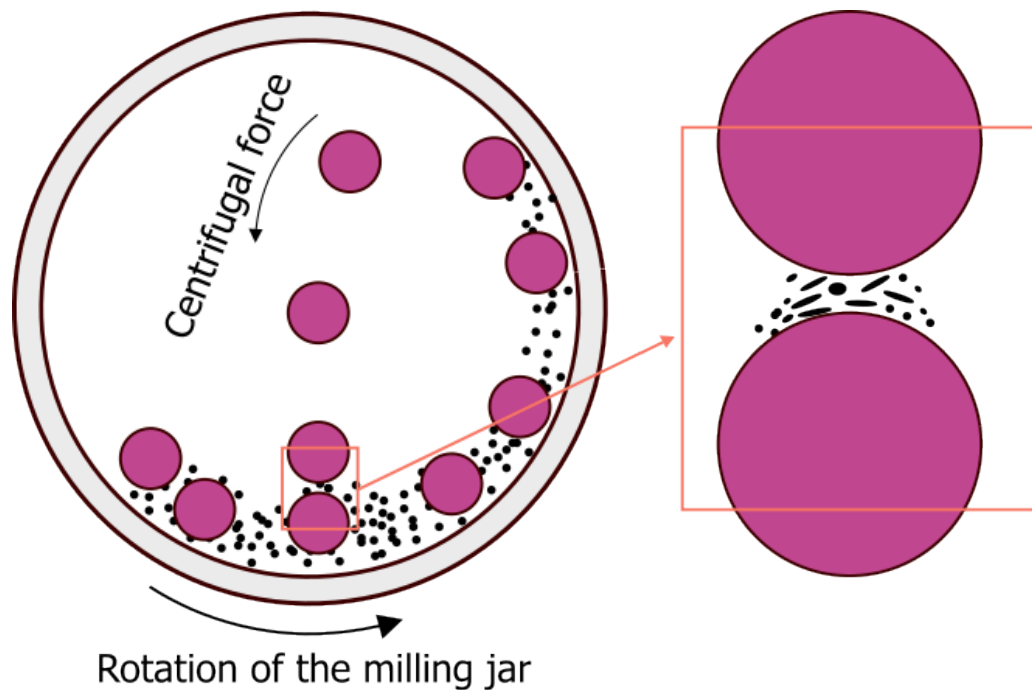


Figure 25. Schematic of the ball-milling process.

The production of powdered nanocrystalline metals or alloys can be achieved through high-energy ball milling (**Figure 25**), which causes coarse-grained structures to dissociate due to the severe cyclic deformation. In this thesis, a tungsten carbide milling jar with tungsten carbide milling balls were used; however, contamination from the milling media (balls and vial) and atmosphere posed a problem (**Chapter 6**). To reduce this contamination, process control agents such as ethanol and hexane, and protective atmospheres such as Ar were employed.

2.9 Magnetron sputtering

Magnetron sputtering is a thin film, physical vapour deposition technique. The process involves ejecting material from a target onto the surface of a substrate material to create film coatings and is typically used in various materials science applications to modify surface properties or to add decoration to products (**Figure 26**).

Sputtering occurs when incident ions of a plasma bombard the surface of a target with sufficient kinetic energy such that the binding energy of the target is overcome. Atoms from the surface of the target material are then subsequently ejected. Magnetron sputtering uses a magnetic and electric field to confine particles near to the surface of the target material, therefore improving ion density and rate of deposition. The physics and technology of magnetron sputtering has recently been reviewed [270].

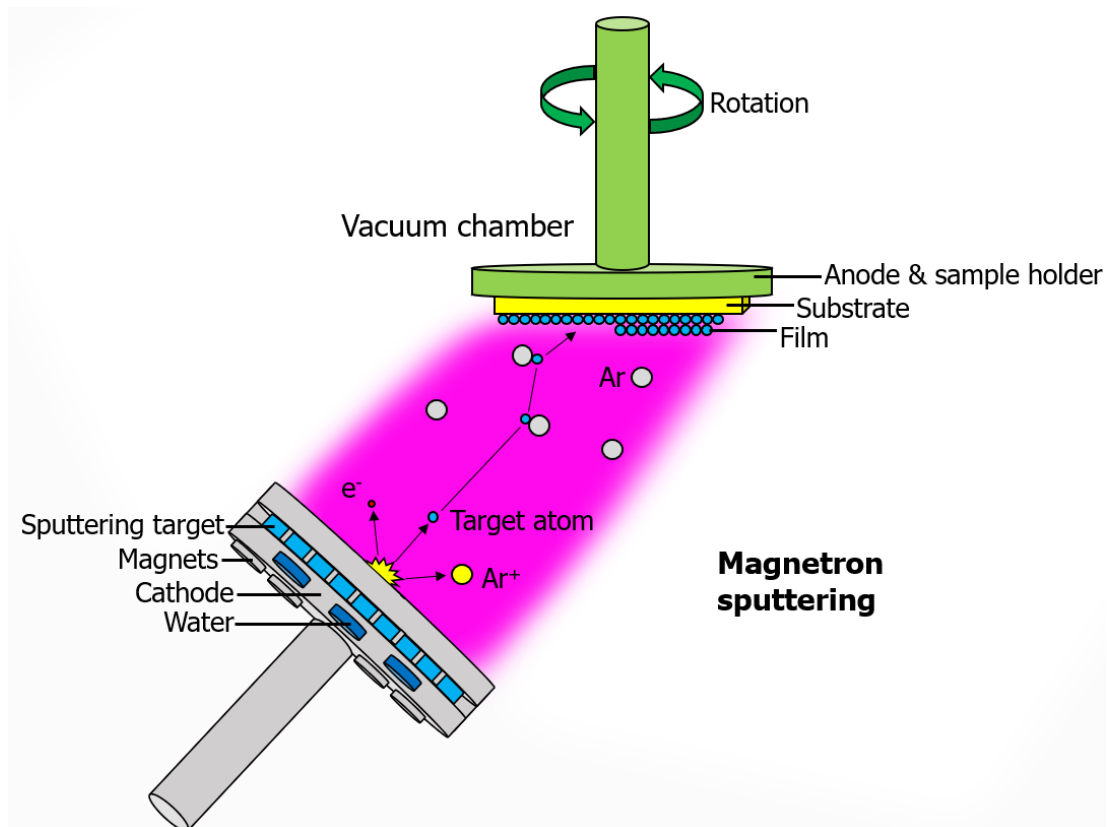


Figure 26. Schematic of the magnetron sputtering apparatus.

Two sputtering targets were used in this thesis: 1) a Cr target, and 2) a MoNbTaW, of nominally equiatomic composition. Both targets were bought from Testbourne Ltd. It is thought that the sputtered composition will closely match that of the source target, although elements will sputter at slightly different rates, even from the same alloyed target (**Chapter 6**). The magnetron sputterer on which this research is based did not have the ability to change the

bias voltage, or magnet field strength, nor were these values known. Ar-polishing was also not available. No post-sputter heat treatments of the coatings were done.

2.10 Surface preparation

Metallographic preparation was performed as follows to achieve a mirror finish. Samples were ground to a 1200 grit via 600 and 1000 grits on SiC papers. Then they were polished using 6 μm , 3 μm , and 1 μm diamond suspension until the required finished was achieved. These metallographic preparations were conducted in **Chapter 6** to all arc-melted alloy samples.

2.11 X-ray diffraction

X-ray diffractometry is a one of the most common methods for characterising crystal structures of solid metals and is used in **Chapter 6** of this thesis for the crystal structure determination of MoNbTaTiW. Incident X-rays have similar wavelengths to the atomic distances within a crystal and are scattered by these atoms (**Figure 27**). Diffracted beams of X-rays interact with each other, either interfering with each other constructively or destructively, giving rise to different intensities in the X-ray diffraction spectrum. This spectrum is then used to identify phases in the sample material. X-ray diffraction also reveals information on how the sample crystal structure deviates from an ideal structure due to stresses and defects that are present.

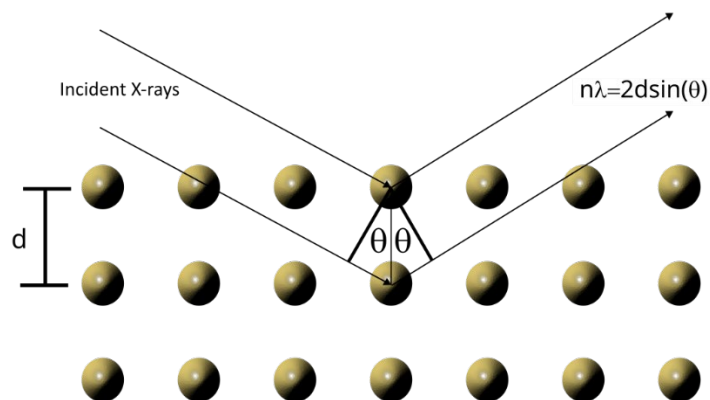


Figure 27. schematic of the x-ray diffraction process.

The distance between lattice planes, d , is given by the Bragg equation $n\lambda = 2d \times \sin(\theta)$, where n is the order of reflection, usually 1, λ is the wavelength of incident X-

rays and refers to the Cu K- α wavelength of 1.5406 Å in this thesis. The angle θ represents the reflection angle of X-rays. Spectra of X-ray diffractions are usually presented as intensity of scattered rays as a function of the scattering angle θ , or more commonly, 2θ . The Bragg equation can then be used to calculate the corresponding d-spacing (**Figure 28**).

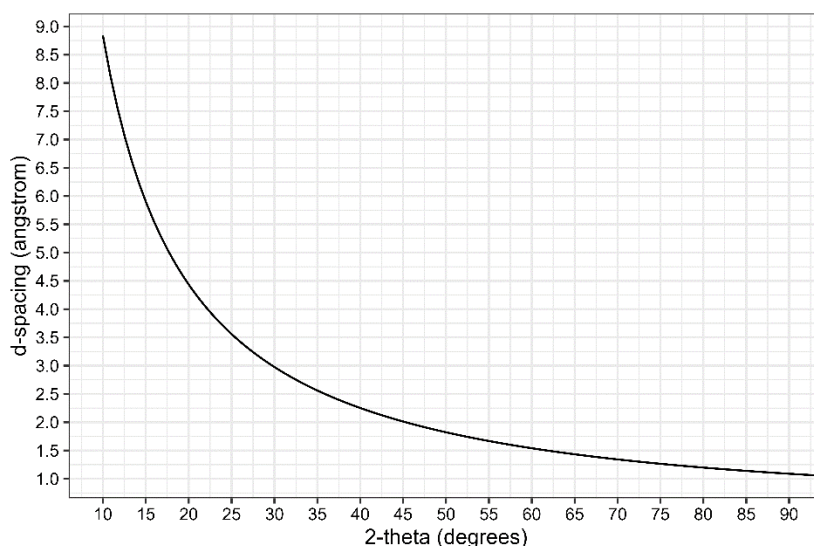


Figure 28. 2θ values and corresponding d-spacing values for a Cu K- α incident wavelength, λ , of 1.5406 Å.

2θ peaks will only appear on the x-ray diffraction spectrum where their reflected waves have interfered with each other constructively. It is therefore possible that due to the symmetry of a crystal, some planes can be systematically absent from the x-ray diffraction spectrum. This means that there are a defined set of observable planes for each crystal structure. For example, the allowable planes for the body-centred cubic crystal structure are (110), (200), (211), (202), (310) and further higher-order planes. The allowable planes for face-centred cubic crystals are (111), (200), (220), (311), (222), and further higher-order planes; planes for hexagonal close packed structures are (100), (002), (101), (102), (110), (103), (200), (112), (201), (004), (202), with further higher-order planes.

2.12 Scanning electron microscopy

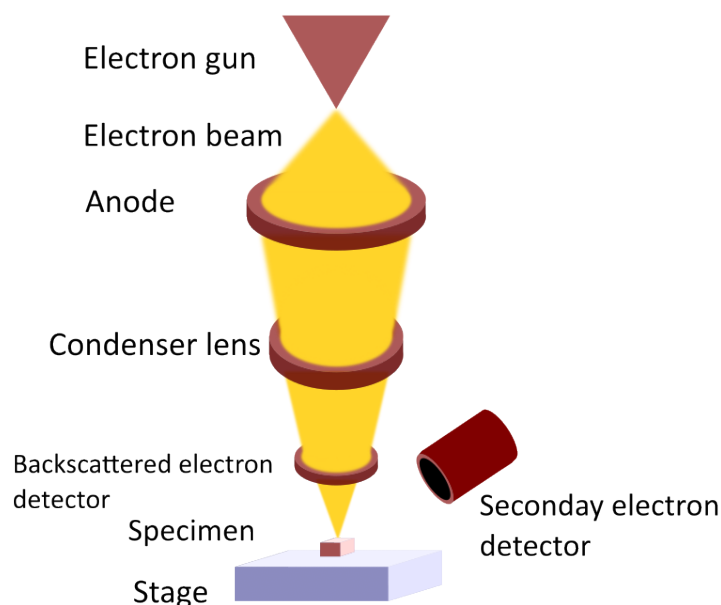


Figure 29. Schematic of the scanning electron microscope operation.

Scanning electron microscopy allows the microstructure and morphology to be imaged. The setup is as follows: an electron gun acts as an electron source and emits electrons through a series of magnetic condenser lenses to the sample, which sits under vacuum throughout the process (**Figure 29**). Electrons have a shorter wavelength than light, meaning that electron microscopy is capable of higher resolution than optical microscopy. The sample material scatters electrons, which are then picked up by various detectors in the vicinity of the vacuum chamber. Typically, larger elements are stronger scatterers of electrons than lighter elements, and typically produce brighter contrasted images on the computer screen.

2.13 Energy dispersive spectroscopy

X-rays are also created during the electron microscopy process, and these can hold useful information to be exploited via *energy dispersive spectroscopy*, which is a useful attachment to the scanning electron microscope. The process is caused by electrons being excited by a packet of X-rays, then dropping from higher energy orbitals to lower ones, and this emits a packet of X-rays which has characteristic energy (and wavelength) to a particular element and electron orbital. The process is rather similar to X-ray fluorescence technique, which is described later within this chapter, but unlike in X-fluorescence spectroscopy, it is an incident beam of electrons, and not X-rays, which dislodges a core valence electron of the specimen atom.

2.14 Simultaneous thermal analysis

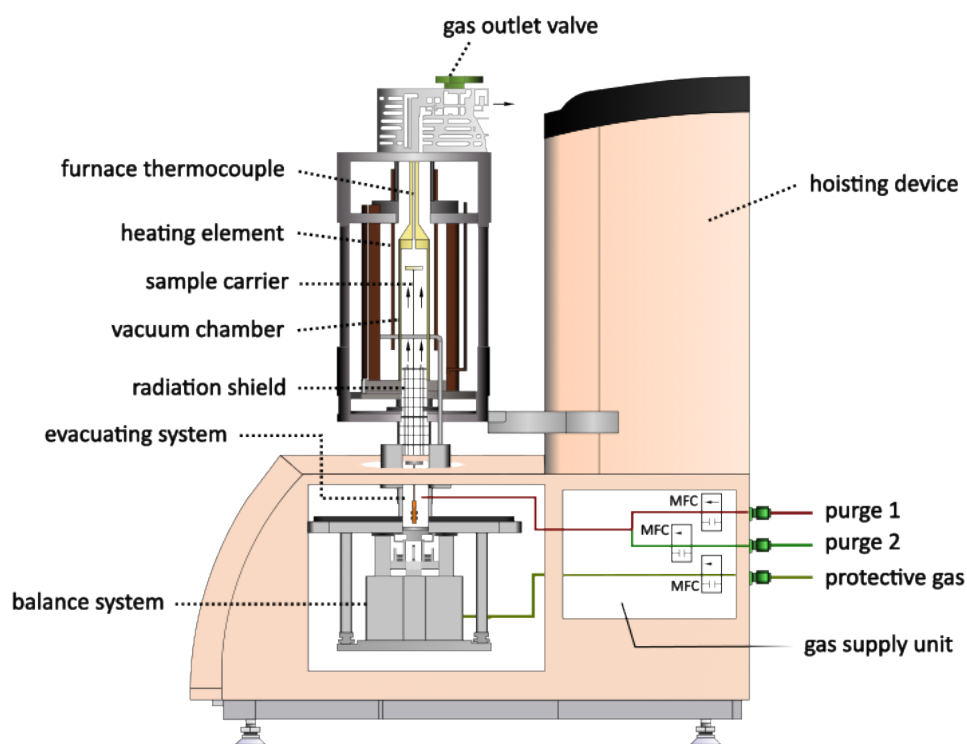


Figure 30. Setup of a simultaneous thermal analyser.

Simultaneous thermal analysis refers to the application of differential scanning calorimetry and thermogravimetric analysis at the same time to the same sample (**Figure 30**). Parameters such as temperature, environment gases and flow rates can be controlled and sensitive changes in sample enthalpy and mass can be measured. In some systems, properties from offput gases can then be captured via mass spectrometry or infrared spectroscopy. Data from simultaneous thermal analysis can be useful in the study of metals and alloys, in that, information like phase transitions, allotropic transformations, and chemical reactions, can all be detected by tracking the release or absorption of energy during heating or cooling. Likewise, oxidation studies can be performed by heating samples in air or in humid conditions and tracking the oxidative weight gain or loss.

2.15 X-ray fluorescence spectroscopy

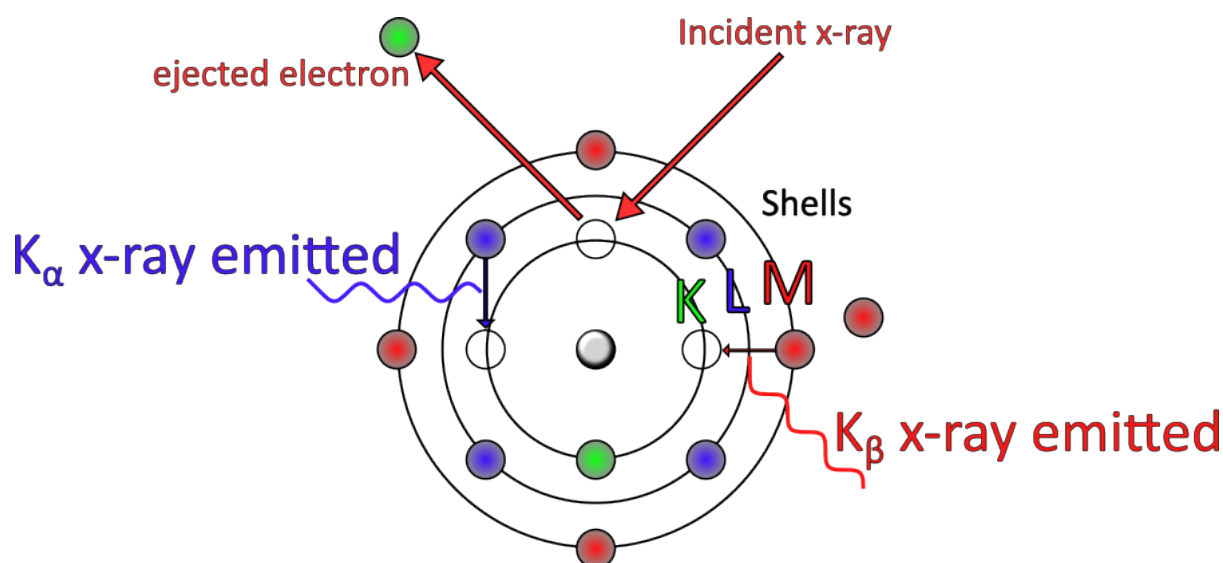


Figure 31. The X-ray fluorescence process.

X-ray fluorescence spectroscopy determines the elemental composition of materials without destroying them in the process. An X-ray fluorescence spectrometer emits primary X-rays into a sample and measures the wavelength of returning secondary X-rays, caused by interactions of incident radiation with the electronic structure of constituent elements in the sample (**Figure 31**). Each element within a sample produces a unique set of fluorescent X-rays, which can be used to determine elemental compositions. An X-ray fluorescence scan can be completed in a few minutes at most and does not require any extensive sample preparation.

A characterisation technique such as X-ray fluorescence is invaluable to the study of metals and alloys. The general methods for fabrication refractory alloys, for example, by arc melting or by magnetron sputtering, cannot easily guarantee a specific composition. Arc melting, for example, may allow lighter elements to volatilise during melting, whereas magnetron sputtering has the problem of each element having a different sputtering rate. Both techniques, therefore, may result in final compositions which differ significantly from the nominal composition. For this reason, it is necessary to be able to characterise fully any alloys made from these techniques.

2.16 Atomic force microscopy

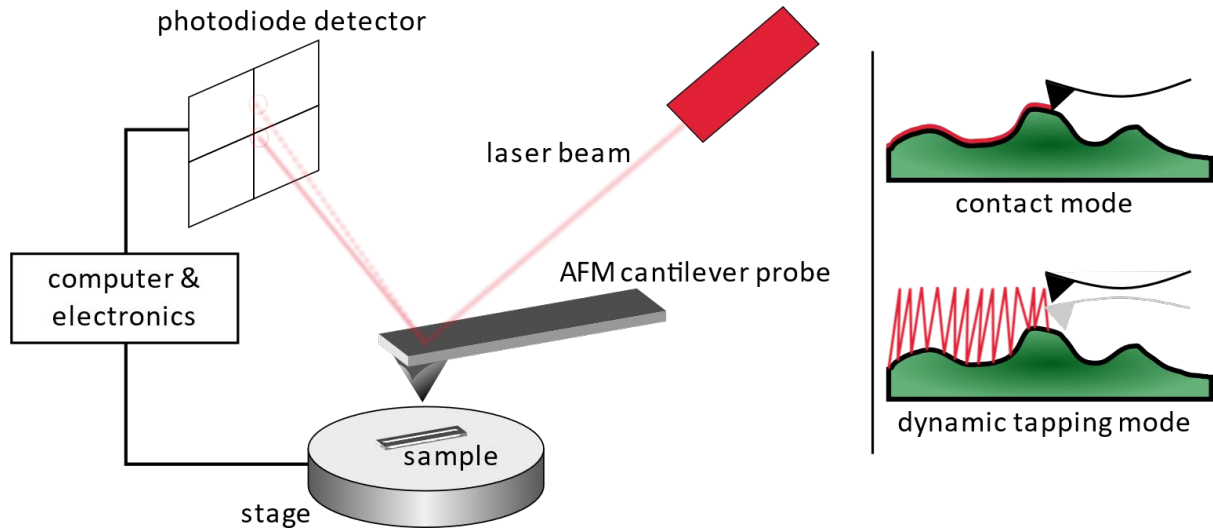


Figure 32. Setup of an atomic force microscopy experiment.

Atomic force microscopy is a scanning probe microscopy technique with resolutions of a fraction of a nanometre. The cantilever probe either prods the sample or scrapes across the surface depending on which mode is activated and reflects an overhead laser beam towards a photodiode detector at an angle dependent surface sample height (**Figure 32**). This data is fed into a computer to generate a mapping of the sample surface complete with sample heights and can provide a full topology of the sample surface. From this, measurements such as sample roughness and sample surface area can be obtained. Atomic force microscopy can also be used to measure forces between probe and sample to determine mechanical properties such as elastic modulus. In this thesis, atomic force microscopy was used to probe the surface of magnetron sputtered MoNbTaW coatings.

Chapter 3. Materials design – selecting an interlayer

Work from this chapter was published in the TopFuel 2021 conference proceedings

J. Wilson, L. Evitts, M. Rushton, D. Goddard, S. Middleburgh, W. Lee, High entropy alloys for accident tolerant fuel applications, in: *TopFuel*, 2021.

3.1 Element screening

3.1.1 Thermal neutron absorption cross-section

A criterion for an interlayer is that it does not degrade the neutronic properties of the fuel cladding. The thermal neutron absorption cross-section is used to determine the probability that the nucleus of an atom will absorb neutrons. The larger the neutron cross section, the more likely a neutron will be absorbed by the nucleus. The unit of neutron cross-section is the *barn*, which is equal to 10^{-28}m^2 . The neutron absorption cross-sections of isotopes can differ by many orders of magnitude. The thermal neutron absorption cross-sections for the elements produces the data in **Figure 33**.

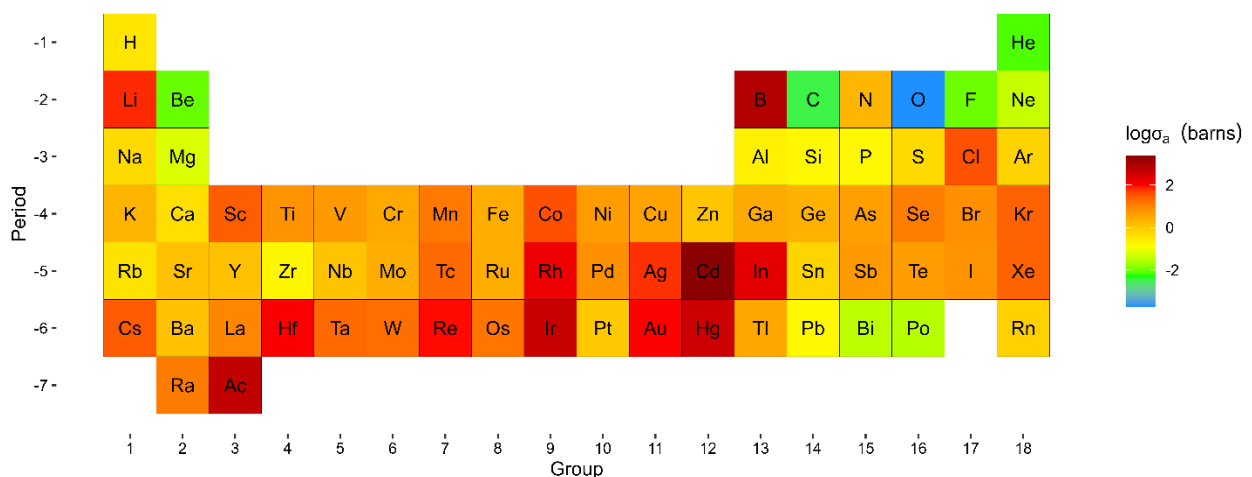
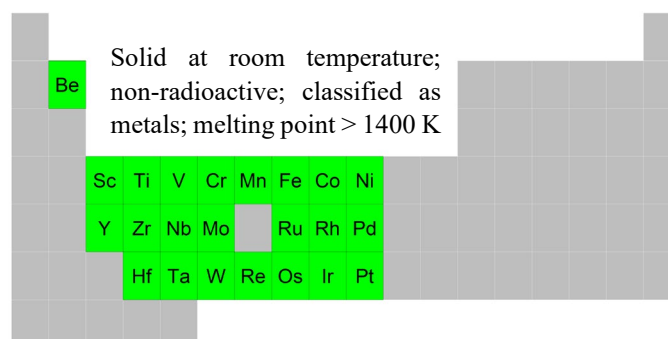


Figure 33. Thermal neutron absorption cross-sections for the elements, weighted by isotopic abundance.

According to **Figure 33**, all refractory elements have a thermal absorption cross-section larger than Zr. Nb has a lower cross-section than Cr, which may confer some neutronic benefits in a coating system. Mo, Ti, and V have comparable absorption cross-sections to Cr, Ta and W have much higher cross-sections than Cr and will therefore incur large neutron penalties.

The interlayer coating is expected to be thin (100 nm – 1 μm) and is not expected to significantly affect the neutronic properties of the fuel cladding. One should, however, take effort to not use elements with large neutronic absorption effects, such as Hf.

3.1.2 Physical properties



Considering the Hume-Rothery rule that two elements should not differ in their atomic radii by more than 15% in order to form a solid solution, chromium (Cr) and zirconium (Zr) differ in their Goldschmidt radii by 15.8%. This significantly surpasses the boundary of the empirical rule, and it is known that Cr and Zr are not miscible. To increase the chances of mutual miscibility, further elements were selected whose atomic radii are between that of Zr

and Cr, such that these elements are more likely to form an intermetallic-free compositionally complex alloy joint between the substrate and coating materials. This shortens the list of elements to 14 (**Figure 35**).

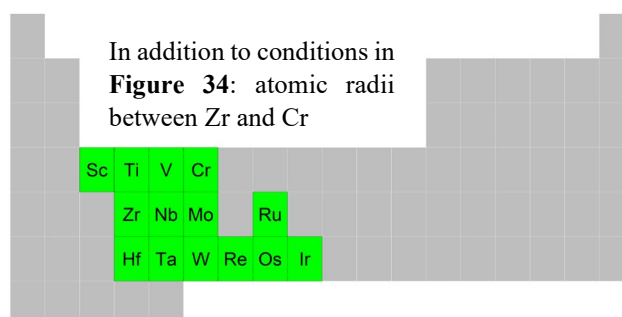


Figure 35. Elements of the periodic table which satisfy the conditions in **Figure 34**, and whose atomic radii are between that of Cr and Zr.

From the earlier defined selection criteria, it was noted that the interlayer should not negatively impact on the thermal conductivity of the coating system, although due to the thin nature of the interlayer and its metallic nature this is not expected to have a significant negative impact. Zirconium alloys have a room-temperature thermal conductivity of $\sim 18 \text{ W m}^{-1} \text{ K}^{-1}$, whereas chromium is $93.9 \text{ W m}^{-1} \text{ K}^{-1}$. The author settles for elements whose thermal conductivity is at least as high as zirconium's. This process eliminates scandium and titanium, although titanium's thermal conductivity is close to zirconium's. Further reductions can be made based on cost, excluding the elements iridium, osmium, rhenium, ruthenium from the selection. Cobalt is known to cause activation issues within nuclear environments so that too is excluded. Hafnium has a very large neutron absorption cross-section (104 barns at thermal neutron energies), so this element is also excluded. Now 7 elements remain (**Figure 36**):

Figure 35: relatively cheap:
low thermal neutron cross-
section; no known activation
issues

Ti	V	Cr
Zr	Nb	Mo
	Ta	W

Given the selection of elements that possess physical properties close to those of chromium (Cr) and zirconium (Zr), it is no surprise that the remaining elements are situated on the periodic table near to both Cr and Zr. Excluding Zr and Cr, there are now five elements to consider: molybdenum (Mo), niobium (Nb), tantalum (Ta), vanadium (V), and tungsten (W). Titanium (Ti) may be reconsidered due to its thermal conductivity being only slightly lower than that of Zr, and due to its conferring of ductility in refractory alloys. The selection criteria for an interlayer, as discussed in **Chapter 1**, determine that both an intermediate thermal expansion and adequate ductility are required for an ideal Cr/Zr interlayer. **Figure 37** plots an estimation of ductility (bulk modulus divided by shear modulus) against thermal expansion coefficients measured at 25°C for a range of elements near Zr and Cr. From this figure, it is hypothesised that combinations of elements can be chosen to obtain the desired thermal expansion coefficient in a concentrated solid solution. For instance, the larger thermal expansions of Ti and V can be used to offset the lower thermal expansion of Mo and W. The applicability of using a compositionally weighted average for thermal expansion (the so-called rule of mixtures) has been supported by work in this thesis and is discussed further in **Chapter 4**. A webapp tool was devised to quickly assess thermal expansion of other concentrated solid solution alloys [271].

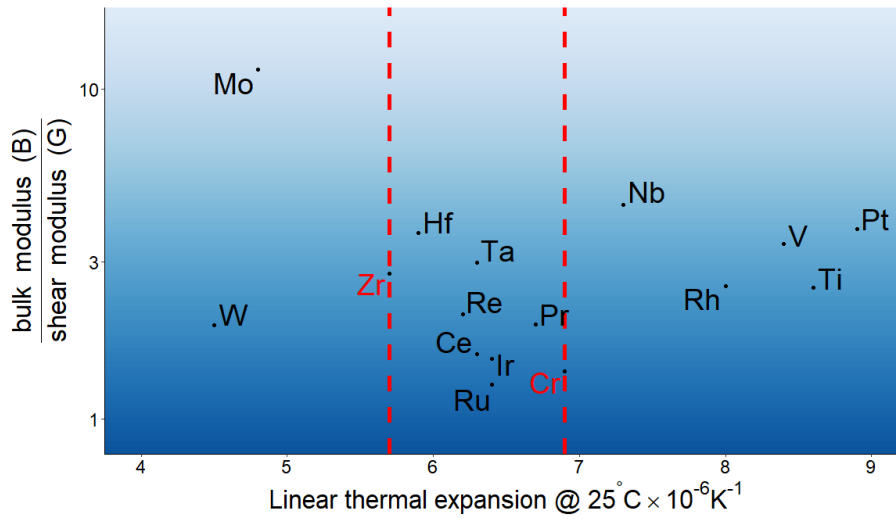


Figure 37. An estimation of ductility vs linear thermal expansion coefficients at 25°C for the elements. The dashed lines refer to the thermal expansion coefficients of Zr and Cr [272].

3.1.3 Oxidation

The formation of a dense and adherent oxide scale is a major criterion of design when considering interlayer oxidation resistance. A reliable method to determine if an oxide can meet this criterion is the Pilling-Bedworth ratio, which is the ratio of the volume of a metal oxide to the volume of the corresponding pure metal.

$$R_{PB} = \frac{V_{oxide}}{n \times V_{metal}} = \frac{M_{oxide}\rho_{metal}}{n \times M_{metal}\rho_{oxide}} \quad (38)$$

where R_{PB} is the Pilling-Bedworth ratio, M is the atomic mass, n is the stoichiometry of metal atoms to oxygen atoms in the oxide, ρ is the density, and V is the molar volume. If the Pilling-Bedworth ratio is too large, then compressive strains result in cracking across the oxide film. Conversely, if the Pilling-Bedworth ratio is too small, then the area formed by the oxide is inadequate to cover the underlying metal and therefore unable to prevent further oxidation.

Figure 38 shows the Pilling-Bedworth ratio of select elements.

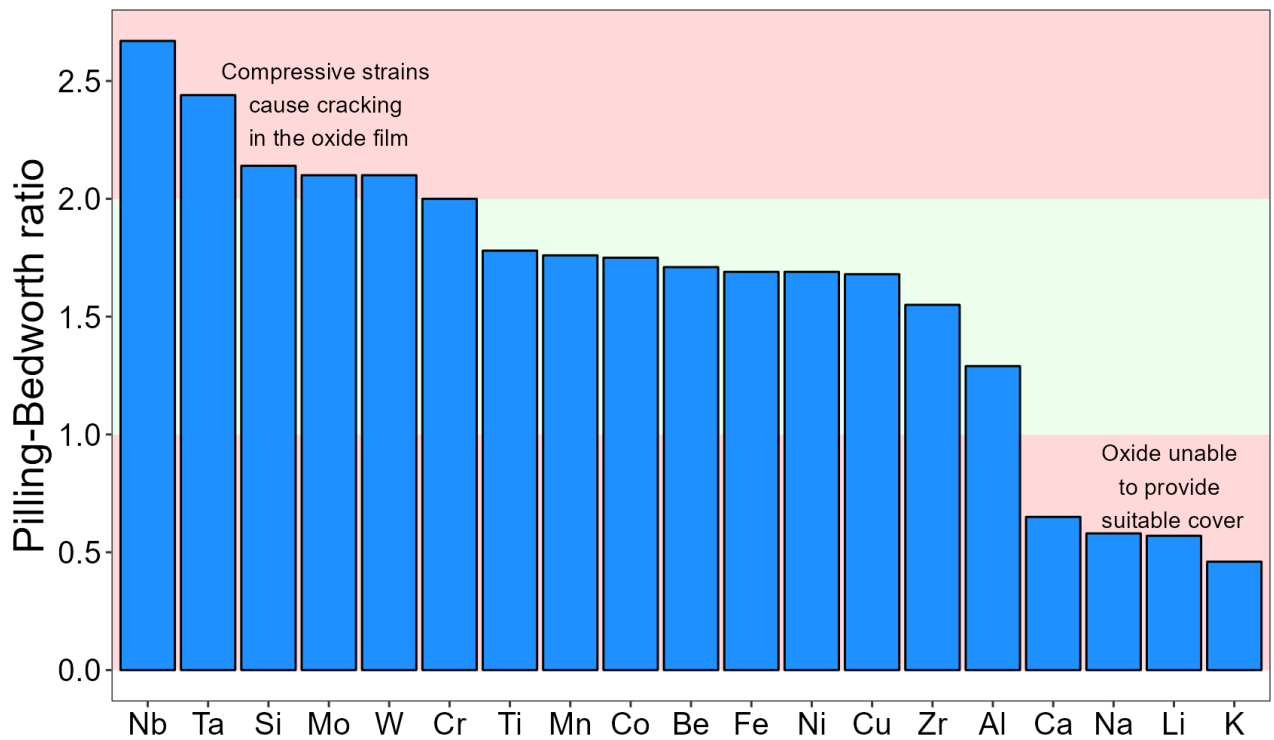


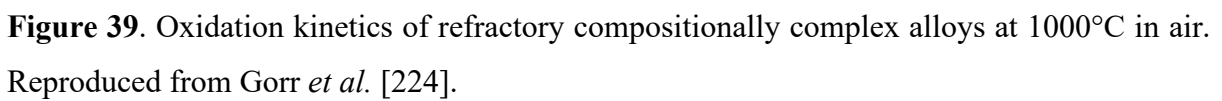
Figure 38. Pilling-Bedworth ratio of select elements. W [273]; Al, Ca, Ta [274]; Cr, Co, Cu, Fe, Ni, Li, Mn, K, Si, Na, Zr [275].

Refractory elements such as Nb and Ta are unable to form suitable oxides due to a Pilling-Bedworth ratio which is too high. Likewise, W has a high Pilling-Bedworth ratio of 3.3 [276]. The alkaline and the alkaline earth metals are unsuitable because their ratios are too small. While titanium has a Pilling-Bedworth ratio capable of forming a dense oxide film, other properties (perhaps such as high differential thermal expansion) make it unable to provide suitable cover under oxidative conditions. Elements such as Zr, Al, Cr, Si, Mn, Co, Ni, Cu, and Fe all have a suitable Pilling-Bedworth ratio. However, Co suffers from activation issues, Ni increases hydrogen ingress into Zr claddings via (n, p) reactions.

Oxidation kinetics of select refractory compositionally complex alloys has been summarised by Gorr *et al.* [224] and are in **Table 4** and plotted in **Figure 39**. The best performing alloy in this dataset in terms of low oxidation kinetics is the AlCrMoTaTi alloy, which contains both the protective elements Al and Cr. Higher concentration of these elements may promote slow oxidation kinetics. However, AlCrMoTiW, which differs to AlCrMoTaTi by a single element, exhibited an order of magnitude faster oxidation, so the relationship between constituent elements and subsequent oxidation performance is not straightforward.

Table 4. Oxidation kinetics of a range of compositionally complex alloys at 1000°C in air. Produced from Gorr *et al.* [224].

System	Oxidative mass gain (mgcm ⁻²)			
	1 hour	3 hours	20 hours	50 hours
CrMo _{0.5} NbTa _{0.5} TiZr	55	110		
CrNbTiZr	13	25	60	83
NbTiVZr	30	100		
AlCrMoNbTi	0.5	0.8	3.5	9
AlCrMoNbTi–1Si	0.5	1	2.4	6.4
AlCrMoTiW	2.3	3.8	6.5	
AlCr _{0.5} Mo _{0.5} NbTiZr	4.29	21		
AlCr _{0.5} Mo _{0.5} NbTiZr	3.46			
Al _{0.5} CrMo _{0.5} NbTiZr	13.38			
Al _{0.5} Cr _{0.5} MoNbTiZr	7.29			
Al _{1.5} Mo _{0.5} NbTiZr	8.25			
AlMoNbTiZr	1.27			
Al _{0.5} Mo _{1.5} NbTiZr	6.3	20		
Al _{1.5} Cr _{0.5} NbTiZr	10.66			
AlCrNbTiZr	6.1	39		
Al _{0.5} Cr _{1.5} NbTiZr	9.4			
Cr _{1.5} Mo _{0.5} NbTiZr	8.77			
CrMoNbTiZr	0.5			
Cr _{0.5} Mo _{1.5} NbTiZr	7.7		13.6	
AlCrNbTiZr	13	13	23	52
AlCrMoTaTi	0.15	0.3	0.5	0.6
AlCrMoTaTi–1Si	0.25	0.4	0.8	1.3
HfNbTaTiZr	17			
Al _{0.5} HfNbTaTiZr	8.5			
AlHfNbTaTiZr	6			
AlNbTiZr	3.8			
HfNbTiZr	0.25			
AlCoCrFeMo _{0.5} NiSiTi	0.3	1	2.2	3.7
AlCrFeMo _{0.5} NiSiTi	1	1.8	2.8	8
CrMoNbTaV	3	13	42	
AlNb _{1.5} Ta _{0.5} Ti _{1.5} Zr _{0.5}	5	10	25	38



92

3.1.4 Thermal expansion

If it is assumed that the thermal expansion behaviour of constituent elements correlates with the thermal expansion behaviour of a concentrated solid solution (which we later show is the case in **Chapter 4**), then one should choose elements with thermal expansion behaviour comparable to that of Cr and Zr. Linear thermal expansion coefficients of refractory elements Mo, Nb, Ta, Ti, V, W, with Cr and Zr are plotted in **Figure 40**.

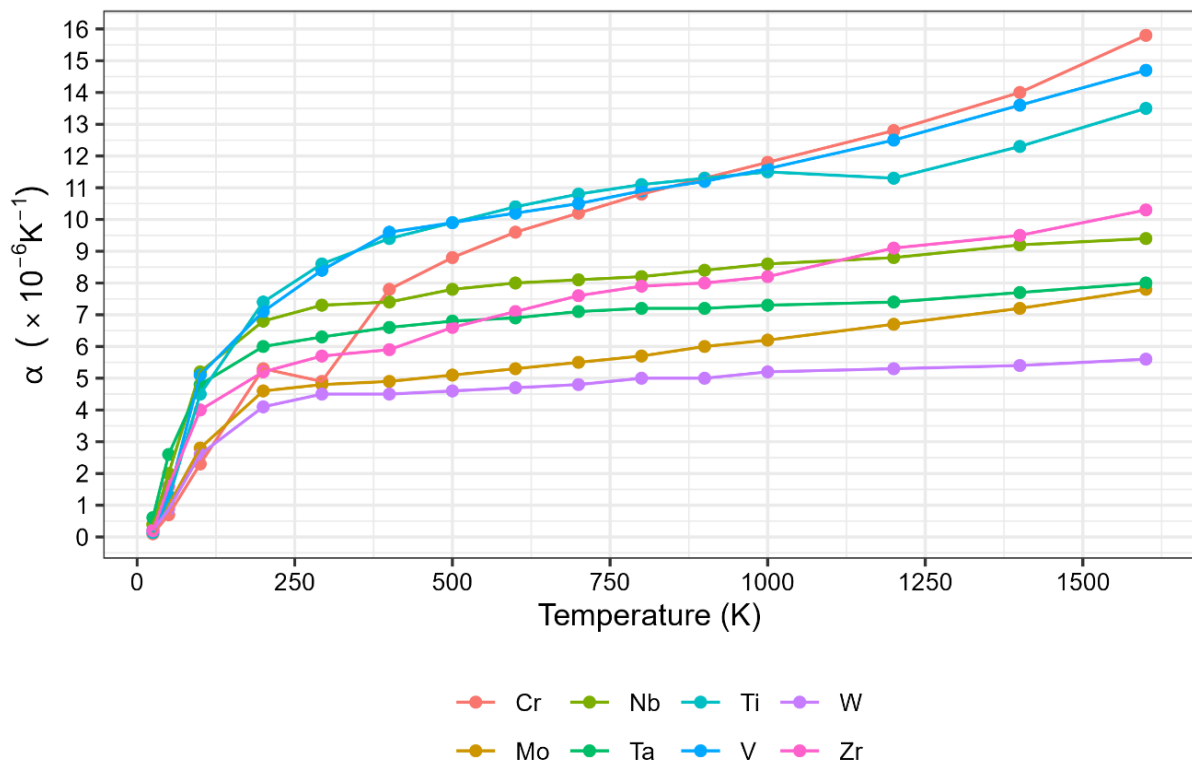


Figure 40. Linear thermal expansion coefficients of refractory elements. Produced via data from Touloukian *et al.* [277].

Cr and Zr already have similar room-temperature thermal expansion coefficients. To select elements to form a compositionally complex alloy, whose expansion coefficients fall between Zr and Cr, it is likely that one must choose elements with low expansion coefficients such as Mo and W, to balance the elements with large expansion coefficients such as Ti, V, and Nb. The entire range of thermal expansion as a function of temperature should be considered, as elements such as Cr, Ti, and V deviate more strongly at high temperatures than low expansion elements such as Mo and W.

3.2 Interlayer selection

From the selection criteria for an interlayer laid out in **Chapter 1**, and the materials design effort conducted in this chapter, it is proposed that two refractory compositionally complex alloys could perform as an interlayer between Cr and Zr. These are MoNbTaTiW, and MoNbTaW. Coincidentally, these two materials are two of the most studied refractory compositionally complex alloys in the academic literature. This is because of their high thermal stability [278], and good high-temperature strength [170]. The addition of Ti to MoNbTaW confers benefits in terms of ductility [160], [279].

The phase equilibria of MoNbTaW and MoNbTaW-Ti are shown in **Figure 41** and **Figure 42**, respectively. Both alloys are expected to form single phase body-centred cubic structures. Thermal stability is crucial for an interlayer system because the reactor conditions (587 – 647 K across 6 – 7 years of fuel lifetime) can precipitate undesired phases during reactor operation. Stable solid solutions are also more predictable, and generally possess greater ductility than intermetallic or ordered phases. Given the vast compositional space of compositionally complex alloys, academic literature on phase equilibria of many alloys is scarce. Pragmatically, it is worthwhile to select alloys which have at least some history of study.

3.2.1 Phase stability in MoNbTaTiW and MoNbTaW

MoNbTaW comprises element which are completely isomorphous with each other. Each element in this system is therefore able to form a disordered solid solution with any other constituent element. The CALPHAD method (using the ThermoCalc HEA4 database), in a one-axis phase equilibria diagram, predicts a body-centred cubic crystal structure above room temperature (**Figure 41**).

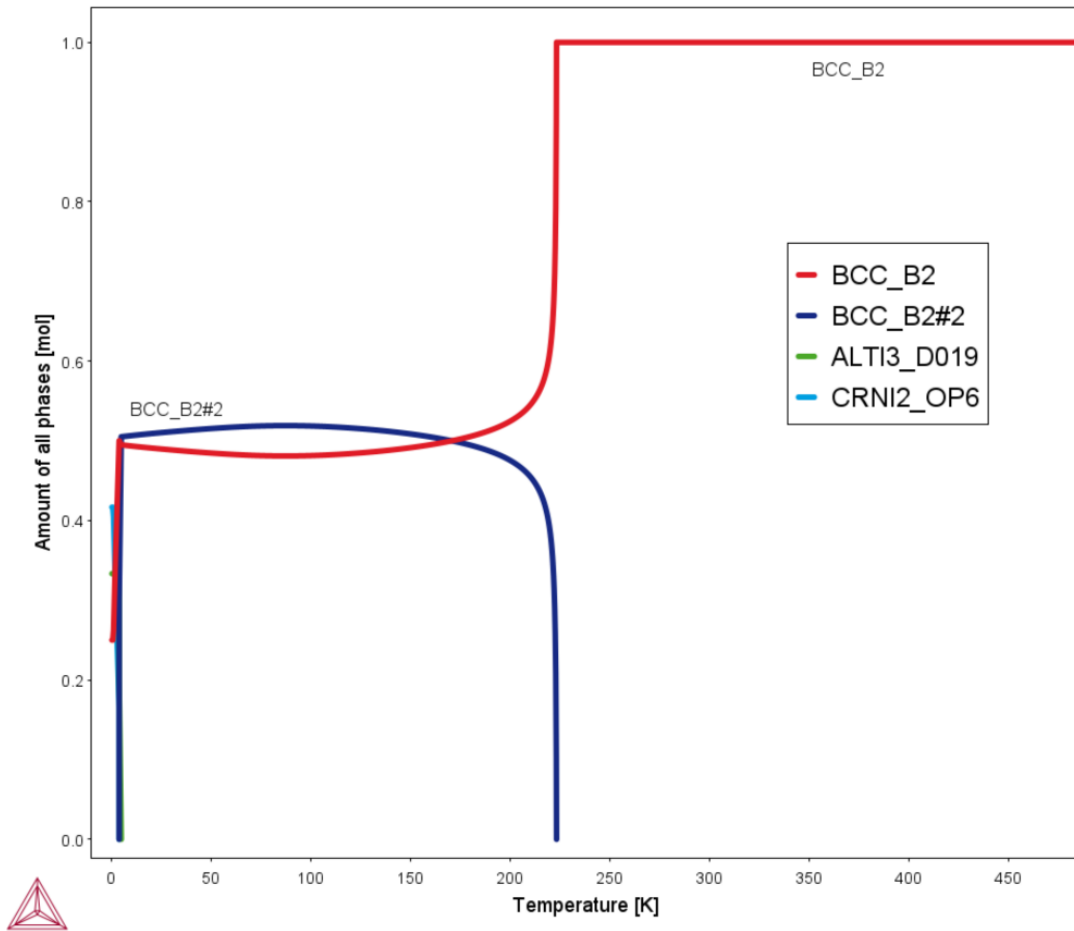


Figure 41. Thermal phase equilibria for MoNbTaW obtained from CALPHAD via the TCHEA4 database.

Ti is known to increase the room-temperature ductility of MoNbTaW [279]. **Figure 42** illustrates the addition of Ti to the equiatomic MoNbTaW alloy. Across the X-axis of this diagram, Ti displaces atoms of the other constituent elements at random, such that Mo, Nb, Ta, and W, are equiatomic with each other at all points in the diagram. The incorporation of Ti is known to increase ductility in this alloy, but also increases the likelihood of Ti precipitating out of solution at low temperatures and high Ti concentration.

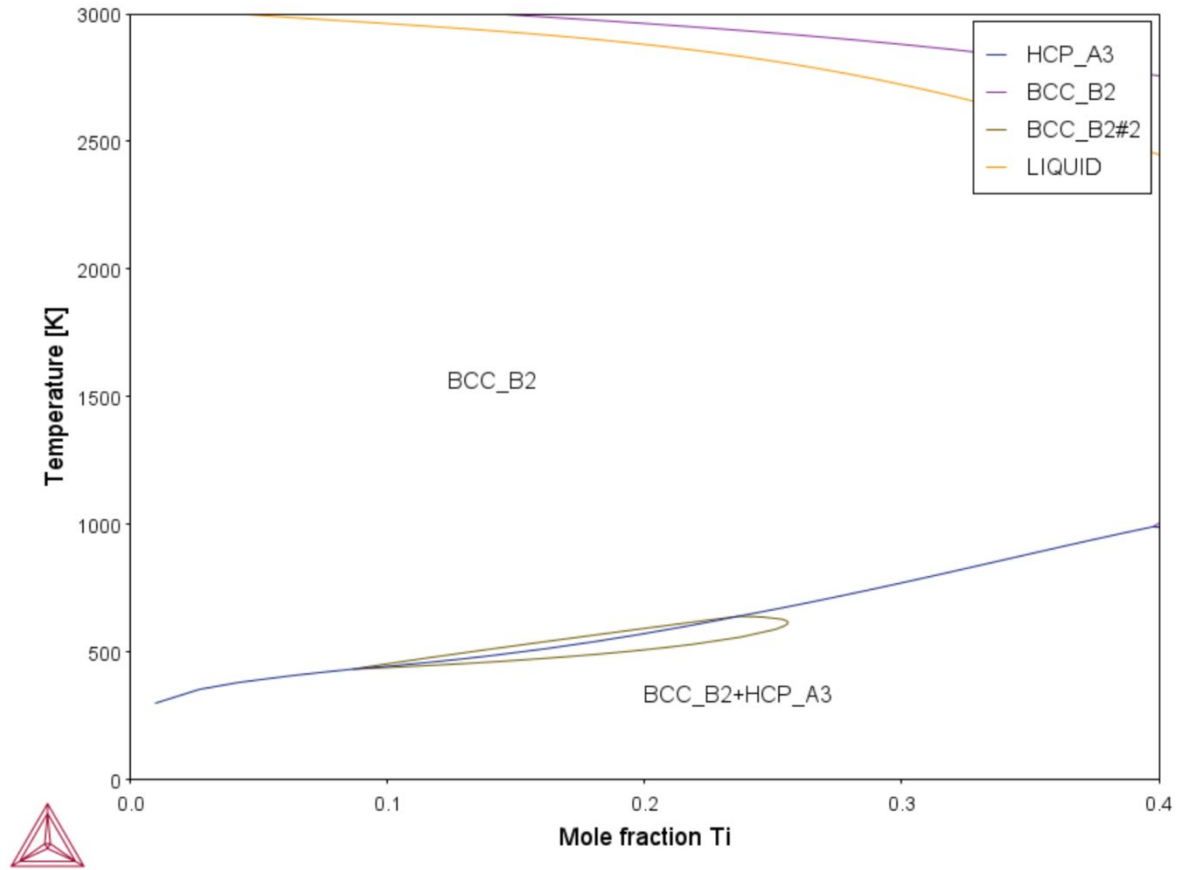


Figure 42. Thermal phase equilibria for the MoNbTaW-Ti system via the CALPHAD method from the TCHEA4 database.

The CALPHAD method can model the interface between two materials in a pseudobinary phase diagram. In the example in **Figure 43**, the phase equilibria present between the potential interlayer material, MoNbTaW, and the Cr coating is suggested. The Cr concentration across the X-axis, is assumed to replace each of the elements of MoNbTaW at random. In this example, there is still a large body-centred cubic miscible phase most notable above 1000 K. During chemical evolution of the system, it is assumed that all compositions across the isotherm in **Figure 43** will be present at least somewhere across MoNbTaW-Cr interface. It must not be overlooked that the phase diagram includes a C15-Laves phase; however, it is uncertain whether this intermetallic is formed in this system and which elements are likely to form it.

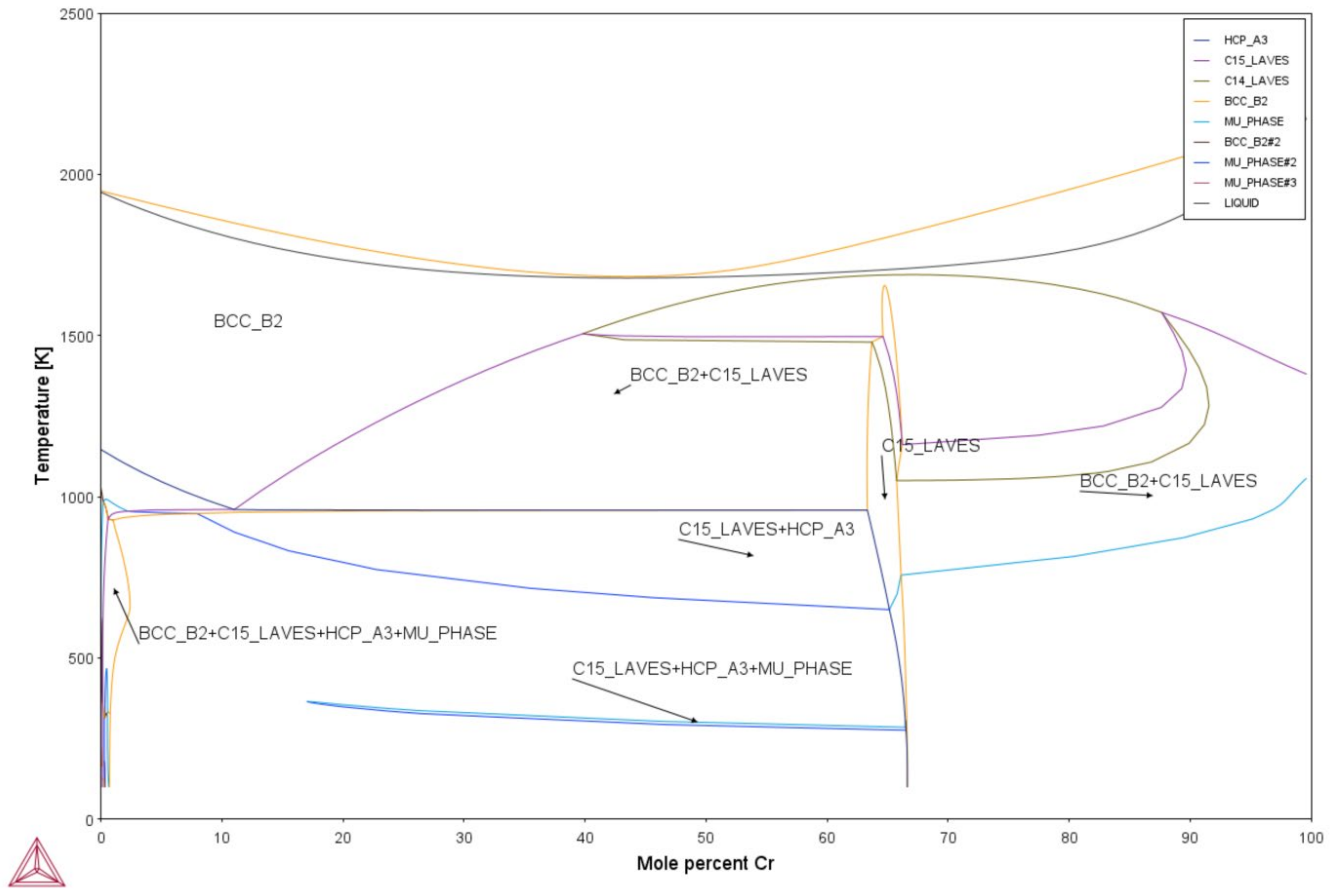


Figure 43. CALPHAD model of the MoNbTaW-Cr interface.

3.2.2 Driving forces for oxidation in the Mo-Nb-Ta-Ti-W system

Backman *et al.* observed that the additional configurational entropy afforded to compositionally complex alloys is unlikely to significantly reduce the driving force for oxidation in these alloys [280]. For example, the additional stabilising effect of the Gibbs energy afforded to a 5-element concentrated solid solution is given by $-T\Delta S_{\text{conf}}$, which, at a temperature of 3000 K will be $-40.14 \text{ kJmol}^{-1}$. Consider that the Gibbs energy of combustion for refractory metals at 25 K is -500 to -1100 kJmol^{-1} , and at 3000 K: -100 to -700 kJmol^{-1} [280], and it is therefore apparent that preventing oxidation through the configurational effect of compositionally complex alloys alone, is unlikely, without forming a high entropy oxide layer, or protective oxide scale.

Although the high entropy effect is unlikely to mitigate the driving force for oxidation in compositionally complex alloys, the disparate driving forces for oxidation among constituent elements may cause them to oxidise preferentially. As a first approximation, the Gibbs energy of formation at 298.15 K is compared for a range of common oxides in the Zr-Mo-Nb-Ta-Ti-W-Cr system, normalised to per mole of reacting oxygen, $O_{2(g)}$ (**Table 5**):

Table 5. Gibbs energy of formation normalised to a reacting mole of $O_{2(g)}$ for a range of oxides in the Zr-Mo-Nb-Ta-Ti-W-Cr system.

Oxide	ΔG_f (kJmol ⁻¹)	ΔG_f (kJmol ⁻¹ per O_2)
ZrO ₂	-1039.7	-1039.7
TiO ₂	-883.3	-883.3
Ta ₂ O ₅	-1911.0	-764.4
NbO ₂	-739.2	-739.2
Cr ₂ O ₃	-1053.1	-702.0
WO ₂	-533.9	-533.9
WO ₃	-764.1	-509.4
MoO ₃	-668.1	-445.4
TaO ₂	-210.9	-210.9
MoO ₂	-21.2	-21.2
TaO	163.5	327.0
MoO	278.0	556.0

Zr is expected to oxidise most readily at room temperature in air. Both Ta and Nb are expected to preferentially oxidise with respect to the Cr coating. Mo and W, conversely, are seen to be more stable with respect to Cr at room temperature. Less stable oxides, such as MoO₂ and TiO₂ are not expected to form, except in cases with low partial pressure of $O_{2(g)}$. The preferential oxidation of certain elements does not appear to change in the functional temperature region for a fuel clad coating system. **Figure 44** shows ΔG_f for a range of potentially relevant oxides:

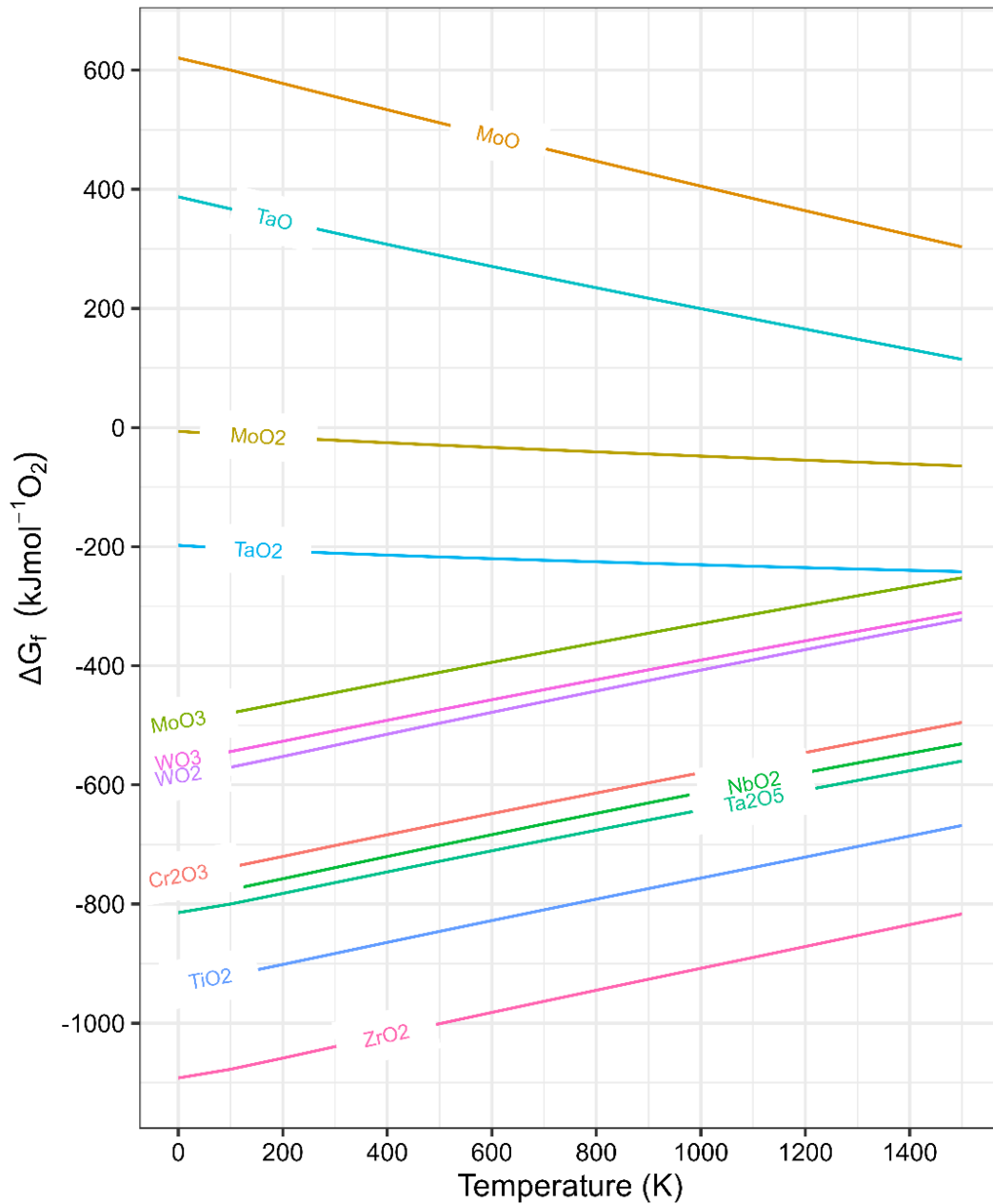


Figure 44. ΔG_f for a range of relevant oxides at standard pressure. Data from the NIST-JANAF thermochemical tables.

The reduction in the driving force for oxidation on account of the higher configurational entropy in compositionally complex alloys is not expected to be significant [280]. Considering only the oxidation of the pure constituent elements, may be applicable to thermodynamics of oxidation in complex alloys. Partial pressure of O_2 also becomes relevant further into the surface of the coating system, as it could contribute to the formation of less common oxides. However, oxidation processes are not solely a function of the thermodynamics. The outer layer of the coating, Cr, is expected to oxidise first because the inner materials are shielded from the

oxidising coolant. Oxidation of the inner materials will be sterically hindered when Cr forms a dense oxide scale. Oxidation will therefore be governed by the rate of oxygen ingress through the Cr_2O_3 film. Additionally, faster diffusing elements in the compositionally complex alloy may preferentially oxidise by virtue of them diffusing to the oxide interface faster than less mobile elements. Compositionally complex alloys have been known to form dense oxide films, as discussed in **Chapter 1**, and these have only superficially been studied. Their tendency to form, their typical compositions, and their ability to form dense oxide films is unknown.

If it is assumed that the diffusion of migrating species did not affect the overall evolution of the coating system during oxidation, then the process may occur as follows: firstly, the outer layer of Cr forms Cr_2O_3 . Then, over time, as O_2 ingress increases, the thermochemical contact between the compositionally complex alloy, the Cr layer, and Cr_2O_3 may facilitate redox reactions between these species. Cr_2O_3 may reduce, reforming the Cr layer, and in turn giving up oxygen to the compositionally complex alloy. The element most likely to oxidise in the alloy is Ti, followed by Ta and Nb. As the system evolves, the species Ta, Nb, and perhaps Mo, and W may oxidise also. Another possibility is that the underlying Zr oxidises, leaving the more noble metals Mo and W relatively unoxidised. Incidentally, it is shown in **Chapter 5** that Ti has the lowest barrier for vacancy migration in MoNbTaTiW, which could make this element a mobile getter of oxygen during the evolution of the coating system. The driving force for the $\text{TiO}_2 + \text{Zr} \rightarrow \text{Ti} + \text{ZrO}_2$ reaction is also much lower than the driving force between the redox reaction between Cr_2O_3 and Zr. This could result in lower slower kinetics of reaction and protect the Zr from oxidation for a longer period.

For a more sophisticated analysis of the oxidation evolution of the coating system, one must consider the real conditions within a light water nuclear reactor:

- Diffusion and kinetic effects: migration of oxygen through the oxide layer.
- The reacting species is likely to be high temperature water or steam, not O_2 .
- The system will not be at standard pressure (PWR: 15 – 16 MPa, or 150 – 160 bar).
- There will be a considerable reduction in partial pressure of O_2 as a function of depth into the coating system.

Chapter 4. Thermal expansion of compositionally complex alloys

Results from this chapter were published in the *Journal of Physics: Energy*

J.A. Wilson, L.J. Evitts, A. Fraile, R.E. Wilson, M.J. D Rushton, D.T. Goddard, W.E. Lee, S.C. Middleburgh, Predicting the thermal expansion of body-centred cubic (BCC) high entropy alloys in the Mo–Nb–Ta–Ti–W system, *J. Phys. Energy*. 4 (2022) 034002.
<https://doi.org/10.1088/2515-7655/AC6F7E>.

In this chapter, the Mo-Nb-Ta-Ti-W system of concentrated solid solutions is investigated using density functional theory, with the purpose of assessing whether the rule of mixtures can be applied to these alloys in terms of thermal expansion. The thermal expansion behaviour of concentrated solid solutions is shown to be an averaging scheme of the constituent elements.

4.1 Introduction

The thermal expansion behaviour of materials is an important property for their application, whether for coatings, fillers for welded joints, or structural components [281]. Thermal expansion behaviour is an integral component of the strategies of numerous industries, including aerospace and energy. For instance, in the selection of materials for metallic alloys, thermal expansion coefficients must be carefully considered to reduce residual thermal stresses between components and provide a robust defence against thermal fatigue or thermal cycling. Large differences in thermal expansion between layers can result in periodic residual stress fields along the film thickness, negatively impacting the coating's strength and adhesion to the substrate. Additionally, thermal expansion is a crucial factor to consider when designing zirconium-based alloy coatings, as reported frequently in the academic literature [39], [48], [222], [282]. Multiple papers describe the mismatch in thermal expansion between Cr and Zr and its implications as a nuclear fuel coating system [81], [283], [284]. For example, Ribis *et al.* identifies thermal expansion matching as a difficulty for the CEA-FRAMATOME-EDF adherent chromium coating concept [284], [285] on Zr-cladding. To prevent interfacial stresses and delamination during thermal cycling, it is crucial to match the thermal expansion coefficients of the coating and substrate precisely.

Compositionally complex alloys could be used as a barrier between Cr and Zr, but their thermal expansion coefficients must match those of the outer metals if they are to outperform existing coating solutions. Cr and Zr already have thermal expansion coefficients that are comparable (α : Cr: 4.9 ppm K⁻¹; Zr: 5.7 ppm K⁻¹). To meet the design criteria of intermediate thermal expansion with Zr and Cr, a compositionally complex alloy may require the addition of low thermal expansion metals, such as Mo and W. Therefore, it is desirable to design an alloy interlayer with an intermediate thermal expansion coefficient. A potential advantage of compositionally complex alloys is their vast compositional variability, which allows their properties to be tailored by changes in chemical composition. It is anticipated that the thermal expansion of these alloys can be tailored to the surrounding Cr and Zr to minimise delamination or cracking under thermal loads. Thermal expansion, however, like many other materials properties, is severely under-described in literature for compositionally complex alloys. Whether or not the mechanism for thermal expansion for compositionally complex alloys is the same as conventional alloys needs to be confirmed [252]. Compositionally complex alloys are increasingly being investigated for use as weld fillers in the joining of dissimilar metals [134], [135], [140]. It is for this reason that a timely treatment of their thermal expansion properties is required.

A prototype compositionally complex alloy is studied here: equiatomic MoNbTaTiW. The refractory MoNbTaTiW alloy and its related systems have industrial relevance due to their high melting temperatures and promising mechanical properties such as high-temperature strength. The high strength of MoNbTaTiW is primarily due to solution hardening via a mechanism proposed by Toda-Caraballo [286] and developed from the earlier approach by Labusch [287]. The nuclear applications of MoNbTaTiW are also of interest due to the relatively low thermal neutron capture cross-section of many of the constituent elements and may therefore find applications as components in fusion or fission systems. Properties such as elastic modulus, density, structure, and cost can reasonably be predicted from the rule-of-mixtures approach [97], [168], [288] but so far the applicability of this approach is not proven in the thermal expansion behaviour of compositionally complex alloys, whose literature on the subject remains scarce. This is surprising, because compositionally complex alloys have a unique flexibility in their available compositions compared to conventional alloys, which could be exploited to fine-tune thermal expansion behaviour for a tailored thermal expansion response. Past work by Laplanche *et al.* [289] reported the thermal expansion behaviour of FCC alloys MnFeNi, MnCoNi, CrFeCoNi, CrFeNi, CoNi, FeCoNi using dilatometry. Here, it

was reported that the thermal expansion behaviour of these alloys was similar to face-centred cubic austenitic steels [290] as well as pure metals [277]. Laplanche *et al.* using the rule of mixtures, observed a systematic underprediction of thermal expansion coefficients at low temperature in a range of medium entropy alloys [289]. It was suggested that this underprediction was due to the constituent elements preferentially adopting different crystal structures in their standard states, reducing the validity of the rule of mixtures. Local ordering on the atomic scale could also be the cause of the deviation from the rule-of-mixtures approach. The rule of mixtures for thermal expansion can be described via:

$$\alpha_{Alloy} = \sum_i^N V_i \alpha_i \quad (39)$$

where α_{alloy} is the thermal expansion coefficient of the compositionally complex alloy, α_i is the thermal expansion coefficient of constituent i , V_i is the volume fraction of phase i , and N is the number of constituent elements. MoNbTaTiW was discovered to be a single phase body-centred cubic (Pearson Symbol: cI2, Strukturbericht Designation: A2) solid solution by Han *et al.* [279], [291] who looked at the effects of Ti additions on the Senkov alloys MoNbTaW and MoNbTaVW in order to improve the room-temperature ductility of these alloys. [292]. MoNbTaW has the highest resistance to softening at high temperatures amongst refractory compositionally complex alloys studied but is limited by its low ductility at room-temperature. Han *et al.* [20] also demonstrated that MoNbTaTiW indeed confers improvements to room-temperature strength and ductility over MoNbTaW. Using the Thermo-calc software with TTNI 8 database they found that MoNbTaTiW has a BCC structure at high temperatures, with an HCP phase appearing below 640°C, although as far as the author is aware this phase has not been reported experimentally. Bhandari *et al.* [160] calculated the thermal expansion coefficient as a function of temperature of the equiatomic MoNbTaTiW alloy using density functional theory, on a 100-atom randomised supercell, and predicted a linear thermal expansion coefficient which rises steeply with temperature and plateaus at 550 K at $9 \times 10^{-6} K^{-1}$ [160]. In this work it is demonstrated that the temperature dependence of compositionally complex alloy thermal expansion coefficients can be predicted using computationally efficient special quasi-random structure supercells and first-principles density functional perturbation theory.

4.2 Methodology

Density functional theory methods [293], [294] were used with projector augmented wave style pseudopotentials [295] as implemented in the Vienna *ab initio* simulation package [40][41]. The exchange-correlation interactions were described by the generalised gradient approximation of the Perdew-Burke-Ernzerhof form [297]. Methfessel-Paxton smearing [298] with a smearing width of 0.5 eV was employed to account for partial occupancies of the metallic compositionally complex alloy systems. The cut-off energy of plane waves was 500 eV. The Brillouin zone was sampled with a gamma centred \mathbf{k} -point mesh with density greater than 0.2 \AA^{-1} .

Binary, ternary, quaternary, and quinary systems were considered in the Mo-Nb-Ta-Ti-W system (a total of 25 compositions). The chemical disorder of the compositionally complex alloys was modelled using special quasi-random structures (SQS), similar to previous work [299]–[302]. Supercells were generated from the *mcsqs* code of the Alloy Theoretic Automated Toolkit [264]. Correlation functions were set to include interactions for up to the third nearest neighbour. A range of supercell sizes were considered, maintaining the stoichiometry of the species to equimolar or near-equimolar concentrations. For example, the MoNbTaTiW 54-atom supercell consisted of $\text{Mo}_{11}\text{Nb}_{11}\text{Ta}_{10}\text{Ti}_{11}\text{W}_{11}$ to fit the description of a body-centred cubic 54-atom cell. This non-stoichiometry is not expected to affect the thermal expansion significantly. For thermal expansion calculations, $2 \times 2 \times 2$ body-centred supercells containing 16 lattice sites or $3 \times 3 \times 3$ supercells containing 54 lattice sites were used. The SQS cells were relaxed at constant pressure, where the atomic positions and lattice parameters could vary; the convergence threshold for the total energy and atomic force were 10^{-8} eV and 10^{-7} eV/Å, respectively.

Thermal properties such as thermal expansion of solids at constant volume can be calculated from the phonon density of states as a function of frequencies. Explicit phonon calculations were therefore carried out similar to previous work [303] and to good dynamic stability, and were then used to predict the thermal expansion of each composition. Phonon spectra are computed using density functional perturbation theory [304] with $6 \times 6 \times 6$ \mathbf{q} -point meshes. Calculations utilised the quasi harmonic approximation (QHA) as implemented in the Phonopy [305][306] code. Force constant calculations were completed to an energy convergence criterion of 10^{-8} eV. The Phonopy code was used to calculate the total free energies for seven volumes for each composition (strained hydrostatically to -8.8% to $+9.3\%$ of the equilibrium volume at 0K). A Birch-Murnaghan equation of state was fitted to each

composition and was subsequently extrapolated to higher temperatures via the quasi-harmonic approximation within the Phonopy code. The volume at each minimum indicates the volume as a function of temperature, which by numeric differentiation gives the thermal expansion coefficients of each composition, similar to previous work [254]. The rule of mixtures approach for thermal expansion of concentrated solid solution alloys was applied by taking a weighted average (by volume fraction) of pure elemental data from Touloukian *et al.* [277] obtained experimentally via dilatometry.

4.2.1 Convergence testing

Convergence testing with respect to the K-point mesh used and the plane wave cut-off energy were conducted (**Figures 45** and **Figure 46**, respectively).

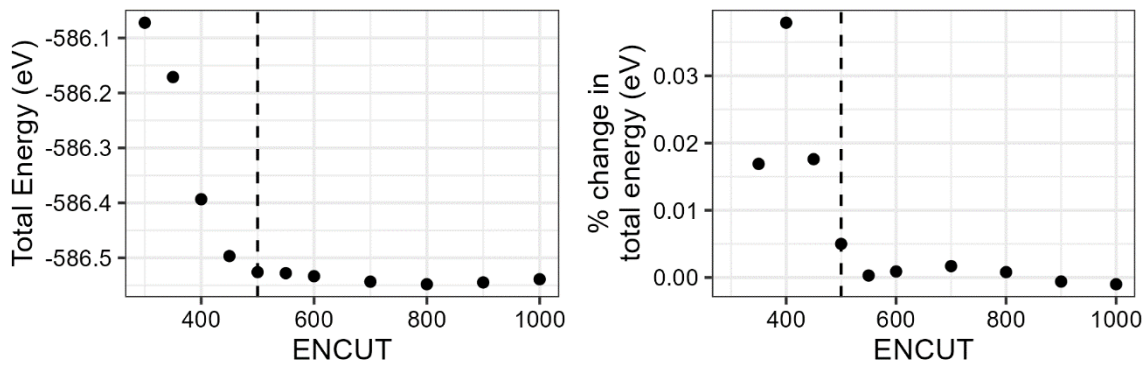


Figure 45. Cut-off energy convergence testing. Convergence testing for cut-off energy values (the plane wave cut-off energy; ENCUT) for a 54-atom body-centred $\text{Mo}_{11}\text{Nb}_{11}\text{Ta}_{11}\text{Ti}_{10}\text{W}_{11}$ supercell. A cut-off energy value (dashed vertical line) was chosen for which an increase of 50 eV resulted in less than 0.01 % change in total energy. **(A)** Total energy plotted against cut-off energy value. **(B)** Percentage change in total energy plotted against plane wave cut-off energy.

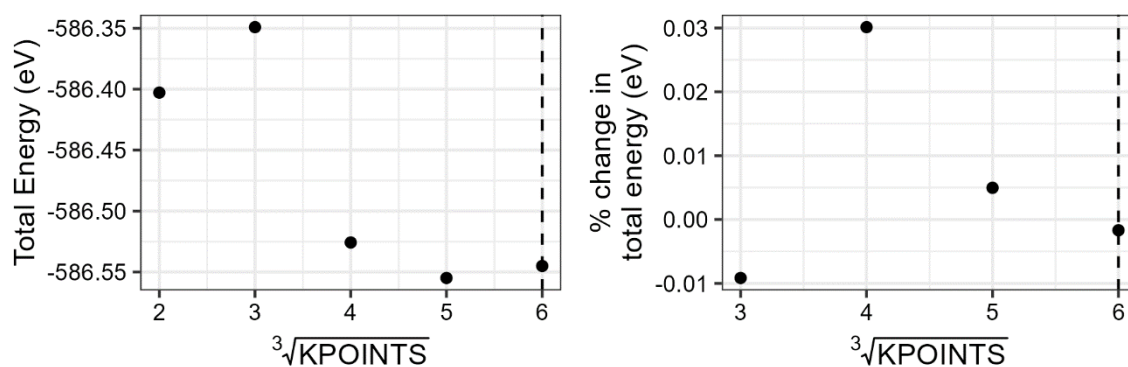


Figure 46. K-points convergence testing. Convergence testing for number of K-points of a 54-atom body-centred $\text{Mo}_{11}\text{Nb}_{11}\text{Ta}_{11}\text{Ti}_{10}\text{W}_{11}$ supercell. A K-points set (dashed vertical line) was chosen for which a further increase of K-points resulted in less than 0.01 % change in total energy. **(A)** Total energy plotted against number of K-points. **(B)** Percentage change in total energy plotted against number of K-points.

4.2.2 The Mo-V system

As an initial attempt at performing these calculations, the simple binary system Mo-V is adopted, which was known to be isomorphous according to the binary phase diagram. In these calculations, the concentrations of both elements were varied, and it was found that there was indeed intermediate thermal expansion behaviour in the solid solutions compared to the pure individual metals. The predicted thermal expansion profile is compared to that found in literature data for the Mo-V system (**Figure 47**). This short study suggested that the thermal expansion coefficients of binary solid solutions is indeed a form of averaging of the expansion coefficients of the constituent pure metals, and that density functional theory may be an appropriate method to study thermal expansion behaviour in disordered alloys.

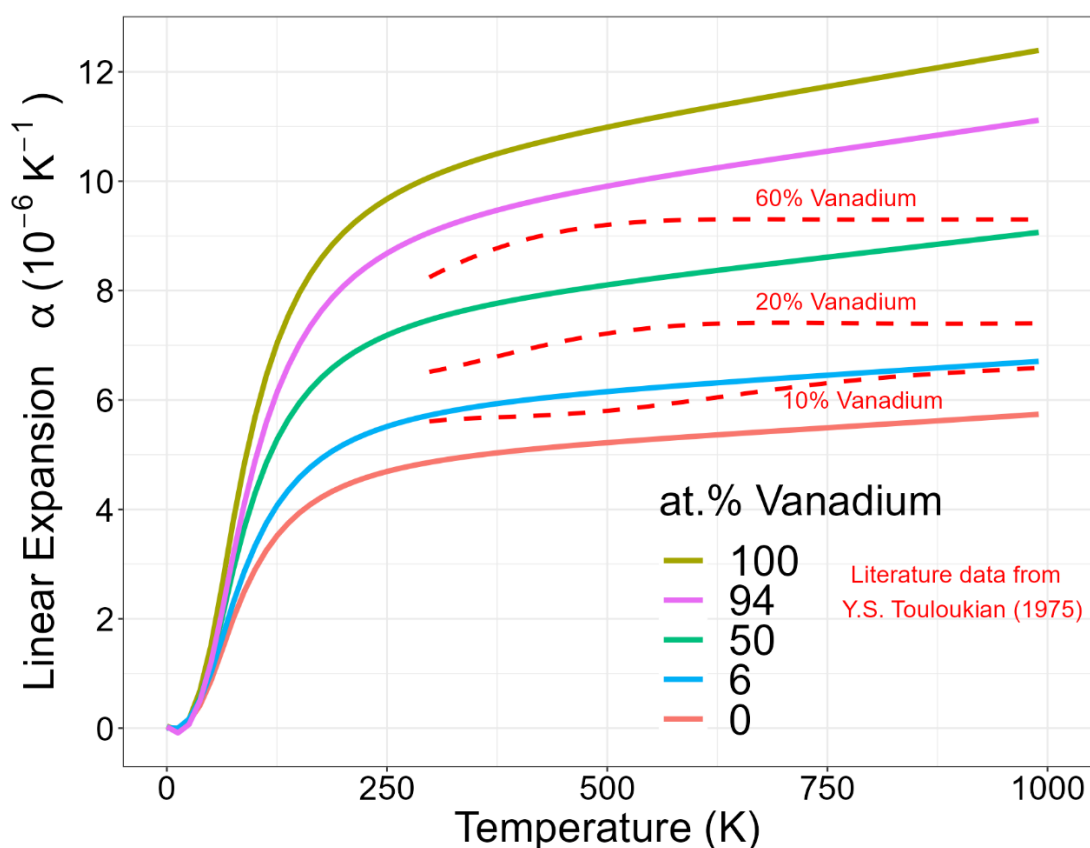


Figure 47. Density functional theory calculated thermal expansion profiles in the Mo-V system. Literature data from Touloukian *et al.* [277].

4.2.3 Choice of pseudopotentials

Incidentally, the thermal expansion profiles of the individual pure elements were extremely sensitive to the choice of pseudopotentials (**Figure 48**). For this reason, many Perdew-Burke-Ernzerhof pseudopotentials were trialled to calculate the thermal expansion profile of each element, and the potential which most closely replicated pure element data obtained from literature [277] was taken forward to perform thermal expansion calculations for the concentrated solid solution alloys.

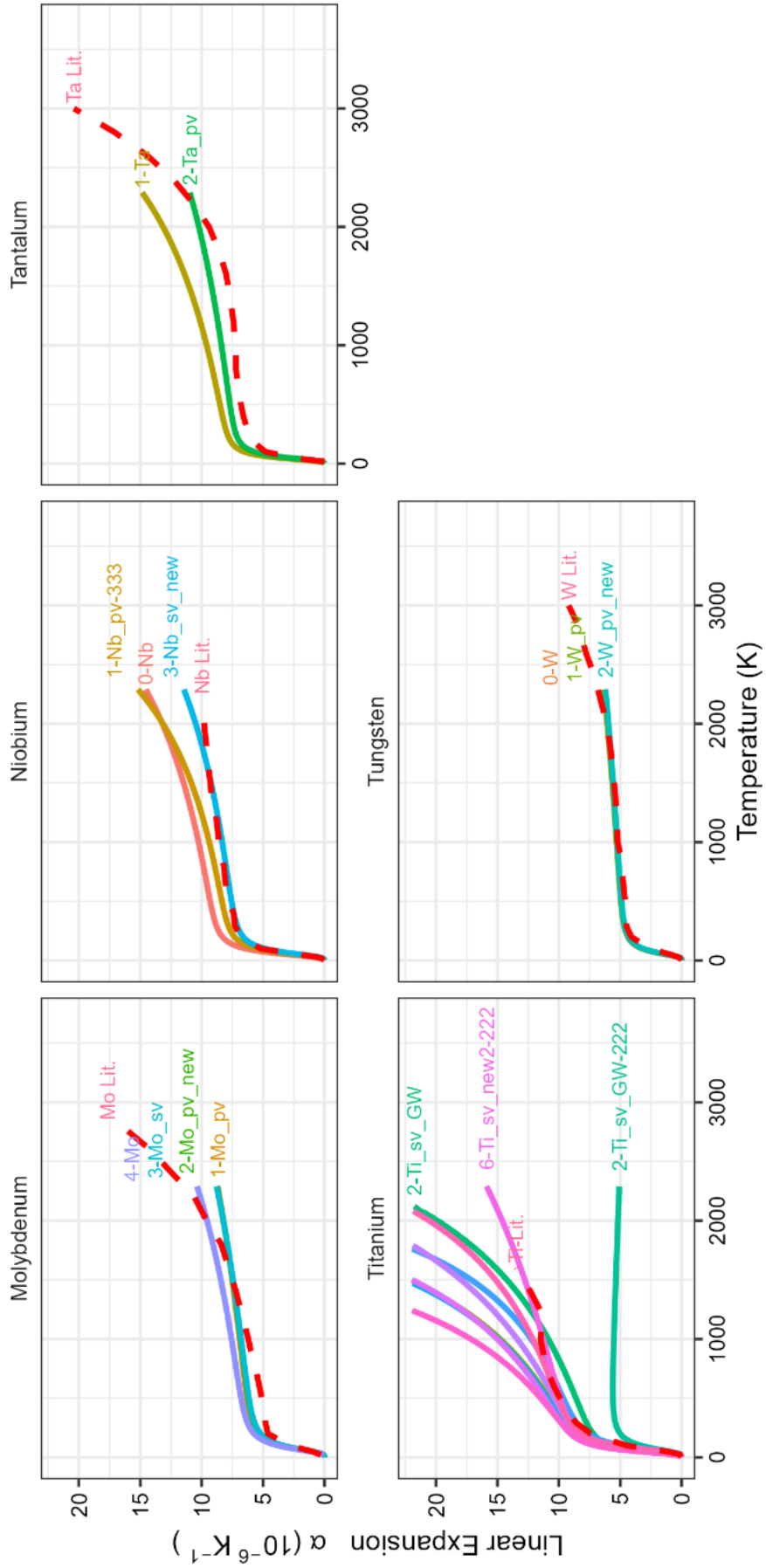


Figure 48. Optimising the choice of pseudopotentials for thermal expansion calculations. Red dashed lines indicate literature data [277] obtained via dilatometry measurements.

The elements whose thermal expansion best matched experimental results was W, followed by Nb. Mo and Ta were slightly overpredicted. Ti was an interesting case as it undergoes a phase transformation of $\alpha_{hcp} \rightarrow \beta_{bcc}$ at 882°C which causes a discontinuity in its thermal expansion profile. This transformation can be captured using optical dilatometry methods, but not by simulation of a single supercell using the quasi-harmonic approach. Nevertheless, the pseudopotential which most closely predicted the polycrystalline thermal expansion profile from literature data [277] was selected. Samples from the expansion profiles at 298 K and 573 K (**Figure 49**) indicate that the best pseudopotentials for each element were able to reproduce values from experimental literature data within $1 \times 10^{-6} \text{K}^{-1}$.

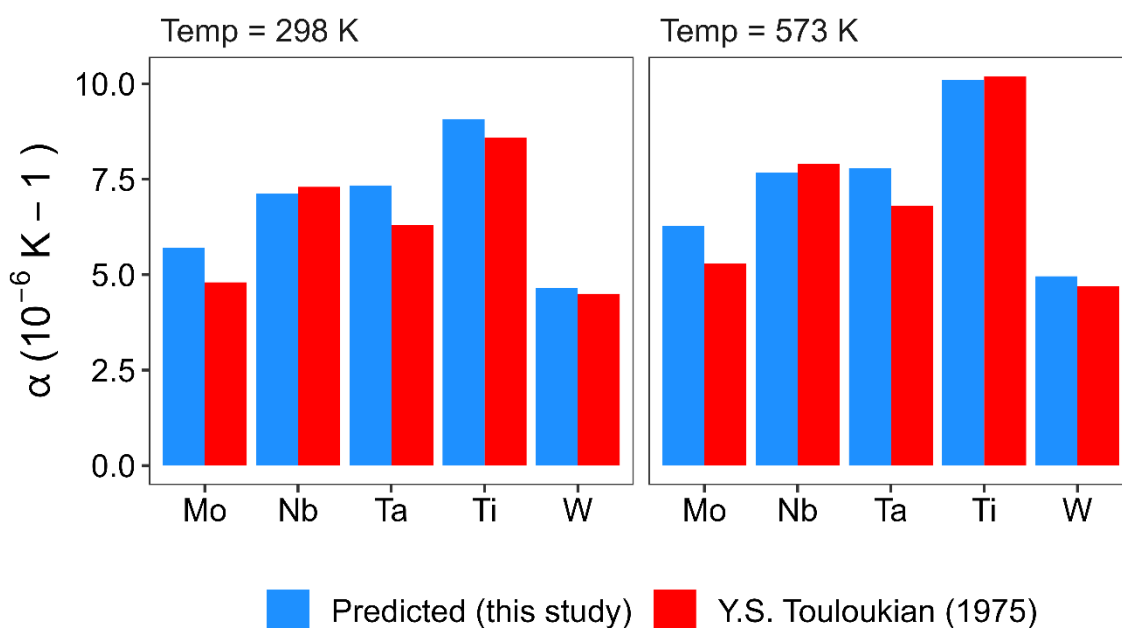


Figure 49. The density functional perturbation theory derived thermal expansion coefficients of the studied pure elements at 298 K and 573 K. Literature data taken from Touloukian *et al.* [277].

The phonon dispersion plots for the MoNbTaTiW alloy exhibited no zero-frequency phonons which would indicate a dynamically stable structure. **Figure 50** shows the phonon dispersion plot for MoNbTaTiW. Dispersion plots for the quaternary alloys are in **Figure 51**.

Alloys MoNbTaTi and NbTaTiW had slightly negative phonons in their plots, which indicate instability in these alloys.

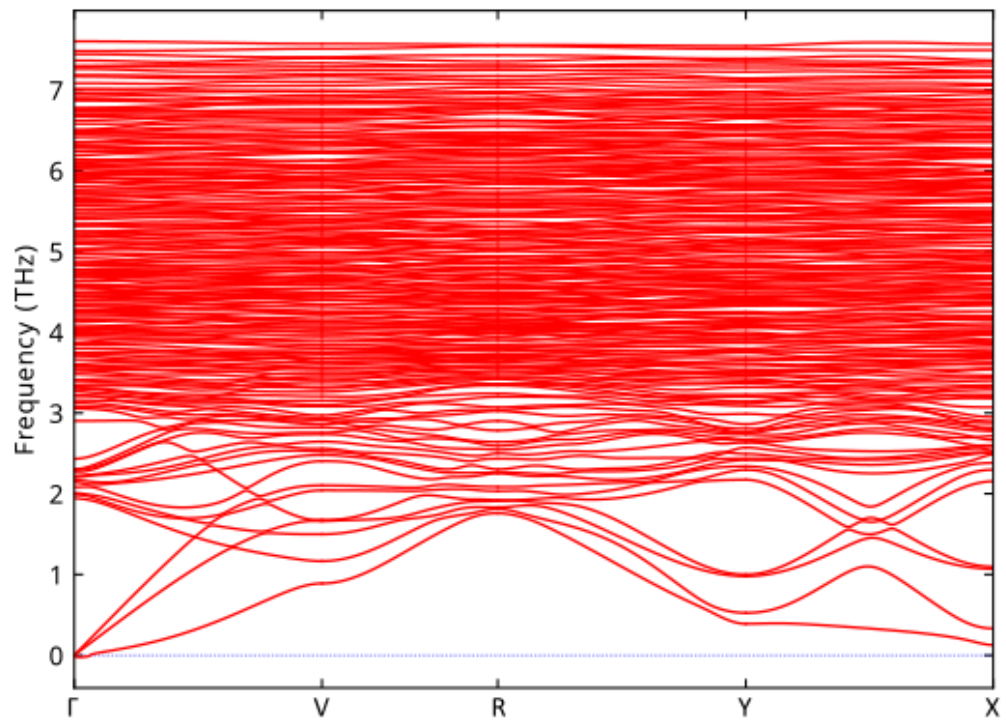
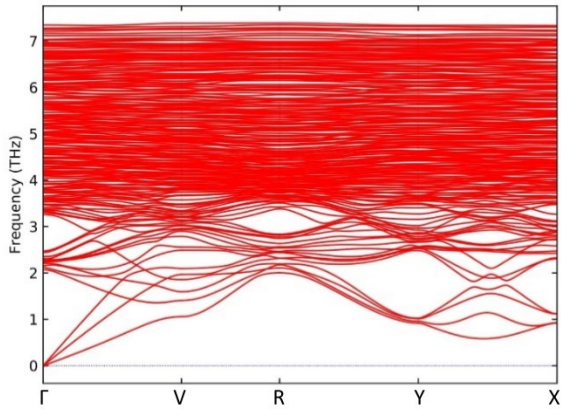
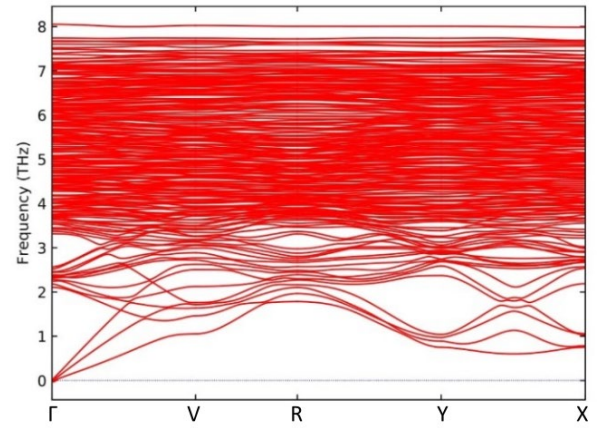


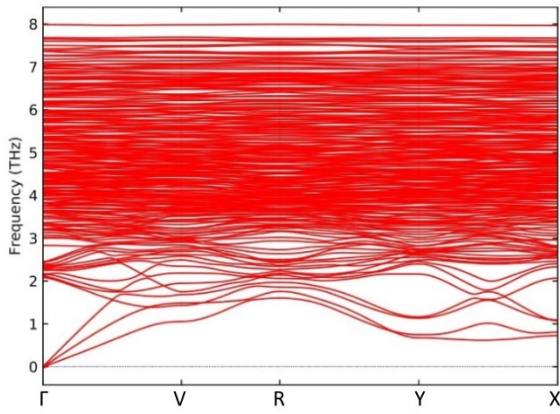
Figure 50. Phonon dispersion plot of 54-atom MoNbTaTiW. Calculation on a 54-atom supercell.



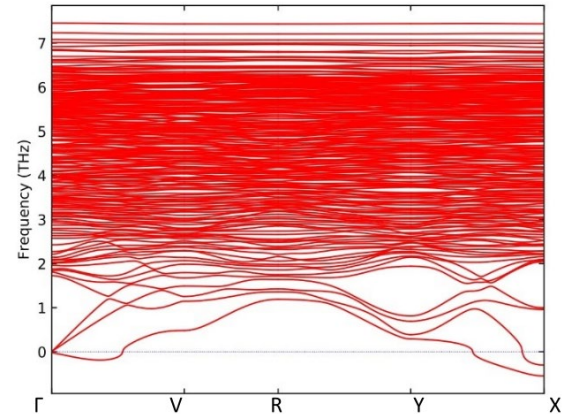
a)



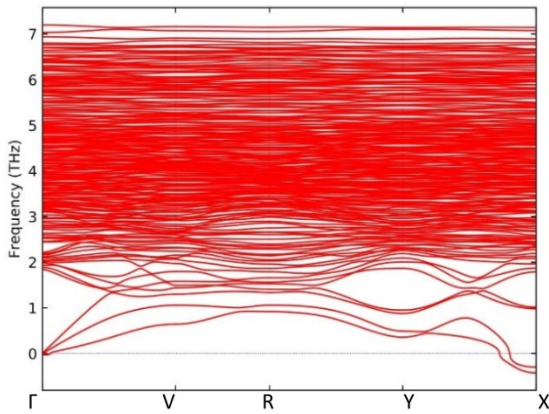
b)



c)



d)



e)

Figure 51. Phonon dispersion plots of the quaternary alloys in the Mo-Nb-Ta-Ti-W system. All phonon spectra calculated from 54-atom supercells. a) MoNbTaW. b) MoNbTiW. c) MoTaTiW. d) MoNbTaTi. e) NbTaTiW

4.3 Results

4.3.1 Lattice constant

Han *et al.* [279] found an experimental room-temperature lattice constant of 3.240 Å for equiatomic MoNbTaTiW. This study predicts a lattice constant of 3.231 Å at 0 K which differs only by 0.3 %. The predicted values for MoNbTaTiW and its subsystems can be found in **Table 6**. Since the lattice constant for concentrated solid solution alloys is not a constant value but a distribution, the mean of second nearest neighbour distances in each supercell is reported with their standard deviations.

Table 6. Predicted lattice constants based on second nearest neighbour distances, where \bar{a} is the mean of second nearest neighbour distances and σ is their associated standard deviation.

Composition	\bar{a} (Å)	σ (Å)
MoNbTaTiW	3.231	0.059
NbTaTiW	3.239	0.054
MoTaTiW	3.211	0.053
MoNbTiW	3.212	0.048
MoNbTaTi	3.254	0.067
MoNbTaW	3.236	0.038
TaTiW	3.242	0.047
NbTiW	3.235	0.048
NbTaW	3.26	0.038
MoTiW	3.17	0.024
MoTaW	3.209	0.028
MoNbW	3.207	0.023
NbTaTi	3.292	0.017
MoTaTi	3.22	0.047
MoNbTi	3.219	0.045
MoNbTa	3.247	0.036
TiW	3.197	0.038
TaW	3.231	0.039
TaTi	3.287	0.02
NbW	3.237	0.03
NbTi	3.282	0.029
NbTa	3.313	0.009
MoW	3.173	0.004
MoTi	3.173	0.043
MoTa	3.234	0.046
MoNb	3.225	0.037

4.3.2 Phase Stability

Before assessing the thermal expansion of the equimolar alloys in the Mo-Nb-Ta-Ti-W system, the thermodynamic stability of these systems is investigated. The stability and crystal structure of a given compositionally complex alloy can be predicted phenomenologically from empirical thermophysical parameters [144], [146]–[149], [307], as part of an extension of the original Hume-Rothery rules [142]. All the combinations of equiatomic alloys in the Mo-Nb-Ta-Ti-W system had a mixing enthalpy between -22 and 7 kJ mol^{-1} indicating favourability towards forming a solid solution. Mixing entropy, ΔS_{mix} , [88] valence electron concentration [146], electronegativity parameter, $\Delta\chi$, [307] and various empirical values including a thermodynamic parameter given by Yang *et al.* [144], Ω , atomic size difference parameter by Yang *et al.* [147], δ , and atomic packing parameter by Guo *et al.* [146], γ , and finally, φ , the ratio between the Gibbs free energy of a completely disordered solid solution to that of the most likely intermetallic or segregated binary system given by King *et al.* [148] have all been suggested to predict the likelihood of single-phase stability for compositionally complex alloys. All alloys satisfied the conditions of these thermophysical parameters to form a solid solution [144], [146], [147], [307]. The valence electron concentration for all alloys was below 6.87 highlighting that the body-centred cubic phase is preferred over the face-centred cubic phase, which was experimentally observed by other authors [291].

The configurational entropy of the equiatomic alloys in the Mo-Nb-Ta-Ti-W system, assuming completely random mixing, is calculated using $\Delta S_{conf} = R \ln(n)$ where R is the universal gas constant in $\text{J K}^{-1} \text{mol}^{-1}$ and n is the number of distinct elements. The configurational entropies span from $5.75 \text{ J K}^{-1} \text{mol}^{-1}$ for the binary alloys to $13.38 \text{ J K}^{-1} \text{mol}^{-1}$ for the quinary alloy. The standard deviation of lattice parameter correlates with number of constituent elements in the equiatomic alloys, indicating increased lattice strain in more complex alloys. Atomic size difference parameter [147], δ , is low for the alloys with the smallest standard deviation in lattice parameter. This makes intuitive sense: an alloy whose constituent elements are of the same size, will have less lattice strain, and consequently a small deviation in lattice parameter.

4.3.3 Thermal expansion in the Mo-Nb-Ta-Ti-W system

The five-element MoNbTaTiW alloy is a well-studied composition known for its high room-temperature ductility and good strength at high temperature [279]. The thermal

expansion of MoNbTaTiW calculated in this work, both through density functional perturbation theory and from the rule of mixtures, are lower than what is previously reported, for example by previous modelling work by Bhandari *et al.* [160]. Below 500 K the rule of mixtures predicts a slightly lower thermal expansion coefficient compared to the predicted expansion profile (**Figure 52**). At these low temperatures little difference is observed between results obtained from the 16-atom supercell and 54-atom supercell.

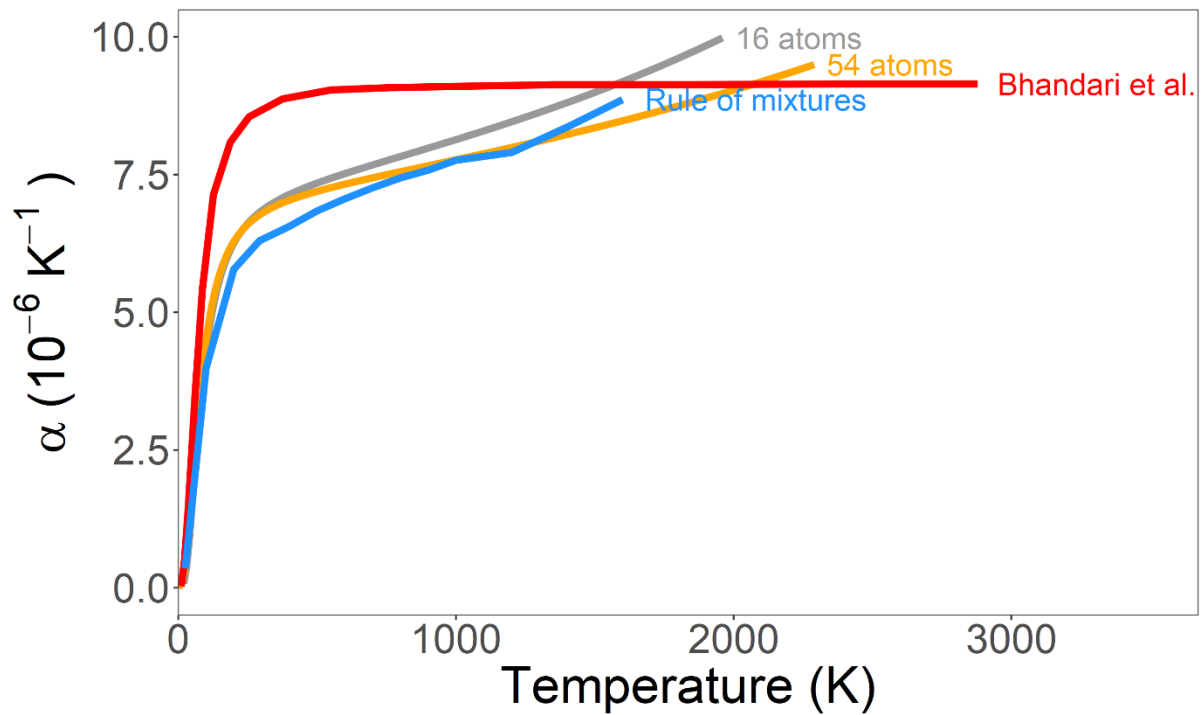


Figure 52. The linear thermal expansion profile calculated for the equiatomic MoNbTaTiW alloy, via density functional perturbation theory and the rule of mixtures using dilatometry data from [277]. Literature data from Bandari *et al.* [160]

As was observed for the quinary MoNbTaTiW alloy, below 500 K the rule of mixtures predicts a lower thermal expansion coefficient compared to the supercell approach for all the sub-quaternary alloys of the Mo-Nb-Ta-Ti-W system shown in **Figure 53**. Thermal expansion profiles calculated from 16-atom supercells and 54-atom supercells were consistent except in the case of MoNbTaTi in which the 16-atom supercell exhibited a larger thermal expansion coefficient from 100 K. Divergent inflections in thermal expansion coefficients were observed in MoNbTaW and NbTaTiW; a larger supercell exhibiting a larger α in the case of MoNbTaW, and a smaller supercell exhibiting a larger α in the case of NbTaTiW.

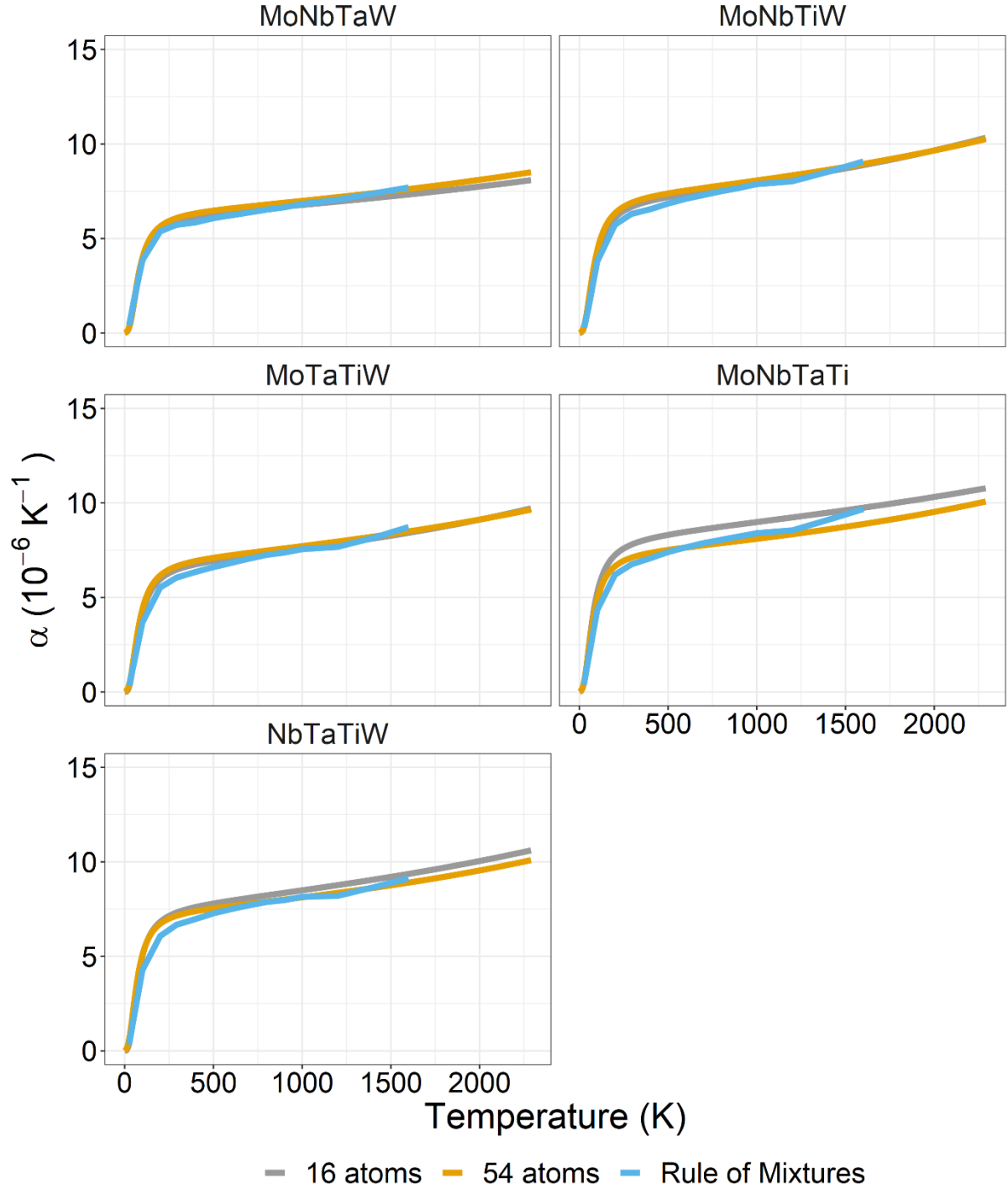


Figure 53. Linear thermal expansion profiles for equiatomic quaternary alloys of the Mo-Nb-Ta-Ti-W system. Rule of mixtures data was calculated from pure elemental data from dilatometry [277]

Little difference was observed in thermal expansion between the 16-atom supercells and 54-atom supercells (**Figure 54**). It can therefore be concluded that thermal expansion behaviour can be predicted reliably enough using smaller 16-atom supercells, and the 54-atom supercells can therefore be dropped from subsequent calculations.

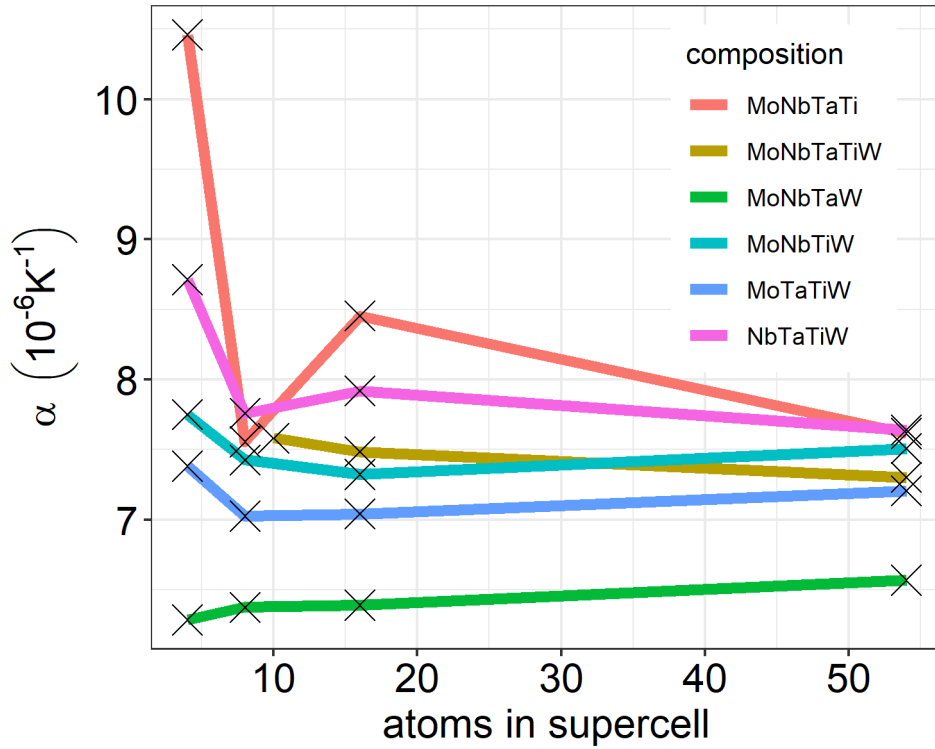


Figure 54. Thermal expansion coefficients at 580 K versus number of atoms in supercell.

Consistent prediction of thermal expansion was obtainable with the 16-atom supercells for both 5- and 4-element systems. The 54-atom supercells were therefore not considered for 3- and 2-element systems. Calculated thermal expansion profiles for the ternary alloys are shown in **Figure 55**. Excellent agreement between the rule of mixtures and 16-atom supercell calculations can be seen in the case of MoNbTa, MoTaW, and NbTaW. It is thought that this is due to the elements Mo, Nb, Ta, W being fully miscible with each other, which extends the applicability for these elements. Good agreement was also observed for the alloys MoNbW, MoTiW, NbTiW and TaTiW. The best agreement between the supercell approach and the rule of mixtures was observed at low temperatures < 100 K, with greater disagreement at temperatures > 500 K.

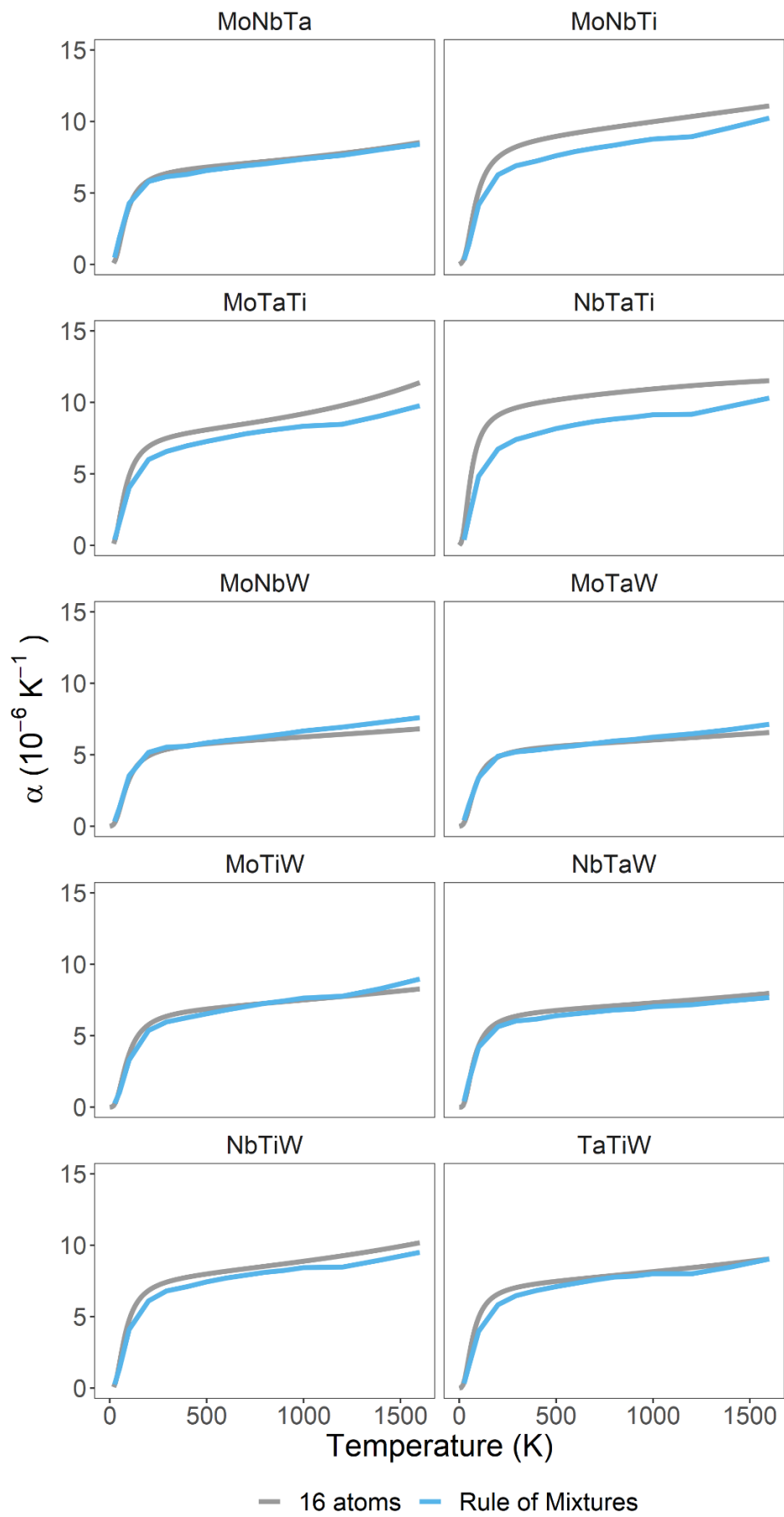


Figure 55. Linear thermal expansion profiles for equiatomic ternary alloys of the Mo-Nb-Ta-Ti-W system. Rule of mixtures data was calculated from pure elemental data from dilatometry [277].

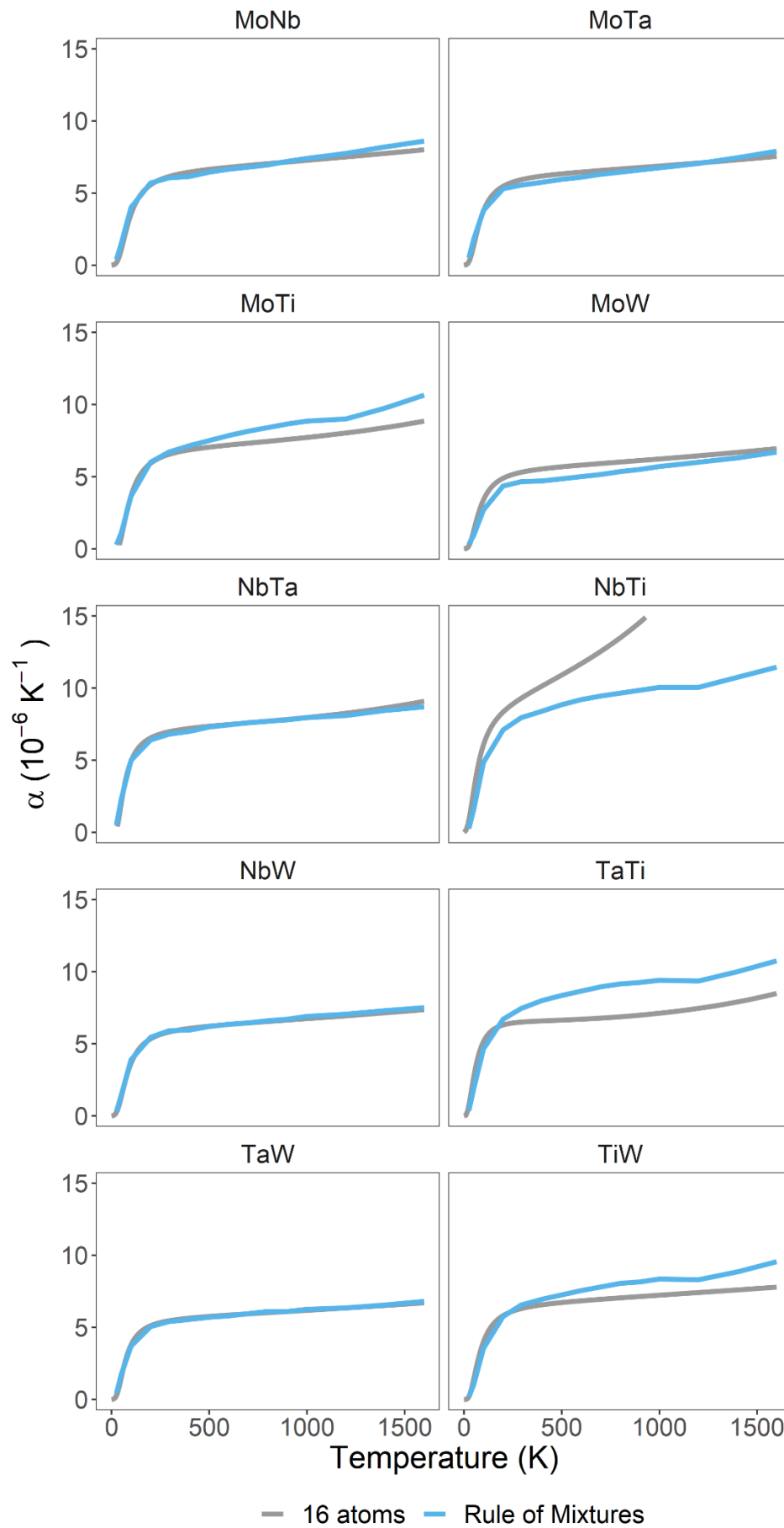


Figure 56. Linear thermal expansion profiles for equiatomic binary alloys of the Mo-Nb-Ta-Ti-W system. Rule of mixtures data was calculated from pure elemental data from dilatometry [277].

Figure 56 shows the thermal expansion profile for equiatomic binary alloys of the Mo-Nb-Ta-Ti-W system. Excellent agreement between the 16-atom supercell calculations and the rule of mixtures was observed for MoNb, MoTa, MoW, NbTa, NbW, TaW alloys. Some underprediction of the rule of mixtures at low temperatures was observed for these alloys, but the largest disagreements were seen in alloys in which Ti was a constituent, for example MoTi, NbTi, TaTi and TiW.

Figure 57 shows how the density functional perturbation theory predicted thermal expansion coefficients compared with the rule of mixtures at 300 K. A Pearson correlation coefficient of 0.85 suggests accuracy of the predictive method. These predictions however must be experimentally validated in future work.

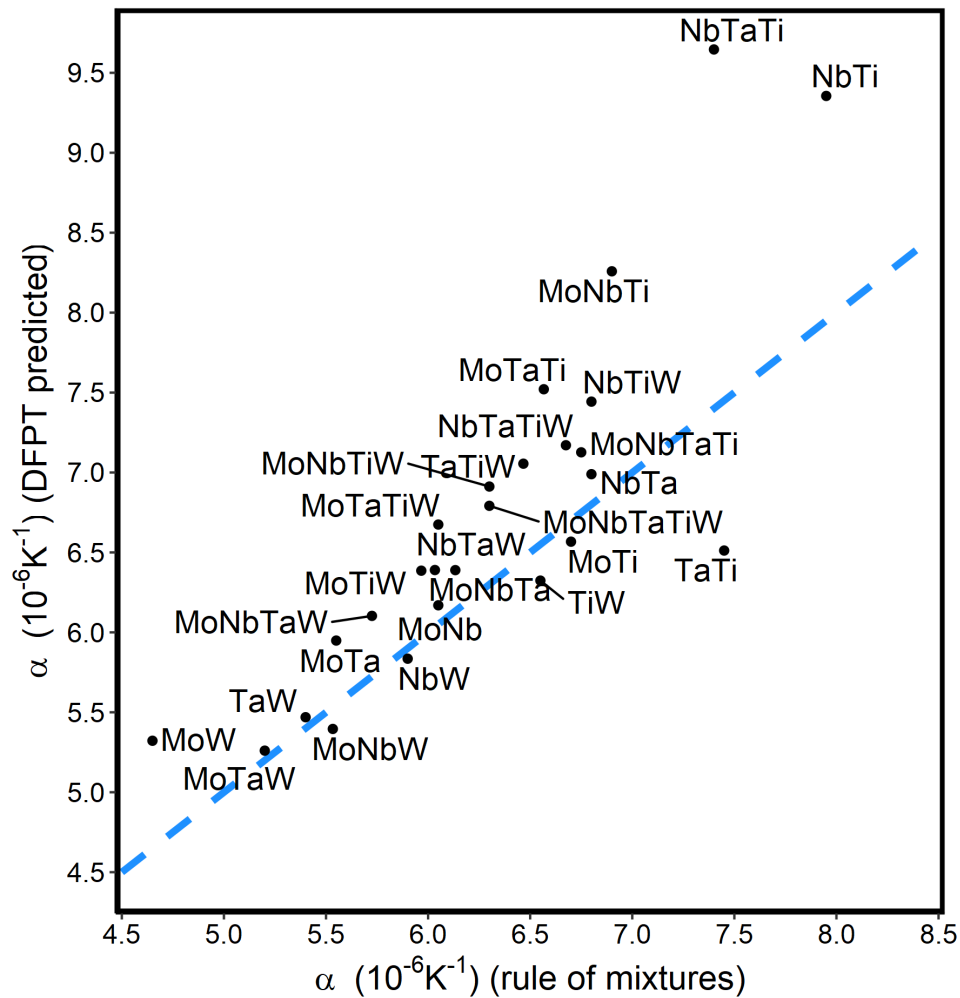


Figure 57. Predicted thermal expansion coefficients via density functional perturbation theory versus predictions by the rule of mixtures at 300 K. Pearson correlation coefficient is 0.85.

No clear correlation was observed between the standard deviation of 2nd nearest neighbour distances and mismatch in thermal expansion, predicted via the rule-of-mixtures or density functional perturbation theory at 300 K. **Figure 58** shows the enthalpy of formation calculated via density functional theory and the quasi-chemical approach based on Miedema's model [145]. It is interesting to note that the alloys whose thermal expansion coefficients substantially differ from the linear fit in **Figure 58**, TaTi, NbTi, and NbTaTi, also have positive enthalpies of formation as calculated both from density functional theory and the quasi-chemical approach.

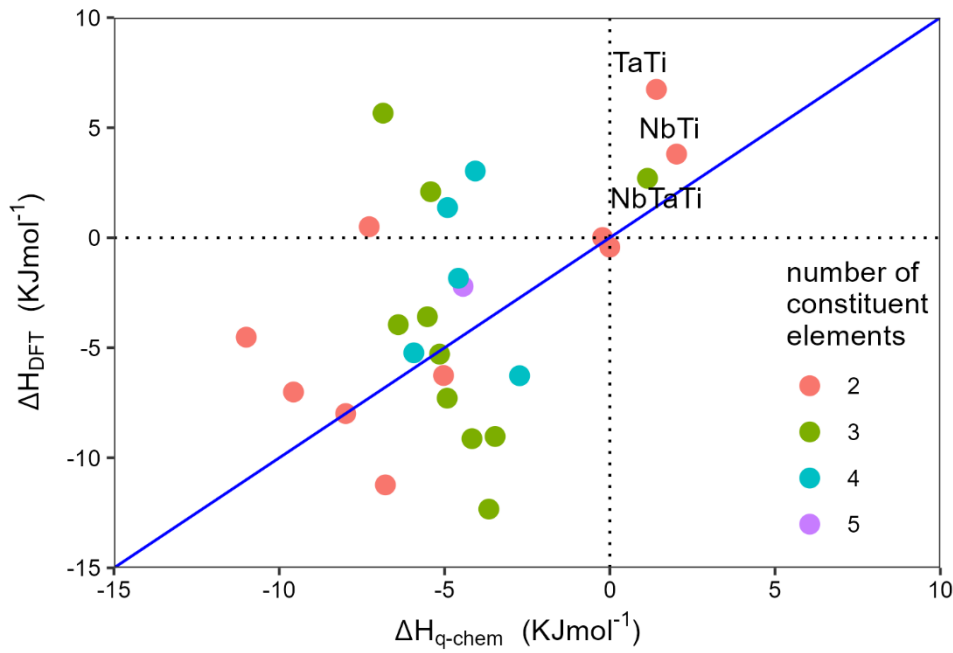


Figure 58. Mixing enthalpy for equiatomic alloys in the Mo-Nb-Ta-Ti-W system, as calculated from density functional theory and the quasi-chemical approach based on Miedema's model. Colours indicate the number of constituent elements in each alloy.

When used as coatings, interlayers, or functional materials the thermal expansion of compositionally complex alloys is a critical property. The solid solutions of these alloys can tolerate impurities or wide ranges in composition, which could unlock the ability to tailor compositionally complex alloys with respect to their thermal expansion behaviour.

Here, the first principles modelling of thermal expansion for the Mo-Nb-Ta-Ti-W system has been reported. Thermal expansion behaviour calculated via density functional perturbation theory and the quasi-harmonic approximation tends to comport with thermal expansion estimated from the rule of mixtures using experimental data. All thermal expansion

curves calculated in this study are characteristic of expected thermal expansion behaviour: the coefficient of thermal expansion rises steeply to 250 K, where the coefficient of thermal expansion plateaus in most cases to a roughly constant value. There are exceptions with this method however: problems may arise with the incorporation of elements which preferentially adopt different crystal structures in their standard states such the inclusion of both Ti (HCP) and Mo (BCC) together; and incorporation of elements which exhibit ordered magnetism such as Cr, Fe, and Mn, which are expected to affect thermal expansion behaviour. Elements which undergo phase transformations within the temperature region of interest, such as the HCP – BCC transition of Ti at 882°C, also can reduce the validity of the rule of mixtures as well as the density functional theory approach. Combinations of elements of the same crystal structure such followed the rule of mixtures well. Discrepancies occurred when combinations of different crystal structures were used. There was little difference in α between the smaller 16-atom supercells and larger 54-atom supercells, suggesting that thermal expansion can be sufficiently well predicted for concentrated solid solutions using a density functional theory approach.

The mechanism of thermal expansion in compositionally complex alloys could be a simple extension of that found in conventional alloys [252]. Recently, Laplanche *et al.* [289] reported the thermal expansion coefficients of the binary and ternary subsystems of the CrMnFeCoNi compositionally complex alloy. They found qualitative agreement in the expansion coefficients of equiatomic binary, ternary, and quaternary alloys and the result obtained using a rule of mixtures, on the constituent elements of each alloy, where X_i represents the atomic fraction of element i , α_i is the thermal expansion of the element i . However, these alloys incorporated elements which exhibit ordered magnetism, and this is expected to shift thermal expansion through the magnetostriction effect. Work by Laplanche *et al.* [289] showed that the rule of mixtures underreports the thermal expansion coefficient at low temperatures, as compared to dilatometry measurements of compositionally complex alloy specimens. It has been suggested that this underprediction is due to the constituent elements preferentially adopting different crystal structures in their pure state, however, in this study this systematic underprediction was observed clearly in MoNbTaW, MoNbTa, MoNbW, NbTaW and MoTaW alloys which all comprise elements with a shared BCC crystal structure in their pure standard states. All of these alloys exhibited the same underprediction of α at low temperatures, a similar phenomenon reported by Laplanche *et al.* [289].

More work is required to determine if these thermal expansion predictions are applicable to compositionally complex alloys tested experimentally. More theoretical investigations need to be done to determine if the same density functional theory approach can be applied to compositionally complex alloys containing elements which exhibit ordered magnetism e.g., Cr, Mn, Fe.

4.4 Summary

First principles density functional perturbation theory and the quasi-harmonic approximation have been used to predict thermal expansion behaviour of near equiatomic alloys of the Mo-Nb-Ta-Ti-W system. Results exhibit good agreement with the simple rule of mixtures.

- Thermal stability and expansion for the MoNbTaTiW compositionally complex alloy and constituent quaternary, ternary, and binary subsystems have been predicted.
- This work has shown that the rule of mixtures works as a suitable first approximation for thermal expansion behaviour in these body-centred cubic solid solutions.
- Provided a reliable method for straightforward calculation of thermal expansion using atomic scale simulation methods.

Future work should assess the impact of high temperature intrinsic defect formation on deviations in the thermal expansion. Locally ordered systems, including some based on hexagonal and cubic compositionally complex alloys [148], [308] may also show some deviation from the rule of mixtures. An experimental campaign will be initiated to experimentally verify the predictions in this work. Being able to reliably predict and match the thermal expansion of a coating, joining material or component of a system is important for a range of applications that see changes in temperature, especially in safety critical components including aerospace and nuclear applications.

4.5 Further considerations

4.5.1 Composite science

There may be scope to improve upon the prediction of the rule of mixtures by borrowing concepts from composite science. Some in-built assumptions of the rule of mixtures [309] are that:

- The sample is fully dense.
- Stress is homogenous all over (thermal expansion of the constituent particles/matrix is the same, and the modulus of elasticity of the components is same).
- Linear thermal expansion of composites is given by the rule of mixtures, a volume-weighted sum of matrix, m, and reinforcement, p:

$$\alpha_c = \alpha_p V_p + \alpha_m V_m \quad (40)$$

where α_c is the linear expansion coefficient of the composite, α_p and α_m are the linear expansion coefficients of the reinforcement and matrix, respectively. V_p and V_m are the volume fractions of p and m, respectively. The most straightforward application of the rule of mixtures as it relates to thermal expansion properties of compositionally complex alloys is as follows:

$$\alpha_{alloy} = \sum_i^j \alpha_i V_i \quad (41)$$

where α_{alloy} is the coefficient of thermal expansion for the alloy; V is the volume fraction of element i ; and i runs through all constituent elements. However, there may be improvements to be made on the initial first approximation, such as considering elastic moduli of the constituent elements. If a compositionally complex alloy could be approximated as a composite of its constituent elements, then adaptations developed from composite science may be appropriate. The following equations have been adapted from Ashby *et al.* [309] and are presented without further validation.

The Turner equation (**Equation 42**), for example, considers the contribution of elastic moduli on thermal expansion:

$$\alpha_{alloy} = \frac{\sum_i^j \alpha_i V_i \left(\frac{K_i}{\rho_i} \right)}{\sum_i^j V_i \left(\frac{K_i}{\rho_i} \right)} \quad (42)$$

where α is the coefficient of thermal expansion; K_i is bulk modulus of element i ; ρ_i is density of element i , and i runs through all constituent elements. Further, from composite science, equations have developed which consider the shape and size of filler material. Of these, the Kerner equation (**Equation 43**) is perhaps the least applicable model when applied to concentrated solid solutions. This is because there is no meaningful distinction between matrix and filler material. In this model the shape of the filler is considered. The initial approximation

as it relates to composites, is that the constituents are in the form of spherical grains and uniformly dispersed in the matrix. In this formulation, the shear strain and isostatic stress contributions have been considered.

$$\alpha_{\text{alloy}} = \sum_i^j \alpha_i V_i + \frac{\sum_i \sum_{j>i} V_i V_j (\alpha_i - \alpha_j)(K_i - K_j)}{V_i K_i + V_j K_j + \left(\frac{3K_i K_j}{4G_m}\right)} \quad (43)$$

where G_m was originally the shear modulus of the matrix. It is thought that the shear modulus of a concentrated solid solution alloy can be approximated by taking a weighted average of the shear moduli of the constituent elements [194]. These equations were tested on an equiatomic alloy MoNbTaTiW and there was noticeable difference between the thermal expansion profiles calculated (**Figure 59**).

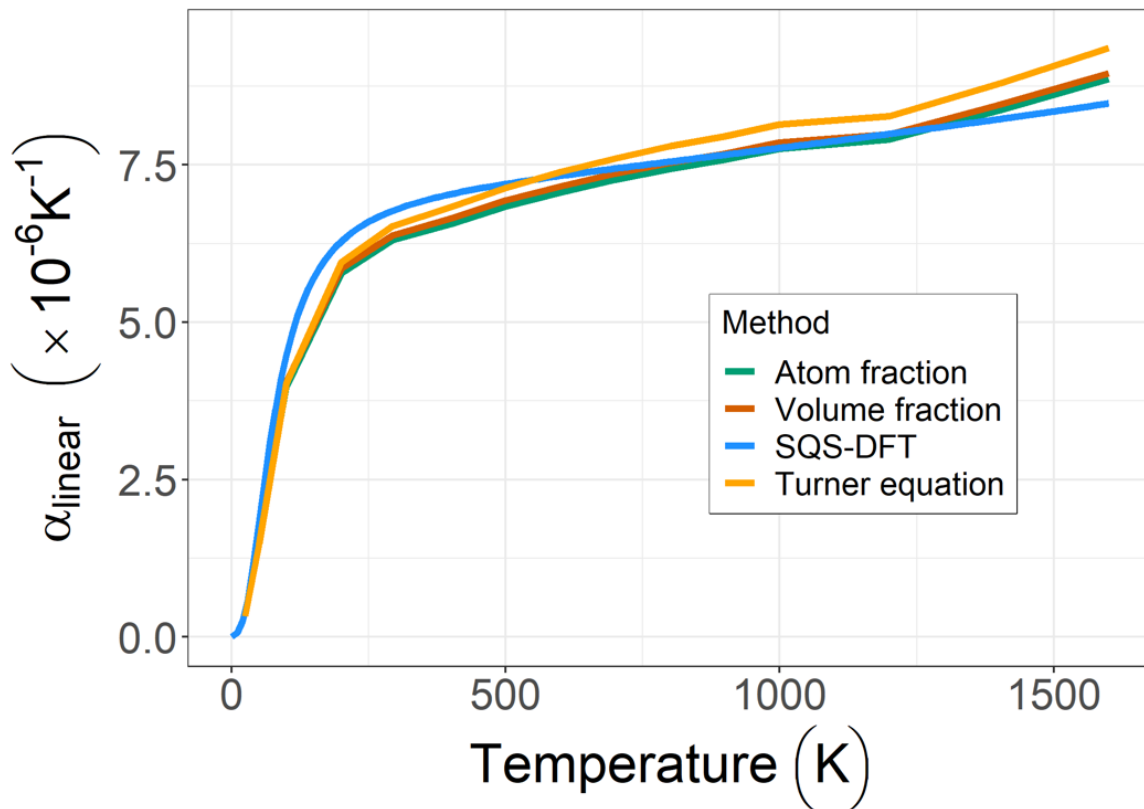


Figure 59. Comparison between methods of estimating thermal expansion of the MoNbTaTiW concentrated solid solution from thermal expansion profiles of the pure constituent metals, data from Touloukian *et al.* [277].

4.5.2 Effect of vacancy concentration on thermal expansion

Thermal expansion profiles are affected also by vacancies and other defects present within the crystal. To understand this, first imagine a simple cubic lattice of atoms within a crystal structure. Suppose that a single atom is removed from the centre and moves to the outer surface of the crystal. This alters the overall volume of the crystal. When an atom is added to the surface of the crystal, the crystal length has increased by the length of that single atom. It follows, therefore, that when we create vacancies in crystal structures, the length of the crystal increases by a third of the total volume change, since we have a choice of 3 planes on which to move the liberated atom.

Since vacancy population is something that is thermally activated, and it also affects the volume of the crystal structure, it follows that it should be incorporated into thermal expansion behaviour. It therefore should be added as an additional contribution to the thermal expansion profile. This type of thermal expansion is ignored by computational techniques such as density functional perturbation theory, or experimental techniques such as X-ray diffraction, but can be measured in dilatometry techniques. In concentrated solid solutions, known for their increased configurational entropy, it is speculated that their vacancies also carry large amounts of configurational entropy, which could stabilise a greater number of vacancies at a given temperature [310].

Vacancy populations can also be determined experimentally without sophisticated techniques such as positron annihilation spectroscopy by using heated stage X-ray diffraction, which measures lattice thermal expansion, and a dilatometry technique which incorporates the additional expansion caused by vacancy populations, the difference in thermal expansion between these techniques can be correlated to provide a measure of the equilibrium vacancy concentration. Similar work was conducted on Al-Cu alloys by King *et al.* [311].

4.5.3 Implications for an interlayer

The interlayered coating can be graduated using state-of-the-art techniques like functional grading. The interlayer material's thermal expansion properties can be tailored through their thickness so that no significant thermal expansion mismatch is visible throughout. This will undoubtedly be difficult because this only applies to static systems which do not evolve with time. The conditions in a nuclear reactor will be dynamic; solid-state diffusion is still possible, and any undesired changes to the coating, such as the formation of new

intermetallic compounds, could significantly alter any custom thermal expansion properties designed into the coating system. **Figure 60** illustrates the predicted thermal expansion behaviour of a prototype MoNbTaTiW alloy, Cr, and Zr.

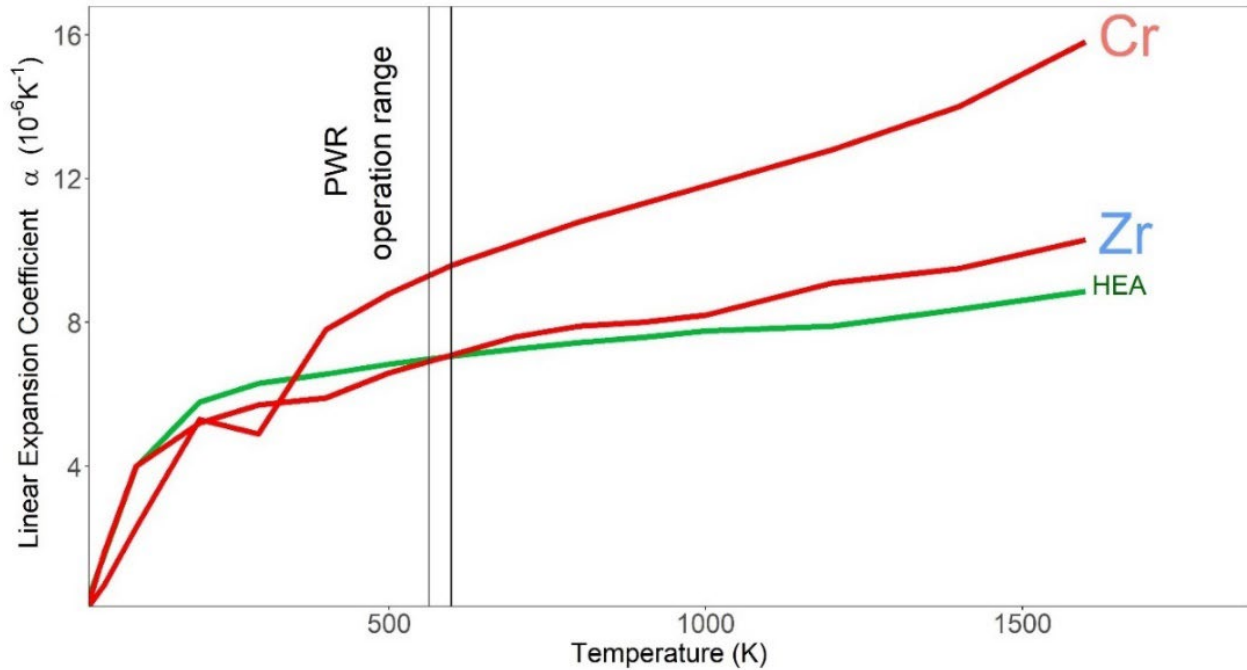


Figure 60. MoNbTaTiW thermal expansion profile as an interlayer between Zr and Cr. All data calculated from literature data [277] obtained via dilatometry. Vertical lines indicate typical pressurised water reactor coolant temperature.

4.5.4 Future work

Potential for future work on the thermal expansion of compositionally complex alloys, as recommended by the author, are summarised as follows:

- The phase equilibria of the compositionally complex alloys in this study should be first investigated to identify stable solid solutions and aid manufacture.
- Those alloys which are stable solid solutions at room temperature should be manufactured using arc melting or similar technique, homogenised and quenched.
- The thermal expansion should then be probed via heated stage X-ray diffraction and optical dilatometry.

The thermal expansion properties of these compositionally complex alloys have been investigated theoretically from a first-principles perspective. Many phenomena, however, uncaptured by density functional theory techniques should also be considered. These include

phase equilibria, second-phase precipitation, intermetallic formation, miscibility gaps, vacancy contribution and the potentially emphasised role of configurational entropy. It is for these reasons the validity of these theoretical predictions must be proven or refuted experimentally. A potential route to achieve this is to identify the stable solid solutions of the present alloys, using CALPHAD techniques, the parametric approach, density functional theory, and experimental techniques such as X-ray diffraction, scanning electron microscopy with energy-dispersive spectroscopy. The stable solid solutions can then be manufactured using a confirmed successful technique to produce refractory compositionally complex alloys, such as arc melting, and the alloys homogenised isothermally with reasonable homogenisation parameters (the author recommends 1400 – 1500°C for a few days up to a week). The resulting alloys should be characterised fully, using a range of techniques including X-ray diffraction (for crystallographic structure), optical and scanning electron microscopy (for phase analysis), X-ray fluorescence (for composition analysis), and differential scanning calorimetry (to identify any precipitation temperatures). The thermal expansion of the stable alloys is then to be investigated using a mixture of techniques; heated-stage X-ray diffraction can probe lattice thermal expansion, and optical dilatometry can be used to study bulk thermal expansion. The comparison of these techniques may be used to suggest the effect of vacancies and defects on the bulk thermal expansion of refractory compositionally complex alloys.

Chapter 5. Vacancy defects in compositionally complex alloys

A paper based upon this chapter has been submitted to a peer reviewed journal.

This chapter investigates vacancy defects in quinary alloys in the Hf-Mo-Nb-Ta-Ti-W-Zr system. Formation enthalpies of monovacancies are calculated via density functional theory and presented for all quinary alloys. It is shown that the equilibrium concentration of vacancies in these disordered systems is greater than in pure metals or dilute alloys. Furthermore, a fundamental mechanism for this is presented which may generalise to all concentrated solid solutions.

5.1 Definitions

5.1.1 Vacancy defects

Compositionally complex alloys could be used as high temperature materials in the nuclear industry. One such promising property of the body-centred cubic refractory class of these alloys could improve on the radiation resistance of conventional alloys as well as mitigate ingress of corrosive/impurity species (e.g., from the substrate or coating). To properly assess these claims requires knowledge of the distribution and migration of point defects such as vacancies, caused by high-energy ion bombardment, as well as under equilibrium conditions.

A vacancy is a space in the crystal lattice where an atom would ordinarily occupy. **Figure 61a** depicts a metal lattice with two vacancies. The presence of vacancy defects in materials affects qualities like strength, as well as the crystal's diffusion behaviour – as most diffusion events in metals are vacancy mediated. **Figure 61b** depicts two vacancies in the lattice of a compositionally complicated alloy.

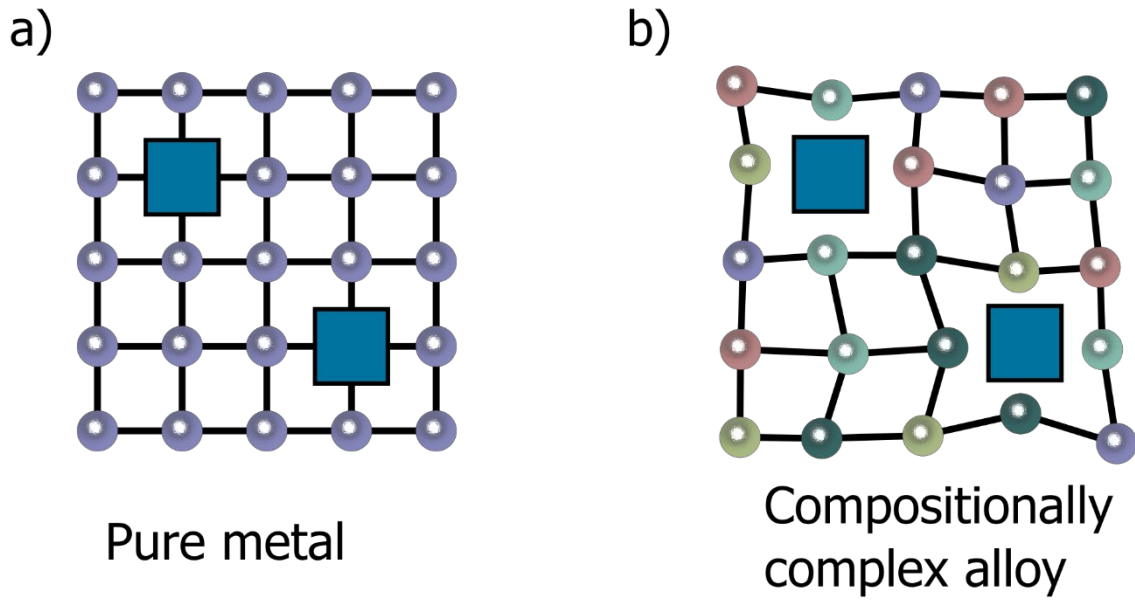


Figure 61. Vacancy defects in a) pure metal and b) a compositionally complex alloy.

Experimental research on vacancy formation relies mainly on positron annihilation lifetime spectroscopy [129], [312] and tracer diffusion experiments [313], but these are expensive, time-consuming, and difficult to interpret. Fortunately, recent advances have enabled the study of vacancy formation in alloys via tools such as density functional theory [314], [315], molecular dynamics [316], and machine learning models [317].

Tungsten is a prime candidate for plasma facing materials (PFMs) in fusion reactors. This is because of tungsten's high melting temperature of 3422°C, high thermal conductivity, low tritium retention, and low sputtering rates in plasma. However, high brittle-to-ductile transition temperatures, low fracture toughness, and nanoscale bubble formation during He ion irradiation [318] all need addressing in this application. An alternative is to use tungsten as a component in a compositionally complex alloy, with a tailored radiation response.

5.1.2 Equilibrium vacancy concentration

The equilibrium vacancy concentration for a pure material can be derived in the following manner. The rates of thermally activated processes such as vacancy formation are described by the Arrhenius equation:

$$K = Ae^{-\left(\frac{E_a}{k_B T}\right)} \quad (44)$$

where K is the process rate constant, A is the pre-exponential factor or jump frequency, E_a is the activation energy (eV), k_B is the Boltzmann constant (eVK⁻¹), and T is the temperature (K). The rates to form a vacancy and annihilate a vacancy can both be modelled respectively as **Equation 45** and **Equation 46**, respectively:

$$K_1 = A_1 e^{-\left(\frac{E_{a1}}{k_B T}\right)} \quad (45)$$

$$K_2 = A_2 e^{-\left(\frac{E_{a2}}{k_B T}\right)} \quad (46)$$

Let N be the number of sites at which a vacancy can form. Similarly, let N_v be the number of lattice sites at which a vacancy can annihilate. The fluxes of both processes, j , can then be written as the product of the number of available sites and the rate at which the process occurs:

$$j_1 = NK_1 \quad (47)$$

$$j_2 = N_v K_2 \quad (48)$$

The system is in equilibrium, which means that the number of vacancies does not change i.e., $j_1 = j_2$. **Equations 47** and **48** are therefore equal and can be conjoined:

$$NK_1 = N_v K_2 \quad (49)$$

From this we can obtain an expression for the equilibrium vacancy concentration in terms of rate constants K_1 and K_2 :

$$\frac{N_v}{N} = \frac{K_1}{K_2} \quad (50)$$

Because $N \gg N_v$, we can approximate N as the number of lattice sites on the lattice. Inserting the equation above into the full Arrhenius equation gives:

$$\frac{N_v}{N} = \left(\frac{A_1}{A_2}\right) e^{-\left(\frac{E_{a1}-E_{a2}}{k_B T}\right)} \quad (51)$$

If the pre-exponential factors, A_1 and A_2 , are equal, and representing the difference between E_{a1} and E_{a2} as the vacancy formation enthalpy, H_f^v , gives:

$$\chi_v = \frac{N_v}{N} = e^{\frac{-H_f^v}{k_B T}} \quad (52)$$

Where χ_v is the equilibrium concentration of vacancies. From **equation 52** the vacancy fraction within a set of lattice sites at a given vacancy formation enthalpy and at a given temperature can be approximated. **Figure 62** shows the vacancy fraction versus temperature for a range of vacancy formation enthalpy values calculated from **equation 52**.

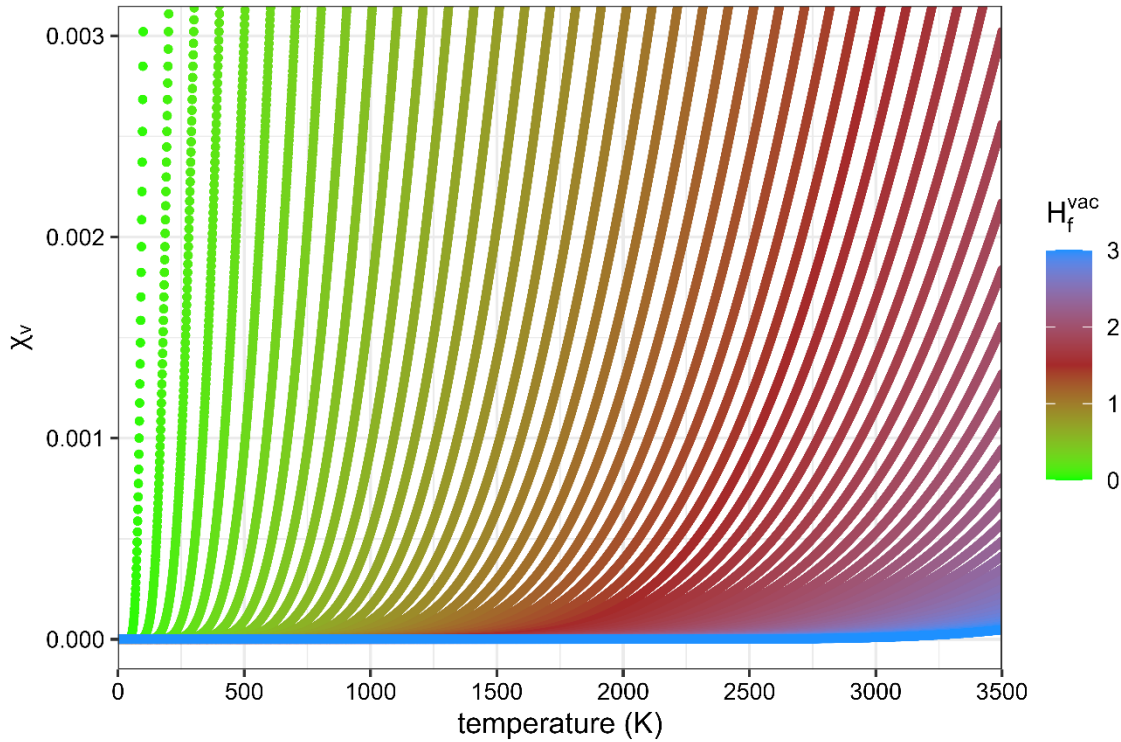


Figure 62. Equilibrium vacancy fraction versus temperature for a range of values of H_f^v .

The vacancy population versus temperature plot is often conveniently plotted as $\ln(\chi_v)$ versus $\frac{1}{T}$. This produces a straight line with gradient, $-H_f^v$. **Figure 63** shows this model:

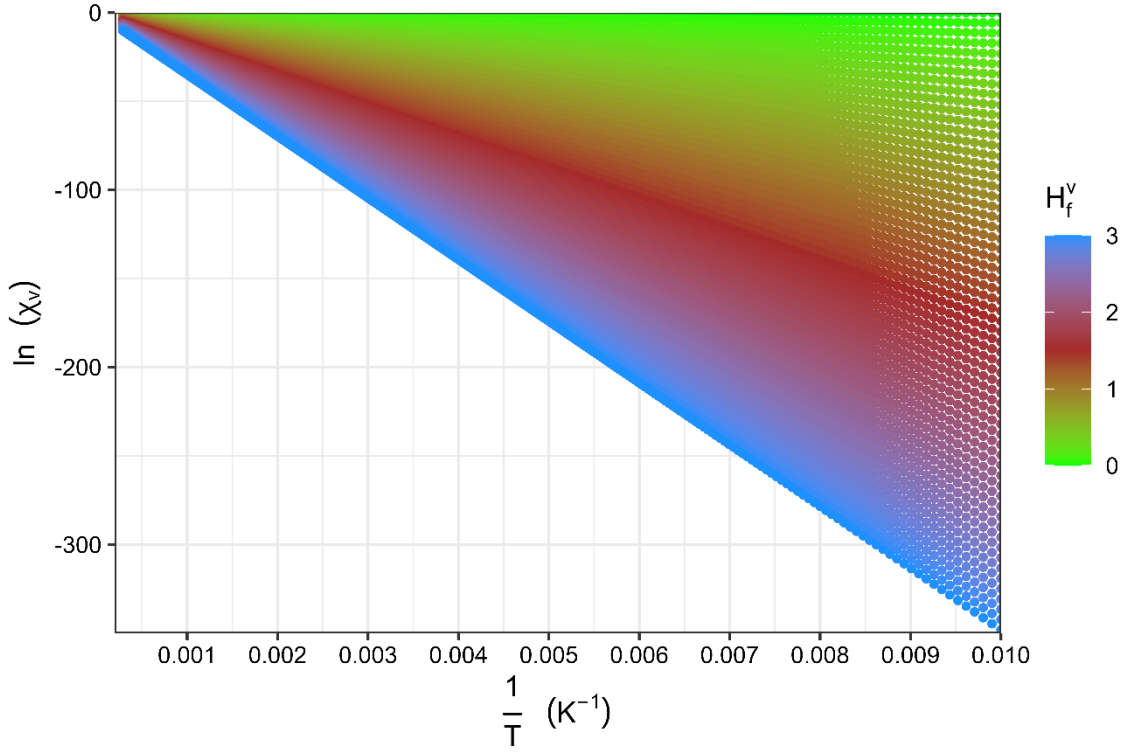


Figure 63. Arrhenius plot of the equilibrium vacancy concentration versus reciprocal temperature.

Figure 62 and **Figure 63** show the relationship between H_f^v and the equilibrium concentration of vacancies in pure metals and dilute alloys. The role of configurational entropy has not been considered in this analysis and may significantly affect the equilibrium concentration of vacancies in concentrated solid solutions. The next section considers how configurational entropy of monovacancies influence vacancy populations.

5.1.3 Role of configurational entropy

Wang *et al.* sought to incorporate the effect of configurational entropy into the calculation for equilibrium vacancy concentration for complex alloys [310]. According to Wang *et al.*, the equilibrium vacancy concentration is calculated as:

$$\frac{N_v}{N} = \frac{e^{n-1-\frac{H_f^{vac}}{k_B T}}}{n + e^{n-1-\frac{H_f^{vac}}{k_B T}}} \quad (53)$$

where n is the number of elements in the alloy. According to this model, the equilibrium vacancy concentration is not just a function of the vacancy formation enthalpy and the temperature but is also a function of the configurational entropy (represented by alloying number, n). The increase of equilibrium concentration can be plotted against alloying number if we assume that H_f^V remains invariant with alloying number (**Figure 64**).

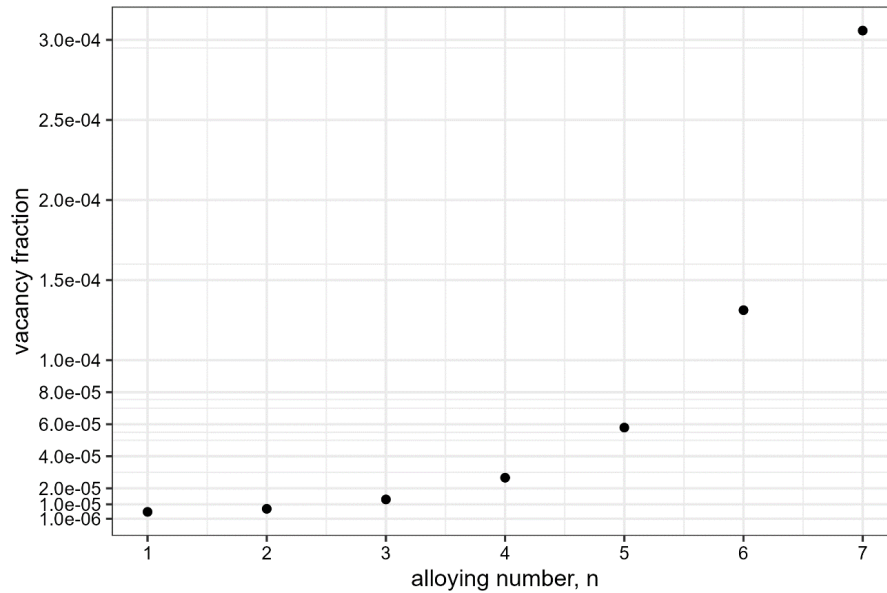


Figure 64. Equilibrium fraction of vacancies versus alloying number, n . $H_f^V = 3.14$ eV; $T = 3000$ K.

Equation 53 implies a vast increase in vacancy population with increasing alloying number. This would explain some positron annihilation spectroscopy results. Although **Equation 53** has been used to calculate equilibrium vacancy concentration by other authors [319]–[321], it has since been disputed by Daigle *et al.* [256]. The configurational entropy for vacancies in disordered compositionally complex alloys was sought to be derived for this reason. Beginning from the Gibbs energy to form a vacancy:

$$\Delta G = \Delta H - T\Delta S \quad (16)$$

where ΔG is the Gibbs free energy to form a vacancy, ΔH is the associated enthalpy of formation for a vacancy and is assumed to be invariant with temperature, ΔS is the entropy of a vacancy, which is assumed to be dominated by the configurational entropy. All units of energy are in electron volts. The configurational entropy is given by Boltzmann's famous equation, $S_{\text{conf}} = k_B \ln(\Omega)$. Here, k_B is the Boltzmann constant (eV K^{-1}) and Ω is the possible number of

microstates in the system. The number of possible microstates for an m -element alloy with vacancies is given by

$$S = k_B \ln \left[\frac{N!}{N_A! N_B! N_C! N_D! N_E! \dots n!} \right] \quad (54)$$

where N is the total number of atoms in the system, N_{A-E} is the number of atoms of element $A-E$, respectively, and n is the number of vacancies in the alloy. Assuming that the alloy is equiatomic (i.e., $N_A! = N_B! = N_C! = N_D! = N_E! = N_i!$)

$$S = k_B \ln \left[\frac{N!}{m(N_i!)n!} \right] \quad (55)$$

where m is the alloying number, and N_i is the number of atoms of each element in the system. N_i can be expressed in terms of N , n , and m : $N_i = \frac{N-n}{m}$. Substituting into **equation 55**:

$$S = k_B \ln \left[\frac{N!}{m \left(\frac{N-n}{m} \right)! n!} \right] \quad (56)$$

and applying Stirling's approximation, which states that $\ln(x!) \approx x \ln(x)$

$$S = k_B \left[\frac{N \ln(N)}{m \left(\frac{N-n}{m} \right) \ln \left(\frac{N-n}{m} \right) n \ln(n)} \right] \quad (57)$$

simplifies to

$$S = k_B \left[\frac{N \ln(N)}{(N-n) \ln \left(\frac{N-n}{m} \right) n \ln(n)} \right] \quad (58)$$

Re-written using the rule of logs:

$$S = k_B \left[N \ln(N) - (N-n) \ln \left(\frac{N-n}{m} \right) - n \ln(n) \right] \quad (59)$$

The configurational entropy is given by the differential with respect to n .

$$\Delta S = k_B \left[\ln \left(\frac{N-n}{m} \right) - \ln(n) \right] \quad (60)$$

which reduces to

$$\Delta S = k_B \left[\ln \left(\frac{N-n}{mn} \right) \right] \quad (61)$$

Assuming that n is small, i.e., $N - n \approx N$, and inversing the natural log

$$\Delta S = -k_B \ln \left(\frac{mn}{N} \right) \quad (62)$$

The Gibbs energy change with respect to n is therefore given by

$$\Delta G = \Delta H + k_B T \ln \left(\frac{mn}{N} \right) \quad (63)$$

Rearranging for vacancy concentration, $\frac{n}{N}$,

$$\chi_v = \frac{n}{N} = \frac{1}{m} e^{\frac{-\Delta H}{k_B T}} \quad (64)$$

This result directly contradicts the result of **equation 53** from Wang *et al.* [149], implying that the configurational entropy of a monovacancy decreases with increasing alloying number. This result makes sense when the configurational entropy of monovacancies is considered in the $m + 1$ model, which treats a monovacancy in high entropy alloys as a new species. For example, a monovacancy in a binary alloy can be treated as a third species (i.e., $m = 3$). The change in configurational entropy is defined as $\Delta S_{\text{conf}} = \frac{\delta S}{\delta n}$, which, at the dilute limit, is taken to be the gradient of the entropy curves in **Figure 65** as the composition of vacancies, x , approaches 0.

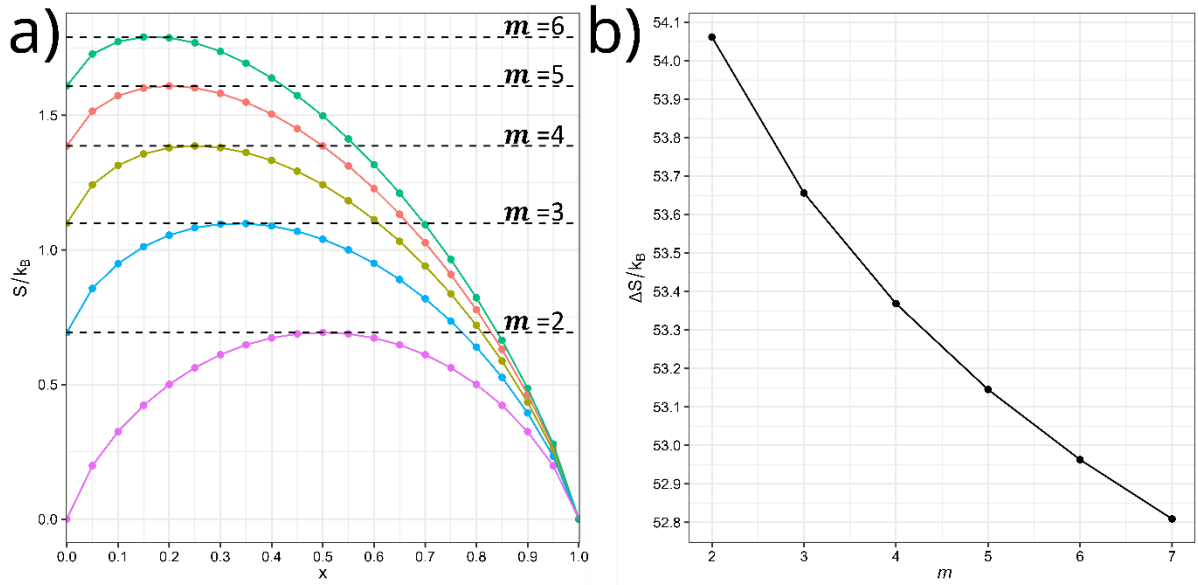


Figure 65. Configurational entropy in the $m + 1$ scheme. Where x is the mol% of an element in an alloy, m is the alloying number, and k_B is the Boltzmann constant; a) configurational entropy for alloys up to the senary alloy; b) configurational entropy of an added vacancy to an equiatomic m -element alloy.

5.2. Assessing vacancies in refractory compositionally complex alloys

Many previous studies on vacancy formation enthalpies of compositionally complex alloys have focussed on the Cantor alloy [322] and derivative alloys thereof [100], [129], [130], [255], [315], [323]–[325]. Although studies on some refractory alloys [314], [326]–[328] do exist. For example, Cunliffe *et al.* proposed a method to easily calculate the vacancy formation enthalpy in multi-component amorphous alloys, including refractory alloys, which involves averaging the vacancy formation enthalpy of the respective pure metals [328]. Roy *et al.* determined the vacancy formation energy of $(\text{Mo}_{0.95}\text{W}_{0.05})_{0.85}\text{Ta}_{0.10}(\text{TiZr})_{0.05}$ via density functional theory to be between 2.87 – 3.84 eV [326]. Zhang *et al.* investigated vacancy energetics in the Al-Hf-Sc-Ti-Zr system, including the binary to quaternary alloys [314]. From this they calculated the temperature dependence of the Gibbs energy of vacancy formation. Zhao *et al.* determined the vacancy formation enthalpy of VTaCrW to be between 2.45 – 3.94 eV, with a mean value of 3.18 eV [329]. The literature however remains sparse on thorough interrogations of vacancy formation enthalpies and their subsequent equilibrium populations in refractory compositionally complex alloys.

The equilibrium vacancy concentration in a range of refractory concentrated solid solutions was sought to be predicted with **Equation 64**, with the enthalpy of vacancy formation being calculated in the density functional theory technique. This was done similarly to **Chapter 4**, utilising special quasi-random structures constructed using the *mcsqs* code in the Alloy Theoretic Automated Toolkit [264]. Cut-off distances were set to include up to third nearest neighbour pair interactions, with triplet and higher-order interactions not considered.

Density functional theory [293], [294] structural relaxation calculations at constant pressure were based on the plane wave pseudopotential approach as implemented in the Vienna *ab initio* simulation package VASP [265], [296] version 5.4.4. Projector augmented-wave (PAW) pseudopotentials are used [295], [330]. There are 12, 12, 13, 14, 10, 11, and 12 electrons treated as valence for elements Ti, Zr, Nb, Mo, Hf, Ta, and W, respectively. The Perdew, Burke, and Ernzerhof version of the generalised gradient approximation exchange-correlation functional was applied [297]. Cut-off energy for plane waves were set to 500 eV for all calculations. A Methfessel-Paxton smearing width of 2 eV was used [298]. A K-point mesh was selected based on convergence of the total energy to 0.01 eV/atom which resulted in a $4 \times 4 \times 4$ Γ -centred mesh for all cells.

5.2.1 Convergence testing

Figure 66 and **Figure 67** are shown with the convergence testing for plane wave cut-off energies and K-points, respectively. A selection of cut-off values was made such that the resulting total energy was not changed by more than 0.01 % with an increase in value.

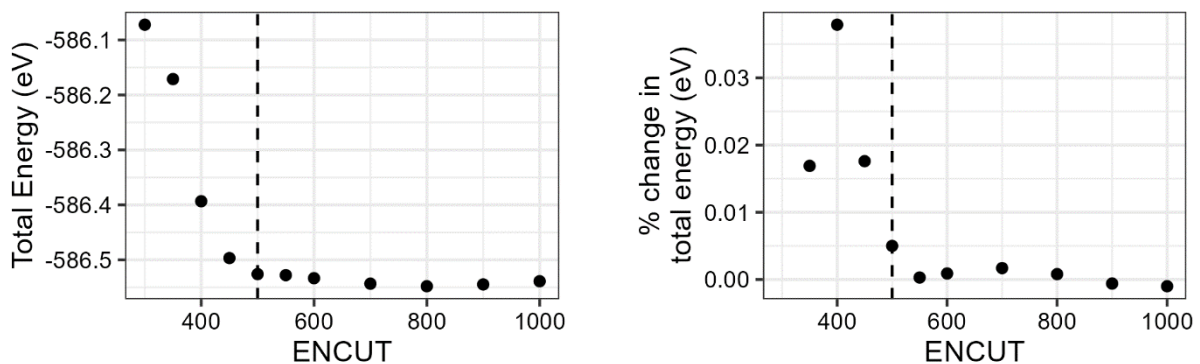


Figure 66. Plane wave cut-off energy convergence testing (ENCUT). Convergence testing for plane wave cut-off energy values for a 54-atom body-centred $\text{Mo}_{11}\text{Nb}_{11}\text{Ta}_{11}\text{Ti}_{10}\text{W}_{11}$ supercell. A cut-off energy (dashed vertical line) was chosen for which an increase of 50 eV resulted in

less than 0.01 % change in total energy. **(Left)** Total energy plotted against cut-off energy value. **(Right)** Percentage change in total energy plotted against cut-off energy.

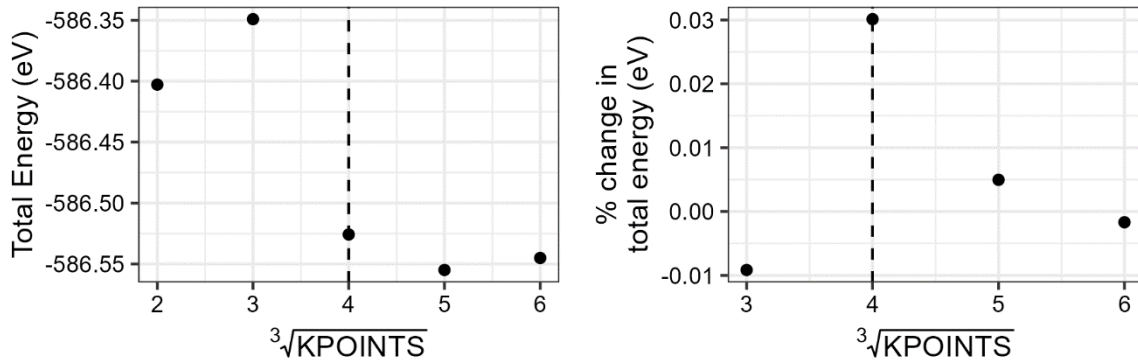


Figure 67. K-point convergence testing. Convergence testing for number of K-points of a 54-atom body-centred $\text{Mo}_{11}\text{Nb}_{11}\text{Ta}_{11}\text{Ti}_{10}\text{W}_{11}$ supercell. A K-points set (dashed vertical line) was chosen for which a further increase of K-points resulted in less than 0.01 % change in total energy. **(Left)** Total energy plotted against number of K-points. **(Right)** Percentage change in total energy plotted against number of K-points.

5.2.2 Calculating local bias

A measure for the bias of the immediate environment of a vacancy towards particular elements has been adopted using nomenclature from Li *et al.* [325]. As an example, a vacancy in a body-centred cubic lattice surrounded by 8 atoms of elements A, B, C, D and E, a measure of (2,2,2,1,1), respectively, would indicate a relatively unbiased arrangement. A measure of (5,3,0,0,0) indicates a biased local arrangement, and a measure of (8,0,0,0,0) indicates that all local atoms within an appropriate cut off distance are of a single element, A. From this notation, an overall measure of local element bias for a vacancy is calculated via

$$\text{local element bias} = \sqrt{\frac{1}{N} \sum_{i=\text{element A}}^E (j_i - nx_i)^2} \quad (65)$$

where N is the total number of elements in the alloy, n is the coordination number (8 for body-centred cubic, 12 for face-centred cubic and hexagonal close-packed), x_i is the atomic fraction of element i , j is the number atoms of each element, A to E, surrounding a vacancy, and

Equation 65 resembles that of the root-mean-square deviation. For the previous examples, (2,2,2,1,1), (5,3,0,0,0), and (8,0,0,0,0), local element biases of 1.04, 3.46, and 4.29 are obtained, respectively, with more examples listed in **Table 7**. Each alloy is assumed to be completely equiatomic among constituent elements in **Equation 65** and has negligible effect on the biases calculated (**Figure 68**).

Table 7. Example calculations of local element bias. Local element biases calculated around vacancy defects in equiatomic quinary body-centred cubic alloys via **Equation 64**. Local element bias calculated independent to the chemistry of each element. Local element bias increases monotonically with bias.

Number of each element A–E					Local element bias
A	B	C	D	E	
2	2	2	1	1	1.04
2	2	2	2	0	1.75
3	2	2	1	0	1.91
3	3	1	1	0	2.37
3	3	2	0	0	2.76
4	3	1	0	0	2.93
4	4	0	0	0	3.82
5	3	0	0	0	3.46
6	2	0	0	0	3.42
7	1	0	0	0	3.72
8	0	0	0	0	4.29

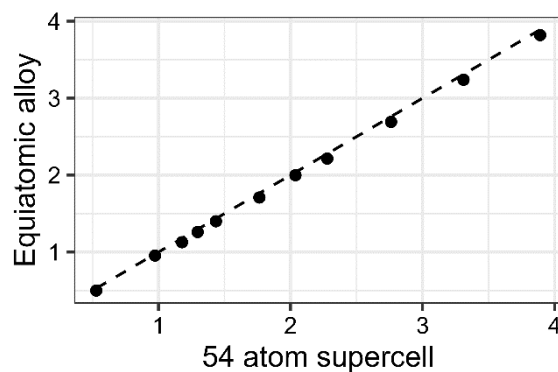


Figure 68. Effect of the equiatomic approximation in calculating local element bias. The coefficient of determination, $R^2 = 1.00$. Local element bias is calculated using **Equation 65** on a range of local vacancy environments listed in **Table 7** for an equiatomic quinary alloy and a 54-atom supercell (comprising elements A–E; A–D: 11 atoms and E: 10 atoms). A dashed line indicates the function $y = x$.

5.2.3 Calculating vacancy volumes

Vacancy volume is calculated by calculating the volume of the convex hull constructed between coordinates of the nearest neighbour atoms to the vacancy chosen with a cut off distance of 2.75 Å to include first nearest neighbours but exclude second and further nearest neighbours. The position of the vacancy is taken to be the coordinate of the atom removed in the relaxed structure. Therefore, this method could incorrectly assign the position of the vacancy in some structures where the vacancy has migrated away from its original position, as has been observed in previous work [261]. Nevertheless, this method was used to estimate the defect volume in this study. **Figure 69a** illustrates a body-centred cubic 53-atom cell with a vacancy. **Figure 69b** indicates the cut off radius around the vacancy used to calculate the vacancy volume. However, in some alloys with large lattice strain some 9 or so neighbours can exist within the cut off distance. Due to the small number of these occurrences, all these atoms are treated as 1st nearest neighbours similar to previous work [317] for calculations involving local bias or vacancy volume.

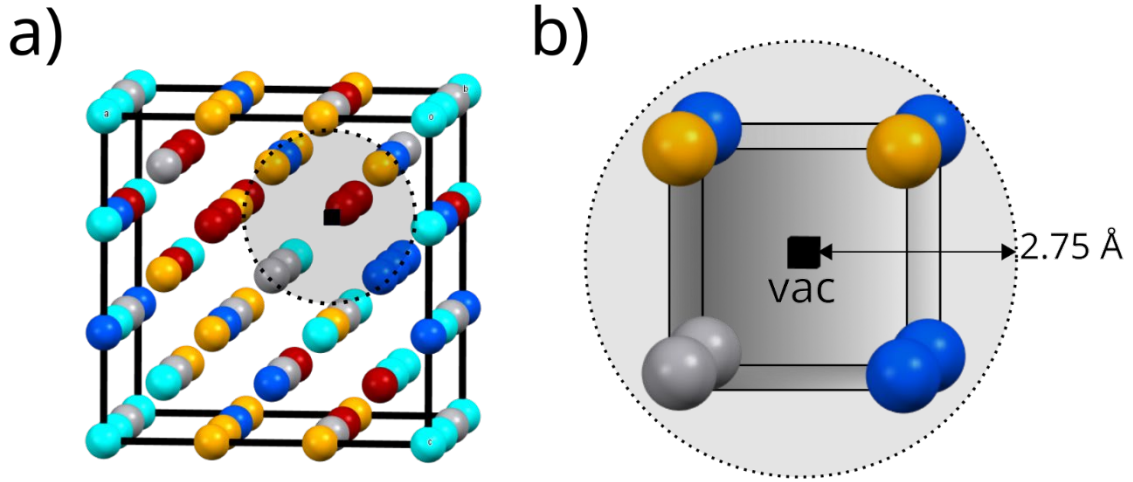


Figure 69. Vacancy volume of body-centred cubic supercells. a) vacancy within a body-centred cubic supercell, and b) atoms within the cut off radius used to calculate vacancy volume.

5.2.4 Vacancy formation enthalpy calculations

Vacancy formation enthalpies were calculated by structurally relaxing each 54-atom supercell at constant pressure. Each atom was then removed in turn, and the supercell allowed to relax around the vacancy, again, at constant pressure. The vacancy formation enthalpy, H_f^V , is calculated via

$$H_f^V = E_v - E_0 + \mu_v \quad (66)$$

where E_v is the total energy of the supercell containing a vacancy, E_0 is the total energy of the supercell without a vacancy, and μ_v is the chemical potential of the removed species. The sign of μ_v corresponds to either a vacancy (+ sign) or an interstitial (– sign). In the literature, variation of μ_v in bulk metals versus in complex alloys were found to be insignificant [315], [326], [329]. For example, Roy *et al.* investigated the relationship between μ_v in the refractory Ti-Zr-Mo-Ta-W system and their constituent pure metals and found that the chemical potential differed by less than 1.1% [326]. Herein, the chemical potential of the defect species is approximated as that in its bulk metal form via the equation

$$H_f^V = E_v - E_0 + E_{\text{defect}} \quad (67)$$

where E_{defect} is the total energy, normalised to energy-per-atom, of the pure metal in its bulk form at 0 K (hexagonal close packed Ti, Zr, and Hf, and body-centred cubic Nb, Mo, Ta, and W). The accuracy of these pure bulk metal lattice energy calculations was similar to that of the alloy supercells.

Each supercell afforded 54 unique vacancy formation enthalpies. These were calculated at least in duplicate for each quinary alloy in the Ti-Zr-Nb-Mo-Hf-Ta-W system (using a different special quasi-random structure supercell each time), yielding a total of at least 108 vacancy formation enthalpies per alloy. The element whose number of atoms is slightly deficient in each supercell, was allowed to vary at random, and no significant effect of this was observed in the resulting distributions of vacancy formation enthalpies (via a two-tailed Kolmogorov-Smirnov test) [331].

To interrogate any correlations between vacancy formation enthalpy and bulk properties, such that H_f^v might be predicted using easily obtained properties, the Pearson product-moment correlation coefficient between H_f^v and several properties were calculated including electron valence concentration, atomic size mismatch factor, and lattice parameter, and are shown in section 5.3.3 below. These properties are easily obtained via the parametric approach to phase stability of concentrated solid solution alloys [148], [332], [333].

5.3 Results

5.3.1 Phase stability and structure

Before assessment of vacancies, the stability and properties of the perfect solid solutions are investigated. The various properties will be subsequently used to assess the impact on vacancy formation enthalpies. The solid solution formability of compositionally complex alloys has been estimated via various parametric approaches in the past [144], [146], [147]. the solid solution mixing enthalpy, ΔH_{mix} , for equiatomic alloys is calculated via the regular solid solution model given by Yang *et al.* [144], ideal configurational entropy, ΔS_{conf} , valence electron concentration (VEC) [307], atomic size mismatch parameter, δ , solid solution formability parameter at the theoretical melting point [144], Ω , and the atomic packing parameter, γ [149].

$$\Delta H_{\text{mix}} = \sum_{i=1, i \neq j}^n 4\Delta H_{ij}^{\text{mix}} c_i c_j \quad (7)$$

$$\Delta S_{\text{conf}} = -R \sum_{i=1}^n (c_i \ln (C_i)) \quad (8)$$

$$\text{VEC} = \sum_{i=1}^n c_i (\text{VEC})_i \quad (9)$$

$$\delta = 100 \times \sqrt{\sum_{i=1}^n c_i \left(1 - \frac{r_i}{\bar{r}}\right)^2} \quad (10)$$

$$\omega_s = 1 - \sqrt{\frac{(r_L + \bar{r})^2 - \bar{r}^2}{(r_L + \bar{r})^2}}; \omega_L = 1 - \sqrt{\frac{(r_s + \bar{r})^2 - \bar{r}^2}{(r_s + \bar{r})^2}}; \gamma = \frac{\omega_s}{\omega_L} \quad (11)$$

$$\Omega = \frac{T_m \Delta S_{\text{mix}}}{|\Delta H_{\text{mix}}|}; T_m = \sum_{i=1}^n c_i (T_m)_i \quad (12)$$

where c_i and c_j are the atomic fractions of elements i and j , respectively. $\Delta H_{ij}^{\text{mix}}$ is the enthalpy of mixing of binary liquid alloys, based on the Miedema macroscopic model for liquid binary alloys obtained from Takeuchi *et al.* [334]. R is the ideal gas constant in $\text{JK}^{-1}\text{mol}^{-1}$, $(\text{VEC})_i$ is the valence electron concentration of the i^{th} element, $\bar{r} = \sum_{i=1}^n c_i r_i$ is the average atomic radius and r_i is the atomic radius of element i , and $(T_m)_i$ is the melting point of the i^{th} element.

The putative boundaries for each parameter for solid-solution formation are: $-15 \text{ kJmol}^{-1} < \Delta H_{\text{mix}} < 5 \text{ kJmol}^{-1}$ [147]; $12 \text{ Jmol}^{-1} < \Delta S_{\text{mix}} < 17.5 \text{ JK}^{-1}\text{mol}^{-1}$ [144], [147]; $\text{VEC} \leq 6.87$ for body-centred cubic structures, $\text{VEC} \geq 8$ for face-centred cubic structures [146]; $\delta \leq 6.6\%$ [147]; $\Omega \geq 1.1$ [144]; and $\gamma \leq 1.175$ [149]. The calculated values for the thermophysical parameters in the present alloys are in **Table 8**.

Table 8. Thermophysical parameters for equiatomic alloys. ΔH_{mix} , δ , VEC, γ , and Ω .

composition	ΔH_{mix} (kJmol ⁻¹)	δ (%)	VEC	γ	Ω
TiHfZrNbTa	2.72	6.46	4.4	1.0523	12.41
TiHfZrNbMo	-1.6	6.68	4.6	1.0523	20.44
TiHfZrTaMo	-1.92	6.73	4.6	1.0523	17.79
TiHfNbTaMo	-1.44	6.23	4.8	1.0526	24.87
TiZrNbTaMo	-1.76	5.97	4.8	1.0526	19.77
HfZrNbTaMo	-1.12	3.56	4.8	1.0341	32.42
TiHfZrNbW	-3.04	3.03	4.8	1.0714	11.46
TiHfZrTaW	-3.36	3.03	4.8	1.0714	10.8
TiHfNbTaW	-2.72	6.11	4.8	1.0719	13.95
TiZrNbTaW	-3.2	5.85	4.8	1.0719	11.54
HfZrNbTaW	-2.56	3.03	4.8	1.0712	15.02
TiHfZrMoW	-5.6	6.7	4.8	1.0714	6.29
TiHfNbMoW	-4.48	6.06	5	1.0719	8.24
TiZrNbMoW	-5.28	5.75	5	1.0719	6.8
HfZrNbMoW	-4.96	3.94	5	1.0712	7.54
TiHfTaMoW	-4.48	6.18	5	1.0719	8.56
TiZrTaMoW	-5.28	5.88	5	1.0719	7.07
HfZrTaMoW	-4.96	3.94	5	1.0712	7.83
TiNbTaMoW	-5.28	4.95	5.2	1.0362	7.39
HfNbTaMoW	-4.64	3.51	5.2	1.0717	8.73
ZrNbTaMoW	-5.44	3.16	5.2	1.0717	7.26

All alloys in **Table 8** satisfy the boundaries for solid solution phase formation for ΔH_{mix} , ΔS_{conf} , Ω , and γ . VEC of the alloys are below 6.87 which indicates a body-centred cubic is preferred. The alloys TiHfZrNbMo, TiHfZrTaMo, and TiHfZrMoW have δ values of 6.68, 6.73, and 6.7, respectively (in orange), which suggest these alloys may not form solid solutions. TiHfZrNbTa has a positive mixing enthalpy of $\Delta H_{\text{mix}} = +2.72$ kJmol⁻¹ (in orange) which suggests a miscibility gap at 0 K.

The parametric method suggests that the alloys investigated in this paper produce stable body-centred cubic solutions. However, there is a lack of information regarding the thermal

stability of the alloys that were investigated in this work. It is possible for local ordering, precipitation, segregation, and clustering of elements to occur, which will influence the vacancy energetics within the alloy. TiHfZrNbTa, for instance, has a positive ΔH_{mix} , indicating a thermodynamic tendency to decompose at low temperatures. MoNbTaTiW is known to undergo B2-like ordering at intermediate temperatures, which may influence the vacancy formation enthalpies of this alloy. Vacancy sinks, such as grain boundaries, are another factor that has an impact on the vacancy concentrations in concentrated solid solutions but are left for future analyses. Further, vacancy migration contributes to the observed vacancy concentrations in real materials. Migration is affected by dislocation density [335], clustering of vacancies, and the presence of defect sinks like grain boundaries.

5.3.2 Lattice constants

There is no generally agreed upon method in literature for calculating lattice constants for compositionally complex alloys or alloys in general. Experimentally, this is normally determined via a technique such as X-ray diffraction where the maximum peak intensity points are used to assess the general structure of the material. Lattice constants for the alloys in this study were predicted via three methods:

- A. The cube root of the total supercell volume is taken and divided by the unit cell width (3 for a $3 \times 3 \times 3$ cubic supercell) and this is taken as an estimate for the lattice constant across the cell.
- B. All neighbour distances across the cell are measured and the mean of those expected around the 2nd nearest neighbour (similar treatment as Wang *et al.* [317]) are taken to be representative of the alloy.
- C. The rule of mixtures (Vegard's law [336]) is applied to lattice constants of fully relaxed body-centred cubic supercells of pure elements in the Ti-Zr-Nb-Mo-Hf-Ta-W system. This third method is known to neglect the influence of lattice distortion on the crystal and is therefore likely to overpredict the lattice parameter of concentrated solid solution alloys.

Figure 70 shows plots for all methods for 10 alloys in the Hf-Mo-Nb-Ta-Ti-W-Zr system. The rule of mixtures is likely to have an overestimation of lattice parameters as enthalpic contributions and lattice distortions are ignored. Taking the mean of second nearest neighbour distances might lead to an underestimation of the lattice parameter when

its distribution overlaps with that of the first nearest neighbours. It is thought to be the most representative method to cube-root the volume and divide it by three, although the spread of atomic distances in the actual supercell is lost. Method A is believed to be the most representative lattice parameter found in bulk materials, while Method B is generally inaccurate when overlap between 1NN and 2NN distances becomes significant e.g., TiHfZrMoW. Method C (Vegard's law) tends to produce larger lattice parameters due to neglecting lattice strain on structure relaxation. The lattice constants for fully relaxed body-centred cubic supercells of pure elements used for Method C, are given as Ti: 3.25; Zr: 3.57; Nb: 3.31; Mo: 3.16.

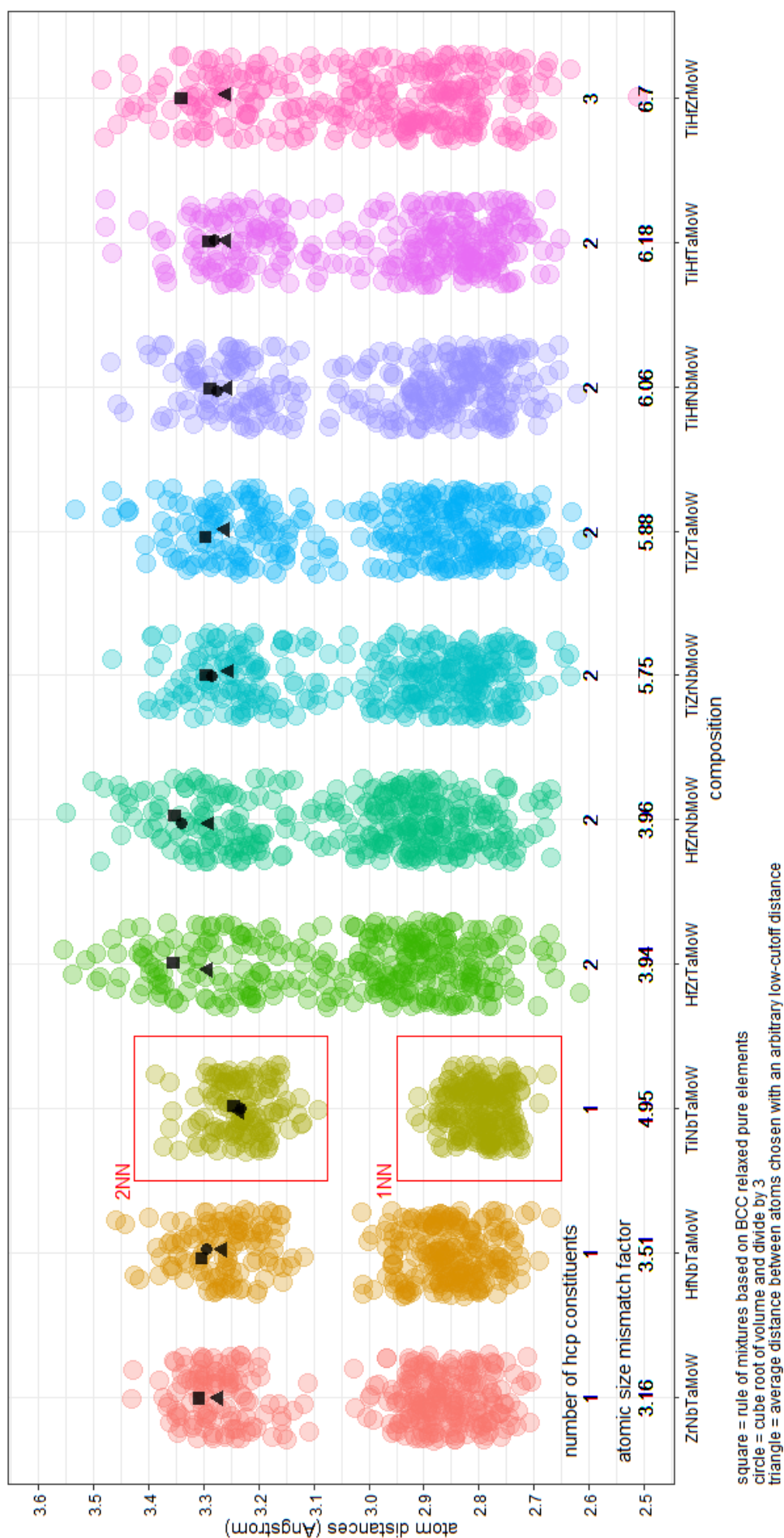


Figure 70. Atomic distances of quinary alloys in the Ti-Zr-Nb-Mo-Hf-Ta-W system for 54-atom supercells.

It was found that by cube rooting the volume and dividing by the unit cell width (Method 1), was able to provide an average lattice constant that considered the diverse range of atomic environments present in the alloy. The lattice constants of the alloys are in **Table 9**. The volume averaging scheme was used for subsequent correlation studies.

Table 9. Lattice parameters calculated for all alloys (Å). Calculated via cube rooting the volume of the relaxed density functional theory supercell and dividing by the unit cell width.

Composition	Lattice parameter (Å)
HfMoTiWZr	3.34
HfMoNbTiW	3.28
MoNbTiWZr	3.28
HfMoNbWZr	3.34
HfMoTaTiW	3.28
MoTaTiWZr	3.29
HfMoTaWZr	3.35
MoNbTaTiW	3.23
HfMoNbTaW	3.29
MoNbTaWZr	3.30
HfNbTaTiZr	3.41
HfMoNbTaTi	3.31
HfMoNbTiZr	3.36
HfMoTaTiZr	3.37
MoNbTaTiZr	3.32
HfMoNbTaZr	3.38
HfNbTiWZr	3.38
HfTaTiWZr	3.37
HfNbTaTiW	3.32
NbTaTiWZr	3.32
HfNbTaWZr	3.38

5.3.3 Vacancy formation enthalpies

At least two unique special quasi-random cells were generated for each of the 21 alloys in the study. The vacancy formation enthalpy adopts a single value in pure elements. However, the local chemical variations in concentrated solid solutions produce a distribution of vacancy formation enthalpies. The calculated enthalpies of the quinary Hf-Mo-Nb-Ta-Ti-W-Zr alloys are in **Figure 71** (ordered from highest to lowest mean values for H_f^V). The largest mean H_f^V belongs to MoNbTaTiW, which, incidentally, is the most reported quinary refractory alloy in

literature [160], [279], [286], [337]. The mean H_f^v for MoNbTaTiW is 3.14 eV and is similar to body-centred cubic W (3.11 [253] – 3.19 [338]) via density functional theory, and 3.1 – 3.4 eV experimentally [339]). HfNbTaTiZr exhibited the lowest mean enthalpy of vacancy formation of 1.04 eV which is similar to low melting face-centred cubic elements like Cu (1.33 eV) and Ag (0.96 eV) [340]. This indicates the possible low thermal stability of these solid solutions and may indicate that these alloys either have a low relative melting point compared to alloys in this study, since both the vacancy formation enthalpy and melting point are related to the cohesiveness of the structure. The rest of the solid solutions considered in this study exhibited intermediate H_f^v , with mean values from 1.46 – 2.93 eV. Mean values of H_f^v for all alloys in this study are in **Table 10**. For completeness, the vacancy formation enthalpies for the pure hexagonal close packed (Ti: 2.04; Zr: 1.98; and Hf: 2.20 eV) and body-centred cubic (Nb: 2.62; Mo: 2.80; Ta: 2.83; W: 3.33 eV) elements were calculated.

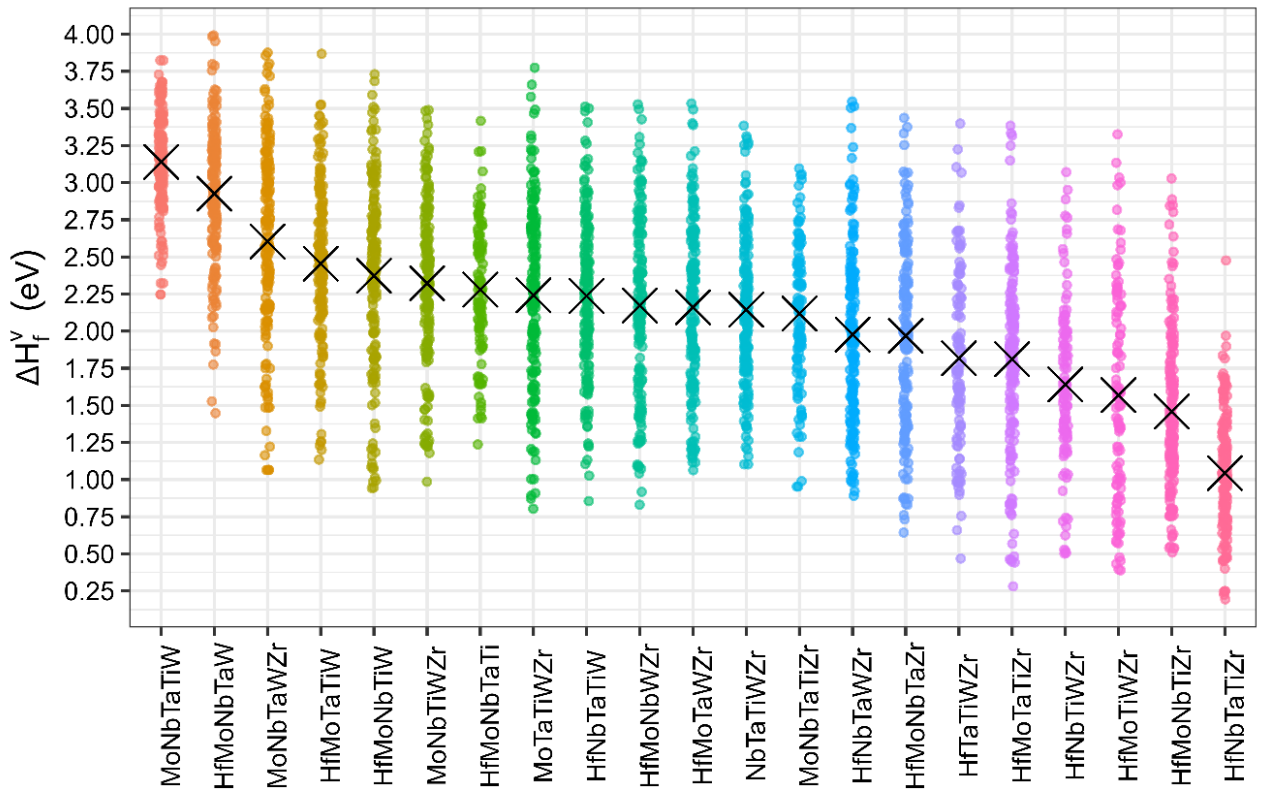


Figure 71. Vacancy formation enthalpy for equiatomic alloys in the Hf-Mo-Nb-Ta-Ti-W-Zr system. A cross indicates mean H_f^v values for each alloy.

Table 10. Mean H_f^V values for concentrated solid solutions. Where σ is the standard deviation of the mean H_f^V .

Composition	mean H_f^V (eV)	σ(eV)
MoNbTaWZr	2.604	0.646
HfMoTaTiZr	1.811	0.624
MoNbTaTiZr	2.119	0.495
HfMoNbTaZr	1.968	0.626
HfNbTiWZr	1.640	0.550
HfNbTaTiW	2.237	0.541
HfMoNbTiW	2.373	0.640
NbTaTiWZr	2.144	0.516
HfNbTaWZr	1.977	0.595
MoNbTiWZr	2.322	0.558
HfMoNbWZr	2.173	0.600
HfMoTaTiW	2.454	0.537
MoTaTiWZr	2.241	0.631
HfMoTaWZr	2.161	0.573
MoNbTaTiW	3.140	0.322
HfMoNbTaW	2.926	0.477
HfMoTiWZr	1.569	0.717
HfNbTaTiZr	1.044	0.394
HfMoNbTiZr	1.458	0.552
HfMoNbTaTi	2.280	0.443
HfTaTiWZr	1.817	0.609

To determine if each special quasi-random cell produced enthalpies likely from the same population distribution, a two-tailed Kolmogorov-Smirnov test was performed between each sample distribution (**Table 11**). In this statistical test, the probability that two sample distributions were drawn from the same (but unknown) probability distribution is calculated. Empirical cumulative distribution functions are produced from each sample distribution, and the largest distance at any given point between them is taken as the test statistic, D . The test is therefore sensitive to both the shape and location of the cumulative distribution functions of each sample. The probability, p , that at least a value as extreme as the D statistic, is taken as level of confidence that the sample distributions draw from the same population distribution. A p value of > 0.05 is typically taken as an acceptable value to conclude that two samples do indeed sample the same population, although this p value is chosen arbitrarily. After confirming the same population distribution for each alloy was likely sampled, each sample distribution was combined to produce a single distribution of energies for each alloy.

Table 11. Two-tailed Kolmogorov–Smirnov test on the vacancy formation enthalpies produced by multiple special quasi-random structures. D indicates the test statistic. p indicates the p-value of the test. A–C indicates the series of SQS cells calculated and is unique between each composition.

composition	D (A–B)	p (A–B)	D (A–C)	p (A–C)	D (B–C)	p (B–C)
HfMoNbTaTi	0.148	0.598	NA	NA	NA	NA
HfMoNbTaW	0.148	0.598	0.13	0.760	0.148	0.598
HfMoNbTaZr	0.278	0.031	0.241	0.087	0.204	0.214
HfMoNbTiW	0.130	0.76	0.148	0.598	0.130	0.76
HfMoNbTiZr	0.222	0.139	0.093	0.977	0.259	0.053
HfMoNbWZr	0.093	0.977	0.167	0.445	0.111	0.897
HfMoTaTiW	0.111	0.897	0.148	0.598	0.185	0.315
HfMoTaTiZr	0.259	0.053	0.185	0.315	0.185	0.315
HfMoTaWZr	0.241	0.087	0.185	0.315	0.130	0.760
HfMoTiWZr	0.204	0.214	NA	NA	NA	NA
HfNbTaTiW	0.167	0.445	0.185	0.315	0.111	0.897
HfNbTaTiZr	0.204	0.214	0.259	0.053	0.315	0.009
HfNbTaWZr	0.204	0.214	0.148	0.598	0.222	0.139
HfNbTiWZr	0.148	0.598	NA	NA	NA	NA
HfTaTiWZr	0.259	0.053	NA	NA	NA	NA
MoNbTaTiW	0.074	0.999	0.074	0.999	0.019	1.00
MoNbTaTiZr	0.111	0.897	NA	NA	NA	NA
MoNbTaWZr	0.167	0.445	0.204	0.214	0.333	0.005
MoNbTiWZr	0.278	0.031	0.111	0.897	0.259	0.053
MoTaTiWZr	0.204	0.214	0.204	0.214	0.167	0.445
NbTaTiWZr	0.185	0.315	0.167	0.445	0.111	0.897

There is little correlation between H_f^V calculated via **Equation 67** and the element being removed [317]. However, H_f^V does depend on the elements which make up the nearest neighbour environment. For example, Hf, Ti, and Zr have vacancy formation enthalpies of 2.20, 1.98, and 2.04 eV, respectively. When these elements form the nearest neighbour environment, H_f^V is likely to decrease. In contrast, the presence of Mo and W as neighbouring

elements (with H_f^V values of 2.80 and 3.33 eV, respectively), is likely to increase H_f^V . Therefore, the resulting vacancy formation energy can be seen as an average of the coordination environments arising in these alloys.

The local environment for each vacancy were characterised in terms of vacancy volume, immediate neighbour atoms, as well as bulk properties of the alloys (valence electron concentration, lattice constant, average electron shell number, and atomic size mismatch factor, δ). The thermophysical parameters are found in **Table 8**. **Figure 72** shows that the mean H_f^V of the studied alloys strongly correlates with valence electron concentration (**Figure 72a**: $r = 0.88$), number of hexagonal close packed alloying elements (**Figure 72b**: $r = -0.91$), and lattice constant (**Figure 72c**: $r = -0.87$). Vacancy volume, calculated from the convex hull between atomic coordinates of atoms within 2.75 Å around the removed atom, was found to weakly correlate with H_f^V . A plot of vacancy volume versus H_f^V is found in **Figure 73**.

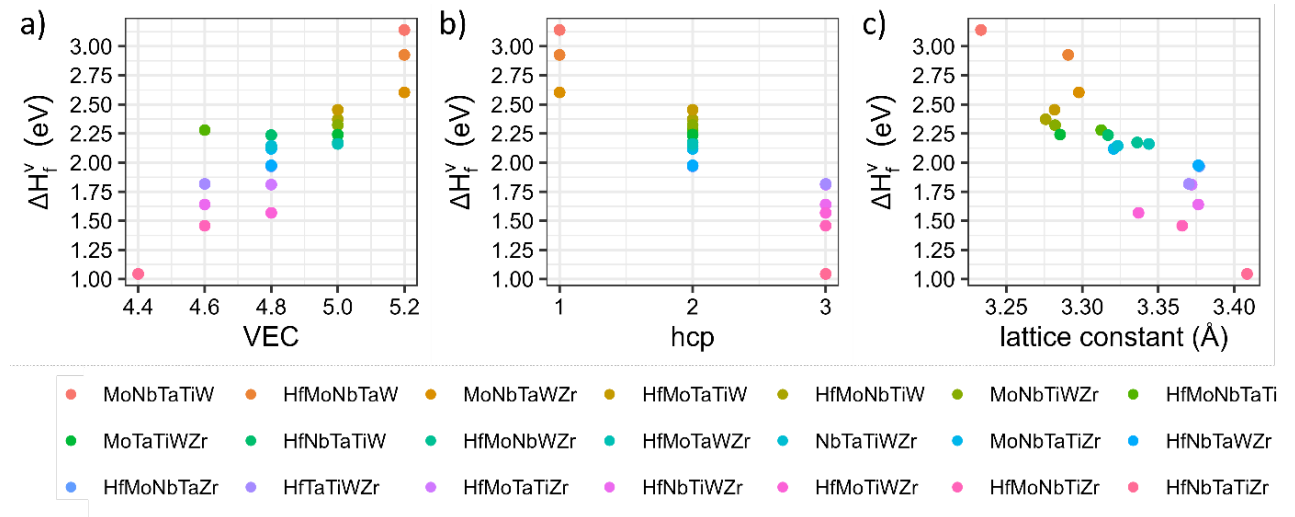


Figure 72. Mean H_f^V values for alloys in the Hf-Mo-Nb-Ta-Ti-W-Zr system plotted versus a) valence electron concentration; b) number of constituent hexagonal close packed elements; and c) calculated lattice constant.

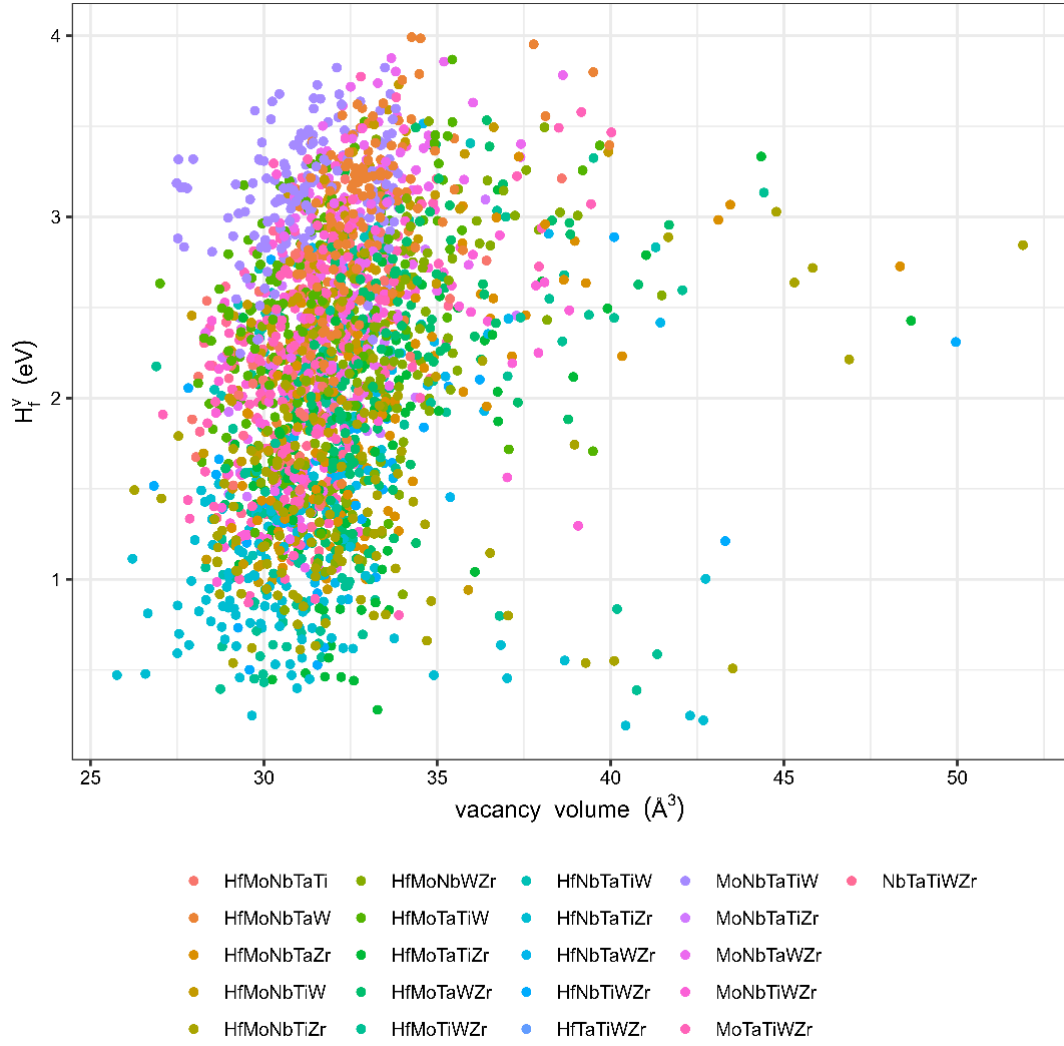


Figure 73. Enthalpy of vacancy formation, H_f^v , versus vacancy volume. $r = 0.28$.

H_f^v is observed to correlate positively with the number of body-centred cubic W, Mo, Ta, and Nb, as first nearest neighbours to the vacancy, with correlation coefficients of +0.37, +0.31, +0.14, and +0.16, respectively. Conversely, hexagonal close packed elements such as Zr and Ti negatively correlate with H_f^v with $r = -0.28$, and -0.07 , respectively. **Figure 74** shows the correlation coefficients between H_f^v and nearest neighbour elements. Local element bias, as calculated from **Equation 65** was found to have no direct correlation with H_f^v , as a strong bias toward a particular element shifts the enthalpy of vacancy formation towards that of the biased element.

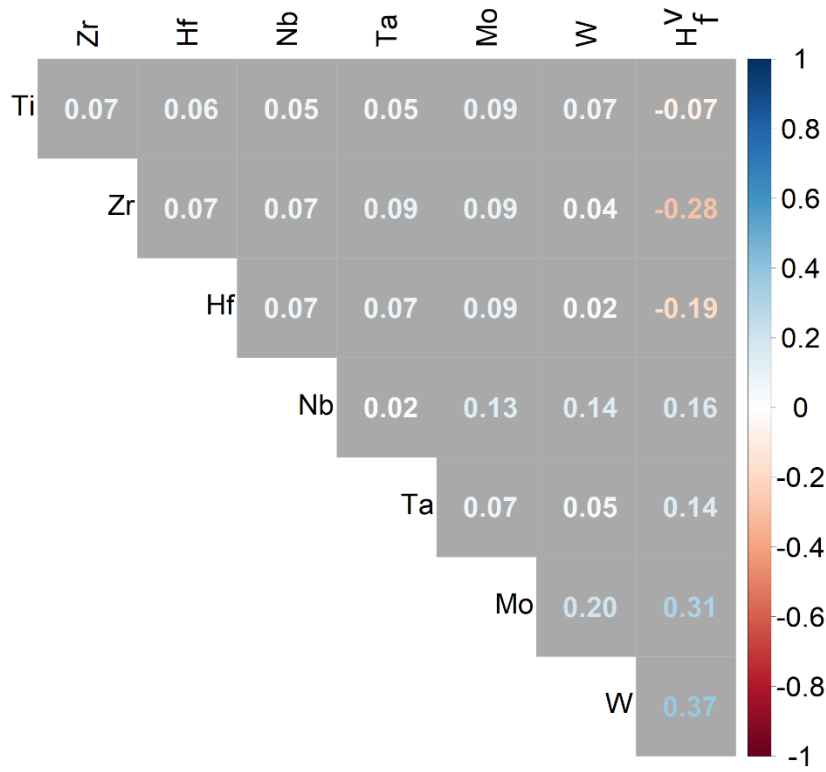


Figure 74. Product-moment correlation coefficient between nearest neighbour atoms (< 2.75 Å) and the calculated vacancy formation enthalpy, H_f^V .

In conclusion, the most significant contribution to H_f^V is observed to come from the removed element's nearest neighbours. This suggests that element clustering and segregation have a significant role in defining the vacancy energies of real materials. In addition, the enthalpies at the lower end of the distribution have a greater impact on the equilibrium vacancy concentration. Future research should make a concerted effort to sample these smaller enthalpies. The enthalpy of vacancy formation has been found to correspond with bulk parameters such as lattice constant, valence electron concentration, and several Hume-Rothery factors including the preferred crystal structure of the constituent elements at 0 K. These parameters may be used as a simple empirical relation to estimate H_f^V as a first approximation.

5.3.4 Migration of monovacancies

Nudged-elastic band (NEB) calculations allow for the calculation of the barrier for migration of species and defects within a system. In this project, the migration barrier energy at 0 K for single vacancies in MoNbTaTiW along the $\langle 111 \rangle$ family of directions which is the

favoured direction for vacancy migration in body-centred cubic metals, is calculated (**Figure 75**). In these calculations the climbing-image nudge elastic band method was used, which can shift images to correspond more closely to the saddle-point than conventional NEB calculations.

These calculations were done with PAW pseudopotentials [295] from the VASP package [40]–[41]. Exchange-correlation interactions were described by the PBE-GGA functionals [297]. Methfessel-Paxton smearing [298] with a smearing width of 0.5 eV was employed to account for partial occupancies of the metallic concentrated solid solution alloy systems. The cut-off energy of plane waves was 500 eV. The Brillouin zone was sampled with a Γ -centred $6 \times 6 \times 6$ K-point mesh. Chemical disorder was modelled using special quasi-random structures, using the *mcsqs* code of the Alloy Theoretic Automated Toolkit [264]. Individual pair correlation functions were set to include interactions up to and including the 3rd nearest neighbour. Triplet correlation functions were not considered. **Figure 75** shows the calculated energies along the migration pathway for migrating atoms in the MoNbTaTiW alloy.

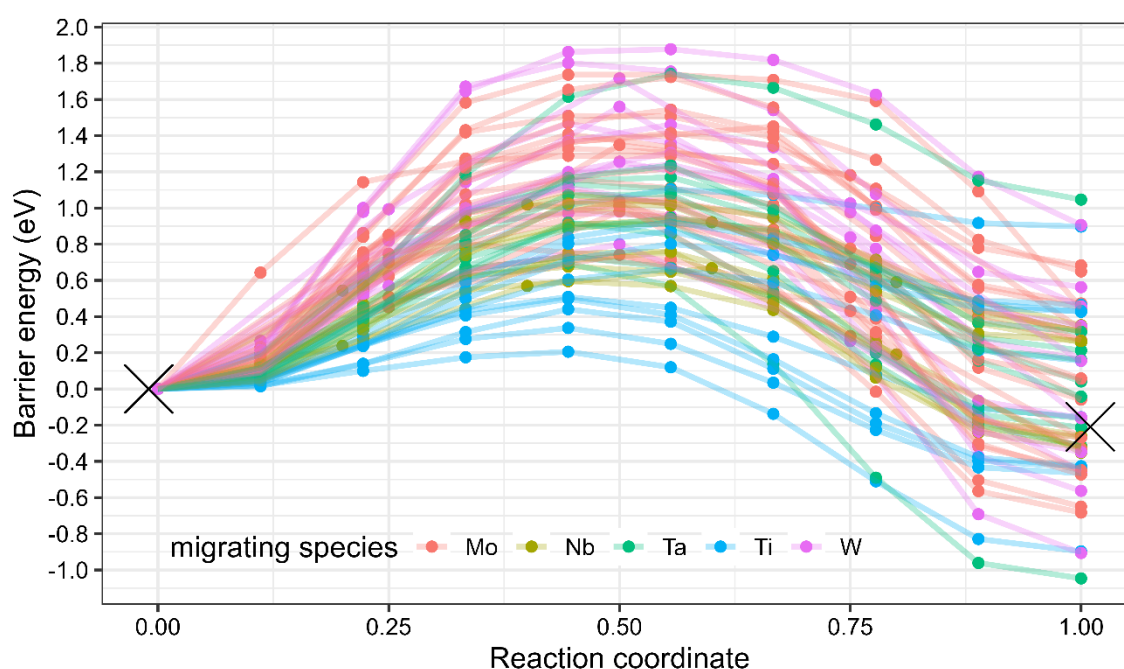


Figure 75. Example energy barrier heights for migrations of vacancies (or inversely, the migration of Mo, Nb, Ta, Ti, and W) at 0 K, as calculated from density functional theory.

Barrier heights are plotted for the migrating elements in **Figure 76**. Ti generally exhibited the lowest migration energy barriers when exchanging with a vacancy. Vacancy migration follows an Arrhenius relationship, with lower energies producing faster migrations.

As a result, lower energy migration pathways predominate over higher energy transitions. For example, Ti in the MoNbTaTiW alloy may exchange with vacancies at a rate orders of magnitude faster than elements such as Mo and W.

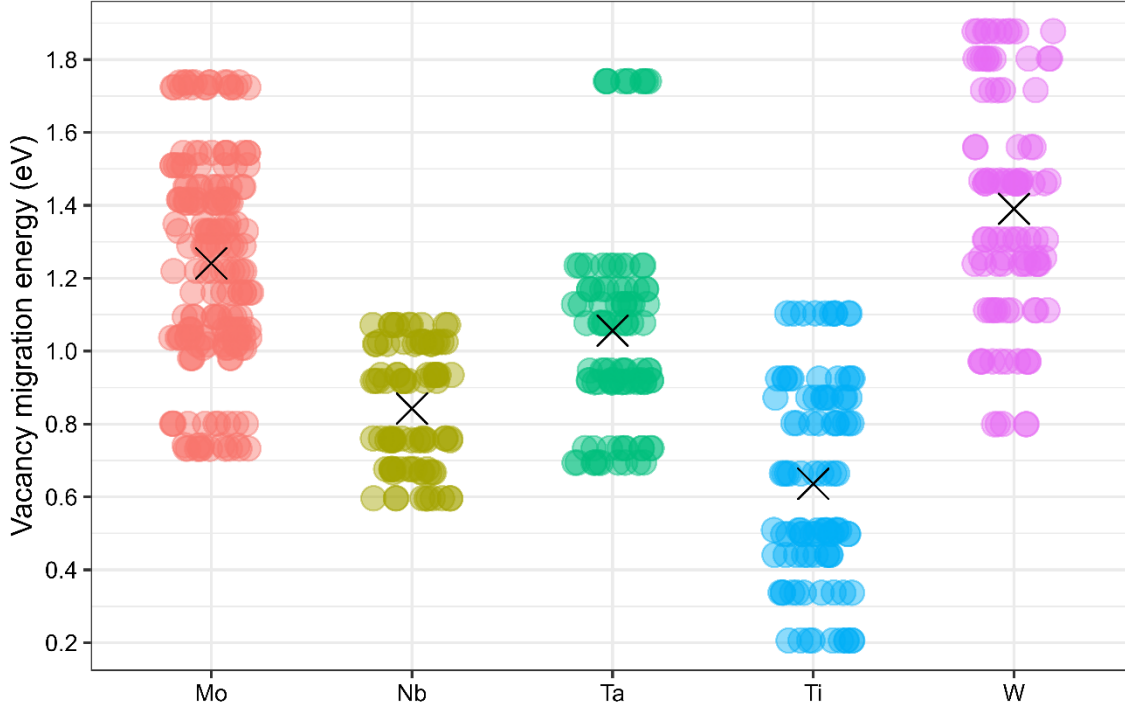


Figure 76. Spread of migration energies of vacancies in equiatomic MoNbTaTiW via exchanges with Mo, Nb, Ta, Ti, and W. Crosses indicate mean energies for each migrating species.

5.3.5 Population of vacancies in Hf-Mo-Nb-Ta-Ti-W-Zr quinary alloys

The value of H_f^V can be used to estimate vacancy concentration, X_i , in a material [341]. In a similar manner to Daigle *et al.* [256], the vacancy concentration in equiatomic concentrated solid solutions with the configurational entropy of the added monovacancy was calculated (**Equation 64**). Furthermore, the vacancy concentration using the entire enthalpy distributions was computed, which considers the preferential formation of vacancies with enthalpies at the lower tail of the H_f^V distribution (**Equation 68**).

$$X_i = \frac{n}{N} = \frac{\sum_{i=1}^n \frac{1}{m} e^{\frac{-\Delta H_f^V(i)}{k_B T}}}{n} \quad (68)$$

where $\frac{n}{N}$ is the fraction of vacancies in the system, m is the alloying number, ΔH_f^v is the mean enthalpy of monovacancy formation (eV), k_B is the Boltzmann constant (eVK⁻¹), T is temperature (K), $\Delta H_f^v(i)$ is the enthalpy of vacancy formation for the i^{th} observation, and n is the number of observations. **Figure 77** shows an example distribution of H_f^v values for MoNbTaTiW.

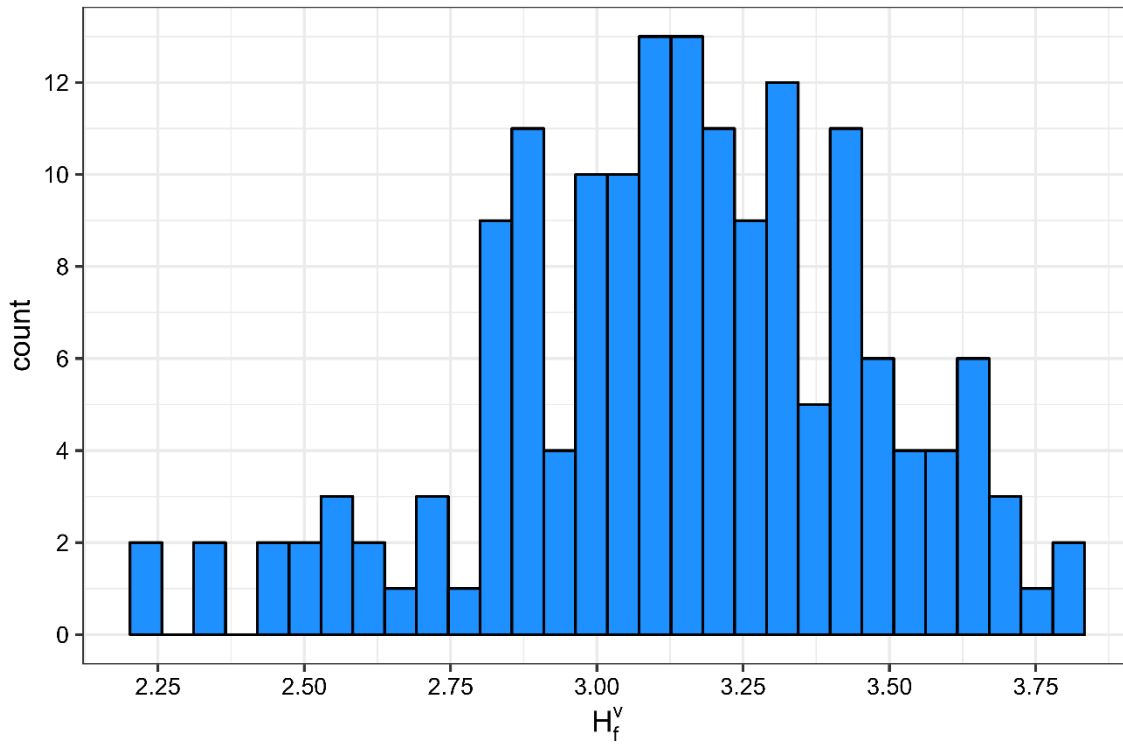


Figure 77. Distribution of H_f^v values for MoNbTaTiW.

Equation 64 considers the configurational entropy of adding a vacancy to an m number of elements at the dilute limit and is with accordance to the $m + 1$ species scheme [342]. Adding a vacancy to concentrated solid solutions results in a lower additional configurational entropy with increasing m (**Figure 65**).

The equilibrium vacancy concentration is calculated here for two alloys, MoNbTaTiW, and HfNbTaTiZr, using a) the mean H_f^v only; b) with the additional configurational entropy of the vacancy; and c) from the entire distribution of H_f^v . From **Figure 78**, additional configurational entropy in compositionally complex alloys reduces vacancy population. However, when the entire distribution of energies is considered, there is a significantly higher concentration of vacancies throughout the entire temperature range. This is because vacancies with lower formation enthalpies preferentially form within the alloy crystal, and therefore contribute most to the equilibrium vacancy concentration. Likewise, the same effect can be

seen in **Figure 79** for HfNbTaTiZr. In both cases, the equilibrium vacancy concentration for the whole distribution significantly deviates from typical Arrhenius behaviour especially at temperatures greater than 2000 K. This non-Arrhenius dependence of vacancy concentration is found to be characteristic for all alloys in the present study and may be a general property of all compositionally complex alloys, caused by the local chemical disorder in these systems.

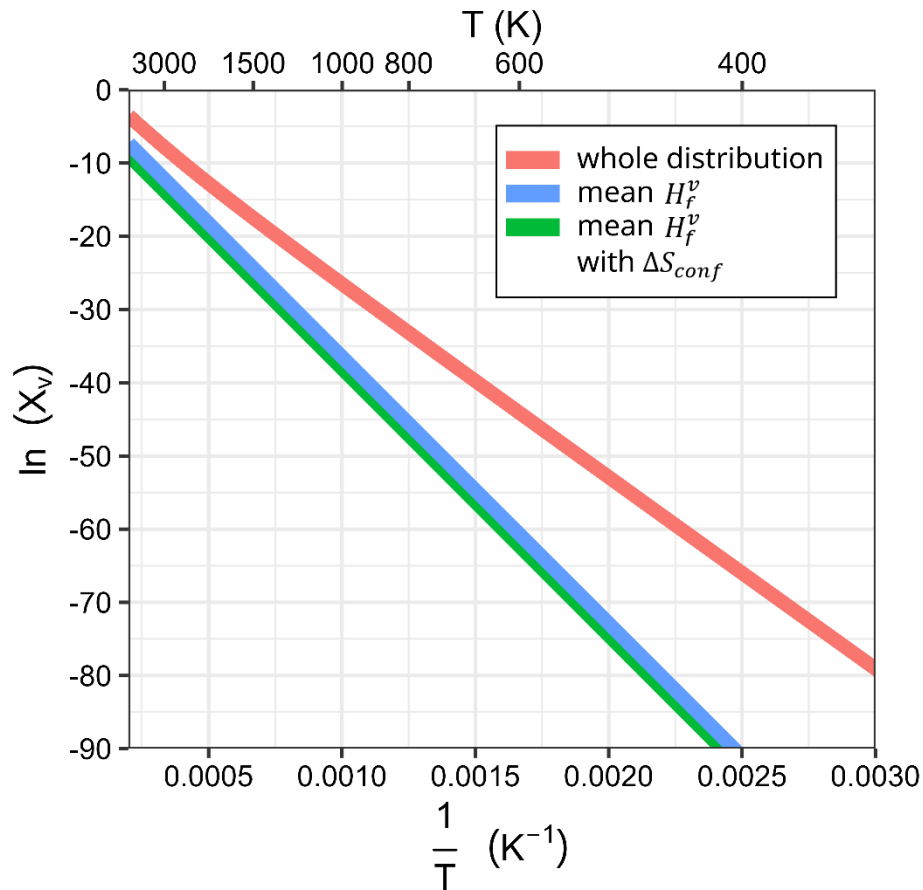


Figure 78. Equilibrium vacancy concentration in MoNbTaTiW. X_v is the equilibrium vacancy concentration, $X_v = \frac{n}{N}$.

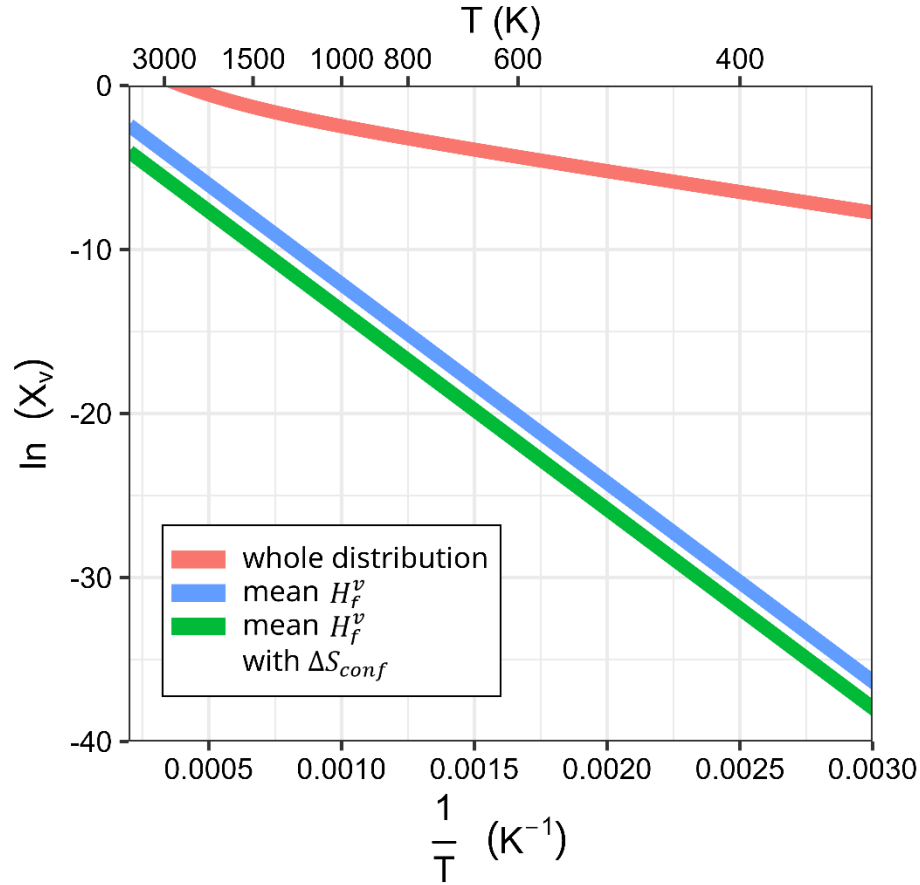


Figure 79. Equilibrium vacancy concentration in HfNbTaTiZr. X_v is the equilibrium vacancy concentration, $X_v = \frac{n}{N}$.

Plots of equilibrium vacancy population versus temperature for the remaining alloys in this study are in **Figure 80**. The role of configurationally entropy only minimally changed the concentrations from when configurational entropy is not included. Therefore, only populations calculated from mean H_f^v values with configurationally entropy, and from the distribution of H_f^v values, is presented in **Figure 80**.

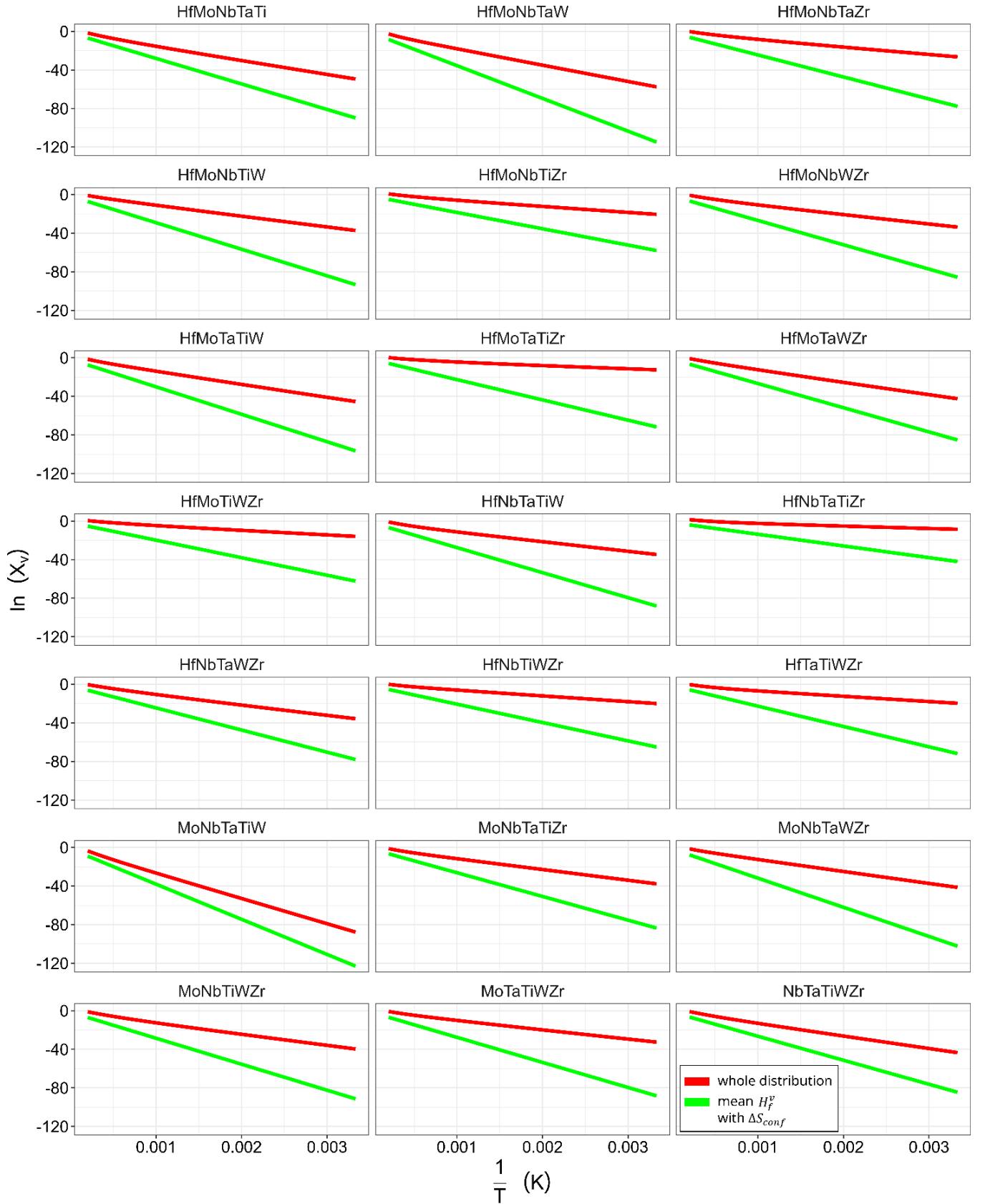


Figure 80. Vacancy population versus reciprocal temperature. X_v is the equilibrium vacancy concentration, $X_v = \frac{n}{N}$.

By considering the entire distribution of monovacancy formation in concentrated solid solutions, it is possible to compute an effective H_f^v as if the solid solution were a pure element (**Equation 69**). For the alloys in this study, this result is significantly lower than the mean H_f^v that is typically used previously to predict vacancies in pure elements and dilute alloys:

$$H_f^v(\text{effective}) = -K_b T \ln \left(\frac{\sum_{i=1}^n \frac{1}{m} e^{\frac{-\Delta H_f^v(i)}{K_b T}}}{n} \right) \quad (69)$$

where $\Delta H_f^v(i)$ is the enthalpy of vacancy formation for the i th observation, and n is the number of observations. The effective H_f^v for MoNbTaTiW and HfNbTaTiZr using **Equation 69** is compute. **Figure 81a** depicts the temperature dependence of the effective H_f^v for MoNbTaTiW. An effective H_f^v below 3.14 eV for MoNbTaTiW implies that monovacancies form much more easily at lower temperatures than if a simple average H_f^v is used. Similarly, **Figure 81b** illustrates effective H_f^v for HfNbTaTiZr. In both cases, the effective H_f^v is significantly lower than the mean H_f^v (MoNbTaTiW: 3.14 eV; HfNbTaTiZr: 1.044 eV).

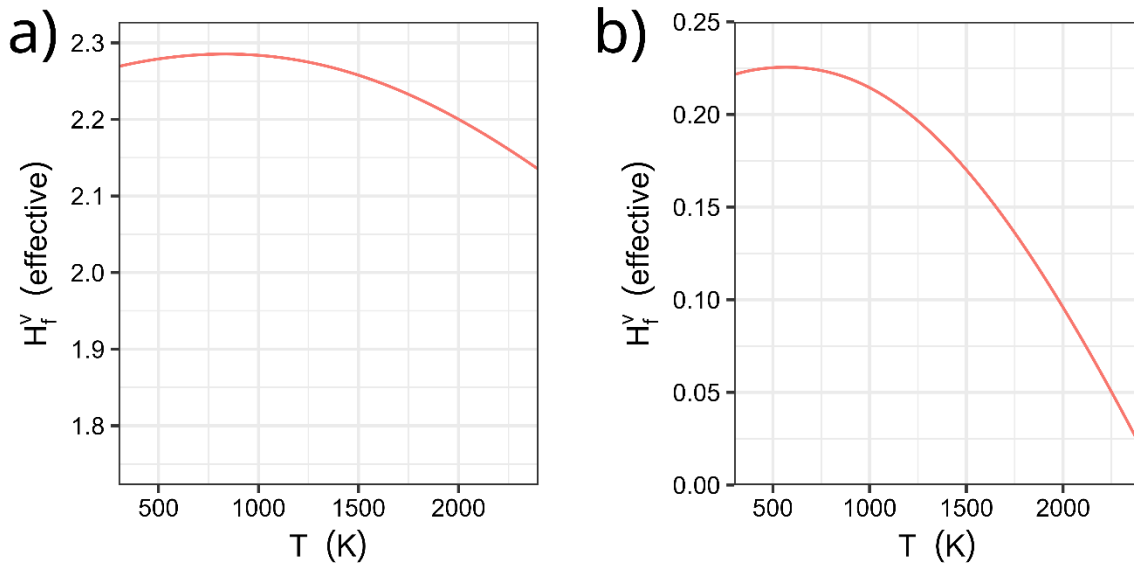


Figure 81. Effective H_f^v versus temperature. a) MoNbTaTiW and b) HfNbTaTiZr.

It is discovered that the higher equilibrium concentration in these alloys is not due to the additional configurational entropy of monovacancies in compositionally complex alloys. Rather, lattice sites with low H_f^v values produced by the H_f^v distribution contribute the most to vacancy concentration, which results in much higher concentrations of monovacancies at

equilibrium in compositionally complex alloys, compared to simple pure metals and conventional alloys. Future research will investigate clustering of vacancies, local ordering of elements, and the effect of these vacancies on diffusion kinetics in compositionally complex alloys.

5.4 Other considerations

5.4.1 Defect volume and effect on thermal expansion

Equilibrium concentrations of vacancies and their clusters are a function of temperature. And since a depletion of atoms from the centre of a crystal produces more atoms at the surface, vacancies also alter the total volume of materials. From these statements, it follows that the formation of vacancies, and their clusters should be folded into the thermal expansion of a crystal for an accurate assessment of its thermal expansion profile.

Thermal expansion can therefore be broken down into components. The first is thermal expansion of the lattice, which is the increase in volume of a crystal caused by the anharmonicity of potential wells for atoms. This type of thermal expansion is captured well via heated-stage X-ray diffraction because vacancies do not alter the average lattice parameter or interplanar spacing within a lattice as much as general lattice expansion does. The second component is vacancy formation thermal expansion, which, in addition to lattice thermal expansion, includes volume effects caused by vacancies in the crystal. The thermal expansion (lattice + vacancy) can be captured using dilatometry techniques. This additional component of thermal expansion is typically neglected in density functional theory techniques and heated-stage X-ray diffraction.

As stated above, the total thermal expansion of a crystal is broken into two components, lattice thermal expansion and vacancy contribution. In terms of linear thermal expansion, this relationship can be represented as:

$$(L + \Delta L)^3 = (N + n)(a + \Delta a)^3 \quad (70)$$

where L is the length of the material in question, N is the total number of atoms in the crystal, n is the number of vacancies in the crystal, and a is the lattice constant. $(L + \Delta L)$ and $(a + \Delta a)$ are the linear bulk and linear lattice thermal expansions, respectively. At low temperatures (i.e., without vacancies) **Equation 70** reduces to:

$$Na^3 = L^3 \quad (71)$$

The equilibrium concentration of vacancies can also be estimated using the differential thermal expansion between the lattice expansion and bulk expansion via:

$$X_v = \frac{n}{N} = 3 \left(\frac{\Delta L}{L} - \frac{\Delta a}{a} \right) \quad (72)$$

This technique has been used previously before positron annihilation spectroscopy became popular [311].

Compositionally complex alloys and concentrated solid solutions, tend to have an increased equilibrium concentration of vacancies compared to conventional alloys and pure metals. These higher concentrations could significantly increase the thermal expansion at high temperatures. In pure metals and dilute alloys, the bulk thermal expansion usually begins to deviate from the lattice thermal expansion at 0.6 – 0.75 of the homologous temperature, but this temperature could be significantly lower in compositionally complex alloys. Considering the possibly unique effects of thermal expansion could become significant in designing structural and functional components made from compositionally complex alloys.

5.4.2 Compositionally complex alloys in the nuclear environment

To summarise:

- The equilibrium concentration of vacancies in compositionally complex alloys is thought to be large compared to pure elements and dilute alloys. This is not attributed to high configurational entropy in these alloys. Rather, it is caused by low vacancy formation enthalpies produced from local chemical environments, which contribute most to vacancy formation.
- Compositionally complex alloys exhibited preferential migration of some elements over others.

These findings have important implications for high-temperature loss-of-coolant scenarios, as the presence of many vacancies could lead to quicker diffusion than expected in non-thermodynamic equilibrium. This could be particularly relevant in the case of neutron and heavy ion bombardment, as well as Frenkel-pair defect recombination after collision cascades. Further research into the thermodynamic properties of compositionally complex alloys is needed to understand the implications of these findings more fully.

The integrity of coating systems consisting of a Cr coating, a Zr substrate, and a compositionally complex alloy interlayer is affected by interlayer mixing. Vacancies can increase equilibrium concentrations and consequently lead to interdiffusion of Zr and Cr into the interlayer material. While some research has been conducted on the diffusion kinetics of compositionally complex alloys, the effects of refractory body-centred cubic compositionally complex alloys have yet to be studied. Further research is needed to better understand the diffusion kinetics of these alloys and their implications for coating system integrity.

Chapter 6. Evaluating MoNbTaW as an interlayer

This chapter explores efforts to fabricate and test refractory compositionally complex alloys. Alloys from the Mo-Nb-Ta-Ti-W system are attempted in bulk form using a sintering technique in section 6.1.1, and by arc melting in 6.1.3. Powders are attempted via high-energy planetary ball-milling in section 6.1.2. Thin films of MoNbTaW are attempted via magnetron sputtering in section 6.1.5. Tests for eutectic reaction temperatures and oxidation of accident tolerant fuel coatings are proposed, and early efforts in this regard are explored.

6.1 Tube furnace sintering

It was initially attempted to produce compositionally complex refractory alloys using a straightforward powder metallurgy process in a tube furnace heated to 1,650°C. This method was attempted multiple times within compositions of equiatomic MoNbTaTiW, which initially met the design criteria, but ultimately failed. Prior to sintering, it was attempted to mill the powders so that the smaller particles would either facilitate mixing or mechanically alloy the powders prior to heat treatment. However, neither expectation was met, and this method was unable to produce a compositionally complex alloy. Additionally, a significant amount of cold-welding occurs between the powders and the tungsten carbide milling jar during dry milling. During wet milling with ethanol as the process control agent, X-ray diffraction identified significant amounts of tungsten carbide contamination.

An examination of the particle size of the powders as received was conducted via particle size analysis (**Figure 82**) using deionised water as the dispersion medium. Median particle diameters for Mo, Nb, Ta, Ti, and W, are 22.78, 29.90, 17.38, 44.94, and 44.94 μm , respectively.

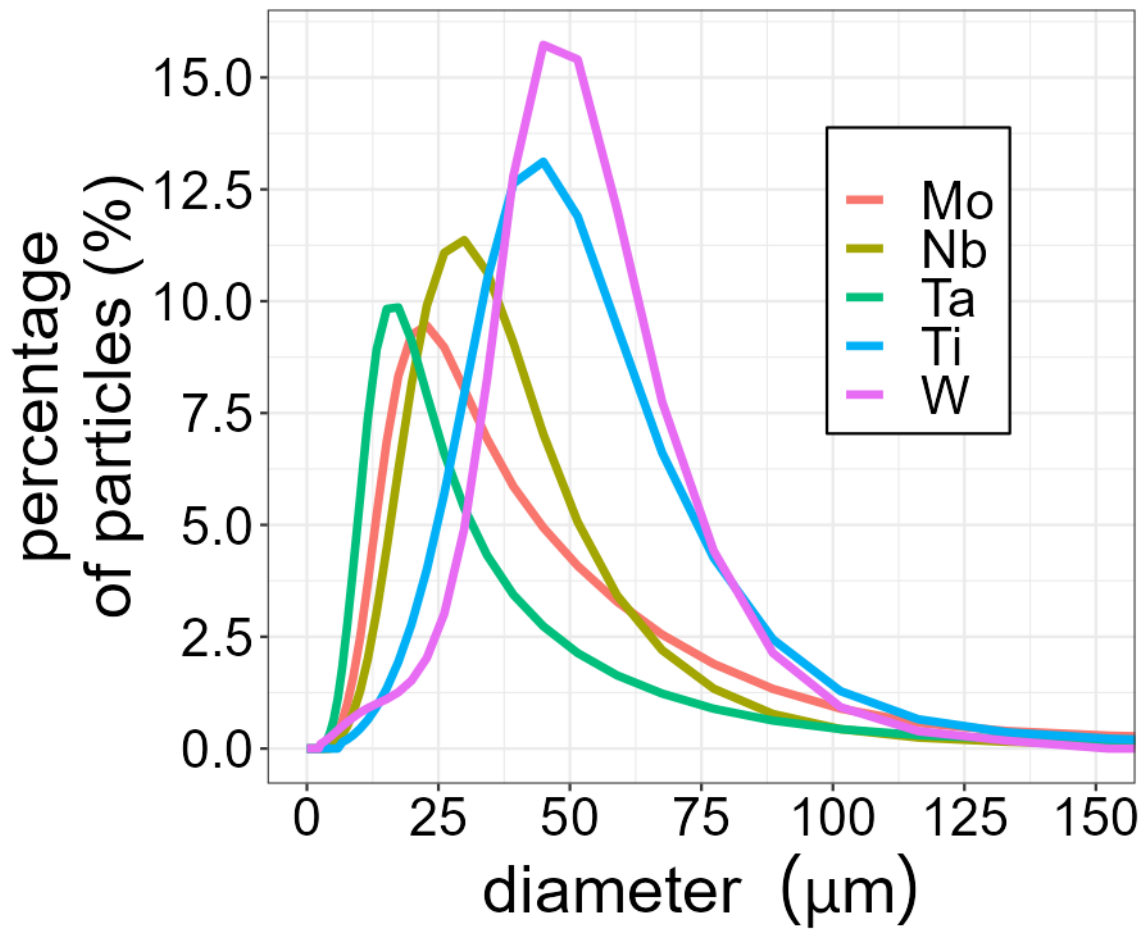


Figure 82. The particle size distribution of as-received refractory metal powders.

Figure 83 shows the as-received powders of Mo, Nb, Ta, Ti, and W. Powders were purchase from Alfa Aesar in size –325 mesh, with at least 99.9 % purity.

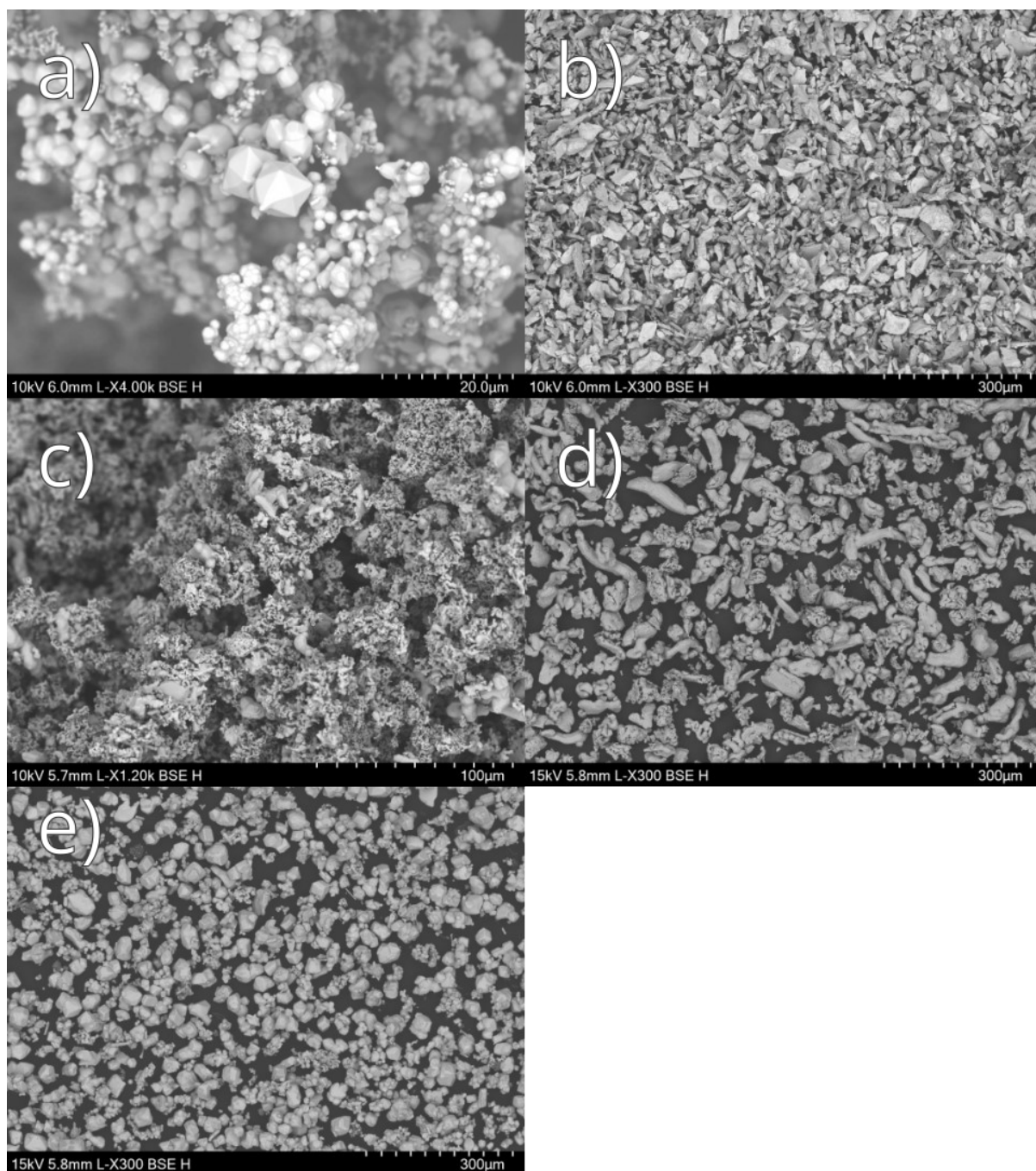


Figure 83. As-received particles of a) Mo, b) Nb, c) Ta, d) Ti, and e) W.

Table 12 indicates select samples attempted to produce refractory MoNbTaTiW. The crucible was made from ZrO_2 (**Figure 84**). The results from these experiments always showed a compacted mixture of pure metals with little to no mixing, and substantial porosity, for example, as shown in the electron micrograph in **Figure 85**.

Table 12. Select samples of mixed MoNbTaTiW powders and processing parameters.

MoNbTaTiW Pellet	Conditions before	Total furnace dwell time after (hours)	Density (g/mL)	Height of pellet (mm)	Diameter of pellet
1	Ball-milled	6	8.83	1.3	8
2	Mixed by hand and sintered for 2 hours	8	10.37	2.3	8
3	Powders ball-milled separately	6	-	-	8



Figure 84. Pellets of equiatomic MoNbTaTiW after sintering for a dwell time of 6 hours, and according to the conditions in **Table 12**. From left to right: pellets 1 – 3.

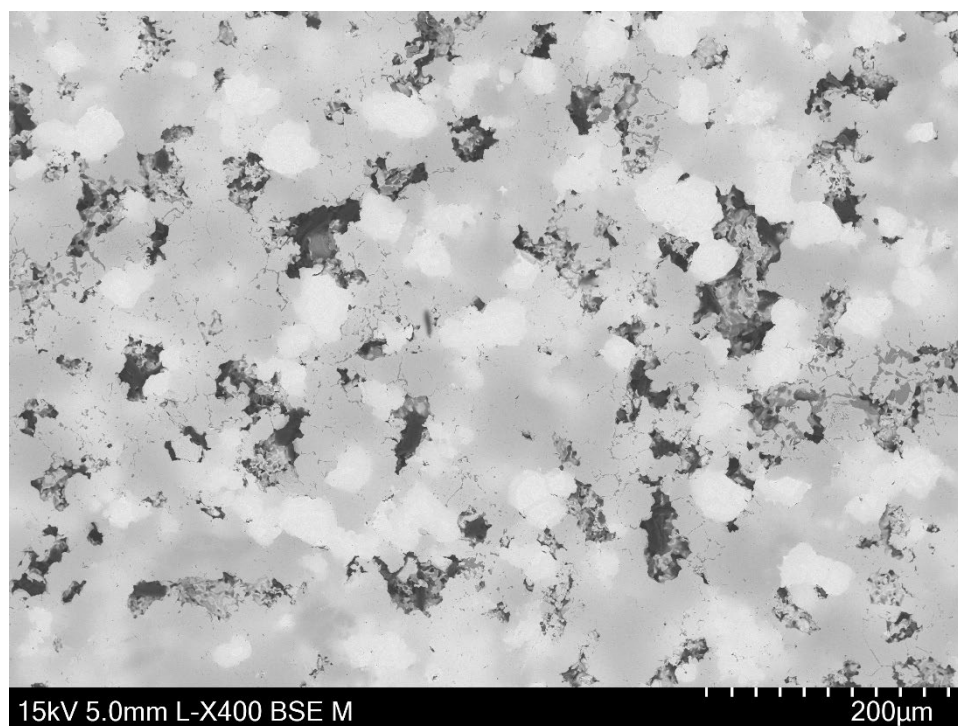


Figure 85. Backscattered electron micrograph of milled and sintered MoNbTaTiW.

The X-ray diffraction spectrum for the sintered material confirmed the results of the micrographic analysis showing an inhomogeneous material (**Figure 86**).

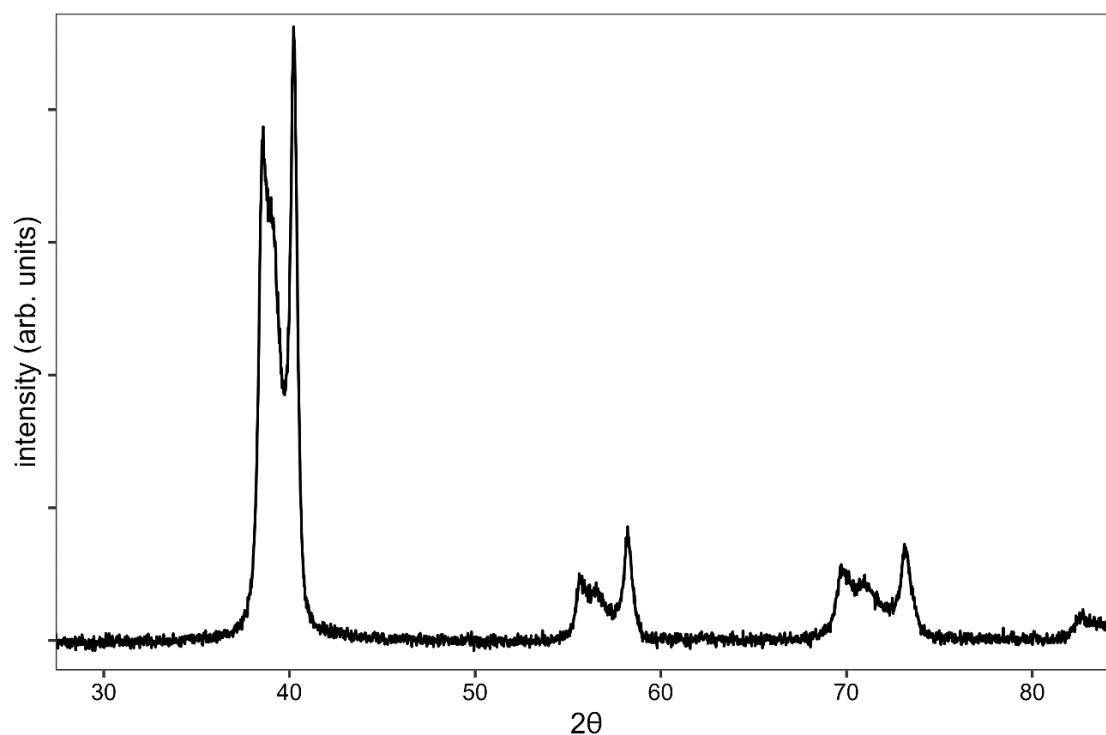


Figure 86. X-ray diffraction spectrum of powdered MoNbTaTiW after sintering for 6 hours at 1650°C under flowing Ar.

6.1.1 High energy ball-milling followed by sintering

An equiatomic MoNbTaTiW compositionally complex alloy was attempted to be synthesised by high energy planetary ball-milling followed by a sintering step. The ball-mill was a Retsch PM 100. Initially, a dry ball-milling was executed for 45 minutes at 350 rpm, with a 50:1 WC ball to powder ratio in a WC milling jar; however, unfortunately more than 90 wt% of the powders became cold-welded to the walls of the milling jar. This was again tried, with ethanol being used as a process control agent to dissipate the local heat generated by the impact of the WC milling balls on the milling jar and themselves. This method resulted in large amounts of contamination of WC into the mixture as revealed with X-ray diffraction.

6.2 Arc melting

Compositionally complex alloys are commonly produced by the method of arc melting, especially those that are of a refractory nature, being too difficult to synthesise with conventional furnace methods due to their high melting points. To create such alloys on a smaller scale, a compact arc furnace was assembled in the laboratory for this project (**Figure 87**).

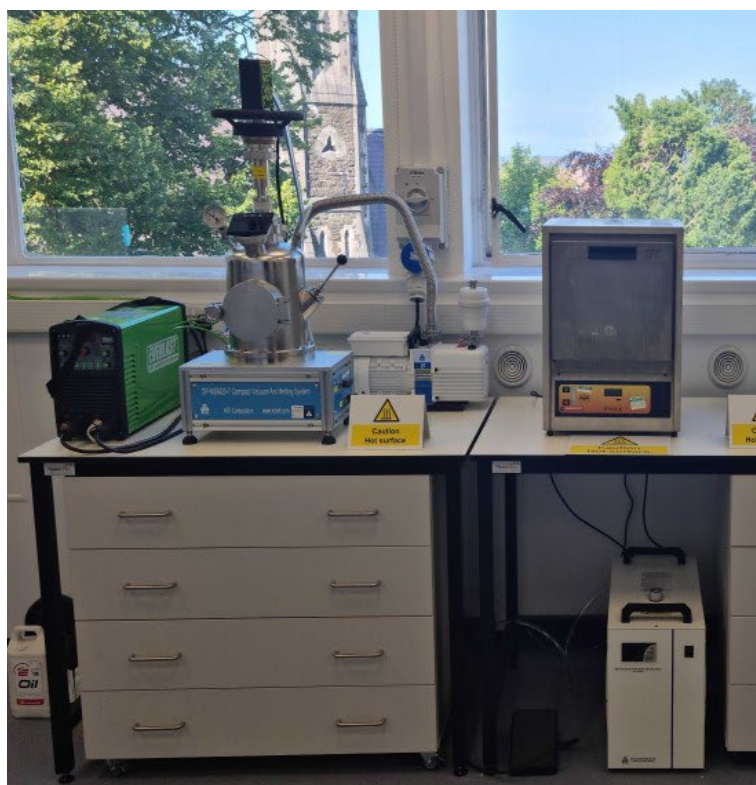


Figure 87. The laboratory compact arc furnace setup.

A 5% H₂ in Ar gas with a Ti oxygen-getter was typically used to keep the melting process away from residual oxygen after purging and to reduce any oxides back to their metals, thereby improving upon the tube furnace and ball milling method. The Ti oxygen getter was a compacted powder of Ti, which was struck with an arc in a separate Cu crucible prior to arcing the sample material.

A method was sought to melt the refractory alloy MoNbTaTiW, taking advantage of the low eutectoid reaction temperature in the W-Ti system in the hope that it might form a thermodynamical steppingstone to the rest of the alloy. Stoichiometric amounts of Ti and W were weighed out and subjected to high-energy ball-milling for 24 hours using ethanol as process control agent, after which it was pressed into a pellet and arc melting was repeated 5 times, flipping the button between each melt similar to other work [124], [189], [192], [193]. This method was successful in dissolving the W and Ti together as shown by X-ray diffractometry (**Figure 88**).

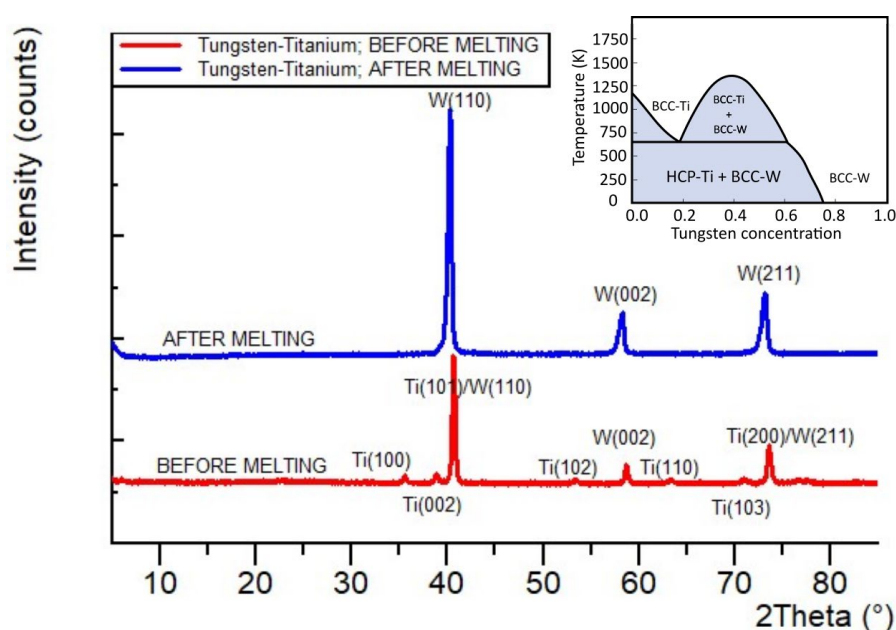


Figure 88. X-ray diffraction spectrum of a Ti₅₀W₅₀ binary alloy.

The button was broken again via the high-energy ball mill, the powders weighed again, and then the necessary weights of Mo, Nb, and Ta powders were added. The resulting powders were again mixed in the ball mill in ethanol for 24 hours, dried, pressed into a pellet and arc melted. The resulting X-ray diffraction patterns unfortunately showed extensive WC contamination from the milling jar. This line of experiments was discontinued.

One could improve this line of study by:

- Using a higher temperature furnace.
- Minimising contamination by experimenting with process control agents.
- Larger pressures in the compaction phase.

As can be seen from the X-ray diffraction spectrum (**Figure 89**), arc melting was eventually able to produce a homogenous body-centred cubic crystal structure of MoNbTaTiW. The lattice constant of the produced compositionally complex alloy was $3.25 \pm 1 \text{ \AA}$ at room temperature. This is in good agreement with Han *et al.* [279] and density functional theory predictions ($3.21 \pm 0.05 \text{ \AA}$).

Han *et al.*, observed interdendritic regions rich in Ti and Nb, and Ta and W rich dendrite arms when melting the same composition. Mo, however, was dispersed evenly between these two phases. In this section arc melting has been shown to be an effective method for fabricating refractory compositionally complex alloys. Pressed powders were generally seen to sputter through the vacuum chamber of the arc furnace. Chunk metal was unable to be obtained during this project, so this work was discontinued.

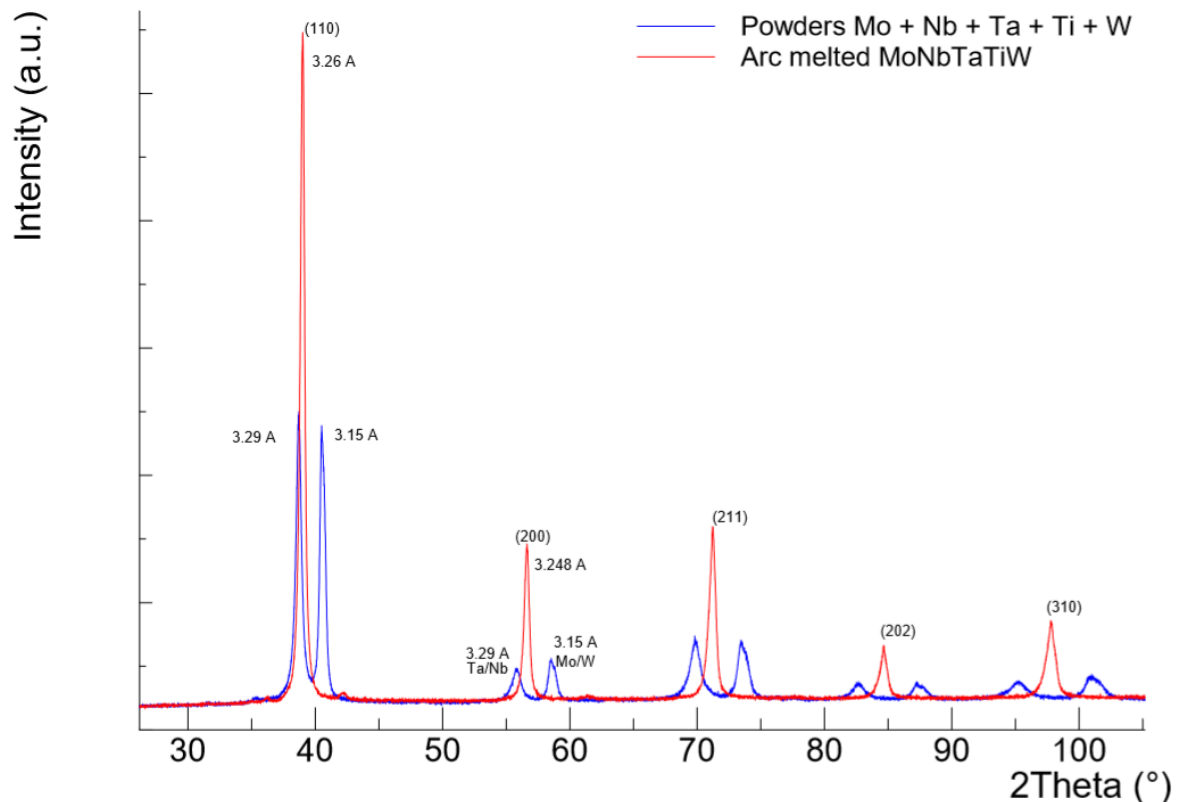


Figure 89. X-ray diffraction spectrum of MoNbTaTiW constituent powders, pre- and post-arc melting. Planes of the elements and corresponding lattice parameters are shown.

6.2.1 Etching

Compositionally complex alloys are a novel class of alloys. For this reason, there are no established protocols for etching these materials. To make the microstructures visible, samples were etched using Murakami's reagent which was prepared according to the following protocol:

- Prepare etchant, 10 g KOH in 100 mL volumetric flask, fill with deionised water, invert flask a few times, take 10 mL aliquot and add 1 g potassium ferricyanide.
- turn on water tap.
- immerse microsection in the etchant for 20 seconds.
- Remove the microsection and rinse in running water for 15 seconds.
- Rinse microsection finally with ethanol, and dried with a hair dryer.

6.3 Magnetron sputtering

MoNbTaW met the requirements outlined in **Chapter 3** for an interlayer material. Consequently, this alloy was selected for further study and synthesis using magnetron sputtering. This alloy promises high melting temperature, potentially high eutectic reaction temperature, slow diffusion, comparable thermal expansion coefficients, and low neutronic penalties. Other properties, such as oxidation resistance or reactivity with Cr and Zr, were unknown and required investigation. The aim of this section is to create an efficient protocol for the small-scale laboratory testing of accident-tolerant fuel coatings. This protocol should be able to swiftly eliminate unsuitable compositions, accelerating the alloy design process. Targets of > 99.9 % purity for MoNbTaW and Cr were manufactured by Testbourne Ltd in Basingstoke, England. Although the exact fabrication process was unknown, the targets were of good quality.

The magnetron sputterer used for this work had two sputtering target holders, with variable rotation of the substrate from 1 – 10 rpm. The working atmosphere was argon, and the pressure could reach 10^{-5} mbar. Deposition parameters for the system are in **Table 13**. The inside of the vacuum chamber is shown in **Figure 90**.

Table 13. Deposition parameters for the sputtering of MoNbTaW and Cr films.

Deposition parameters	Film preparation	
	MoNbTaW	Cr
Working gas	Ar	Ar
Based pressure	10^{-5} mbar	10^{-5} mbar
Working pressure	1.5 ± 0.1 mbar	1.5 ± 0.1 mbar
Substrate temperature	Unknown	Unknown
Rotating speed	10 rpm	10 rpm

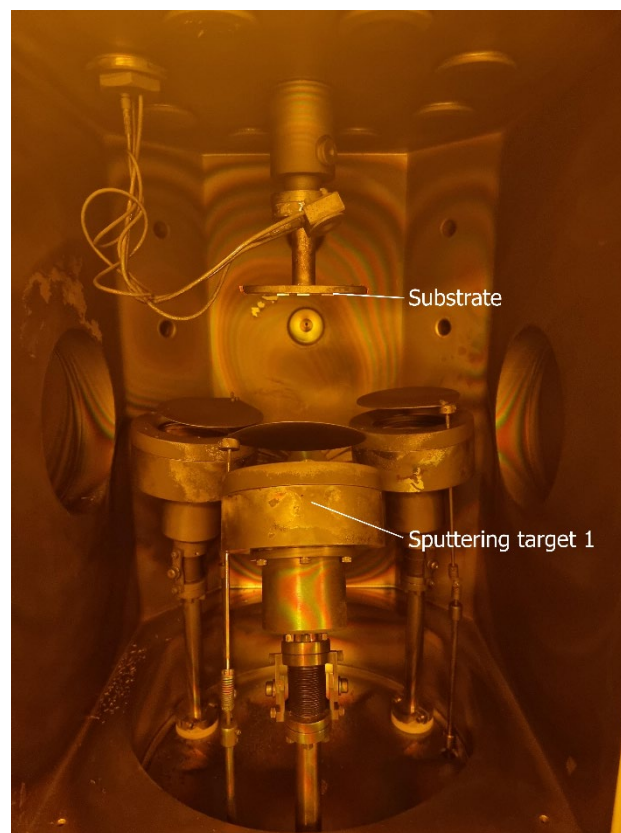


Figure 90. The magnetron sputterer vacuum chamber. The sputtering target holder and substrate location is labelled.

6.3.1 Magnetron sputtering of MoNbTaW and Cr

Accuracy in measurement of the thickness of sputtered films could not be achieved using the magnetron sputterer sensor. As a result, the development of a simple model for the description of film growth was sought. To correlate sputtering time with film growth, MoNbTaW and Cr were sputtered onto glass microscope slides. **Figure 91** shows an example set up of MoNbTaW sputtered onto a glass microscope slide. Cu tape was used to secure the specimens in the vacuum chamber and were removed after sputtering so that the step height could be measured with profilometry techniques.

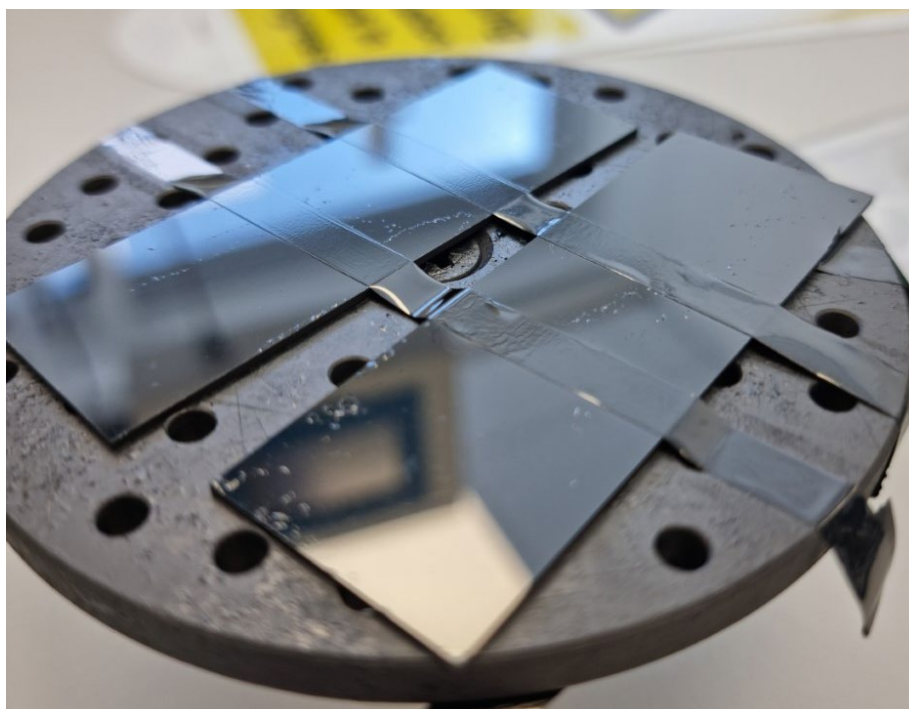


Figure 91. MoNbTaW sputtered onto glass microscope slides.

Film thickness was tested with a profilometer in contact mode. With respect to MoNbTaW (**Figure 92**) the film-growth was linear with time. The fabrication parameters were as follows: 80 W forward; < 4 W reflectance. Absolute vacuum chamber pressure: $1.5 \pm 0.1 \times 10^{-2}$ mbar. Film growth rate: 6.575 nm/min. Target purity: > 99.99 at%. Substrate: glass microscope slide. **Figure 92a** shows the profilometry line scan towards the deposited coating, where the step height is taken as the thickness of the coating. **Figure 92b** shows the thickness of coating as a function of sputtering time. Error bars indicate the profilometer resolution of 8 nm.

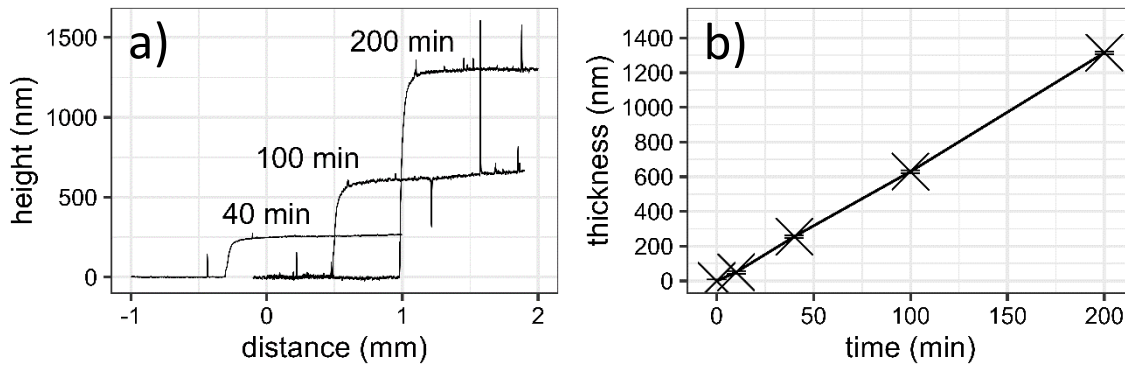


Figure 92. Nominal composition $\text{Mo}_{25}\text{Nb}_{25}\text{Ta}_{25}\text{W}_{25}$ film thickness optimisation.

It was expected that the growth of the film thickness would be linear with respect to time. However, it cannot be assumed that the composition of a certain alloy film across multiple forward powers would remain the same due to the possibility of different sputtering rates of each element. Nonetheless, a test was conducted to investigate the sputtering rate of MoNbTaW when subjected to various forward powers (**Figure 93**). The fabrication parameters were as follows: sputtering time: 30 minutes; < 4 W reflectance. Target purity: > 99.99 at%. Substrate: glass microscope slide. Absolute vacuum chamber pressure: $1.5 \pm 0.1 \times 10^{-2}$ mbar. Film growth given by the polynomial $0.000330x^2 + 0.0442x - 0.105$ nm/Wmin where x is forward watts. **Figure 93a** shows the profilometry line scan towards the deposited coating, where the step height is taken as the thickness of the coating. **Figure 93b** shows the thickness of coating as a function of forward power. Error bars indicate highest and lowest thicknesses observed across 3 scans. As it was anticipated that the MoNbTaW target would be fragile, it was purchased with indium bonding to a copper backplate so that it would not break in the vacuum chamber. Significant indium debonding was observed as the power increased > 120 W.

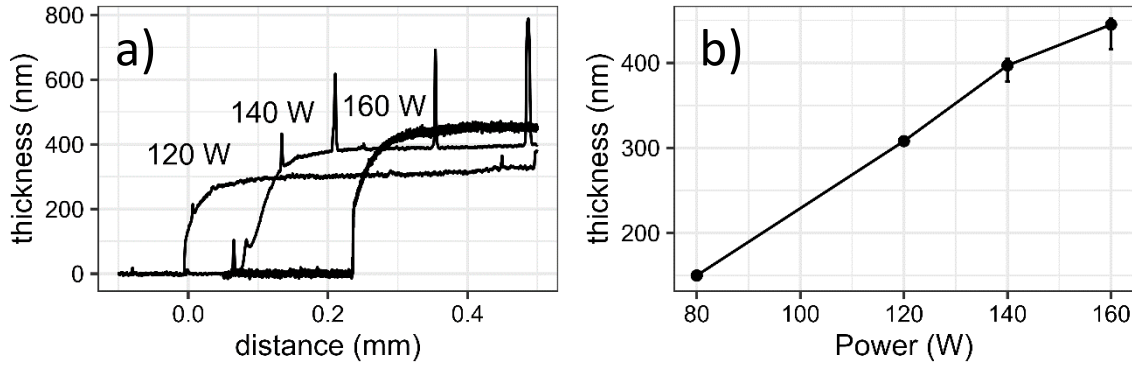


Figure 93. Nominal composition $\text{Mo}_{25}\text{Nb}_{25}\text{Ta}_{25}\text{W}_{25}$ variation of film thickness with forward power. a) profilometry line scan towards the deposited coating. b) thickness of the coating versus forward power when sputtered for 30 minutes.

Debonding was mitigated by using a lower forward power during sputtering, or by employing a stop-start procedure in which the target was allowed to sputter for 30 minutes, followed by 15 minutes of cooling. Both strategies were effective in preventing the indium joining material from dissociating. Each MoNbTaW was sputtered onto glass, and significant delamination was observed after a few days.

The forward power with respect to growth of sputtered Cr films was also tested (**Figure 94**). Film growth with respect to time was assumed to be constant. The fabrication parameters used in **Figure 94** are as follows: sputtering time: 30 minutes; < 4 W reflectance. Absolute vacuum chamber pressure: $1.5 \pm 0.1 \times 10^{-2}$ mbar. Film growth: ≤ 80 W: 0.004 nm/Wmin; $80 \text{ W} < x \leq 160 \text{ W}$: $-0.0000257x^3 + 0.00797x^2 - 0.627x + 12.2$ (nm/Wmin) where x is forward watts; > 160 W: 10.9 nm/min. Target purity: > 99.99 at%. Substrate: glass microscope slide. **Figure 94a** shows the Cr film thickness at different forward watts. **Figure 94b** shows the thickness of coating as a function of forward power.

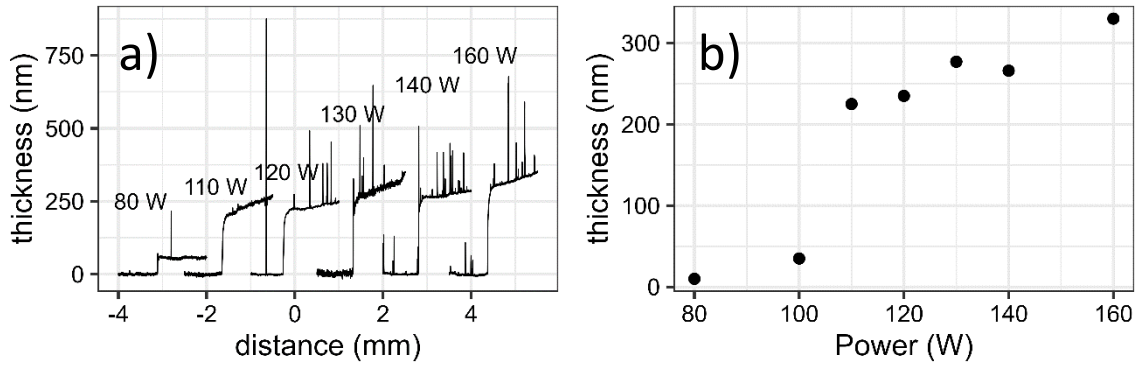


Figure 94. Cr variation of film thickness with forward power.

Plotting thickness of film coating against forward power resulted in a characteristic sigmoidal curve for both MoNbTaW and Cr. For Cr, forward powers of 110 W and 130 W, appearing as outliers in **Figure 94**, were measured together on a different day to the other measurements, which alludes to hitherto extraneous variables. These variables may include ambient temperature, coolant temperature, pressure, and chamber geometry.

6.3.2 Crystal structure determination of MoNbTaW thin films

In lieu of grazing incidence X-ray diffraction or similar technique, a target of nominal atomic composition $\text{Mo}_{25}\text{Nb}_{25}\text{Ta}_{25}\text{W}_{25}$ is DC magnetron sputtered onto glass microscope slides at 120 W forward power; growth rate ~ 10 nm/min, until the film is thicker than twice the penetration depth for X-rays (expected > 6 microns). **Figure 95** shows the calculated penetration depth for X-rays in MoNbTaW.

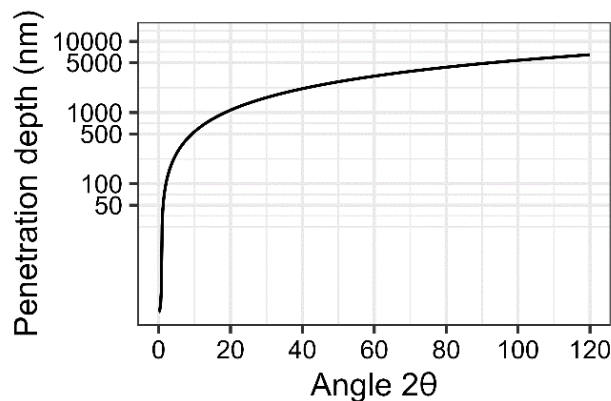


Figure 95. Penetration depth for X-rays in MoNbTaW films. Cu k- α $\lambda = 1.5406$ Å; $E = 8.04$ KeV; $\text{Mo}_1\text{Nb}_1\text{Ta}_1\text{W}_1$; $\rho = 11.87$ gcm $^{-3}$. Ref: [343].

1.24 μm was selected as a required film thickness so that body-centred cubic 2θ values would be captured via X-ray diffractometry. MoNbTaW was sputtered towards a glass microscope slide at 120 W for 30 minutes followed by 15 minutes off to limit indium debonding for a total sputtering time of 20 hours (30 hours with breaks), i.e., 4 hours (6 hours with breaks) per day for 5 days. The glass slide was then bisected with a diamond glass cutter for X-ray diffractometry analysis (**Figure 96**).

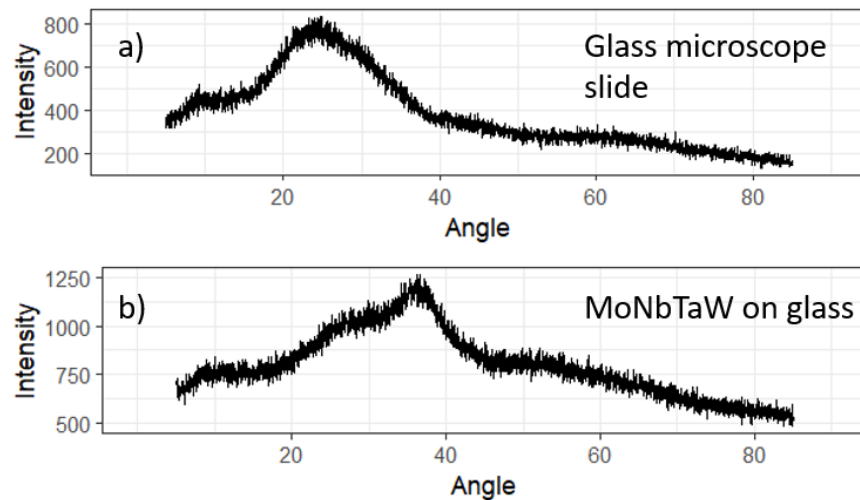


Figure 96. X-ray diffraction patterns of (a) a glass microscope slide for baseline and (b) magnetron sputtered MoNbTaW onto a glass microscope slide.

The X-ray diffraction pattern of the magnetron sputtered MoNbTaW indicated only an amorphous phase. This could be due to a couple reasons; either a) the thickness of coating was not sufficient, and the spectrum belonged to the glass substrate, or b) the sputtered MoNbTaW is amorphous in its as-sputtered condition. It is interesting to note that there is some evidence to suggest that amorphous metallic glasses and thin films tend to have better corrosion resistance [344]–[346].

This process could be improved by:

- Sputtering onto a crystalline substrate with known structure.
- Equilibrating the compositionally complex alloy film via a heat treatment to manifest a crystal structure.

Alternatively, glancing angle X-ray diffraction can be used to characterise thin films [347]. The penetration depth of standard X-ray diffraction tends to be microns thick, and so is not well suited for the characterisation of thin films. Grazing incidence configurations have

been developed to overcome such limitations, e.g., to make X-ray diffraction measurements more sensitive to the sample's near-surface region and to minimise the substrate's contribution to the diffraction response [347]. The same X-ray diffraction samples were used to obtain an X-ray fluorescence scan of the MoNbTaW coating (**Figure 97**).

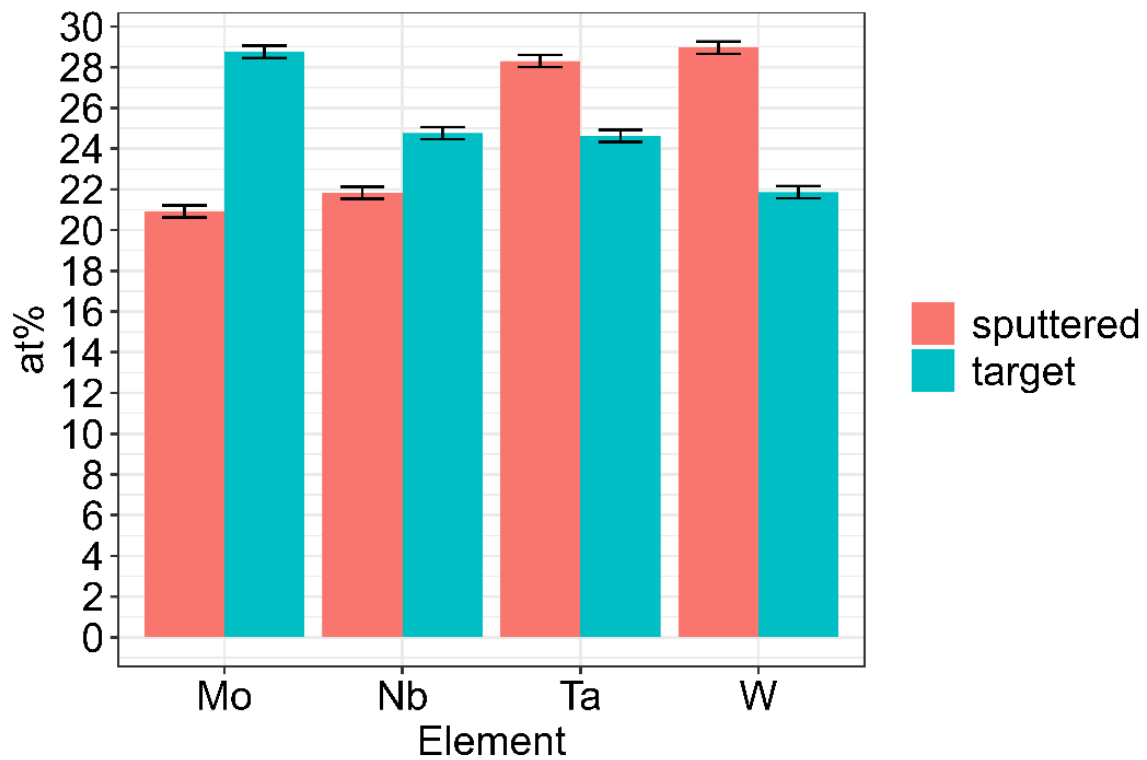


Figure 97. X-ray fluorescence spectra of the MoNbTaW sputtering target and the as-sputtered composition. Error bars indicate the largest deviation in composition seen across 4 scans.

6.3.4. Adherence of MoNbTaW-Cr coatings

Cr exhibited excellent adherence to Zircaloy-4 (ZIRLO™) indefinitely (**Figure 98**).

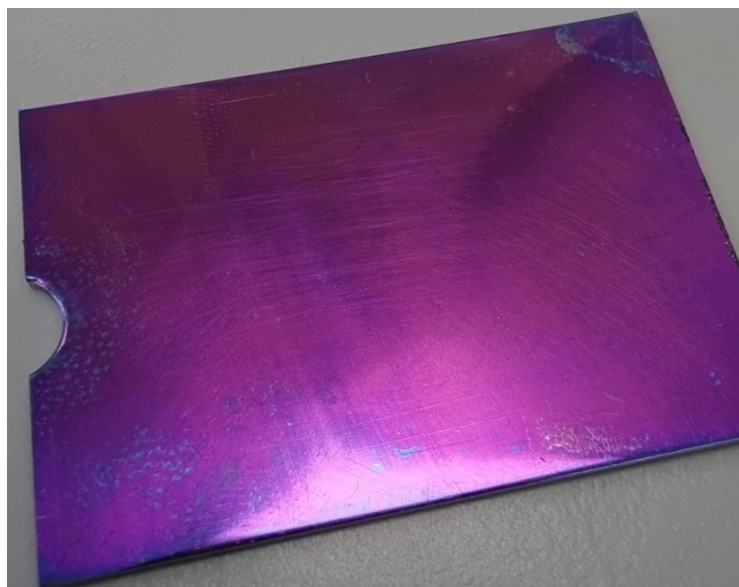


Figure 98. Magnetron sputtered Cr onto ZIRLO™ zirconium-based cladding material.

However, MoNbTaW was sputtered onto an unpolished sample of Zircaloy-2, which was prone to spalling almost immediately after coating (**Figure 99**; **Figure 100**). MoNbTaW/Cr coatings also spalled. One factor which may have caused spalling was that the Zircaloy-2 was used as-received and had a rough surface of ZrO_2 . In future, samples should be polished, possibly Ar^+ -polished using an alternative magnetron sputterer.

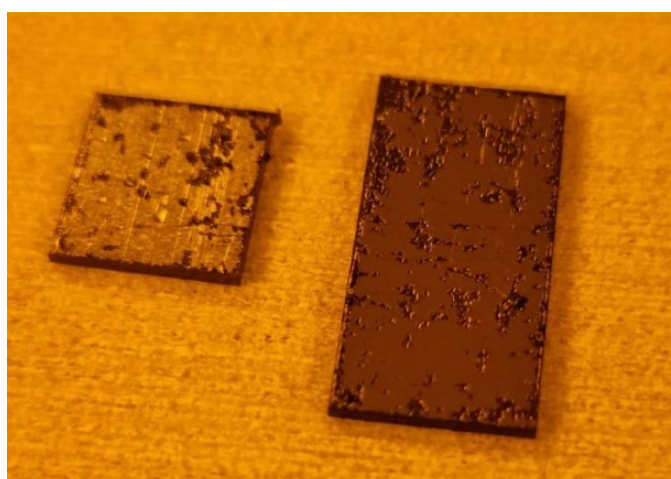


Figure 99. Cr and MoNbTaW sputtered onto Zircaloy-2 cladding material. Picture taken in a cleanroom with filtered lighting.



Figure 100. Optical microscope image of Cr-MoNbTaW sputtered onto Zircaloy-2 cladding material. 59 images were taken and manually stitched together in the *Inkscape* software. Light grey: Zr; brown: Cr.

6.4 Eutectic reaction temperatures

One of the requirements of an accident tolerant fuel coating system is that we improve (or at least do not negatively affect) the solidus temperature of the system. As it relates to compositionally complex alloys, there are few predictive techniques to interrogate solidus temperatures in these systems, and even fewer are reliable. The CALculation of PHase Diagrams (CALPHAD) method extrapolates from lower-order phase diagrams to produce higher-order phase diagrams, but all likely phases must already exist in the thermodynamic database prior to modelling. It is for this reason an experimental campaign was started to determine melting points of MoNbTaW as well as any eutectic reaction temperatures MoNbTaW may have with Zr and Cr. These experiments were to be performed in the simultaneous thermal analyser in differential scanning calorimetry mode.

The eutectic reaction temperature of the Cr-Zr system is approximately 1300°C. The interlayered coating must increase this reaction temperature to be viable as a coating solution. Comparison should also be made to the lowest eutectic reaction temperature known within the

binary alloy systems, i.e., a Zr-Mo eutectic alloy. **Table 14** shows the eutectic reaction temperatures.

Table 14. Eutectic reaction temperatures of metals in the Cr-Mo-Nb-Ta-Ti-W-Zr system (°C). Green indicates a eutectic reaction temperature greater than Cr-Zr (1310°C)

	Mo	Nb	Ta	W	Cr	Zr
Mo	2623					
Nb	2469	2469				
Ta	2623	2469	3020			
W	2623	2469	3020	3422		
Cr	1820	1668	1760	1860	1863	
Zr	1550	1750	1820	1735	1310	1855

According to the binary eutectic temperatures, any interlayer at all should produce a system with a higher eutectic reaction temperature. This ignores, however, any reactions which could take place between the metals, or any higher order eutectics which could exist in this system.

Table 15 indicates the samples for this experiment. First, the eutectic reaction temperature of Zr-Cr should be captured as a baseline, from which the eutectic reaction temperatures of Zr-MoNbTaW, Cr-MoNbTaW, and finally, Zr-MoNbTaW-Cr, can be compared.

Table 15. Eutectic reaction temperatures sought.

Coating system
Zr-Cr
Zr-MoNbTaW
Cr-MoNbTaW
Zr-MoNbTaW-Cr

Samples were to be prepared (using the direct current magnetron sputterer, isomet precision cutter, and polishing station). The simultaneous thermal analyser was set up with differential scanning calorimetry mode; mass spectrometry enabled; fresh 6.7 mm, 85 μL Y_2O_3 crucibles; triple-purged with Ar before each trial; calibration run before each trial. Samples underwent a temperature ramping cycle under flowing $\text{Ar}_{(\text{g})}$ to 1500°C.

To avoid adverse reactions between the sample and crucible during simultaneous thermal analysis trials, a Gibbs energy of combustion diagram (**Figure 101**) was constructed to aid in the identification of a suitable crucible material. In this diagram, any species can reduce a species laying above it and will itself form an oxide.

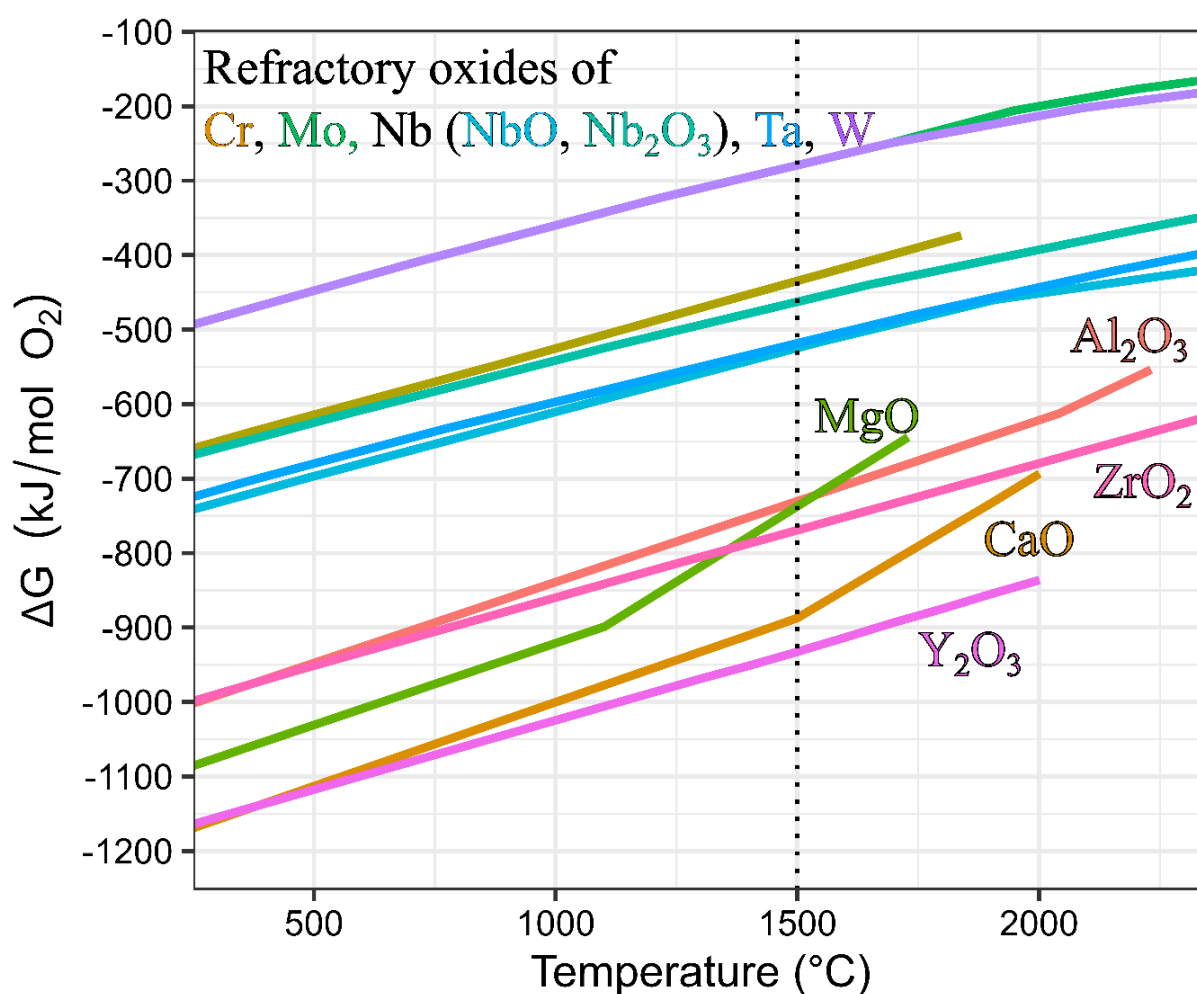
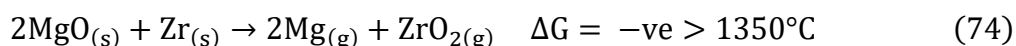
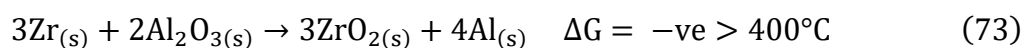


Figure 101. Gibbs energy of combustion diagram of crucible materials and experiment metals [348]. The dashed vertical line indicates the maximum temperature in the sample chamber during experiment.

Reactions of concern:



Use of Al_2O_3 crucibles was avoided due to the redox reaction between Zr and Al_2O_3 (**Equation 73**) which becomes spontaneous above approximately 400°C . MgO was also avoided because it spontaneously reduces to gaseous Mg metal when in contact with Zr above 1350°C (**Equation 74**). CaO and Y_2O_3 have no reactions of concern with respect to redox reactions with sample metals & Pt DSC tray. Y_2O_3 crucibles are chosen over CaO because they are readily available from the supplier (Netzsch).

The Y_2O_3 crucible initially required heat treatment, as it was causing erratic behaviour in the differential scanning calorimetry signal. **Figure 102** shows a 6-hour heat treatment of Y_2O_3 crucibles at 1000°C .

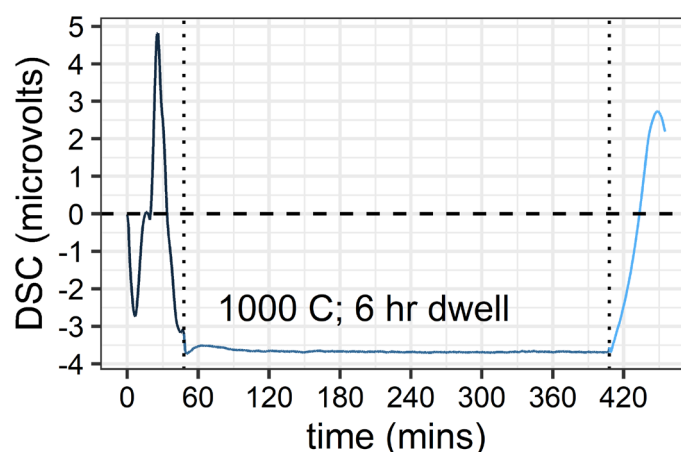


Figure 102. Heat treatment of Y_2O_3 crucibles.

The programme for the simultaneous thermal analyser was set up as follows: Starting temperature: 50°C ; ramp up rate: $10^\circ\text{C}/\text{min}$; max temperature: 1500°C ; hold time: 5 mins (the temperature was expected to normalise in less than 2 minutes.); ramp down rate ($10^\circ\text{C}/\text{min}$); maximum total scan time: 5 hrs. The setup of the eutectic reaction experiment and experiment programme is shown in **Figure 103**.

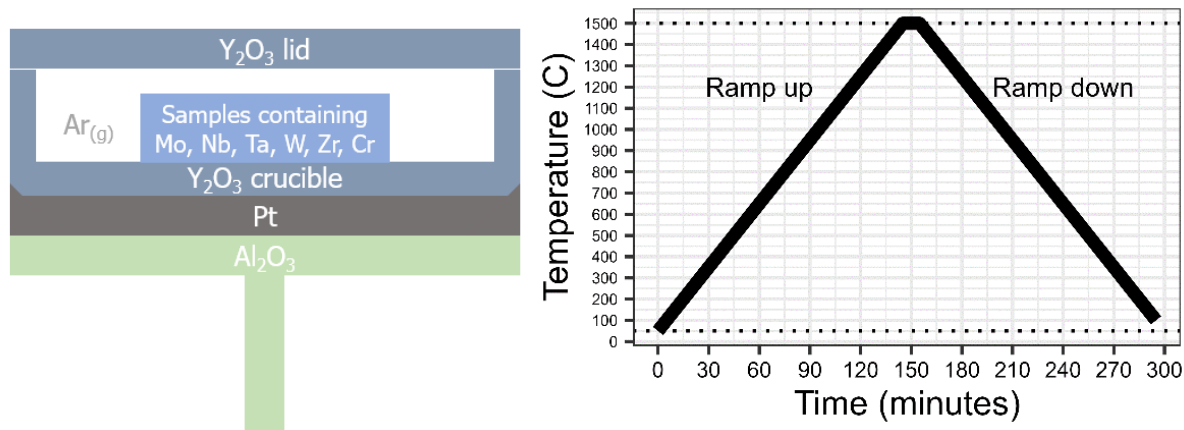


Figure 103. (Left) Simultaneous thermal analyser stalk setup. (Right) experiment programme.

Several baselines were run to ensure confidence in the simultaneous thermal analyser results. The baseline runs also allowed important microstructural changes, such as the $\alpha \rightarrow \beta$ transition in Zr, to be isolated.

6.4.1 Gold calibration

A calibration standard of Au was first run in the simultaneous thermal analyser (**Figure 104**). The experiment parameters were as follows: Ramping rate: $10^\circ\text{C}/\text{min}$. Melting temperatures: 1079.5°C and 1078.7°C ramp up, and 1045.6°C and 1042.2°C ramp down. The experimental melting point of Au from literature is 1064°C . There is a discrepancy of around $15 - 20^\circ\text{C}$ in these studies, with the literature value falling around the mean of the ramp-up and ramp-down components. The quick heating and cooling rate of $10^\circ\text{C}/\text{min}$ could be responsible for these observed discrepancies. Other factors may be the need for supercooling in order to solidify molten metals, or the exact location of the temperature probes in the simultaneous thermal analyser setup.

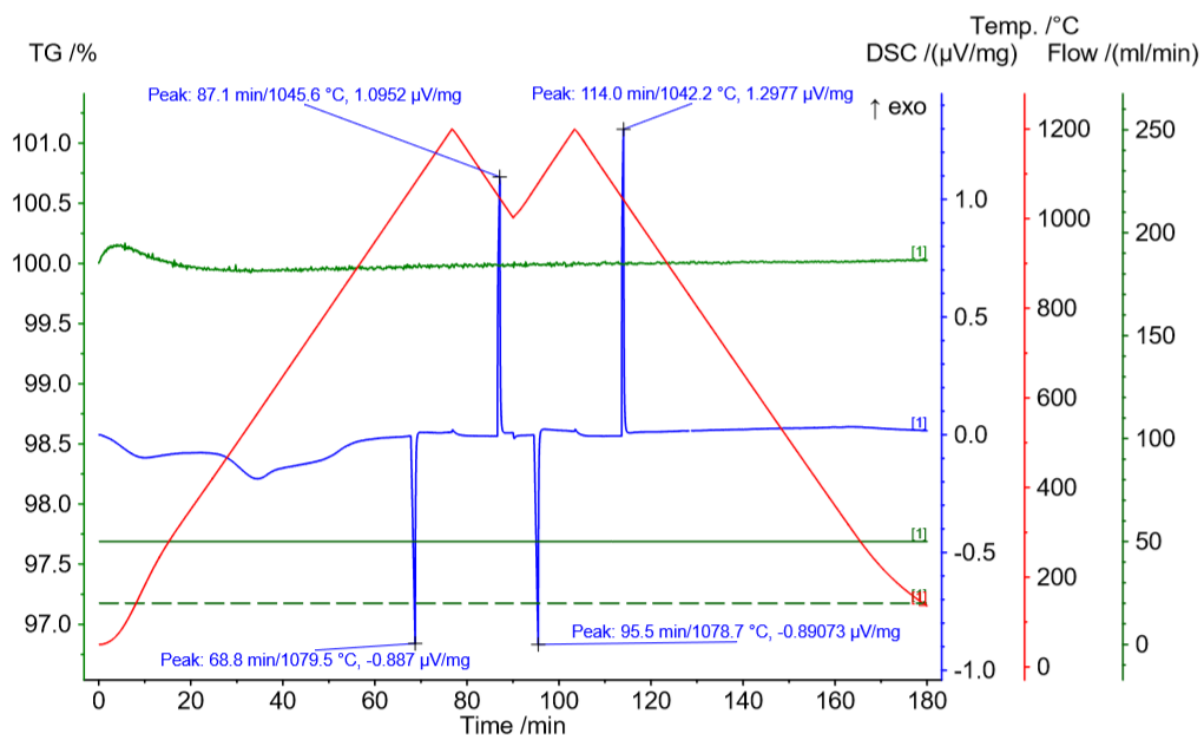


Figure 104. Differential scanning calorimetry spectrum of pure Au in an Al_2O_3 crucible.

An image of the melted gold wire is in **Figure 105**. No interaction with the Y_2O_3 crucible was observed.



Figure 105. Au wire heated to 1200 in Ar in a Y_2O_3 crucible.

6.4.2 Zirconium

To isolate heat changes caused solely by the sample elements themselves, an experiment was run on pure Zr. The $\alpha \rightarrow \beta$ phase transformation (body-centred cubic to hexagonal close-packed) for Zr was captured during the differential scanning calorimetry run at 883.2°C and 873.7°C (**Figure 106**). This compares to literature data of 863°C [349].

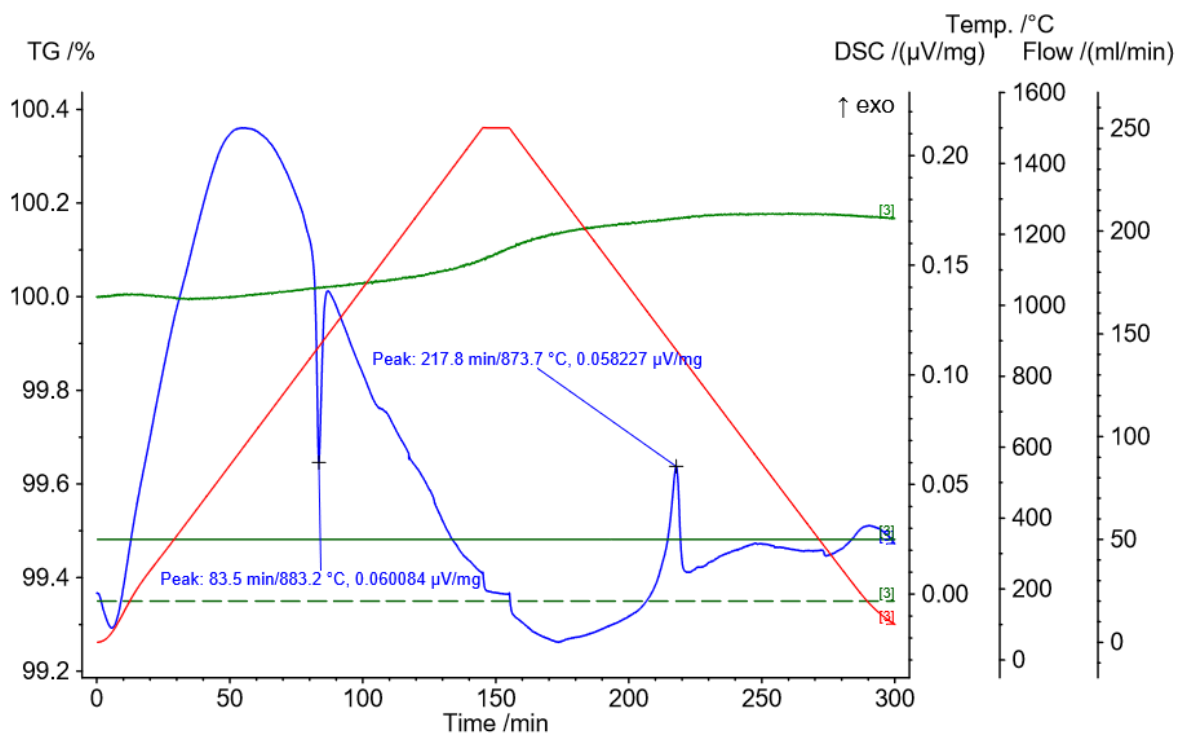


Figure 106. Differential scanning calorimetry spectrum of pure Zr in a Y_2O_3 crucible. Ramping rate: 10 $^{\circ}\text{C}/\text{min}$. Mass: 182 mg. $\alpha \rightarrow \beta$ phase transition: 883.2 $^{\circ}\text{C}$ ramp up; 873.7 $^{\circ}\text{C}$ ramp down.

6.4.3 Chromium

Chromium metal exhibited oxidation during the trial, which is attributed to a significant leak of oxygen into the vacuum chamber. The simultaneous thermal analysis spectrum is in **Figure 107**; the oxidised sample is in **Figure 108**.

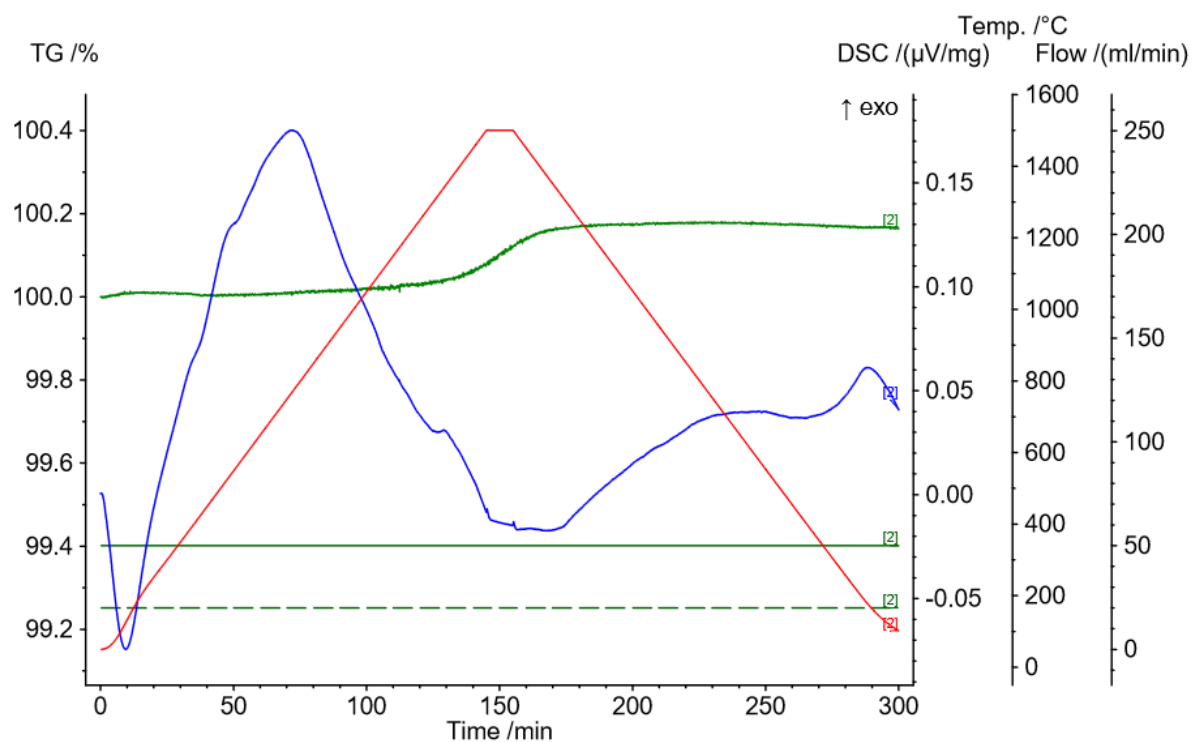


Figure 107. Differential scanning calorimetry spectrum of pure Cr in a Y_2O_3 crucible. Ramping rate: $10^\circ\text{C}/\text{min}$. Mass: 160.1 mg.

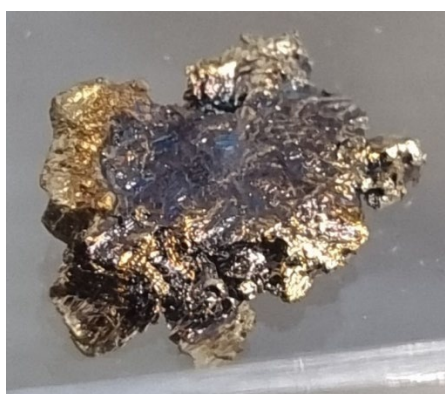


Figure 108. Cr heated in Ar atmosphere to 1500°C . Oxidation is observed on the surface.

6.4.5 Zirconium-chromium eutectic

To capture the eutectic reaction temperature of the Zr-Cr system, a 90 mg of pressed chunk of Zr and Cr were run using a Y_2O_3 crucible using a heating rate of $10^\circ\text{C}/\text{min}$ (The sample is shown in **Figure 109**). The measured Zr $\alpha \rightarrow \beta$ transition temperature was observed at 886.7°C (**Figure 110**), similar to previous trials. The Zr-Cr eutectic reaction temperature is observed $\sim 1134^\circ\text{C}$, and is not well-observed during the ramp up, which could be due to the low interfacial surface area between Cr and Zr resulting in slow diffusion and therefore a slow reaction. This causes a concomitant broadening of the differential scanning calorimetry signal. Upon melting, however, solidification of the Cr-Zr eutectic is almost immediate and is captured easily at 1334.8°C during the ramp-down segment (**Figure 110**).



Figure 109. Zr and Cr after heating in Ar to 1500°C . Discolouration of the Y_2O_3 crucible can be observed compared to **Figure 105**.

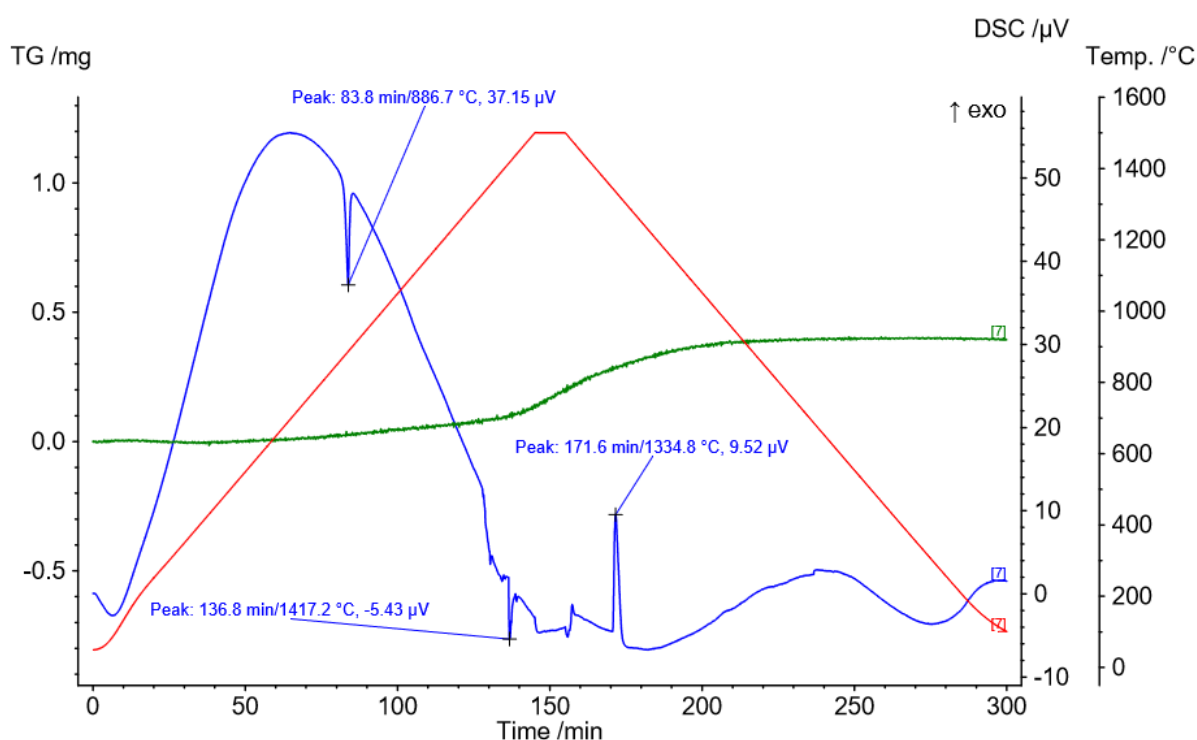


Figure 110. Differential scanning calorimetry spectrum of Zr-Cr eutectic in a Y_2O_3 crucible. Ramping rate: 10 $^{\circ}C/min$.

Necessary precautions to prevent air from entering the vacuum chamber were not taken in these experiments, this being because the model of simultaneous thermal analyser we had was prone to leakage unless fitted with an additional oxygen trap system accessory. This leakage effect can be clearly seen in the thermogravimetric analysis spectra by the oxidative mass gains observed. Furthermore, during the eutectic reaction between Cr and Zr, it was evident via energy dispersive spectroscopy (**Figure 111**) that the product had reacted with the Y_2O_3 crucible, and some additional interaction had taken place between the crucible and the platinum tray underneath.

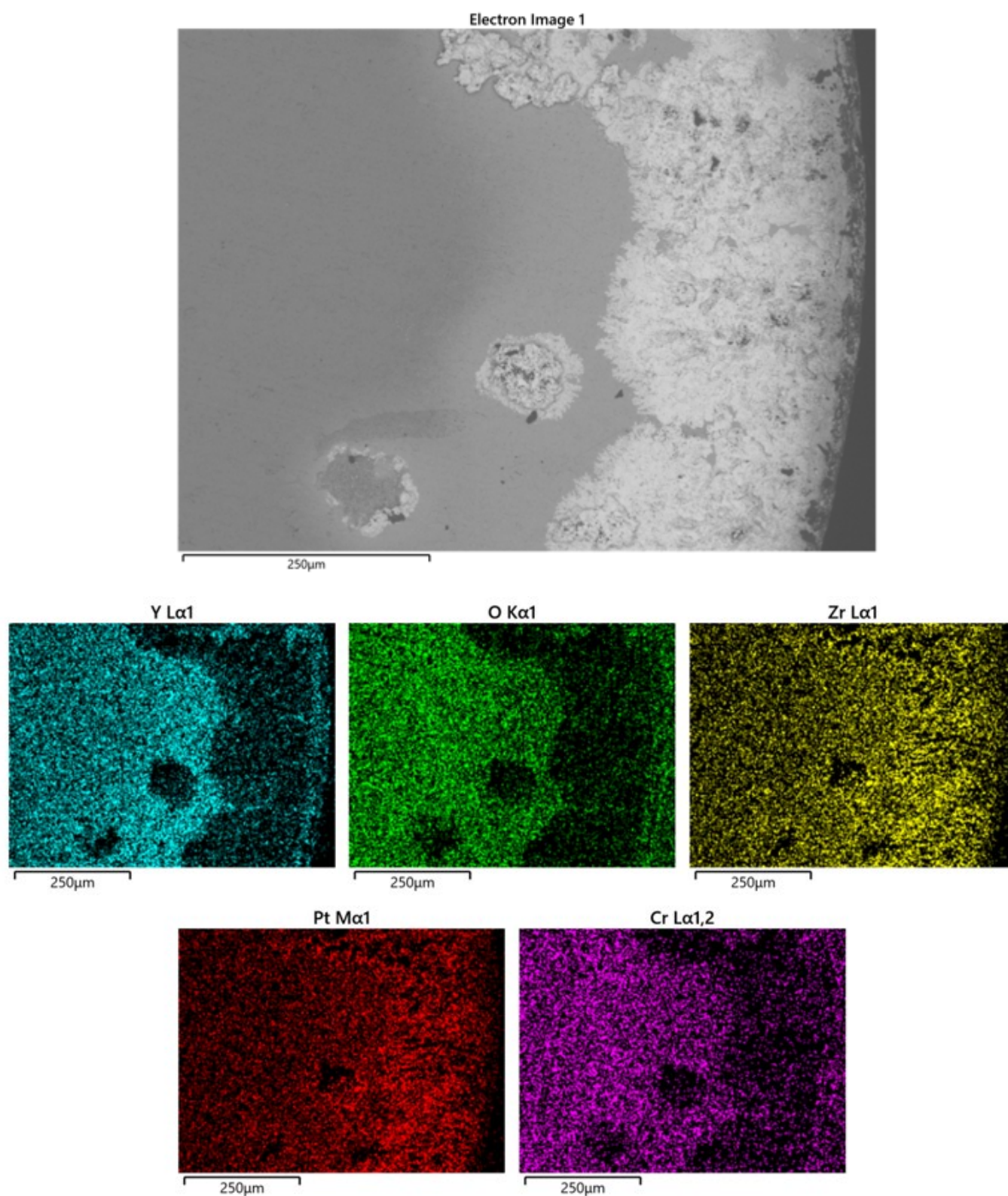


Figure 111. Energy dispersive spectroscopy scan of the underside of the Y_2O_3 crucible, indicating a reaction between Zr and Pt.

Oxidation was observed during a run of this experiment with Cr and Zr and these oxides had permeated through the Y_2O_3 crucible to the lower platinum tray. Energy dispersive spectroscopy scans of the underside of the crucible showed an oxygen depleted Zr/Pt zone indicating a Pt-Zr intermetallic. Cr_2O_3 also permeated throughout the crucible but was not involved in attacking Pt. The chemical processes involved are believed to be as follows:

1. Oxygen leaks into the vacuum chamber and oxidises both Cr and Zr.
2. Cr_2O_3 & ZrO_2 readily dissolve into the Y_2O_3 crucible and migrate towards the Pt/ Y_2O_3 interface.
3. This area of the interface between the Y_2O_3 crucible and Pt tray is oxygen-poor, and Zr released oxygen to any surrounding Y.
4. Zr & Pt then form an intermetallic.

It is thought that this process can be mitigated by minimising the leakage of oxygen into the chamber, via controlling the following four parameters:

- The flowing Ar gas should be at least 5N purity.
- An oxygen trap system should be installed onto the vacuum chamber.
- Use as little sample in the crucible as possible (<20 mg)
- Use a set of spacers between crucible and platinum tray.

These experiments were discontinued. However, a proper evaluation of a potential interlayer should establish that the interlayer does not have a detrimental effect on the eutectic reaction temperature of the current Cr coating solution.

6.5 Oxidation and interdiffusion tests of MoNbTaW-Cr coatings

6.5.1 Oxidative mass gain

Oxidation resistance is important for an accident tolerant fuel coating solution. It is therefore necessary to prove that a Cr-MoNbTaW optimised coating confers benefits in terms of oxidation, or at least does not impinge on oxidation properties of already-existing Cr solutions. The oxidation behaviour, however, may be different between these two systems and clarifying this difference will inform the case for Cr-MoNbTaW coatings. Devising a method to compare the oxidation behaviour of these two systems (and other accident tolerant fuel coatings) will also aid future feasibility studies for Zircaloy ATF coatings. The evolution of

the coating system at high temperatures (1200, 1300, $x - 30^{\circ}\text{C}$, where x is the eutectic reaction temperature of the coating system) will need to be observed. **Table 16** indicates samples for this experiment.

Table 16. Oxidation studies of Cr-MoNbTaW-Zr coating systems.

Coating system
Zr-ZrO ₂
Zr-Cr
Zr-MoNbTaW
Cr-MoNbTaW
Zr-MoNbTaW-Cr

A $3 \times 3 \times 3$ mm cube of Fe was oxidised at 400°C to begin this line of study. A baseline trial was run that took into consideration the buoyancy of the setup and the flowing of gases around the sample carrier. The baseline trial is then subtracted from the sample-run such that any changes measured from the balance can be attributed solely to the mass changes in the sample. The temperature of the sample is raised to 400°C under an Ar atmosphere, then dwelled isothermally for 3 hours in air (**Figure 112**).

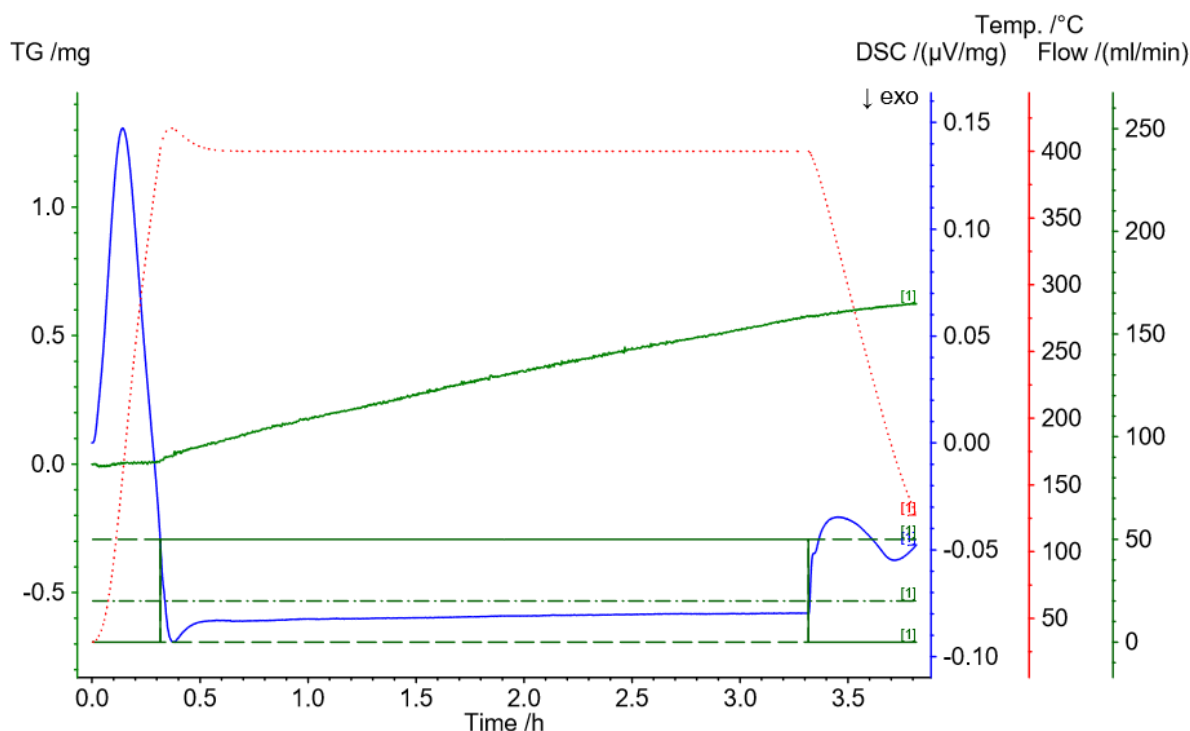


Figure 112. A thermogravimetric profile of pure Fe in air at 400°C (DSC signal in blue; TGA signal in green).

The resulting oxidative mass gain was recorded. This can then be related to the oxidative mass gain per square-centimetre of surface. Usually, this requires an accurate estimation of the surface area of the sample. A discrepancy was observed when this data was compared to literature data obtained in similar conditions [332] (**Figure 113**).

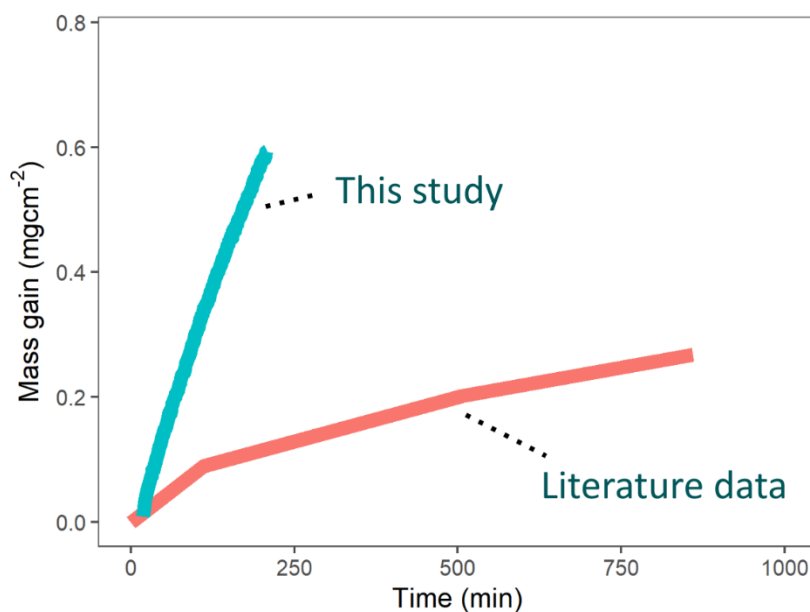


Figure 113. Oxidative mass gain of Fe. Literature data from Bertrand *et al.* [350].

The data in **Figure 113** was normalised to the surface area of the sample, which makes the oxidative mass gain sensitive to the surface area estimate. This discrepancy, therefore, was attributed to an incorrect approximation of the surface area of the specimen. In fact, for oxidative mass gain to match the data from literature, it would have to be at least 70 times greater than the approximation of a perfect cube that was used in this case. Therefore, a suitable method for estimating the surface area of samples prior to oxidation is needed. As an example, atomic force microscopy could be used to map an area of surface, which can be extrapolated to estimate the surface area of the entire sample. **Figure 114** illustrates the surface roughness of a $20 \times 20 \mu\text{m}$ surface of an unpolished Zircaloy-2 sample used in this work, which can then be used to determine surface area of the samples for oxidation studies.

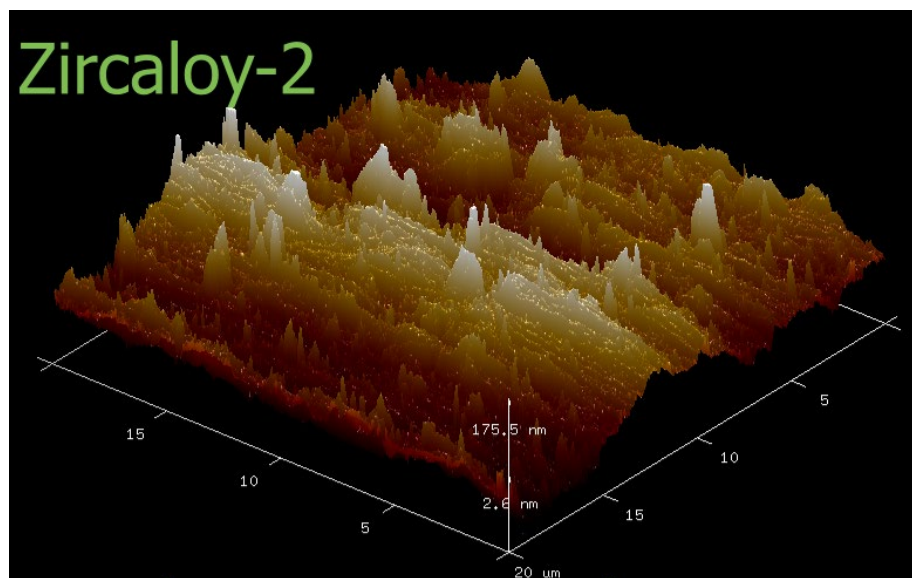


Figure 114. Atomic force micrograph of the surface of unpolished Zircaloy-2.

6.5.2 Rapid-onset oxidation temperature

A makeshift basket sample holder, made of Pt and shown in **Figure 121** and **Figure 122**, was devised to compare the oxidation behaviour of MoNbTaW/Cr fuel coating systems. This protocol would also aid future feasibility studies for other Zircaloy ATF coatings. It was hypothesised that Cr-MoNbTaW layered coating would confer general benefits over conventional Cr coatings in terms of eutectic reactions, thermal expansion, and slow interdiffusion, but an interlayered coating system may also be different compared to the simple Cr coating. To this end, a measure of the rapid-onset oxidation temperature was sought for each

coating system. The hypothesis is that the MoNbTaW interlayered coating does quicken the onset of rapid oxidation

1 × 1 cm and 1 × 2 cm samples of either uncoated or coated Zircaloy-2 were prepared (using the isomet precision cutter and direct current magnetron sputterer (**Figure 115**). The samples sought are listed in **Table 17**.

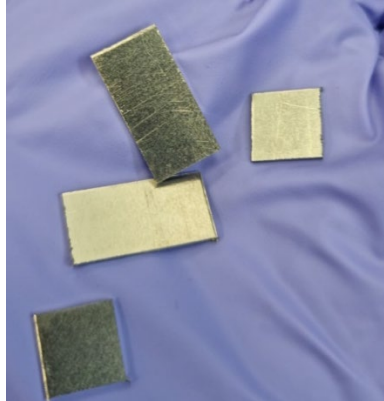


Figure 115. Example Zircaloy-2 pieces used in oxidation tests

Table 17. Rapid-onset of oxidation study for Cr-MoNbTaW-Zr coating systems.

Sample	Form
Zircaloy-2	Sheet
Zircaloy-2-MoNbTaW	Sputtered onto sheet
Zircaloy-2-Cr	Sputtered onto sheet
Zircaloy-2-MoNbTaW-Cr	Sputtered onto sheet

6.5.2.1 Preliminary Zircaloy-2 oxidations

The simultaneous thermal analyser was set up with thermogravimetric analysis mode; mass spectrometry enabled; synthetic air (20% O₂; 80% N₂); A calibration run was performed before each trial. An initial Zr sample underwent a temperature ramping cycle under flowing synthetic air to 1100°C in a staged approach (each trial of the experiment succeeded the temperature of the previous run. Subsequent design parameters were proposed from this initial experiment (**Figure 116**).

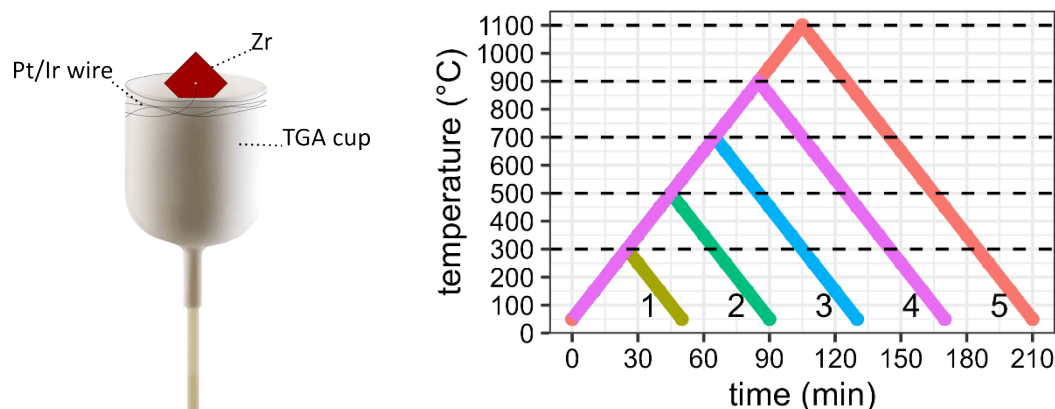


Figure 116. Oxidation study – preliminary test schematic.

The purpose of this experiment was to ensure that the Zr did not react with either the Pt/Ir wire or the Al_2O_3 TGA cup. In a more sophisticated run of this experiment, it is possible to use a DSC dangling sample holder, whose Pt thermocouples hang directly below the sample. To prove a case for using DSC in these studies, it must be proven that the sample will not compromise the integrity of the Pt thermocouples through spalling or any other reactions.

The composition of Zircaloy-2 samples was measured using X-ray fluorescence and is listed in **Table 18**.

Table 18. Composition of Zircaloy-2 sheet sample using x-ray fluorescence spectroscopy.

Scan	Zr (wt%)	Sn (wt%)	K (wt%)	Al (wt%)	Cl (wt%)	Cr (wt%)	Fe (wt%)	Mg (wt%)
1	96.5	1.2	0.9	0.3	0.2	0.2	0.2	0.1
2	96.4	1.2	1	0.3	0.2	0.2	0.2	0.2
3	96.6	1.1	0.9	0.3	0.0	0.2	0.2	0.2

The Zircaloy-2 dynamic trials in synthetic air showed little mass gain until 600 – 700°C. **Figure 117** shows the ramp up to 500°C. The trials up to 700, 900, 1100°C are in **Figure 118**, **Figure 119**, and **Figure 120**, respectively.

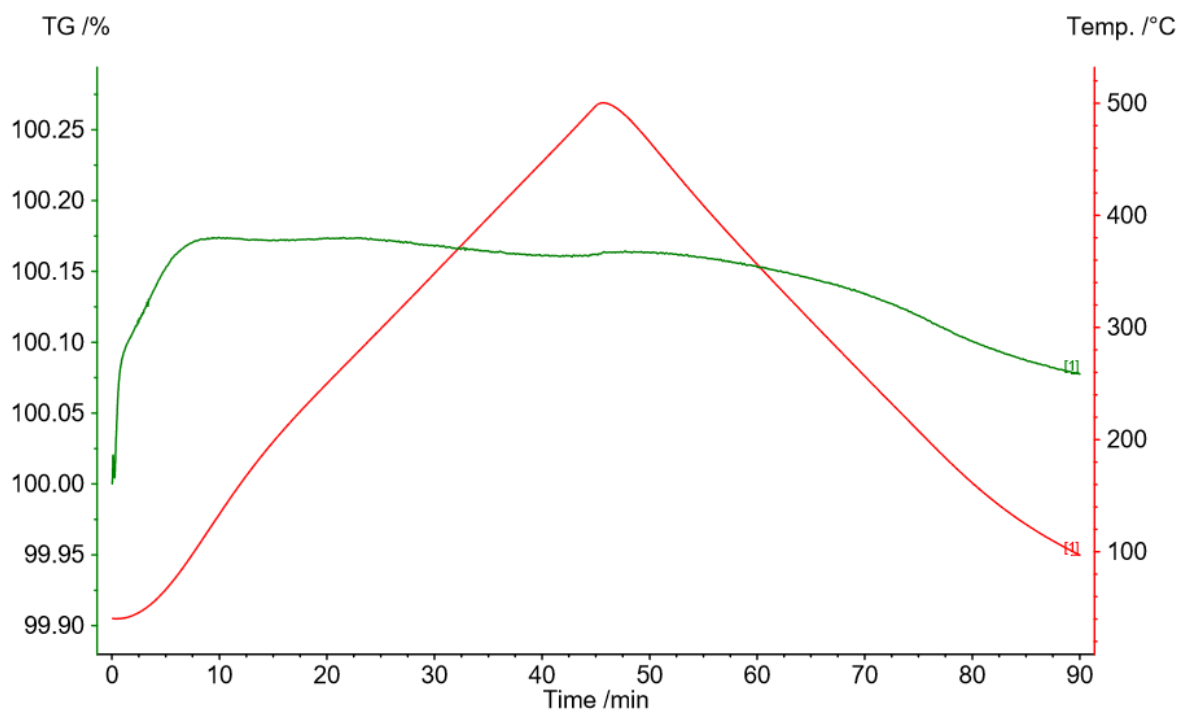


Figure 117. 500°C thermogravimetric run of Zircaloy-2. Magnitude of oxidative mass-gain is arbitrary. Gas flow rates: 50 mL/min 80% N₂ / 20% O₂; 20 mL/min Ar.

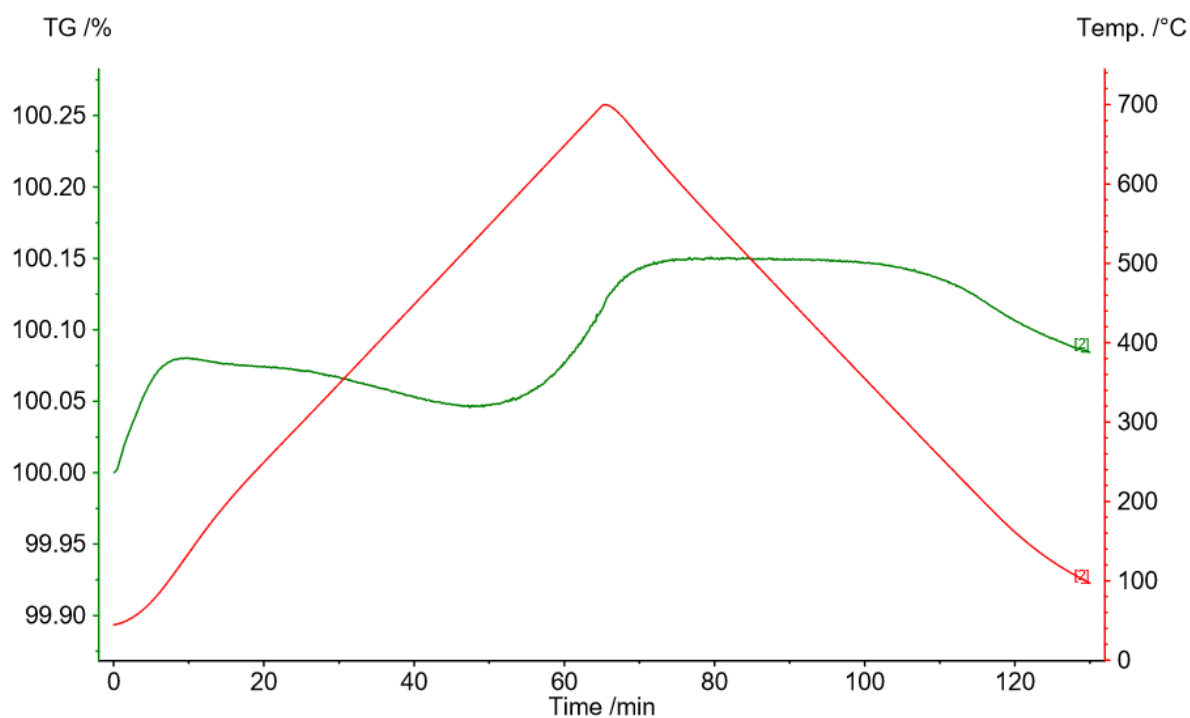


Figure 118. 700°C thermogravimetric run of Zircaloy-2. Magnitude of oxidative mass-gain is arbitrary. Gas flow rates: 50 mL/min 80% N₂ / 20% O₂; 20 mL/min Ar.

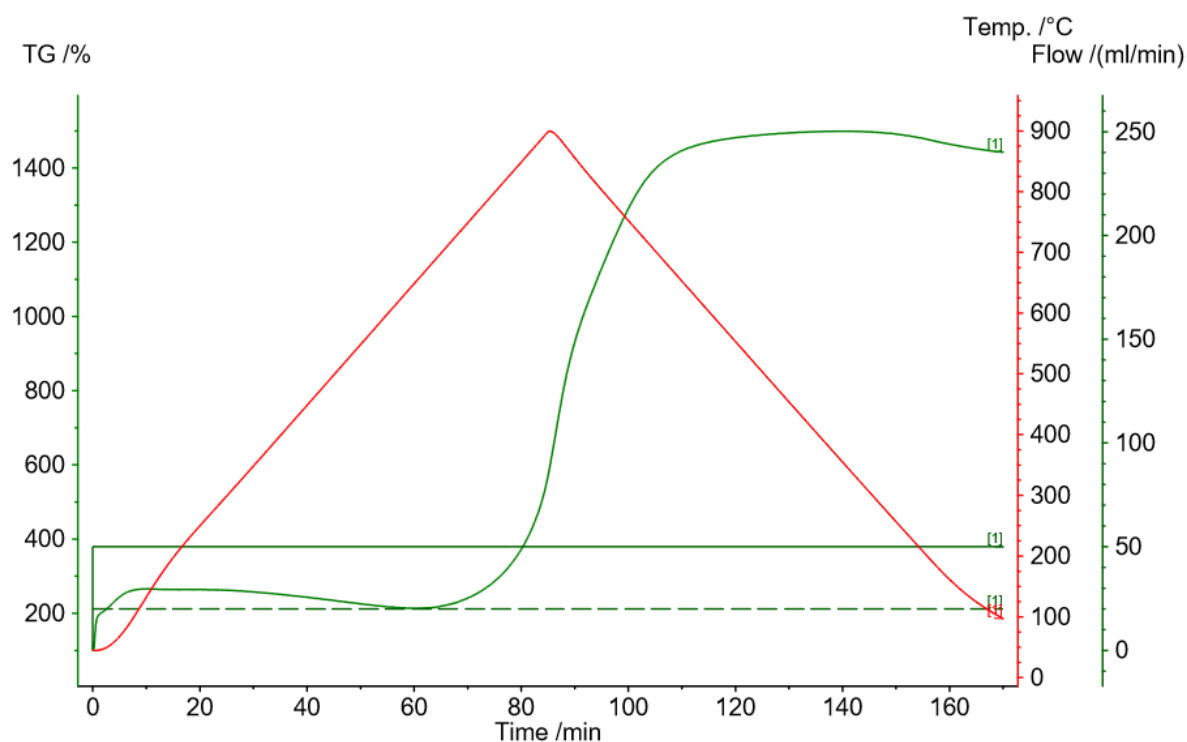


Figure 119. 900°C thermogravimetric run of Zircaloy-2. Magnitude of oxidative mass-gain is arbitrary.

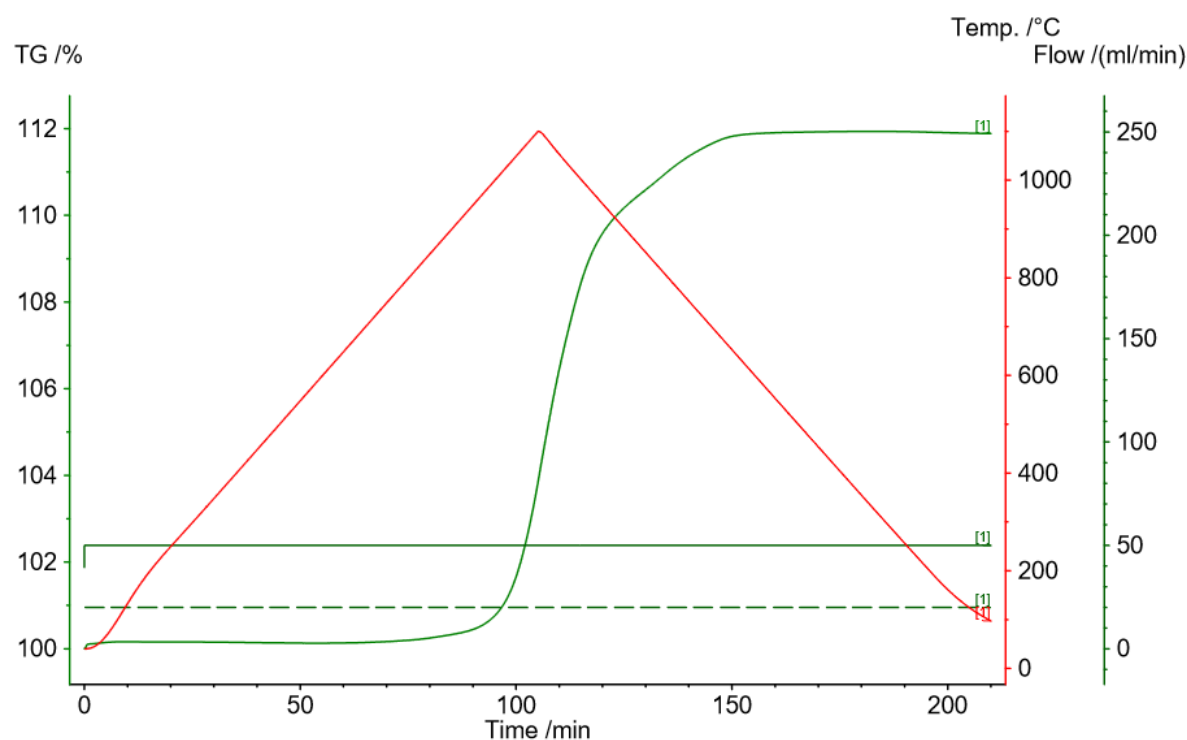


Figure 120. 1100°C thermogravimetric run of Zircaloy-2. Magnitude of oxidative mass-gain is arbitrary.

There was some minor oxidation around the sample's edges after the 300°C test. After being subjected to 500°C, the sample became darker. The sample continued to darken after 700 °C. Following an overnight trial run at 900°C, the Pt/Ir wire became significantly brighter. However, the reflectance of the sample did not revert to its initial state, indicating the presence of an oxide film. After 1100°C, where the Pt/Ir appeared to have lost its tarnish, the sample was still brightly coloured. Some specks appeared at the bottom of the TGA cup when the temperature exceeded 500°C, indicating minor spalling, but was not apparent from the camera photographs. **Figure 121** shows images of the Zircaloy-2 sample after 300 – 900°C trials. **Figure 122** shows the sample after 1100°C.

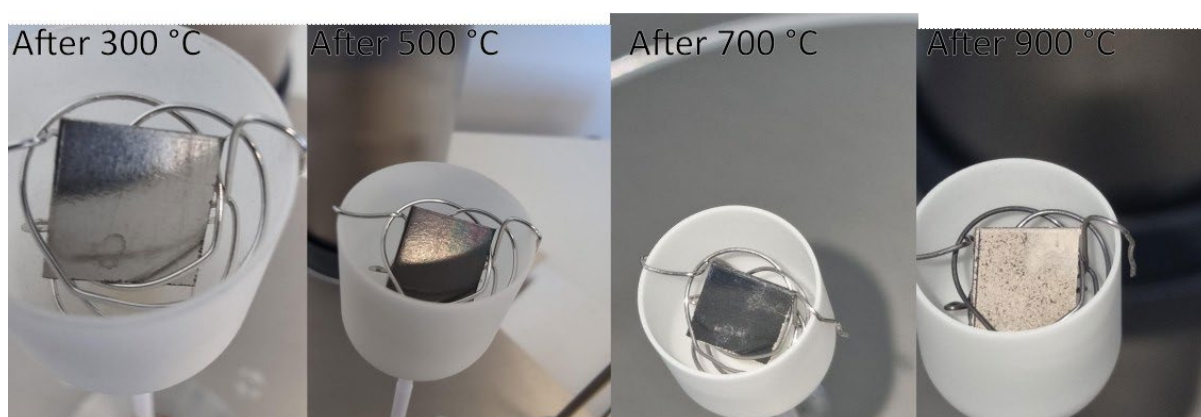


Figure 121. Photographs of Zircaloy-2 after ramp-up and ramp-down segments from 300 – 900°C.

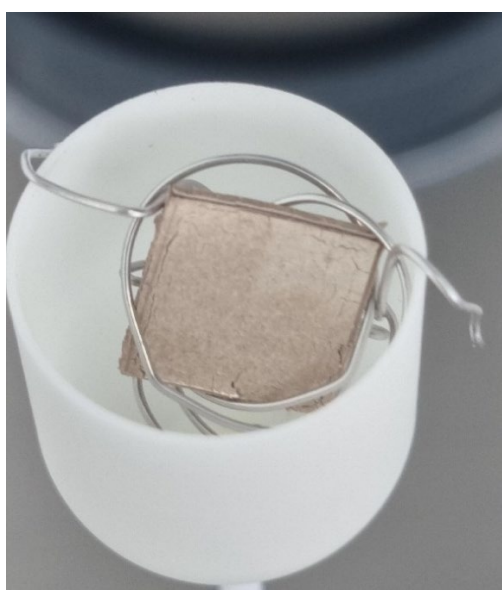


Figure 122. Photographs of Zircaloy-2 after ramp-up and ramp-down segments from 1100°C.

6.5.2.2 Zircaloy-2 oxidation baselines

Zircaloy-2 samples were heated in synthetic air (80% N₂; 20% O₂) to 1000°C to form a baseline from which to compare coated samples (**Figure 123**).

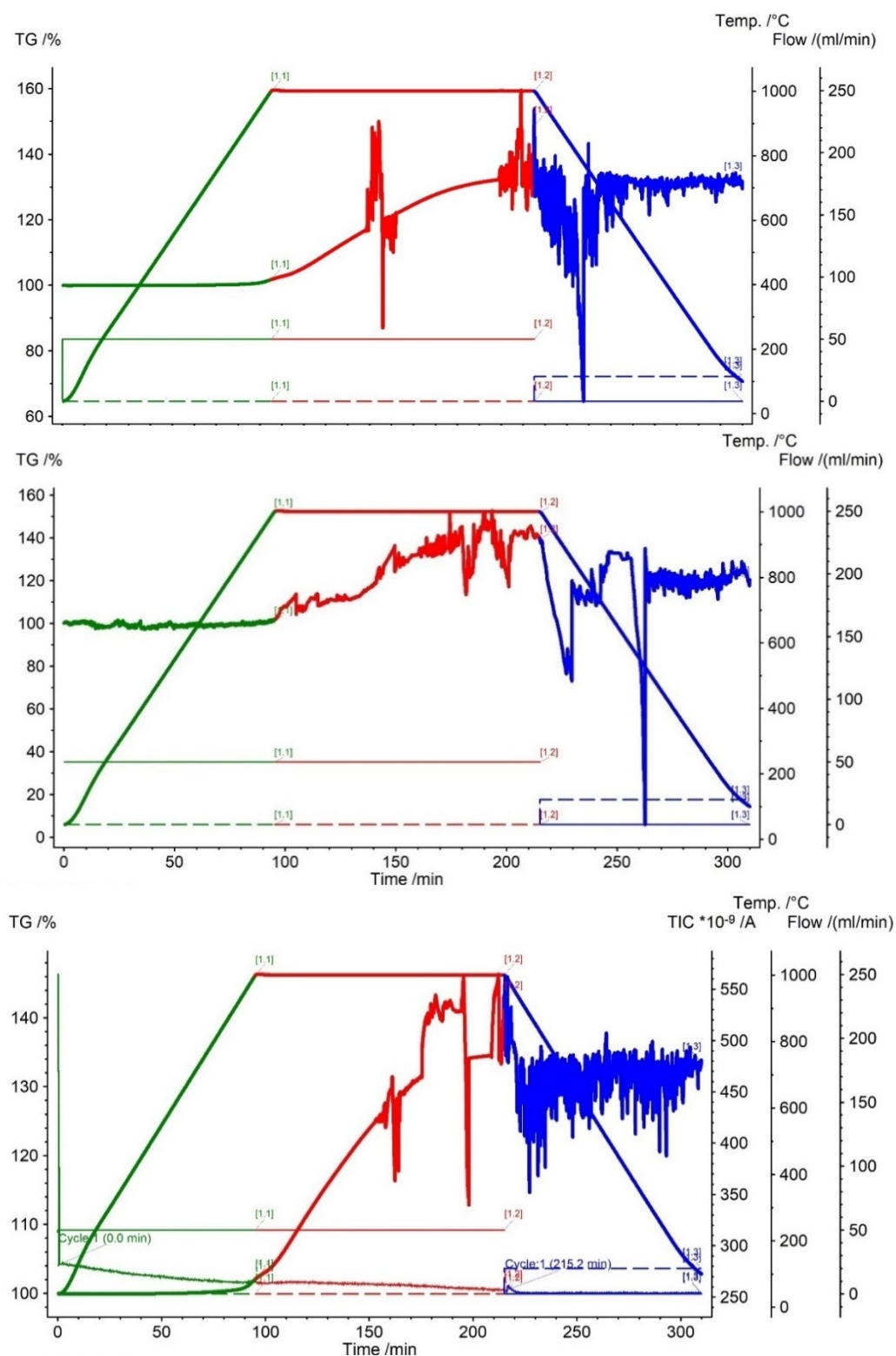


Figure 123. Three oxidation trials with Zircaloy-2 pieces. (Top) a: 869.9 mg; (Middle) b: 982.3 mg; and (Bottom) c: 927.6 mg.

In all three baseline trials, the samples oxidised, resulting in the total mass change corresponding to the oxidation of all Zr to ZrO_2 . The erratic mass changes depicted in **Figure 123** are attributed to the sample breaking up during oxidation. **Figure 124** shows an example of a Zircaloy-2 piece which has undergone oxidation in this way.



Figure 124. ZrO_2 produced from oxidising Zircaloy-2.

Figure 125 shows all three trials plotted together. Rapid-onset oxidation occurs within a few minutes of each other; however, the oxidation rate differs slightly depending on the trial. This is attributed to difference in initial masses of the Zircaloy-2 pieces (e.g., larger masses of sample will take longer to reach the same % mass change than smaller samples).

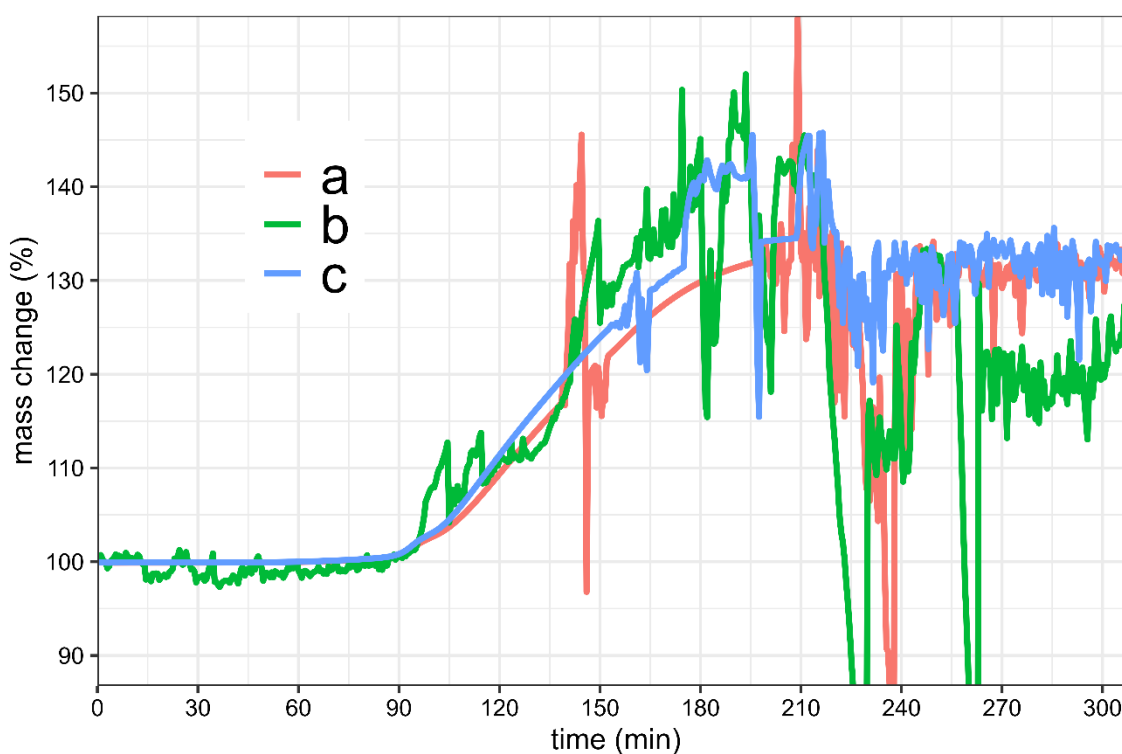


Figure 125. Oxidation trials of Zircaloy-2 pieces to 1000°C in synthetic air.

The viability of rapid-onset oxidation studies for testing the protectiveness of zirconium-based alloy coatings is suggested by this work. Onset of rapid oxidation is determined by the mass gain of the sample, which can be measured via thermogravimetric analysis. Coating systems of zirconium-based fuel claddings can be tested via this method to ensure that they delay the onset of rapid oxidation of bare Zircaloy.

To produce viable coating systems for these alloys, future effort should be dedicated to acquiring a magnetron sputterer capable of polishing samples to enhance the adherence of compositionally complex alloys onto zirconium-based substrates. The erratic mass changes in these samples can be minimised by using smaller samples of material.

Chapter 7. Conclusion

In **Chapter 1**, an introduction to accident tolerant fuels was given, with an emphasis on the necessity of such fuels and the attempts to create them. The most likely solution, chromium coatings, was highlighted, and its action was examined, as well as the problem of Zr-Cr interdiffusion which results in the formation of a ZrCr_2 intermetallic. The idea of the interlayer was introduced, and there was an overview of efforts to develop interlayers such as Mo and Ta. The founding principles and general characteristics of compositionally complex alloys were then elucidated, including their behaviour under irradiation and their beneficial properties for use in the nuclear environment. Furthermore, the phase stability and general attributes of such alloys were discussed, and the ideal properties for an interlayer material between Zr and Cr were laid out, with the potential for compositionally complex alloys to fill this role being explored.

Having conducted a thorough screening of the periodic table in **chapter 3**, several elements were identified that could form a suitable interlayer material between chromium coatings and zirconium-based alloy fuel claddings. After assessing their various physical and chemical properties, such as melting point, neutronics, ductility, thermal expansion, phase equilibria and eutectic reaction temperatures of the elements, two alloy compositions were deemed to be the most suitable. These were MoNbTaTiW, and MoNbTaW, which were found to meet the criteria presented in the literature review. Consequently, it has been established that certain alloy compositions can be employed as an interlayer material between chromium coatings and zirconium-based alloy fuel claddings. Therefore, the potential of these two complex alloy compositions should be further explored in order to optimise their performance in this application.

The assessments of the thermal expansion properties of the MoNbTaTiW and its subsystems in **Chapter 4** were carried out using density functional theory techniques, with it being demonstrated that concentrated solid solution alloys display thermal expansion behaviour which is a result of the averaging of their constituent elements. In addition, suggestions to enhance the prediction of thermal expansion in compositionally complex alloys were proposed, based on equations which had been extrapolated from composite science. Finally, the influence of vacancy defect volume on the expansion properties in compositionally complex alloys was investigated.

The results of **Chapter 5** showed that the vacancy defect enthalpies were distributed across a range of energies, which was caused by the specific atomic environment surrounding each vacancy. Additionally, it was determined that the configurational entropy associated with compositionally complex alloys had a diminishing effect on the concentration of vacancies. Further, it was found that the low-enthalpy vacancies contributed most significantly to the formation of vacancies, thus leading to solid solutions with a higher concentration of vacancies than what is found in pure metals or dilute alloys.

In **Chapter 6**, it was demonstrated that simple sintering techniques were not viable for producing refractory complex alloys. However, it was also shown that arc melting was capable of producing these alloys, and that magnetron sputtering could sputter compositionally complex alloys with only small variations in coating compositions. In light of this, some investigations were initiated in order to assess the properties of the model system MoNbTaW for accident tolerant fuel coatings. These properties, which had been highlighted in Chapter 1 as being important for a viable Cr-Zr interlayer material, included oxidation behaviour and eutectic reaction temperature. The preliminary work done thus far has not progressed enough to be able to draw reliable conclusions concerning the potential of MoNbTaW as a Cr-Zr interlayer material; however, it does provide a path for further investigation.

Chapter 8. Further work suggestions

This thesis has identified compositionally complex refractory alloys as potential interlayers between Zr and Cr in light water reactor fuel coatings. To make them suitable for nuclear environments, some of their fundamental properties, such as thermal expansion, vacancy population and migration, and phase stability, have been studied. This section proposes three future research avenues to further investigate these alloys. First, MoNbTaW and MoNbTaTiW alloys can be experimentally studied as potential interlayered coatings in real systems. Second, multicomponent CALPHAD databases and a better understanding of compositionally complex alloy systems can be used to more accurately down-select potential alloy systems for Zr coatings. Lastly, further investigations are needed to understand the general fundamental mechanisms of compositionally complex alloys, including diffusion, radiation response, microstructural evolution, propensity for elements to cluster or segregate, thermal stability, general mechanical properties, and thermophysical properties such as thermal conductivity and thermal expansion.

7.1 MoNbTaW and MoNbTaTiW as a Zr-Cr interlayered coating system.

From these investigations, the alloys MoNbTaW and MoNbTaTiW are proposed as prototypes to test interlayered coating systems. If these materials are to be investigated in small-scale laboratory experiments, then there are some important questions to answer:

- Can these alloys suitably keep Cr and Zr apart for an amount of time in loss-of-coolant conditions (1000 – 1300°C)?
- Can these alloys suppress intermetallics to a greater degree than single elements such as Mo.
- Do these alloys improve on the eutectic reaction temperature between Zr and Cr, and other single element interlayers?
- If intermetallic compounds form during evolution of the coating system, how then do the mechanical, thermal, and physical properties compare to the $\text{Zr}(\text{Cr}, \text{Fe})_2$ Laves phase observed in Cr-coatings?

From these initial experiments, it can be determined if MoNbTaW and MoNbTaTiW are suitable alloys to pursue for more thorough investigations on things such as effect on thermal transfer through the coating, effect on oxidation/redox reactions, and effect on

neutronic penalties. Moreover, experiments based on thermal diffusion couples could be set up to investigate elemental migration through the interlayer. If the small-scale laboratory tests are encouraging, then the potential interlayer system can be tested in autoclaves for longer-term oxidation studies. Characterisation techniques could include electron-probe microanalysis or glow-discharge optical emission spectroscopy.

An example experiment to assess the benefits that matching the thermal expansion coefficient of the complex alloy interlayer is given in the next section.

7.1.1 Thermal cycling of MoNbTaW coating

One of the reasons for choosing MoNbTaW as an interlayer was for the compatibility of thermal expansion properties. This property should in theory result in less spalling during thermal cycling. This can be tested through thermal cycling test for Zircaloy ATF coatings. Previous thermal expansion results (**Chapter 4**) can be validated by showing that an optimised MoNbTaW coating confers benefits over conventional Cr coatings in a series of thermal cycling tests. **Table 19** shows example samples for this experiment.

Table 19. Plan for thermal cycling tests of Cr-MoNbTaW-Zr coating systems.

Coating system	Time to spall (Arb.)
Zr-ZrO ₂	X
Zr-Cr	Y
Zr-MoNbTaW	Z
Cr-MoNbTaW	A
Zr-MoNbTaW-Cr	B

Such a test can be done in a simultaneous thermal analyser in Ar atmosphere. Spalling may be detected using the change in mass of the sample over time. Alternatively, a furnace with a camera attached may allow to observe spalling during heating cycles.

7.2. Searching the multi-dimensional phase space for potential alloys.

This dissertation does not even consider the vast range of alloys that could be employed as an interlayer material between Cr and Zr. The sheer number of alloy compositions for

complex alloys is staggering, and the literature has barely begun to explore them. Development of CALPHAD techniques to characterize multi-component systems for complex alloys is underway, but so far only limited to ternary systems, which are usually only evaluated tentatively. A comprehensive thermochemical model for certain compositionally complicated alloy systems would, however, be beneficial in identifying suitable alloy systems. Coupled with suitable fabrication facilities for complex alloys, the CALPHAD technique is an effective way to study these systems.

The parametric approach for phase stability of concentrated solid solutions has the unique benefit of being able to rapidly gather data. It is, however, a purely phenomenological technique, and must be used in conjunction with experiment or other theoretical models to be of any use. There is potential to improve this technique through the creation of databases based on single-phase alloys which have been thoroughly characterised, as well as by exploring more useful parameters to explain the capacity of an alloy to form a single-phase. Furthermore, it could be beneficial to incorporate mechanical properties into such a database, allowing for potential alloy systems to be screened more effectively. If such a database existed in combination with a program to automatically describe the formability of concentrated solid solutions, it would be of great use to the compositionally complex alloy community.

7.3. Fundamentals of refractory compositionally complex alloys.

This thesis has advanced the understanding of equilibrium concentrations of vacancy defects in concentrated solid solutions. It was suggested that vacancies are much more abundant in compositionally complex alloys than in their conventional alloy counterparts. Nevertheless, further investigation is still required to explore defect clustering, migration, and mechanical property effects. Kinetic Monte-Carlo codes, which are capable of modelling vacancy-mediated diffusion, could be beneficial in comprehending the migration of vacancies in compositionally complex alloys.

Compositionally complex alloys, such as those made from a variety of metals, have been found to possess remarkable radiation resistance. This is an impressive characteristic that has been the impetus for much research, yet a satisfying fundamental explanation for this radiation resistance does not yet exist. Various hypotheses have been proposed, but none definitively explain the phenomenon. Further experiments are needed to provide a greater understanding of the radiation resistance of these alloys.

Bibliography

- [1] “Analysis: A month on, Japan nuclear crisis still scarring - International Business Times.” [Online]. Available: <https://web.archive.org/web/20120815080111/http://www.ibtimes.co.in/articles/132391/20110409/japan-nuclear-crisis-radiation.htm>. [Accessed: 22-Sep-2020].
- [2] R. A. Eddy and R. P. Clarke, *Warnings: Finding Cassandras to stop catastrophe*. Ecco Press, 2017.
- [3] “Report Finds Japan Underestimated Tsunami Danger - The New York Times.” [Online]. Available: <https://www.nytimes.com/2011/06/02/world/asia/02japan.html>. [Accessed: 22-Sep-2020].
- [4] H. Rickover, L. Geiger, and B. Lustman, “History of the Development of Zirconium Alloys for Use in Nuclear Reactors,” 1975.
- [5] N. Nakazato, H. Kishimoto, Y. Kohno, and A. Kohyama, “SiC/SiC Fuel Cladding by Nite Process for Innovative LWR-Cladding Forming Process Development,” *Ceram. Trans.*, vol. 246, pp. 109–115, Mar. 2014.
- [6] D. Kim, H. G. Lee, J. Y. Park, and W. J. Kim, “Fabrication and measurement of hoop strength of SiC triplex tube for nuclear fuel cladding applications,” *J. Nucl. Mater.*, vol. 458, pp. 29–36, Mar. 2015.
- [7] K. Shapovalov, G. M. Jacobsen, L. Alva, N. Truesdale, C. P. Deck, and X. Huang, “Strength of SiCf-SiCm composite tube under uniaxial and multiaxial loading,” *J. Nucl. Mater.*, vol. 500, pp. 280–294, Mar. 2018.
- [8] C. Azevedo, “Selection of fuel cladding material for nuclear fission reactors,” *Eng. Fail. Anal.*, vol. 18, no. 8, pp. 1943–1962, Dec. 2011.
- [9] S. Bragg-Sitton, “Development of advanced accident-tolerant fuels for commercial LWRs,” *Nuclear News*, no. March, pp. 83–91, 2014.
- [10] M. F. Beaux *et al.*, “Chemical vapor deposition of Mo tubes for fuel cladding applications,” *Surf. Coatings Technol.*, vol. 337, pp. 510–515, Mar. 2018.

- [11] H. Andren, L. Mattsson, and U. Rolander, “Atom-Probe Analysis of Zircaloy,” *J. Phys. Colloq.*, vol. 47, no. C2, 1986.
- [12] L. Baker Jr. and L. C. Just, “Studies of Metal-Water Reactions at High Temperatures. III. Experimental and Theoretical Studies of the Zirconium-Water Reaction (ANL-6548),” *United States N. p.*, May 1962.
- [13] “The Japanese Nuclear Emergency – Sydney Technical Presentation,” *Engineers Australia*, 30-Sep-2011. [Online]. Available: https://web.archive.org/web/20110930143152/http://www.engineersaustralia.org.au/shadomx/apps/fms/fmsdownload.cfm?file_uuid=624CEC6F-F845-73AA-003E-B1433462956D&siteName=ieaust. [Accessed: 22-Sep-2020].
- [14] G. Saji, “Root cause study on hydrogen generation and explosion through radiation-induced electrolysis in the Fukushima Daiichi accident,” *Nucl. Eng. Des.*, vol. 307, pp. 64–76, Oct. 2016.
- [15] S. B. Sitten, “Application of MELCOR to ATF concepts for severe accident analysis,” in *EPRI/INL/DOE Workshop on Accident Tolerant Fuel*, 2014.
- [16] I. Charit, “Accident Tolerant Nuclear Fuels and Cladding Materials,” *JOM*, vol. 70, no. 2. Minerals, Metals and Materials Society, pp. 173–175, 01-Feb-2018.
- [17] H. Chen, X. Wang, and R. Zhang, “Application and Development Progress of Cr-Based Surface Coating in Nuclear Fuel Elements: II. Current Status and Shortcomings of Performance Studies,” *Coatings*, vol. 10, no. 9, p. 835, Aug. 2020.
- [18] “Development Strategy for Advanced LWR Fuels with Enhanced Accident Tolerance (Conference) | OSTI.GOV.” [Online]. Available: <https://www.osti.gov/biblio/1133810>. [Accessed: 24-Feb-2021].
- [19] H. Shah *et al.*, “Development of Surface Coatings for Enhanced Accident Tolerant Fuel,” *Water React. Fuel Perform. Meet.*, no. October, 2017.
- [20] J. Bischoff *et al.*, “Cr-coated cladding development at Framatome,” in *Topfuel 2018 - Light Water Reactor (LWR) Fuel Performance Meeting*, 2018.
- [21] B. Cheng, Y. J. Kim, and P. Chou, “Improving Accident Tolerance of Nuclear Fuel

- with Coated Mo-alloy Cladding,” *Nuclear Engineering and Technology*, vol. 48, no. 1, pp. 16–25, 2016.
- [22] J.-C. C. Brachet *et al.*, “Behavior under LOCA conditions of enhanced accident tolerant chromium coated zircaloy-4 claddings,” in *Top Fuel 2016: LWR Fuels with Enhanced Safety and Performance*, 2016, pp. 1173–1178.
 - [23] H.-G. Kim *et al.*, “Progress of surface modified Zr cladding development for ATF in Korea,” in *Water Reactor Fuel Performance Meeting*, 2017, vol. 10.
 - [24] H. G. Kim *et al.*, “Out-of-pile performance of surface-modified Zr cladding for accident tolerant fuel in LWRs,” *J. Nucl. Mater.*, vol. 510, pp. 93–99, Nov. 2018.
 - [25] J. yong J. H. J. yong Park, H. G. Kim, J. yong J. H. J. yong Park, Y. Il Jung, D. J. Park, and Y. H. Koo, “High temperature steam-oxidation behavior of arc ion plated Cr coatings for accident tolerant fuel claddings,” *Surf. Coatings Technol.*, vol. 280, pp. 256–259, Oct. 2015.
 - [26] S. J. Zinkle, K. A. Terrani, J. C. Gehin, L. J. Ott, and L. L. Snead, “Accident tolerant fuels for LWRs: A perspective,” *J. Nucl. Mater.*, vol. 448, no. 1–3, pp. 374–379, May 2014.
 - [27] M. T. Farmer, L. Leibowitz, K. A. Terrani, and K. R. Robb, “Scoping assessments of ATF impact on late-stage accident progression including molten core-concrete interaction,” *J. Nucl. Mater.*, vol. 448, no. 1–3, pp. 534–540, May 2014.
 - [28] K. A. Terrani, S. J. Zinkle, and L. L. Snead, “Advanced oxidation-resistant iron-based alloys for LWR fuel cladding,” *J. Nucl. Mater.*, vol. 448, no. 1–3, pp. 420–435, May 2014.
 - [29] C. Tang, M. Stueber, H. J. Seifert, and M. Steinbrueck, “Protective coatings on zirconium-based alloys as accident-Tolerant fuel (ATF) claddings,” *Corros. Rev.*, vol. 35, no. 3, pp. 141–165, Aug. 2017.
 - [30] K. Hauffe and V. Martinez, “Oxidation and Corrosion of Tin-Coated Zircaloy-4,” *J. Electrochem. Soc.*, vol. 123, no. 5, pp. 595–602, May 1976.
 - [31] I. Idarraga-Trujillo *et al.*, “Assessment at CEA of coated nuclear fuel cladding for

- LWRS with increased margins in loca and beyond loca conditions,” in *LWR Fuel Performance Meeting, Top Fuel 2013*, 2013, vol. 2, pp. 860–867.
- [32] H.-G. Kim *et al.*, “High-temperature oxidation behavior of Cr-coated Zirconium alloy,” in *LWR Fuel Performance Meeting, TopFuel*, 2013.
 - [33] H. G. Kim, I. H. Kim, Y. Il Jung, D. J. Park, J. Y. Park, and Y. H. Koo, “Adhesion property and high-temperature oxidation behavior of Cr-coated Zircaloy-4 cladding tube prepared by 3D laser coating,” *J. Nucl. Mater.*, vol. 465, pp. 531–539, Jul. 2015.
 - [34] D. J. Park, H. G. Kim, Y. Il Jung, J. H. Park, J. H. Yang, and Y. H. Koo, “Behavior of an improved Zr fuel cladding with oxidation resistant coating under loss-of-coolant accident conditions,” *J. Nucl. Mater.*, vol. 482, pp. 75–82, Dec. 2016.
 - [35] J. Carr, G. Vasudevamurthy, L. Snead, B. Hinderliter, and C. Massey, “Investigations of Aluminum-Doped Self-Healing Zircaloy Surfaces in Context of Accident-Tolerant Fuel Cladding Research,” *J. Mater. Eng. Perform.*, vol. 25, no. 6, pp. 2347–2355, Jun. 2016.
 - [36] W. G. Luscher, E. R. Gilbert, S. G. Pitman, and E. F. Love, “Surface modification of Zircaloy-4 substrates with nickel zirconium intermetallics,” *J. Nucl. Mater.*, vol. 433, no. 1–3, pp. 514–522, Feb. 2013.
 - [37] K. A. Terrani, C. M. Parish, D. Shin, and B. A. Pint, “Protection of zirconium by alumina- and chromia-forming iron alloys under high-temperature steam exposure,” *J. Nucl. Mater.*, vol. 438, no. 1–3, pp. 64–71, Jul. 2013.
 - [38] W. Zhong, P. A. Mouche, X. Han, B. J. Heuser, K. K. Mandapaka, and G. S. Was, “Performance of iron-chromium-aluminum alloy surface coatings on Zircaloy 2 under high-temperature steam and normal BWR operating conditions,” *J. Nucl. Mater.*, vol. 470, pp. 327–338, Mar. 2016.
 - [39] R. H. Baney, P. Butt, G. Demkowicz, and J. S. Tulenko, “An Innovative Ceramic Corrosion Protection System for Zircaloy Cladding,” Oakland, CA, Feb. 2003.
 - [40] Y. Al-Olayyan, G. E. Fuchs, R. Baney, and J. Tulenko, “The effect of Zircaloy-4 substrate surface condition on the adhesion strength and corrosion of SiC coatings,” *J.*

Nucl. Mater., vol. 346, no. 2–3, pp. 109–119, Nov. 2005.

- [41] M. Pantano, V. Avincola, P. A. De Seze, T. McKrell, and M. S. Kazimi, “High temperature steam oxidation performance of max phase (Ti 2AlC) coated ZIRLO,” in *International Congress on Advances in Nuclear Power Plants*, 2014, vol. 3, pp. 2126–2135.
- [42] B. R. Maier, B. L. Garcia-Diaz, B. Hauch, L. C. Olson, R. L. Sindelar, and K. Sridharan, “Cold spray deposition of Ti₂AlC coatings for improved nuclear fuel cladding,” *J. Nucl. Mater.*, vol. 466, pp. 712–717, Nov. 2015.
- [43] H. Yeom *et al.*, “Laser surface annealing and characterization of Ti₂AlC plasma vapor deposition coating on zirconium-alloy substrate,” *Thin Solid Films*, vol. 615, pp. 202–209, Sep. 2016.
- [44] D. A. Roberts, “Magnetron Sputtering and Corrosion of Ti-Al-C and Cr-Al-C coatings for Zr-alloy Nuclear Fuel Cladding,” University of Tennessee, 2016.
- [45] F. Khatkhatay *et al.*, “Superior corrosion resistance properties of TiN-based coatings on Zircaloy tubes in supercritical water,” *J. Nucl. Mater.*, vol. 451, no. 1–3, pp. 346–351, Aug. 2014.
- [46] E. Alat, A. T. Motta, R. J. Comstock, J. M. Partezana, and D. E. Wolfe, “Ceramic coating for corrosion (c3) resistance of nuclear fuel cladding,” *Surf. Coatings Technol.*, vol. 281, pp. 133–143, Nov. 2015.
- [47] K. Daub, R. Van Nieuwenhove, and H. Nordin, “Investigation of the impact of coatings on corrosion and hydrogen uptake of Zircaloy-4,” *J. Nucl. Mater.*, vol. 467, pp. 260–270, Dec. 2015.
- [48] D. Jin *et al.*, “A study of the zirconium alloy protection by Cr₃C₂-NiCr coating for nuclear reactor application,” *Surf. Coatings Technol.*, vol. 287, pp. 55–60, Feb. 2016.
- [49] A. S. Kuprin, V. Belous, and V. V Bryk, “High-temperature air oxidation of E110 and Zr-1Nb alloys claddings with coatings View project.”
- [50] A. S. Kuprin *et al.*, “Vacuum-arc chromium-based coatings for protection of zirconium alloys from the high-temperature oxidation in air,” *J. Nucl. Mater.*, vol. 465, pp. 400–

406, Jun. 2015.

- [51] U. Wiklund, P. Hedenqvist, S. Hogmark, B. Stridh, and M. Arbell, “Multilayer coatings as corrosion protection of Zircaloy,” *Surf. Coatings Technol.*, vol. 86–87, no. PART 2, pp. 530–534, Dec. 1996.
- [52] J. Bischoff, C. Delafoy, C. Vauglin, ... P. B.-N. E., and undefined 2018, “AREVA NP’s enhanced accident-tolerant fuel developments: focus on Cr-coated M5 cladding,” *Elsevier*.
- [53] J. C. Brachet *et al.*, “CEA studies on advanced nuclear fuel claddings for enhanced Accident Tolerant LWRs Fuel(LOCA and beyond LOCA conditions),” in *Fontevraud 8 - Contribution of Materials Investigations and Operating Experience to LWRs’ Safety, Performance and Reliability*, 2014, no. September, p. 10.
- [54] J.-C. Brachet, M. Le Saux, and M. Tupin, “On-going studies at CEA on chromium coated zirconium based nuclear fuel claddings for enhanced accident tolerant LWRs fuel,” in *Topfuel - Enhanced Accident Tolerant Fuels for Nuclear Light Water Reactors*, 2015.
- [55] J. Bischoff *et al.*, “AREVA NP’s enhanced accident-tolerant fuel developments: Focus on Cr-coated M5 cladding,” *Nucl. Eng. Technol.*, vol. 50, no. 2, pp. 223–228, Mar. 2018.
- [56] J. Brachet *et al.*, “Behavior of chromium coated M5TM claddings under loca conditions,” in *Water Reactor Fuel Performance Meeting*, 2017, vol. 10.
- [57] J. C. J. Brachet *et al.*, “Early studies on Cr-Coated Zircaloy-4 as enhanced accident tolerant nuclear fuel claddings for light water reactors,” *J. Nucl. Mater.*, vol. 517, pp. 268–285, Apr. 2019.
- [58] J. C. Brachet *et al.*, “High temperature steam oxidation of chromium-coated zirconium-based alloys: Kinetics and process,” *Corros. Sci.*, vol. 167, p. 108537, May 2020.
- [59] M. Ševeček *et al.*, “Development of Cr cold spray-coated fuel cladding with enhanced accident tolerance,” *Nucl. Eng. Technol.*, vol. 50, no. 2, pp. 229–236, Mar. 2018.

- [60] B. Maier *et al.*, “Development of cold spray chromium coatings for improved accident tolerant zirconium-alloy cladding,” *J. Nucl. Mater.*, vol. 519, pp. 247–254, Jun. 2019.
- [61] X. Hu *et al.*, “High-temperature oxidation of thick Cr coating prepared by arc deposition for accident tolerant fuel claddings,” *J. Nucl. Mater.*, vol. 519, pp. 145–156, Jun. 2019.
- [62] M. Wagih, B. Spencer, J. Hales, and K. Shirvan, “Fuel performance of chromium-coated zirconium alloy and silicon carbide accident tolerant fuel claddings,” *Annals of Nuclear Energy*, vol. 120, pp. 304–318, 2018.
- [63] A. K. Evans *et al.*, “Fabrication, characterization, and testing of Cr-coated Zr alloy nuclear fuel rod cladding for enhanced accident tolerance,” in *Top Fuel 2019 - Light Water Reactor Fuel Performance*, 2019, pp. 846–872.
- [64] I. Idarraga-Trujillo *et al.*, “Assessment at CEA of coated nuclear fuel cladding for LWRs with increasing margins in LOCA and beyond LOCA conditions,” in *TopFuel LWR Fuel Performance Meeting*, 2013, vol. 2, pp. 860–867.
- [65] J. Krejčí *et al.*, “Development and testing of multicomponent fuel cladding with enhanced accidental performance,” *Nucl. Eng. Technol.*, vol. 52, no. 3, pp. 597–609, Mar. .
- [66] H.-B. Ma *et al.*, “Oxidation behavior of Cr-coated zirconium alloy cladding in high-temperature steam above 1200 °C,” *npj Mater. Degrad.*, vol. 5, no. 1, p. 7, Dec. 2021.
- [67] H. Yeom, B. Maier, G. Johnson, T. Dabney, J. Walters, and K. Sridharan, “Development of cold spray process for oxidation-resistant FeCrAl and Mo diffusion barrier coatings on optimized ZIRLO™,” *J. Nucl. Mater.*, vol. 507, pp. 306–315, Aug. 2018.
- [68] J.-C. Brachet *et al.*, “Assessment at CEA of coated nuclear fuel cladding for LWRs with increasing margins in LOCA and beyond LOCA conditions,” in *LWR Fuel Performance Meeting*, 2013, pp. 860–867.
- [69] J. Bischoff *et al.*, “Development of Cr-coated Zirconium Alloy Cladding for Enhanced Accident Tolerance,” in *Top Fuel - Light Water Reactor (LWR) Fuel Performance*

Meeting, 2016.

- [70] W. Zhong, P. A. Mouche, and B. J. Heuser, “Response of Cr and Cr-Al coatings on Zircaloy-2 to high temperature steam,” *J. Nucl. Mater.*, vol. 498, pp. 137–148, Jan. 2018.
- [71] International Atomic Energy Agency, “Advances in control assembly materials for water reactors,” in *Technical Committee meeting*, 1993.
- [72] J. Yang *et al.*, “Review on chromium coated zirconium alloy accident tolerant fuel cladding,” *J. Alloys Compd.*, vol. 895, p. 162450, Feb. 2022.
- [73] D. Arias and J. P. Abriata, “The Cr-Zr (Chromium-Zirconium) system,” *Bull. Alloy Phase Diagrams*, vol. 7, no. 3, pp. 237–244, Jun. 1986.
- [74] R. Oelrich *et al.*, “Overview of Westinghouse Lead Accident Tolerant Fuel Program,” in *TopFuel 2018*, 2018, p. A0151.
- [75] M. C. Billone, Y. Yan, T. A. Burtseva, and R. Daum, “Cladding embrittlement during postulated loss-of-coolant accidents,” *J. Nucl. Mater.*, vol. 433, no. 1–3, pp. 431–448, Jul. 2008.
- [76] J.-C. Brachet and A. Lesbros, “Influence of Long Service Exposures on the Thermal-Mechanical Behavior of Zy-4 and M5TM Alloys in LOCA Conditions,” *J. ASTM Int.*, Jan. 2005.
- [77] E. J. Lahoda, P. Xu, R. Sumit, and L. Hallstadius, “Potential Performance Improvements of New Fuels,” in *Minerals, Metals and Materials Society*, 2012.
- [78] X. Han, J. Xue, S. Peng, and H. Zhang, “An interesting oxidation phenomenon of Cr coatings on Zry-4 substrates in high temperature steam environment,” *Corros. Sci.*, vol. 156, pp. 117–124, Aug. 2019.
- [79] E. A. G. Shillington and D. R. Clarke, “Spalling failure of a thermal barrier coating associated with aluminum depletion in the bond-coat,” *Acta Mater.*, vol. 47, no. 4, pp. 1297–1305, Mar. 1999.
- [80] H.-G. Kim *et al.*, “Oxidation behavior and mechanical property of Cr-coated

- zirconium cladding prepared by 3D laser coating,” in *Water Reactor Fuel Performance Meeting*, 2014.
- [81] A. Michau, M. Ougier, J.-C. Brachet, and M. Ougier, “Interlayers for Cr-coated nuclear fuel claddings Preliminary study of Mo,” in *NuMat 2020*, 2020, no. November, pp. 8–12.
 - [82] B. Li, H. Yang, R. Holmes, Z. Wei, S. Kano, and H. Abe, “Microstructure evolution and mechanical property of high temperature solid-state diffusion bonded Cr-Zr₄ with and without a 316 SS interlayer,” *Nucl. Mater. Energy*, vol. 32, p. 101233, Sep. 2022.
 - [83] E. Kashkarov, B. Aforu, D. Sidelev, M. Krinitcyn, V. Gouws, and A. Lider, “Recent advances in protective coatings for accident tolerant zr-based fuel claddings,” *Coatings*, vol. 11, no. 5, p. 557, May 2021.
 - [84] M. S. Syrtanov, E. B. Kashkarov, A. V. Abdulmenova, and D. V. Sidelev, “High-temperature oxidation of Zr1Nb zirconium alloy with protective Cr/Mo coating,” *Surf. Coatings Technol.*, vol. 439, p. 128459, Jun. 2022.
 - [85] T. B. Massalski, J. L. Murray, and L. H. Bennet, *Binary alloy phase diagrams*, vol. 2. 1986.
 - [86] K. Pasamehmetoglu *et al.*, “State-of-the-Art Report on Light Water Reactor Accident-Tolerant Fuels,” 2018.
 - [87] A. Giannattasio, Z. Yao, E. Tarleton, and S. G. Roberts, “Brittle-ductile transitions in polycrystalline tungsten,” *Philos. Mag.*, vol. 90, no. 30, pp. 3947–3959, Oct. 2010.
 - [88] J. W. Yeh *et al.*, “Nanostructured high-entropy alloys with multiple principal elements: Novel alloy design concepts and outcomes,” *Adv. Eng. Mater.*, vol. 6, no. 5, pp. 299–303+274, May 2004.
 - [89] B. Cantor, I. T. H. Chang, P. Knight, and A. J. B. Vincent, “Microstructural development in equiatomic multicomponent alloys,” *Mater. Sci. Eng. A*, vol. 375–377, no. 1–2, pp. 213–218, Jul. 2004.
 - [90] J. W. Yeh *et al.*, “Formation of simple crystal structures in Cu-Co-Ni-Cr-Al-Fe-Ti-V

- alloys with multiprincipal metallic elements,” *Metall. Mater. Trans. A* 2004 358, vol. 35, no. 8, pp. 2533–2536, 2004.
- [91] J. W. Yeh, “Recent progress in high-entropy alloys,” *Ann. Chim. Sci. des Mater.*, vol. 31, no. 6, pp. 633–648, Nov. 2006.
- [92] J. W. Yeh, Y. L. Chen, S. J. Lin, and S. K. Chen, “High-Entropy Alloys – A New Era of Exploitation,” *Mater. Sci. Forum*, vol. 560, pp. 1–9, Nov. 2007.
- [93] S. Praveen, B. S. Murty, and R. S. Kottada, “Alloying behavior in multi-component AlCoCrCuFe and NiCoCrCuFe high entropy alloys,” *Mater. Sci. Eng. A*, vol. 534, pp. 83–89, Feb. 2012.
- [94] K. G. Pradeep, N. Wanderka, P. Choi, J. Banhart, B. S. Murty, and D. Raabe, “Atomic-scale compositional characterization of a nanocrystalline AlCrCuFeNiZn high-entropy alloy using atom probe tomography,” *Acta Mater.*, vol. 61, no. 12, pp. 4696–4706, Jul. 2013.
- [95] F. Otto, Y. Yang, H. Bei, and E. P. George, “Relative effects of enthalpy and entropy on the phase stability of equiatomic high-entropy alloys,” *Acta Mater.*, vol. 61, no. 7, pp. 2628–2638, 2013.
- [96] M. C. Tropicovsky, J. R. Morris, P. R. C. Kent, A. R. Lupini, and G. M. Stocks, “Criteria for predicting the formation of single-phase high-entropy alloys,” *Phys. Rev. X*, vol. 5, no. 1, p. 011041, Mar. 2015.
- [97] O. N. Senkov, J. D. Miller, D. B. Miracle, and C. Woodward, “Accelerated exploration of multi-principal element alloys with solid solution phases,” *Nat. Commun.*, vol. 6, no. 1, pp. 1–10, Mar. 2015.
- [98] O. N. Senkov, J. D. Miller, D. B. Miracle, and C. Woodward, “Accelerated exploration of multi-principal element alloys for structural applications,” *Calphad*, vol. 50, pp. 32–48, Sep. 2015.
- [99] O. N. Senkov, G. B. Wilks, J. M. Scott, and D. B. Miracle, “Mechanical properties of Nb₂₅Mo₂₅Ta₂₅W₂₅ and V₂₀Nb₂₀Mo₂₀Ta₂₀W₂₀ refractory high entropy alloys,” *Intermetallics*, vol. 19, no. 5, pp. 698–706, May 2011.

- [100] S. C. Middleburgh, D. M. King, G. R. Lumpkin, M. Cortie, and L. Edwards, “Segregation and migration of species in the CrCoFeNi high entropy alloy,” *J. Alloys Compd.*, vol. 599, pp. 179–182, Jun. 2014.
- [101] M. C. Gao *et al.*, “Thermodynamics of concentrated solid solution alloys,” *Curr. Opin. Solid State Mater. Sci.*, vol. 21, no. 5, pp. 238–251, Oct. 2017.
- [102] S. Gorsse, D. B. Miracle, and O. N. Senkov, “Mapping the world of complex concentrated alloys,” *Acta Mater.*, vol. 135, pp. 177–187, Aug. 2017.
- [103] M. A. Tunes, V. M. Vishnyakov, and S. E. Donnelly, “Synthesis and characterisation of high-entropy alloy thin films as candidates for coating nuclear fuel cladding alloys,” *Thin Solid Films*, vol. 649, no. January, pp. 115–120, Mar. 2018.
- [104] M. A. Tunes *et al.*, “A candidate accident tolerant fuel system based on a highly concentrated alloy thin film,” *Mater. Today Energy*, vol. 12, pp. 356–362, Jun. 2019.
- [105] W. Li, D. Xie, D. Li, Y. Zhang, Y. Gao, and P. K. Liaw, “Mechanical behavior of high-entropy alloys,” *Progress in Materials Science*, vol. 118. Elsevier Ltd, p. 100777, 01-May-2021.
- [106] S. Gorsse, J. P. Couzinié, and D. B. Miracle, “From high-entropy alloys to complex concentrated alloys,” *Comptes Rendus Phys.*, vol. 19, no. 8, pp. 721–736, Dec. 2018.
- [107] D. B. Miracle and O. N. Senkov, “A critical review of high entropy alloys and related concepts,” *Acta Mater.*, vol. 122, pp. 448–511, Jan. 2017.
- [108] K. B. Zhang *et al.*, “Nanocrystalline CoCrFeNiCuAl high-entropy solid solution synthesized by mechanical alloying,” *J. Alloys Compd.*, vol. 485, no. 1–2, pp. L31–L34, Oct. 2009.
- [109] C. J. Tong *et al.*, “Mechanical performance of the Al_xCoCrCuFeNi high-entropy alloy system with multiprincipal elements,” *Metall. Mater. Trans. A*, vol. 36, no. 5, pp. 1263–1271, 2005.
- [110] Z. Fu, W. Chen, S. Fang, D. Zhang, H. Xiao, and D. Zhu, “Alloying behavior and deformation twinning in a CoNiFeCrAl 0.6Ti0.4 high entropy alloy processed by spark plasma sintering,” *J. Alloys Compd.*, vol. 553, pp. 316–323, Mar. 2013.

- [111] W. Chen, Z. Fu, S. Fang, Y. Wang, H. Xiao, and D. Zhu, "Processing, microstructure and properties of Al_{0.6}CoNiFeTi_{0.4} high entropy alloy with nanoscale twins," *Mater. Sci. Eng. A*, vol. 565, pp. 439–444, Mar. 2013.
- [112] B. Chanda and J. Das, "Composition Dependence on the Evolution of Nanoeutectic in CoCrFeNiNb_x ($0.45 \leq x \leq 0.65$) High Entropy Alloys," *Adv. Eng. Mater.*, vol. 20, no. 4, p. 1700908, Apr. 2018.
- [113] W. H. Liu, J. Y. He, H. L. Huang, H. Wang, Z. P. Lu, and C. T. Liu, "Effects of Nb additions on the microstructure and mechanical property of CoCrFeNi high-entropy alloys," *Intermetallics*, vol. 60, pp. 1–8, May 2015.
- [114] F. He *et al.*, "Designing eutectic high entropy alloys of CoCrFeNiNb_x," *J. Alloys Compd.*, vol. 656, pp. 284–289, Jan. 2016.
- [115] H. Luo, Z. Li, and D. Raabe, "Hydrogen enhances strength and ductility of an equiatomic high-entropy alloy," *Sci. Rep.*, vol. 7, no. 1, Dec. 2017.
- [116] Z. Lei *et al.*, "Enhanced strength and ductility in a high-entropy alloy via ordered oxygen complexes," *Nature*, vol. 563, no. 7732, pp. 546–550, Nov. 2018.
- [117] Z. Wang, I. Baker, Z. Cai, S. Chen, J. D. Poplawsky, and W. Guo, "The effect of interstitial carbon on the mechanical properties and dislocation substructure evolution in Fe_{40.4}Ni_{11.3}Mn_{34.8}Al_{7.5}Cr₆ high entropy alloys," *Acta Mater.*, vol. 120, pp. 228–239, Nov. 2016.
- [118] M. Klimova, D. Shaysultanov, A. Semenyuk, S. Zherebtsov, G. Salishchev, and N. Stepanov, "Effect of nitrogen on mechanical properties of CoCrFeMnNi high entropy alloy at room and cryogenic temperatures," *J. Alloys Compd.*, vol. 849, p. 156633, Dec. 2020.
- [119] P. L. Andresen and G. S. Was, "Irradiation Assisted Stress Corrosion Cracking," *Compr. Nucl. Mater.*, vol. 5, pp. 177–205, Jan. 2012.
- [120] T. Egami, W. Guo, P. D. Rack, and T. Nagase, "Irradiation resistance of multicomponent alloys," *Metall. Mater. Trans. A Phys. Metall. Mater. Sci.*, vol. 45, no. 1, pp. 180–183, Jan. 2014.

- [121] S. qin Xia, Z. Wang, T. fei Yang, and Y. Zhang, “Irradiation Behavior in High Entropy Alloys,” *J. Iron Steel Res. Int.*, vol. 22, no. 10, pp. 879–884, Oct. 2015.
- [122] F. Granberg *et al.*, “Mechanism of Radiation Damage Reduction in Equiatomic Multicomponent Single Phase Alloys,” *Phys. Rev. Lett.*, vol. 116, no. 13, p. 135504, Apr. 2016.
- [123] N. A. P. K. Kumar, C. Li, K. J. Leonard, H. Bei, and S. J. Zinkle, “Microstructural stability and mechanical behavior of FeNiMnCr high entropy alloy under ion irradiation,” *Acta Mater.*, vol. 113, pp. 230–244, Jul. 2016.
- [124] Z. Zhang, E. H. Han, and C. Xiang, “Irradiation behaviors of two novel single-phase bcc-structure high-entropy alloys for accident-tolerant fuel cladding,” *J. Mater. Sci. Technol.*, vol. 84, pp. 230–238, Sep. 2021.
- [125] L. Yang *et al.*, “High He-ion irradiation resistance of CrMnFeCoNi high-entropy alloy revealed by comparison study with Ni and 304SS,” *J. Mater. Sci. Technol.*, vol. 35, no. 3, pp. 300–305, Mar. 2019.
- [126] T. Egami, M. Ojha, O. Khorgolkhuu, D. M. Nicholson, and G. M. Stocks, “Local Electronic Effects and Irradiation Resistance in High-Entropy Alloys,” *JOM*, vol. 67, no. 10, pp. 2345–2349, 2015.
- [127] Y. Zhang *et al.*, “Influence of chemical disorder on energy dissipation and defect evolution in concentrated solid solution alloys,” *Nat. Commun.*, vol. 6, no. 1, pp. 1–9, Oct. 2015.
- [128] C. Lu *et al.*, “Enhancing radiation tolerance by controlling defect mobility and migration pathways in multicomponent single-phase alloys,” *Nat. Commun.*, vol. 7, no. 1, pp. 1–8, Dec. 2016.
- [129] K. Sugita, N. Matsuoka, M. Mizuno, and H. Araki, “Vacancy formation enthalpy in CoCrFeMnNi high-entropy alloy,” *Scr. Mater.*, vol. 176, pp. 32–35, Feb. 2020.
- [130] Z.-S. Nong, Z.-H. Gu, Y.-W. Liu, Z.-Y. Wang, and J.-C. Zhu, “Formation and migration behavior of vacancy in multi-component alloys,” *Intermetallics*, vol. 151, p. 107724, Dec. 2022.

- [131] O. El-Atwani *et al.*, “Outstanding radiation resistance of tungsten-based high-entropy alloys,” *Sci. Adv.*, vol. 5, no. 3, pp. 1–10, Mar. 2019.
- [132] Y. Lu *et al.*, “A promising new class of irradiation tolerant materials: Ti₂ZrHfV_{0.5}Mo_{0.2} high-entropy alloy,” *J. Mater. Sci. Technol.*, vol. 35, no. 3, pp. 369–373, Mar. 2019.
- [133] O. El Atwani *et al.*, “An innovative materials design protocol for the development of novel refractory high-entropy alloys for extreme environments,” *arXiv:2210.16409*, Oct. 2022.
- [134] D. Luo *et al.*, “High Entropy Alloys as Filler Metals for Joining,” *Entropy*, vol. 23, no. 1, p. 78, Jan. 2021.
- [135] O. A. Waseem, “Can High-Entropy Interlayers Develop Intermetallic-Free Welded Joints of Dissimilar Metals?,” *Eng*, vol. 1, no. 2, pp. 183–187, Oct. 2020.
- [136] D. Bridges *et al.*, “Laser brazing of a nickel-based superalloy using a Ni-Mn-Fe-Co-Cu high entropy alloy filler metal,” *Mater. Lett.*, vol. 215, pp. 11–14, Mar. 2018.
- [137] J. G. Lopes and J. P. Oliveira, “A Short Review on Welding and Joining of High Entropy Alloys,” *Metals (Basel)*, vol. 10, no. 2, p. 212, Feb. 2020.
- [138] L. X. Zhang, J. M. Shi, H. W. Li, X. Y. Tian, and J. C. Feng, “Interfacial microstructure and mechanical properties of ZrB₂SiCC ceramic and GH99 superalloy joints brazed with a Ti-modified FeCoNiCrCu high-entropy alloy,” *Mater. Des.*, vol. 97, pp. 230–238, May 2016.
- [139] W. Tillmann, T. Ulitzka, L. Wojarski, M. Manka, H. Ulitzka, and D. Wagstyl, “Development of high entropy alloys for brazing applications,” *Weld. World*, vol. 64, no. 1, pp. 201–208, Jan. 2020.
- [140] G. Wang, Y. Yang, R. He, C. Tan, M. Huttula, and W. Cao, “A novel high entropy CoFeCrNiCu alloy filler to braze SiC ceramics,” *J. Eur. Ceram. Soc.*, vol. 40, no. 9, pp. 3391–3398, Aug. 2020.
- [141] G. Wang *et al.*, “Brazing ZrB₂-SiC ceramics to Nb with a novel CoFeNiCrCu high entropy alloy,” *J. Eur. Ceram. Soc.*, vol. 41, no. 1, pp. 54–61, Jan. 2021.

- [142] S. Freed, “The structure of metals and alloys,” *J. Chem. Educ.*, vol. 17, no. 12, p. 600, 1940.
- [143] G. B. Bokas, W. Chen, A. Hilhorst, P. J. Jacques, S. Gorsse, and G. Hautier, “Unveiling the thermodynamic driving forces for high entropy alloys formation through big data ab initio analysis,” *Scr. Mater.*, vol. 202, p. 114000, Sep. 2021.
- [144] X. Yang and Y. Zhang, “Prediction of high-entropy stabilized solid-solution in multi-component alloys,” *Mater. Chem. Phys.*, vol. 132, no. 2–3, pp. 233–238, Feb. 2012.
- [145] A. R. Miedema, P. F. de Châtel, and F. R. de Boer, “Cohesion in alloys - fundamentals of a semi-empirical model,” *Phys. B+C*, vol. 100, no. 1, pp. 1–28, Apr. 1980.
- [146] S. Guo, C. Ng, J. Lu, and C. T. Liu, “Effect of valence electron concentration on stability of fcc or bcc phase in high entropy alloys,” *J. Appl. Phys.*, vol. 109, no. 10, 2011.
- [147] Y. Zhang, Y. J. Zhou, J. P. Lin, G. L. Chen, and P. K. Liaw, “Solid-solution phase formation rules for multi-component alloys,” *Adv. Eng. Mater.*, vol. 10, no. 6, pp. 534–538, 2008.
- [148] D. J. M. M. King, S. C. Middleburgh, A. G. McGregor, and M. B. Cortie, “Predicting the formation and stability of single phase high-entropy alloys,” *Acta Mater.*, vol. 104, pp. 172–179, Feb. 2016.
- [149] Z. Wang, Y. Huang, Y. Yang, J. Wang, and C. T. Liu, “Atomic-size effect and solid solubility of multicomponent alloys,” *Scr. Mater.*, vol. 94, pp. 28–31, Jan. 2015.
- [150] E. J. Pickering, R. Muñoz-Moreno, H. J. Stone, and N. G. Jones, “Precipitation in the equiatomic high-entropy alloy CrMnFeCoNi,” *Scr. Mater.*, 2016.
- [151] E. J. Pickering and N. G. Jones, “High-entropy alloys: a critical assessment of their founding principles and future prospects,” *Int. Mater. Rev.*, vol. 61, no. 3, pp. 183–202, Apr. 2016.
- [152] S. Fang, X. Xiao, L. Xia, W. Li, and Y. Dong, “Relationship between the widths of supercooled liquid regions and bond parameters of Mg-based bulk metallic glasses,” *J. Non. Cryst. Solids*, vol. 321, no. 1–2, pp. 120–125, Jun. 2003.

- [153] Y. Zhang *et al.*, “Microstructures and properties of high-entropy alloys,” *Prog. Mater. Sci.*, vol. 61, pp. 1–93, Apr. 2014.
- [154] J. M. Rickman *et al.*, “Materials informatics for the screening of multi-principal elements and high-entropy alloys,” *Nat. Commun.*, vol. 10, no. 1, pp. 1–10, Dec. 2019.
- [155] J. M. Smith, *Introduction to chemical engineering thermodynamics*, 8th ed. New York, USA: McGraw-Hill Education, 2017.
- [156] D. A. Porter, K. E. Easterling, and M. Y. Sherif, *Phase transformations in metals and alloys, third edition*, 3rd ed. Boca Raton: CRC Press, 2009.
- [157] L. Kaufman and H. Bernstein, *Computer calculation of phase diagrams. With special reference to refractory metals*. New York, USA: United States: Academic Press Inc., 1970.
- [158] Y. A. Chang *et al.*, “Phase diagram calculation: Past, present and future,” in *Progress in Materials Science*, 2004, vol. 49, no. 3–4, pp. 313–345.
- [159] U. R. Kattner, “The CALPHAD method and its role in material and process development,” *Tecnol. Met. Mater. Min.*, vol. 13, no. 1, p. 3, 2016.
- [160] U. Bhandari, C. Zhang, S. Guo, and S. Yang, “First-principles study on the mechanical and thermodynamic properties of MoNbTaTiW,” *Int. J. Miner. Metall. Mater.*, vol. 27, no. 10, pp. 1398–1404, Aug. 2020.
- [161] T. Abe, “Thermal Vacancies in High-Entropy Alloys,” *Mater. Trans.*, vol. 61, no. 4, pp. 610–615, Apr. 2020.
- [162] T. M. Butler and M. L. Weaver, “Oxidation behavior of arc melted AlCoCrFeNi multi-component high-entropy alloys,” *J. Alloys Compd.*, vol. 674, pp. 229–244, Jul. 2016.
- [163] F. Zhang, C. Zhang, S. L. Chen, J. Zhu, W. S. Cao, and U. R. Kattner, “An understanding of high entropy alloys from phase diagram calculations,” *Calphad Comput. Coupling Phase Diagrams Thermochem.*, vol. 45, pp. 1–10, Jun. 2014.
- [164] S. Raghavan, G. Singh, S. Sondhi, and S. Srikanth, “Construction of a pseudo-binary phase diagram for multi-component Ni-base superalloys,” *Calphad*, vol. 38, pp. 85–91,

Sep. 2012.

- [165] M. Gao and D. Alman, “Searching for Next Single-Phase High-Entropy Alloy Compositions,” *Entropy*, vol. 15, no. 10, pp. 4504–4519, 2013.
- [166] O. N. Senkov, F. Zhang, and J. D. Miller, “Phase composition of a CrMo_{0.5}NbTa_{0.5}TiZr high entropy alloy: Comparison of experimental and simulated data,” *Entropy*, vol. 15, no. 9, pp. 3796–3809, Sep. 2013.
- [167] S. Y. Chen *et al.*, “Phase transformations of HfNbTaTiZr high-entropy alloy at intermediate temperatures,” *Scr. Mater.*, vol. 158, pp. 50–56, Jan. 2019.
- [168] D. Miracle, J. Miller, O. Senkov, C. Woodward, M. Uchic, and J. Tiley, “Exploration and Development of High Entropy Alloys for Structural Applications,” *Entropy*, vol. 16, no. 1, pp. 494–525, Jan. 2014.
- [169] M. Moorehead *et al.*, “High-throughput synthesis of Mo-Nb-Ta-W high-entropy alloys via additive manufacturing,” *Mater. Des.*, vol. 187, p. 108358, Feb. 2020.
- [170] H. Dobbstein, M. Thiele, E. L. Gurevich, E. P. George, and A. Ostendorf, “Direct metal deposition of refractory high entropy alloy MoNbTaW,” *Phys. Procedia*, vol. 83, pp. 624–633, Jan. 2016.
- [171] Y. A. Alshataif, S. Sivasankaran, F. A. Al-Mufadi, A. S. Alaboodi, and H. R. Ammar, “Manufacturing Methods, Microstructural and Mechanical Properties Evolutions of High-Entropy Alloys: A Review,” *Met. Mater. Int.*, vol. 26, no. 8, pp. 1099–1133, Aug. 2020.
- [172] J. Kim, A. Wakai, and A. Moridi, “Materials and manufacturing renaissance: Additive manufacturing of high-entropy alloys,” *J. Mater. Res.*, vol. 35, no. 15, pp. 1963–1983, Aug. 2020.
- [173] H. Cheng, X. Liu, Q. Tang, W. Wang, X. Yan, and P. Dai, “Microstructure and mechanical properties of FeCoCrNiMnAl_x high-entropy alloys prepared by mechanical alloying and hot-pressed sintering,” *J. Alloys Compd.*, vol. 775, pp. 742–751, Feb. 2019.
- [174] D. Oleszak, A. Antolak-Dudka, and T. Kulik, “High entropy multicomponent

- WMoNbZrV alloy processed by mechanical alloying,” *Mater. Lett.*, vol. 232, pp. 160–162, Dec. 2018.
- [175] A. I. Yurkova, V. V. Cherniavsky, V. Bolbut, M. Krüger, and I. Bogomol, “Structure formation and mechanical properties of the high-entropy AlCuNiFeCr alloy prepared by mechanical alloying and spark plasma sintering,” *J. Alloys Compd.*, vol. 786, pp. 139–148, May 2019.
- [176] A. Emamifar, B. Sadeghi, P. Cavaliere, and H. Ziaei, “Microstructural evolution and mechanical properties of AlCrFeNiCoC high entropy alloy produced via spark plasma sintering,” *Powder Metall.*, vol. 62, no. 1, pp. 61–70, Jan. 2019.
- [177] G. Štefanić, S. Krehula, and I. Štefanić, “Phase development during high-energy ball-milling of zinc oxide and iron – the impact of grain size on the source and the degree of contamination,” *Dalt. Trans.*, vol. 44, no. 43, pp. 18870–18881, Oct. 2015.
- [178] V. Shivam, J. Basu, V. K. Pandey, Y. Shadangi, and N. K. Mukhopadhyay, “Alloying behaviour, thermal stability and phase evolution in quinary AlCoCrFeNi high entropy alloy,” *Adv. Powder Technol.*, vol. 29, no. 9, pp. 2221–2230, Sep. 2018.
- [179] F. J. Baldenebro-Lopez, J. M. Herrera-Ramírez, S. P. Arredondo-Rea, C. D. Gómez-Esparza, and R. Martínez-Sánchez, “Simultaneous effect of mechanical alloying and arc-melting processes in the microstructure and hardness of an AlCoFeMoNiTi high-entropy alloy,” *J. Alloys Compd.*, vol. 643, no. S1, pp. S250–S255, Sep. 2015.
- [180] Z. Xu, M. A. Hodgson, and P. Cao, “A comparative study of powder metallurgical (PM) and wrought Fe–Mn–Si alloys,” *Mater. Sci. Eng. A*, vol. 630, pp. 116–124, Apr. 2015.
- [181] Z. Fu *et al.*, “Microstructure and strengthening mechanisms in an FCC structured single-phase nanocrystalline Co₂₅Ni₂₅Fe₂₅Al_{7.5}Cu_{17.5} high-entropy alloy,” *Acta Mater.*, vol. 107, pp. 59–71, Apr. 2016.
- [182] C. Sun, P. Li, S. Xi, Y. Zhou, S. Li, and X. Yang, “A new type of high entropy alloy composite Fe₁₈Ni₂₃Co₂₅Cr₂₁Mo₈WNb₃C₂ prepared by mechanical alloying and hot pressing sintering,” *Mater. Sci. Eng. A*, vol. 728, pp. 144–150, Jun. 2018.

- [183] Z. Tang *et al.*, “Tensile ductility of an AlCoCrFeNi multi-phase high-entropy alloy through hot isostatic pressing (HIP) and homogenization,” *Mater. Sci. Eng. A*, vol. 647, pp. 229–240, Oct. 2015.
- [184] J. Pan, T. Dai, T. Lu, X. Ni, J. Dai, and M. Li, “Microstructure and mechanical properties of Nb₂₅Mo₂₅Ta₂₅W₂₅ and Ti₈Nb₂₃Mo₂₃Ta₂₃W₂₃ high entropy alloys prepared by mechanical alloying and spark plasma sintering,” vol. 738, pp. 362–366, Dec. 2018.
- [185] F. Otto, N. L. Hanold, and E. P. George, “Microstructural evolution after thermomechanical processing in an equiatomic, single-phase CoCrFeMnNi high-entropy alloy with special focus on twin boundaries,” *Intermetallics*, vol. 54, pp. 39–48, Nov. 2014.
- [186] L. Hou, J. Hui, Y. Yao, J. Chen, and J. Liu, “Effects of Boron Content on microstructure and mechanical properties of AlFeCoNiB_x High Entropy Alloy Prepared by vacuum arc melting,” *Vacuum*, vol. 164, pp. 212–218, Jun. 2019.
- [187] S. Abhaya, R. Rajaraman, S. Kalavathi, and G. Amarendra, “Positron annihilation studies on FeCrCoNi high entropy alloy,” *J. Alloys Compd.*, vol. 620, pp. 277–282, Jan. 2015.
- [188] A. Akbari and T. J. Balk, “Combinatorial thin film screening to identify single-phase, non-equiatomic high entropy alloys in the MnFeCoNiCu system,” *MRS Commun.*, vol. 9, no. 2, pp. 750–755, Jun. 2019.
- [189] E. Strumza and S. Hayun, “Comprehensive study of phase transitions in equiatomic AlCoCrFeNi high-entropy alloy,” *J. Alloys Compd.*, vol. 856, p. 158220, Mar. 2021.
- [190] Y. Yu, F. He, Z. Qiao, Z. Wang, W. Liu, and J. Yang, “Effects of temperature and microstructure on the tribological properties of CoCrFeNiNb_x eutectic high entropy alloys,” *J. Alloys Compd.*, vol. 775, pp. 1376–1385, Feb. 2019.
- [191] P. Wang, Y. Bu, J. Liu, Q. Li, H. Wang, and W. Yang, “Atomic deformation mechanism and interface toughening in metastable high entropy alloy,” *Mater. Today*, vol. 37, pp. 64–73, Jul. 2020.

- [192] C. Xiang *et al.*, “Design of single-phase high-entropy alloys composed of low thermal neutron absorption cross-section elements for nuclear power plant application,” *Intermetallics*, vol. 104, pp. 143–153, Jan. 2019.
- [193] J. Zýka *et al.*, “Microstructure and room temperature mechanical properties of different 3 and 4 element medium entropy alloys from HfNbTaTiZr system,” *Entropy*, vol. 21, no. 2, Feb. 2019.
- [194] Y. Y. Jia *et al.*, “Microstructure and Mechanical Properties of Nb–Ti–V–Zr Refractory Medium-Entropy Alloys,” *Front. Mater.*, vol. 7, p. 172, Jun. 2020.
- [195] G. Ek *et al.*, “Elucidating the Effects of the Composition on Hydrogen Sorption in TiVZrNbHf-Based High-Entropy Alloys,” *Inorg. Chem.*, vol. 60, no. 2, pp. 1124–1132, Jan. 2021.
- [196] H. Qiu, H. Zhu, J. Zhang, and Z. Xie, “Effect of Fe content upon the microstructures and mechanical properties of Fe_xCoNiCu high entropy alloys,” *Mater. Sci. Eng. A*, vol. 769, p. 138514, Jan. 2020.
- [197] D. G. Kim *et al.*, “Effects of annealing temperature on microstructures and tensile properties of a single FCC phase CoCuMnNi high-entropy alloy,” *J. Alloys Compd.*, vol. 812, p. 152111, Jan. 2020.
- [198] C. C. Yang, J. L. Hang Chau, C. J. Weng, C. S. Chen, and Y. H. Chou, “Preparation of high-entropy AlCoCrCuFeNiSi alloy powders by gas atomization process,” *Mater. Chem. Phys.*, vol. 202, pp. 151–158, Dec. 2017.
- [199] S. Zhou *et al.*, “Microstructure evolution of Al_{0.6}CoCrFeNi high entropy alloy powder prepared by high pressure gas atomization,” *Trans. Nonferrous Met. Soc. China*, vol. 28, no. 5, pp. 939–945, May 2018.
- [200] D. Yim *et al.*, “Compaction behavior of water-atomized CoCrFeMnNi high-entropy alloy powders,” *Mater. Chem. Phys.*, vol. 210, pp. 95–102, May 2018.
- [201] Y. Liu, J. Wang, Q. Fang, B. Liu, Y. Wu, and S. Chen, “Preparation of superfine-grained high entropy alloy by spark plasma sintering gas atomized powder,” *Intermetallics*, vol. 68, pp. 16–22, Jan. 2016.

- [202] J. Wang *et al.*, “Flow behavior and microstructures of powder metallurgical CrFeCoNiMo_{0.2} high entropy alloy during high temperature deformation,” *Mater. Sci. Eng. A*, vol. 689, pp. 233–242, Mar. 2017.
- [203] H. Kim *et al.*, “Mechanical and electrical properties of NbMoTaW refractory high-entropy alloy thin films,” *Int. J. Refract. Met. Hard Mater.*, vol. 80, pp. 286–291, Apr. 2019.
- [204] Q. S. Chen *et al.*, “Microstructure and corrosion characteristics of CrCuFeMoNi HEA coatings with different compositions in high-temperature and high-pressure water,” *Mater. Res. Express*, vol. 6, no. 8, p. 086511, May 2019.
- [205] Y. Ma, Y. H. Feng, T. T. Debela, G. J. Peng, and T. H. Zhang, “Nanoindentation study on the creep characteristics of high-entropy alloy films: fcc versus bcc structures,” *Int. J. Refract. Met. Hard Mater.*, vol. 54, pp. 395–400, Jan. 2016.
- [206] L. Casillas-Trujillo *et al.*, “Experimental and theoretical evidence of charge transfer in multi-component alloys – how chemical interactions reduce atomic size mismatch,” *Mater. Chem. Front.*, vol. 5, no. 15, pp. 5746–5759, Jul. 2021.
- [207] X. Feng, J. Utama Surjadi, and Y. Lu, “Annealing-induced abnormal hardening in nanocrystalline NbMoTaW high-entropy alloy thin films,” *Mater. Lett.*, vol. 275, p. 128097, Sep. 2020.
- [208] Y. Zou, H. Ma, and R. Spolenak, “Ultrastrong ductile and stable high-entropy alloys at small scales,” *Nat. Commun.*, vol. 6, Jul. 2015.
- [209] L. He *et al.*, “Microstructure, mechanical and corrosion properties of high hardness TiVZrCrAl HEA coatings prepared by magnetron sputtering,” *Surf. Coatings Technol.*, vol. 441, p. 128532, Jul. 2022.
- [210] S. Zhao *et al.*, “Mechanical and high-temperature corrosion properties of AlTiCrNiTa high entropy alloy coating prepared by magnetron sputtering for accident-tolerant fuel cladding,” *Surf. Coatings Technol.*, vol. 417, p. 127228, Jul. 2021.
- [211] P. Ren *et al.*, “Sputter-deposited TiVCrZrW high entropy alloy film: Structure and tribological properties,” *Ceram. Int.*, vol. 48, no. 24, pp. 37383–37393, Dec. 2022.

- [212] M. H. Tsai, J. W. Yeh, and J. Y. Gan, “Diffusion barrier properties of AlMoNbSiTaTiVZr high-entropy alloy layer between copper and silicon,” *Thin Solid Films*, vol. 516, no. 16, pp. 5527–5530, Jun. 2008.
- [213] Y. Xu, G. Li, and Y. Xia, “Synthesis and characterization of super-hard AlCrTiVZr high-entropy alloy nitride films deposited by HiPIMS,” *Appl. Surf. Sci.*, vol. 523, p. 146529, Sep. 2020.
- [214] W. Zhang *et al.*, “Preparation, structure, and properties of an AlCrMoNbZr high-entropy alloy coating for accident-tolerant fuel cladding,” *Surf. Coatings Technol.*, vol. 347, pp. 13–19, Aug. 2018.
- [215] W. Zhang *et al.*, “Interface stability, mechanical and corrosion properties of AlCrMoNbZr/(AlCrMoNbZr)N high-entropy alloy multilayer coatings under helium ion irradiation,” *Appl. Surf. Sci.*, vol. 485, pp. 108–118, Aug. 2019.
- [216] M. D. Cropper, “Thin films of AlCrFeCoNiCu high-entropy alloy by pulsed laser deposition,” *Appl. Surf. Sci.*, vol. 455, pp. 153–159, Oct. 2018.
- [217] T. W. Lu *et al.*, “Microstructures and mechanical properties of CoCrFeNiAl_{0.3} high-entropy alloy thin films by pulsed laser deposition,” *Appl. Surf. Sci.*, vol. 494, pp. 72–79, Nov. 2019.
- [218] H. Guan *et al.*, “Microstructure and hardness of NbTiZr and NbTaTiZr refractory medium-entropy alloy coatings on Zr alloy by laser cladding,” *Appl. Surf. Sci.*, vol. 549, p. 149338, May 2021.
- [219] K. C. Cheng, J. H. Chen, S. Stadler, and S. H. Chen, “Properties of atomized AlCoCrFeNi high-entropy alloy powders and their phase-adjustable coatings prepared via plasma spray process,” *Appl. Surf. Sci.*, vol. 478, pp. 478–486, Jun. 2019.
- [220] A. Meghwal, A. Anupam, B. S. Murty, C. C. Berndt, R. S. Kottada, and A. S. M. Ang, “Thermal Spray High-Entropy Alloy Coatings: A Review,” *J. Therm. Spray Technol.* 2020 295, vol. 29, no. 5, pp. 857–893, May 2020.
- [221] A. Sharma, “High Entropy Alloy Coatings and Technology,” *Coatings 2021, Vol. 11, Page 372*, vol. 11, no. 4, p. 372, Mar. 2021.

- [222] J. Kim, J. Ryu, H. J. Ryu, and J. Ryu, “Development of High Temperature Oxidation Resistant High Entropy Alloys for Coating Materials of Accident Tolerance Fuel Cladding,” in *Transactions of the Korean Nuclear Society Spring Meeting Jeju*, 2017.
- [223] O. N. Senkov, S. V. Senkova, D. M. Dimiduk, C. Woodward, and D. B. Miracle, “Oxidation behavior of a refractory NbCrMo 0.5Ta 0.5TiZr alloy,” *J. Mater. Sci.*, vol. 47, no. 18, pp. 6522–6534, Sep. 2012.
- [224] B. Gorr, S. Schellert, F. Müller, H. J. Christ, A. Kauffmann, and M. Heilmaier, “Current Status of Research on the Oxidation Behavior of Refractory High Entropy Alloys,” *Adv. Eng. Mater.*, vol. 23, no. 5, p. 2001047, May 2021.
- [225] T. E. Tietz and J. W. Wilson, *Behavior and properties of refractory metals*. Stanford University Press, Stanford, Calif., 1965.
- [226] E. A. Gulbransen, K. F. Andrew, and F. A. Brassart, “Kinetics of Oxidation of Pure Tungsten, 1150°–1615°C,” *J. Electrochem. Soc.*, vol. 111, no. 1, p. 103, Jan. 1964.
- [227] C. M. Liu, H. M. Wang, S. Q. Zhang, H. B. Tang, and A. L. Zhang, “Microstructure and oxidation behavior of new refractory high entropy alloys,” *J. Alloys Compd.*, vol. 583, pp. 162–169, Jan. 2014.
- [228] R. A. Perkins and G. H. Meier, “The oxidation behavior and protection of niobium,” *JOM*, vol. 42, no. 8, pp. 17–21, Aug. 1990.
- [229] M. R. Jackson, B. P. Bewlay, R. G. Rowe, D. W. Skelly, and H. A. Lipsitt, “High-temperature refractory metal-intermetallic composites,” *JOM*, vol. 48, no. 1, pp. 39–44, 1996.
- [230] D. Yao, C. Zhou, J. Yang, and H. Chen, “Experimental studies and modeling of the oxidation of multiphase niobium-base alloys,” *Corros. Sci.*, vol. 51, no. 11, pp. 2619–2627, Nov. 2009.
- [231] F. Müller *et al.*, “On the oxidation mechanism of refractory high entropy alloys,” *Corros. Sci.*, vol. 159, no. December 2018, p. 108161, Oct. 2019.
- [232] X. H. Wang and Y. C. Zhou, “High-Temperature Oxidation Behavior of Ti₂AlC in Air,” *Oxid. Met.* 2003 593, vol. 59, no. 3, pp. 303–320, Apr. 2003.

- [233] Y. Hua *et al.*, “Laser shock processing effects on isothermal oxidation resistance of GH586 superalloy,” *Appl. Surf. Sci.*, vol. 330, pp. 439–444, Mar. 2015.
- [234] M. A. Azim *et al.*, “Creep Resistance and Oxidation Behavior of Novel Mo-Si-B-Ti Alloys,” *JOM*, vol. 67, no. 11, pp. 2621–2628, Aug. 2015.
- [235] C. S. Giggins and F. S. Pettit, “Oxidation of Ni-Cr-Al Alloys Between 1000° and 1200°C,” *J. Electrochem. Soc.*, vol. 118, no. 11, p. 1782, Nov. 1971.
- [236] B. Gorr *et al.*, “High temperature oxidation behavior of an equimolar refractory metal-based alloy 20Nb20Mo20Cr20Ti20Al with and without Si addition,” *J. Alloys Compd.*, vol. 688, pp. 468–477, Dec. 2016.
- [237] B. Gorr, M. Azim, H. J. Christ, T. Mueller, D. Schliephake, and M. Heilmaier, “Phase equilibria, microstructure, and high temperature oxidation resistance of novel refractory high-entropy alloys,” *J. Alloys Compd.*, vol. 624, pp. 270–278, Mar. 2015.
- [238] B. Gorr *et al.*, “High-Temperature Oxidation Behavior of Refractory High-Entropy Alloys: Effect of Alloy Composition,” *Oxid. Met.*, vol. 88, no. 3–4, pp. 339–349, Oct. 2017.
- [239] F. F. Han, J. X. Chang, H. Li, L. H. Lou, and J. Zhang, “Influence of Ta content on hot corrosion behaviour of a directionally solidified nickel base superalloy,” *J. Alloys Compd.*, vol. 619, pp. 102–108, Jan. 2015.
- [240] W. Ren *et al.*, “The influence of CrTaO₄ layer on the oxidation behavior of a directionally-solidified nickel-based superalloy at 850–900 °C,” *J. Alloys Compd.*, vol. 724, pp. 565–574, Nov. 2017.
- [241] T. M. Butler, K. J. Chaput, J. R. Dietrich, and O. N. Senkov, “High temperature oxidation behaviors of equimolar NbTiZrV and NbTiZrCr refractory complex concentrated alloys (RCCAs),” *J. Alloys Compd.*, vol. 729, pp. 1004–1019, Dec. 2017.
- [242] H. P. Chou, Y. S. Chang, S. K. Chen, and J. W. Yeh, “Microstructure, thermophysical and electrical properties in Al_xCoCrFeNi (0 ≤ x ≤ 2) high-entropy alloys,” *Mater. Sci. Eng. B*, vol. 163, no. 3, pp. 184–189, Jul. 2009.
- [243] O. A. Waseem and H. J. Ryu, “Combinatorial synthesis and analysis of Al_xTa_yV_z-

- Cr₂₀Mo₂₀Nb₂₀Ti₂₀Zr₁₀ and Al₁₀CrMoxNbTiZr₁₀ refractory high-entropy alloys: Oxidation behavior,” *J. Alloys Compd.*, vol. 828, p. 154427, Jul. 2020.
- [244] F. Müller, B. Gorr, H. J. Christ, H. Chen, A. Kauffmann, and M. Heilmaier, “Effect of Y Additions on the Oxidation Behaviour of Novel Refractory High-Entropy Alloy NbMoCrTiAl at 1000 °C in Air,” *Oxid. Met.*, vol. 94, no. 1–2, pp. 147–163, Aug. 2020.
- [245] L. C. Li *et al.*, “Enhanced oxidation resistance of MoTaTiCrAl high entropy alloys by removal of Al,” *Sci. China Mater.* 2020 641, vol. 64, no. 1, pp. 223–231, Jun. 2020.
- [246] T. E. Graedel, E. M. Harper, N. T. Nassar, P. Nuss, B. K. Reck, and B. L. Turner, “Criticality of metals and metalloids,” in *Proceedings of the National Academy of Sciences of the United States of America*, 2015, vol. 112, no. 14, pp. 4257–4262.
- [247] M. B. Elmoselhi, K. Tashiro, and A. C. Wallace, “Hydrogen ingress into zirconium alloys as a life-limiting factor-methods of in-line monitoring, prediction and control,” *Int. Conf. Nucl. Eng. Proceedings, ICONE*, vol. 1, pp. 301–307, 2012.
- [248] T. Laursen, G. R. Palmer, J. E. Haysom, J. Nolan, and R. L. Tapping, “Hydrogen ingress into oxidized Zr-2.5Nb,” *J. Nucl. Mater.*, vol. 209, no. 1, pp. 52–61, Mar. 1994.
- [249] C. Jones *et al.*, “Evidence of hydrogen trapping at second phase particles in zirconium alloys,” *Sci. Rep.*, vol. 11, no. 1, pp. 1–12, Feb. 2021.
- [250] R. Hall, R. Sweet, R. Belles, and W. A. Wieselquist, “Extended-Enrichment Accident-Tolerant LWR Fuel Isotopic and Lattice Parameter Trends,” Oak Ridge, TN (United States), 2021.
- [251] E. J. Pickering, A. W. Carruthers, P. J. Barron, S. C. Middleburgh, D. E. J. Armstrong, and A. S. Gandy, “High-entropy alloys for advanced nuclear applications,” *Entropy*, vol. 23, no. 1. MDPI AG, pp. 1–28, 01-Jan-2021.
- [252] B. S. Murty, S. Ranganathan, J. W. Yeh, and P. P. Bhattacharjee, *High-entropy alloys*, 2nd ed. Elsevier, 2019.
- [253] C. S. Becquart and C. Domain, “Ab initio calculations about intrinsic point defects and

- He in W,” *Nucl. Instruments Methods Phys. Res. Sect. B Beam Interact. with Mater. Atoms*, vol. 255, no. 1, pp. 23–26, Feb. 2007.
- [254] R. Bodlos, T. Dengg, A. V Ruban, M. Dehghani, L. Romaner, and J. Spitaler, “Ab initio investigation of the atomic volume, thermal expansion, and formation energy of WTi solid solutions,” *Phys. Rev. Mater.*, vol. 5, p. 43601, 2021.
- [255] W. Chen *et al.*, “Vacancy formation enthalpies of high-entropy FeCoCrNi alloy via first-principles calculations and possible implications to its superior radiation tolerance,” *J. Mater. Sci. Technol.*, vol. 34, no. 2, pp. 355–364, Feb. 2018.
- [256] S. E. Daigle and D. W. Brenner, “Statistical approach to obtaining vacancy formation energies in high-entropy crystals from first principles calculations: Application to a high-entropy diboride,” *Phys. Rev. Mater.*, vol. 4, no. 12, p. 123602, Dec. 2020.
- [257] T. Duong, Y. Wang, X. Yan, A. Couet, and S. Chaudhuri, “A First-Principles-Based Approach to The High-Throughput Screening of Corrosion-Resistant High Entropy Alloys,” 2021.
- [258] J. Hu *et al.*, “A Density Functional Theory Study of the Hydrogen Absorption in High Entropy Alloy TiZrHfMoNb,” *Inorg. Chem.*, vol. 59, no. 14, pp. 9774–9782, Jul. 2020.
- [259] Y. Ikeda, B. Grabowski, and F. Körmann, “Ab initio phase stabilities and mechanical properties of multicomponent alloys: A comprehensive review for high entropy alloys and compositionally complex alloys,” *Mater. Charact.*, vol. 147, no. March 2018, pp. 464–511, Jan. 2019.
- [260] D. J. M. King *et al.*, “High temperature, low neutron cross-section high-entropy alloys in the Nb-Ti-V-Zr system,” *Acta Mater.*, vol. 166, pp. 435–446, Mar. 2019.
- [261] A. X. Lin-Vines *et al.*, “Defect behaviour in the MoNbTaVW high entropy alloy (HEA),” *Results Mater.*, vol. 15, p. 100320, Sep. 2022.
- [262] A. Zunger, S. H. Wei, L. G. Ferreira, and J. E. Bernard, “Special quasirandom structures,” *Phys. Rev. Lett.*, vol. 65, no. 3, pp. 353–356, 1990.
- [263] S. H. Wei, L. G. Ferreira, J. E. Bernard, and A. Zunger, “Electronic properties of

- random alloys: Special quasirandom structures,” *Phys. Rev. B*, vol. 42, no. 15, pp. 9622–9649, Nov. 1990.
- [264] A. Van De Walle *et al.*, “Efficient stochastic generation of special quasirandom structures,” *Calphad Comput. Coupling Phase Diagrams Thermochem.*, vol. 42, pp. 13–18, Sep. 2013.
- [265] G. Kresse and J. Furthmüller, “Efficiency of ab-initio total energy calculations for metals and semiconductors using a plane-wave basis set,” *Comput. Mater. Sci.*, vol. 6, no. 1, pp. 15–50, Jul. 1996.
- [266] S. J. Clark *et al.*, “First principles methods using CASTEP,” *Zeitschrift für Krist.*, vol. 220, no. 5–6, pp. 567–570, May 2005.
- [267] A. P. Thompson *et al.*, “LAMMPS - a flexible simulation tool for particle-based materials modeling at the atomic, meso, and continuum scales,” *Comput. Phys. Commun.*, vol. 271, p. 108171, Feb. 2022.
- [268] D. S. Sholl and J. A. Steckel, *Density Functional Theory: A Practical Introduction*. John Wiley & Sons, Inc., 2009.
- [269] J. O. Andersson, T. Helander, L. Höglund, P. Shi, and B. Sundman, “Thermo-Calc & DICTRA, computational tools for materials science,” *Calphad*, vol. 26, no. 2, pp. 273–312, Jun. 2002.
- [270] Z.-Z. Wu, S. Xiao, al -, and J. T. Gudmundsson, “Physics and technology of magnetron sputtering discharges,” *Plasma Sources Sci. Technol.*, vol. 29, no. 11, p. 113001, Nov. 2020.
- [271] J. Wilson and R. Wilson, “Thermal Expansion webapp for compositionally complex alloys,” 2022. [Online]. Available: alloys.one. [Accessed: 20-Dec-2022].
- [272] “ElementData,” *Wolfram Research (2007), Wolfram Language Forum*. [Online]. Available: <https://reference.wolfram.com/language/ref/ElementData.html> (updated 2014). [Accessed: 20-Dec-2022].
- [273] C. Bagnall, J. Capo, and W. J. Moorhead, “Oxidation Behavior of Tungsten Carbide-6% Cobalt Cemented Carbide,” *Metallogr. Microstruct. Anal.*, vol. 7, no. 6, pp. 661–

679, Dec. 2018.

- [274] S. D. Cramer and B. S. J. Covino, *ASM Handbook Volume 13B, Corrosion: Materials*. ASM International, 2005.
- [275] N. B. Pilling and R. E. Bedworth, “Mechanism of Metallic Oxidation at High Temperatures,” in *Rochester Meeting*, 1922.
- [276] N. Birks, G. H. Meier, and F. S. Pettit, *Introduction to the high temperature oxidation of metals*, 2nd ed. Cambridge University Press, 2006.
- [277] Y. S. Touloukian, R. K. Kirby, R. E. Taylor, and P. D. Desai, *Thermal Expansion*. 1975.
- [278] W. P. Huhn and M. Widom, “Prediction of A2 to B2 Phase Transition in the High-Entropy Alloy Mo-Nb-Ta-W,” *JOM*, vol. 65, no. 12, pp. 1772–1779, Oct. 2013.
- [279] Z. D. Han *et al.*, “Effect of Ti additions on mechanical properties of NbMoTaW and VNbMoTaW refractory high entropy alloys,” *Intermetallics*, vol. 84, pp. 153–157, May 2017.
- [280] L. Backman, J. Gild, J. Luo, and E. J. Opila, “Part I: Theoretical predictions of preferential oxidation in refractory high entropy materials,” *Acta Mater.*, vol. 197, pp. 20–27, Sep. 2020.
- [281] R. A. Serway, J. W. Jewett, and V. Perroomian, *Physics for scientists and engineers*. Brooks/Cole, Cengage Learning, 2010.
- [282] T. Usui, A. Sawada, M. Amaya, A. Suzuki, T. Chikada, and T. Terai, “SiC coating as hydrogen permeation reduction and oxidation resistance for nuclear fuel cladding,” *J. Nucl. Sci. Technol.*, vol. 52, no. 10, pp. 1318–1322, Oct. 2015.
- [283] Y. Lee, J. I. Lee, and H. C. NO, “Mechanical analysis of surface-coated zircaloy cladding,” *Nucl. Eng. Technol.*, vol. 49, no. 5, pp. 1031–1043, Aug. 2017.
- [284] J. Ribis, A. Wu, J. C. Brachet, F. Barcelo, and B. Arnal, “Atomic-scale interface structure of a Cr-coated Zircaloy-4 material,” *J. Mater. Sci.*, vol. 53, no. 14, pp. 9879–9895, 2018.

- [285] I. Younker and M. Fratoni, “Neutronic evaluation of coating and cladding materials for accident tolerant fuels,” *Prog. Nucl. Energy*, vol. 88, pp. 10–18, Apr. 2016.
- [286] I. Toda-Caraballo, “A general formulation for solid solution hardening effect in multicomponent alloys,” *Scr. Mater.*, vol. 127, pp. 113–117, Jan. 2017.
- [287] R. Labusch, “A Statistical Theory of Solid Solution Hardening,” *Phys. status solidi*, vol. 41, no. 2, pp. 659–669, Jan. 1970.
- [288] D. R. Askeland, “The Science and Engineering of Materials,” *Eur. J. Eng. Educ.*, 1994.
- [289] G. Laplanche *et al.*, “Elastic moduli and thermal expansion coefficients of medium-entropy subsystems of the CrMnFeCoNi high-entropy alloy,” *J. Alloys Compd.*, vol. 746, pp. 244–255, May 2018.
- [290] S. M. C. Van Bohemen, “The nonlinear lattice expansion of iron alloys in the range 100-1600 K,” *Scr. Mater.*, vol. 69, no. 4, pp. 315–318, Aug. 2013.
- [291] Z. D. Han *et al.*, “Microstructures and mechanical properties of $\text{Ti}_{1-x}\text{NbMoTaW}$ refractory high-entropy alloys,” *Mater. Sci. Eng. A*, vol. 712, pp. 380–385, Jan. 2018.
- [292] O. N. Senkov, G. B. Wilks, D. B. Miracle, C. P. Chuang, and P. K. Liaw, “Refractory high-entropy alloys,” *Intermetallics*, vol. 18, no. 9, pp. 1758–1765, Sep. 2010.
- [293] P. Hohenberg and W. Kohn, “Inhomogeneous electron gas,” *Phys. Rev.*, vol. 136, no. 3B, p. B864, Nov. 1964.
- [294] W. Kohn and L. J. Sham, “Self-consistent equations including exchange and correlation effects,” *Phys. Rev.*, vol. 140, no. 4A, p. A1133, Nov. 1965.
- [295] P. E. Blöchl, “Projector augmented-wave method,” *Phys. Rev. B*, vol. 50, no. 24, pp. 17953–17979, Dec. 1994.
- [296] G. Kresse, “Ab initio molecular dynamics for liquid metals,” *J. Non. Cryst. Solids*, vol. 192–193, pp. 222–229, Dec. 1995.
- [297] J. P. Perdew, K. Burke, and M. Ernzerhof, “Generalized gradient approximation made simple,” *Phys. Rev. Lett.*, vol. 77, no. 18, pp. 3865–3868, 1996.

- [298] M. Methfessel and A. T. Paxton, “High-precision sampling for Brillouin-zone integration in metals,” *Phys. Rev. B*, vol. 40, no. 6, pp. 3616–3621, Aug. 1989.
- [299] H. Oh *et al.*, “Lattice Distortions in the FeCoNiCrMn High Entropy Alloy Studied by Theory and Experiment,” *Entropy*, vol. 18, no. 9, p. 321, Sep. 2016.
- [300] A. J. Zaddach, C. Niu, C. C. Koch, and D. L. Irving, “Mechanical properties and stacking fault energies of NiFeCrCoMn high-entropy alloy,” *JOM*, vol. 65, no. 12, pp. 1780–1789, Dec. 2013.
- [301] C. Lee *et al.*, “Lattice distortion in a strong and ductile refractory high-entropy alloy,” *Acta Mater.*, vol. 160, pp. 158–172, Nov. 2018.
- [302] F. Körmann and M. Sluiter, “Interplay between Lattice Distortions, Vibrations and Phase Stability in NbMoTaW High Entropy Alloys,” *Entropy*, vol. 18, no. 8, p. 403, Aug. 2016.
- [303] G. Grimvall, B. Magyari-Köpe, OzoliņENM, and K. A. Persson, “Lattice instabilities in metallic elements,” *Rev. Mod. Phys.*, vol. 84, no. 2, pp. 945–986, 2012.
- [304] S. Baroni, S. De Gironcoli, A. Dal Corso, and P. Giannozzi, “Phonons and related crystal properties from density-functional perturbation theory,” *Reviews of Modern Physics*, vol. 73, no. 2. American Physical Society, pp. 515–562, 06-Apr-2001.
- [305] A. Togo, L. Chaput, I. Tanaka, and G. Hug, “First-principles phonon calculations of thermal expansion in Ti₃SiC₂, Ti₃AlC₂, and Ti₃GeC₂,” *Phys. Rev. B - Condens. Matter Mater. Phys.*, vol. 81, no. 17, p. 174301, May 2010.
- [306] A. Togo and I. Tanaka, “First principles phonon calculations in materials science,” *Scr. Mater.*, vol. 108, pp. 1–5, Nov. 2015.
- [307] S. Guo and C. T. Liu, “Phase stability in high entropy alloys: Formation of solid-solution phase or amorphous phase,” *Prog. Nat. Sci. Mater. Int.*, vol. 21, no. 6, pp. 433–446, Dec. 2011.
- [308] D. J. M. King, P. A. Burr, E. G. Obbard, and S. C. Middleburgh, “DFT study of the hexagonal high-entropy alloy fission product system,” *J. Nucl. Mater.*, vol. 488, pp. 70–74, May 2017.

- [309] M. F. Ashby, “Designing Hybrid Materials,” in *Materials Selection in Mechanical Design*, Elsevier, 2011, pp. 299–340.
- [310] Z. Wang, C. T. Liu, and P. Dou, “Thermodynamics of vacancies and clusters in high-entropy alloys,” *Phys. Rev. Mater.*, vol. 1, no. 4, p. 043601, Sep. 2017.
- [311] A. D. King and J. Burke, “The equilibrium vacancy concentration in an aluminium-copper alloy,” *Acta Metall.*, vol. 18, no. 2, pp. 205–210, Feb. 1970.
- [312] D. E. Jodi, T. A. Listyawan, P. Hruska, J. Cizek, N. Park, and U. Lee, “Study of vacancies in $\text{Fe}_{100-x}(\text{CoCrMnNi})_x$ medium- and high-entropy alloys by positron annihilation spectroscopy,” *Scr. Mater.*, vol. 194, p. 113654, Mar. 2021.
- [313] M. Vaidya, K. G. Pradeep, B. S. Murty, G. Wilde, and S. V. Divinski, “Bulk tracer diffusion in CoCrFeNi and CoCrFeMnNi high entropy alloys,” *Acta Mater.*, vol. 146, pp. 211–224, Mar. 2018.
- [314] X. Zhang, S. V. Divinski, and B. Grabowski, “Ab initio prediction of vacancy energetics in HCP Al-Hf-Sc-Ti-Zr high entropy alloys and the subsystems,” *Acta Mater.*, p. 117677, Jan. 2022.
- [315] M. Mizuno, K. Sugita, and H. Araki, “Defect energetics for diffusion in CrMnFeCoNi high-entropy alloy from first-principles calculations,” *Comput. Mater. Sci.*, vol. 170, p. 109163, Dec. 2019.
- [316] D. Vizoso and C. Deo, “Determination of Vacancy Formation Energies in Binary UZr Alloys Using Special Quasirandom Structure Methods,” *Front. Mater.*, vol. 8, p. 243, Jul. 2021.
- [317] Y. Wang *et al.*, “Prediction of vacancy formation energies at tungsten grain boundaries from local structure via machine learning method,” *J. Nucl. Mater.*, vol. 559, p. 153412, Feb. 2022.
- [318] J. Marian *et al.*, “Recent advances in modeling and simulation of the exposure and response of tungsten to fusion energy conditions,” *Nucl. Fusion*, vol. 57, no. 9, p. 092008, Jun. 2017.
- [319] J. P. Du *et al.*, “Chemical domain structure and its formation kinetics in CrCoNi

- medium-entropy alloy,” *Acta Mater.*, vol. 240, p. 118314, Nov. 2022.
- [320] M. J. Abere *et al.*, “A predictive analytical model of thermal conductivity for aluminum/transition metal high-entropy alloys,” *Scr. Mater.*, vol. 208, p. 114330, Feb. 2022.
- [321] Z. Shen, J. P. Du, S. Shinzato, Y. Sato, P. Yu, and S. Ogata, “Kinetic Monte Carlo simulation framework for chemical short-range order formation kinetics in a multi-principal-element alloy,” *Comput. Mater. Sci.*, vol. 198, p. 110670, Oct. 2021.
- [322] Y. Z. Wang and Y. J. Wang, “Disentangling diffusion heterogeneity in high-entropy alloys,” *Acta Mater.*, vol. 224, p. 117527, Feb. 2022.
- [323] Y. Zhang, A. Manzoor, C. Jiang, D. Aidhy, and D. Schwen, “A statistical approach for atomistic calculations of vacancy formation energy and chemical potentials in concentrated solid-solution alloys,” *Comput. Mater. Sci.*, vol. 190, p. 110308, Apr. 2021.
- [324] A. Esfandiarpour and M. N. Nasrabadi, “Vacancy formation energy in CuNiCo equimolar alloy and CuNiCoFe high entropy alloy: ab initio based study,” *Calphad*, vol. 66, p. 101634, Sep. 2019.
- [325] C. Li *et al.*, “First principle study of magnetism and vacancy energetics in a near equimolar NiFeMnCr high entropy alloy,” *J. Appl. Phys.*, vol. 125, no. 15, p. 155103, Apr. 2019.
- [326] A. Roy, P. Singh, G. Balasubramanian, and D. D. Johnson, “Vacancy formation energies and migration barriers in multi-principal element alloys,” *Acta Mater.*, vol. 226, p. 117611, Mar. 2022.
- [327] P. Singh *et al.*, “Vacancy-mediated complex phase selection in high entropy alloys,” *Acta Mater.*, vol. 194, pp. 540–546, Aug. 2020.
- [328] A. Cunliffe, J. Plummer, I. Figueroa, and I. Todd, “Glass formation in a high entropy alloy system by design,” *Intermetallics*, vol. 23, pp. 204–207, Apr. 2012.
- [329] S. Zhao, “Defect properties in a VTaCrW equiatomic high entropy alloy (HEA) with the body centered cubic (bcc) structure,” *J. Mater. Sci. Technol.*, vol. 44, pp. 133–139,

May 2020.

- [330] G. Kresse and D. Joubert, “From ultrasoft pseudopotentials to the projector augmented-wave method,” *Phys. Rev. B*, vol. 59, no. 3, p. 1758, Jan. 1999.
- [331] G. Marsaglia, W. W. Tsang, and J. Wang, “Evaluating Kolmogorov’s Distribution,” *J. Stat. Softw.*, vol. 8, pp. 1–4, Nov. 2003.
- [332] Tazuddin, N. P. Gurao, and K. Biswas, “In the quest of single phase multi-component multiprincipal high entropy alloys,” *J. Alloys Compd.*, vol. 697, pp. 434–442, Mar. 2017.
- [333] R. Li, L. Xie, W. Y. Wang, P. K. Liaw, and Y. Zhang, “High-Throughput Calculations for High-Entropy Alloys: A Brief Review,” *Front. Mater.*, vol. 7, p. 290, Sep. 2020.
- [334] A. Takeuchi and A. Inoue, “Classification of Bulk Metallic Glasses by Atomic Size Difference, Heat of Mixing and Period of Constituent Elements and Its Application to Characterization of the Main Alloying Element,” *Mater. Trans.*, vol. 46, no. 12, pp. 2817–2829, Dec. 2005.
- [335] M. Glienke *et al.*, “Grain boundary diffusion in CoCrFeMnNi high entropy alloy: Kinetic hints towards a phase decomposition,” *Acta Mater.*, vol. 195, pp. 304–316, Aug. 2020.
- [336] A. R. Denton and N. W. Ashcroft, “Vegard’s law,” *Phys. Rev. A*, vol. 43, no. 6, p. 3161, Mar. 1991.
- [337] A. Mishra, G. Priyadarshan, D. Clark, Y. Lu, and R. Shi, “Theoretical Investigations on Structural Stability and Elastic Properties of MoNbTaW-X (=Ti/V) High Entropy Alloys,” Nov. 2019.
- [338] W. H. He *et al.*, “Effects of Grain Boundary Characteristics on Its Capability to Trap Point Defects in Tungsten,” *Chinese Phys. Lett.*, vol. 35, no. 2, p. 026101, Feb. 2018.
- [339] K. Maier, M. Peo, B. Saile, H. E. Schaefer, and A. Seeger, “High-temperature positron annihilation and vacancy formation in refractory metals,” vol. 40, no. 5, pp. 701–728, 2006.

- [340] P. A. Korzhavyi, I. A. Abrikosov, B. ; Johansson, A. ; Ruban, and H. L. Skriver, “First-principles calculations of the vacancy formation energy in transition and noble metals,” *Phys. Rev. B*, vol. 59, no. 18, pp. 11693–11703, 1999.
- [341] M. A. Tschopp, K. N. Solanki, F. Gao, X. Sun, M. A. Khaleel, and M. F. Horstemeyer, “Probing grain boundary sink strength at the nanoscale: Energetics and length scales of vacancy and interstitial absorption by grain boundaries in α -Fe,” *Phys. Rev. B - Condens. Matter Mater. Phys.*, vol. 85, no. 6, p. 064108, Feb. 2012.
- [342] C. M. Rost *et al.*, “Entropy-stabilized oxides,” *Nat. Commun. 2015 61*, vol. 6, no. 1, pp. 1–8, Sep. 2015.
- [343] “Penetration depth for X-rays.” [Online]. Available: <https://gixa.ati.tuwien.ac.at/tools/penetrationdepth.xhtml>. [Accessed: 22-Dec-2022].
- [344] D. P. Wang, S. L. Wang, and J. Q. Wang, “Relationship between amorphous structure and corrosion behaviour in a Zr–Ni metallic glass,” *Corros. Sci.*, vol. 59, pp. 88–95, Jun. 2012.
- [345] S. Calderon, C. F. A. Alves, N. K. Manninen, A. Cavaleiro, and S. Carvalho, “Electrochemical corrosion of nano-structured magnetron-sputtered coatings,” *Coatings*, vol. 9, no. 10, p. 682, Oct. 2019.
- [346] K. Leelaruedee *et al.*, “Electrochemical and surface chemistry of amorphous chromium-zirconium film prepared by magnetron sputtering,” *Surfaces and Interfaces*, vol. 31, p. 102036, Jul. 2022.
- [347] M. Bouroushian and T. Kosanovic, “Characterization of Thin Films by Low Incidence X-Ray Diffraction,” *Cryst. Struct. Theory Appl.*, vol. 1, pp. 35–39, 2012.
- [348] “The interactive Ellingham diagram.” [Online]. Available: https://www.doitpoms.ac.uk/tlplib/ellingham_diagrams/interactive.php. [Accessed: 27-Dec-2022].
- [349] A. Cezairliyan and F. Righini, “Thermodynamic Studies of the $\alpha \rightarrow \beta$ Phase Transformation in Zirconium Using a Subsecond Pulse Heating Technique,” *J. Res. Natl. Bur. Stand. Sect. A, Phys. Chem.*, vol. 79A, no. 1, p. 81, Jan. 1975.

- [350] N. Bertrand, C. Desgranges, D. Poquillon, M. C. Lafont, and D. Monceau, “Iron oxidation at low temperature (260-500 °c) in air and the effect of water vapor,” *Oxid. Met.*, vol. 73, no. 1–2, pp. 139–162, 2010.